Development and Study of Earth-Abundant Oxide Based Thin Films for Solar Cells by Ultrasonic Spray Pyrolysis : From Unbeknownst to Erudite Processes

Sourav Bose

THÈSE

Pour l'obtention du titre de

DOCTEUR de L'UNIVERSITÉ DE LORRAINE

Spécialité : Science des Matériaux

Présentée par

Sourav BOSE

Development and Study of Earth-Abundant Oxide Based Thin Films for Solar Cells by Ultrasonic Spray Pyrolysis: *From Unbeknownst to Erudite Processes*

Soutenue publiquement le 16 septembre 2022 à Metz devant le jury composé de :

Jean-François PIERSON	Président	Professeur, Université de Lorraine, Institut Jean Lamour, CNRS; Nancy, France
Thomas HEISER	Rapporteur	Professeur, Université de Strasbourg, ICUBE, CNRS; Strasbourg, France
Marie GUEUNIER-FARRET	Rapportrice	Maîtresse de Conférences-HDR, Université Paris-Saclay, GeePs, CNRS; Gif-sur-Yvette, France
Carmen MARCO DE LUCAS	Examinatrice	Professeur, Université Bourgogne Franche-Comté, ICB, CNRS; Dijon, France
Alessandra ALBERTI	Examinatrice	Senior Researcher, CNR IMM; Catania, Italy
Céline TERNON	Examinatrice	Maîtresse de Conférences-HDR, Grenoble-INP, LMGP, CNRS; Grenoble, France
Sidi OULD SAAD HAMADY	Directeur de Thèse	Professeur, Université de Lorraine, LMOPS, CentraleSupélec; Metz, France
Nicolas FRESSENGEAS	Codirecteur de Thèse	Professeur, Université de Lorraine, LMOPS, CentraleSupélec; Metz, France

Invitée :

Alison LENNON	Professor, UNSW, Chief Scientist, Sundrive; Syndey, Australia

UNIVERSITÉ DE LORRAINE
Ecole doctorale : Chimie – Mécanique – Matériaux – Physique (C2MP)
LMOPS – Laboratoire Matériaux Optiques, Photonique et Systèmes – UR 4423
Campus CentraleSupélec – 57070 Metz, FRANCE

Abstract

In this research work, the results on preparation of environmentally compatible, earth-abundant metal oxide thin films using the technique of ultrasonic spray pyrolysis are presented. This technique is a promising technique for preparing low-cost, high-efficiency photovoltaic devices. Three essential materials are developed for the purpose of realization efficiency of an “all-oxide” solar cell device: zinc oxide (ZnO) as window layer; zinc magnesium oxide (ZnMgO) as a buffer layer and cuprous oxide (Cu_2O) used as an absorber layer. Comprehensive design of experiments was set up for the preparation of each material to understand the effect of a particular spray preparation parameter on the properties of the prepared films. Optical, structural, morphological, and electrical characterizations were used to investigate the film properties. The results are discussed and analyzed thoroughly. We were able to successfully demonstrate the spray preparation parameters that needs to be fixed for preparing a high-quality film. Highly transparent ZnO was prepared in wide range of thickness with high crystalline qualities with specific preparation temperature with a precise control on the concentration of the precursors. ZnMgO was prepared by varying the molar compositions of the magnesium precursor in the precursor solution. Up to nearly 30 % of Mg, the ZnMgO films exhibited single crystalline phase with high transparencies as evidenced from the structural, chemical, and optical characterizations. The magnesium miscibility limit (nearly 30 % in our case) is higher than usually obtained in non-vacuum solution-based methods. High-absorbing Cu_2O preparation was optimized with effective control on the preparation temperature and the concentration of a new reducing agent: D-sorbitol. To expand the horizon of efficiency of our preparation process, two more materials, ZnAlO and ZnAlMgO, were prepared. It was found with low molar concentrations of aluminum the optical, electrical, and structural properties of the ZnAlO films could be modulated for use as window cum top-contact layer in “all-oxide” solar cells. The fixed low molar concentrations of aluminum were used in conjunction with varying magnesium (up to 7 mol%) to prepare ZnAlMgO films. The bandgap energies and the electrical properties of the films were modulated with the co-incorporation so that they can be integrated as window/top-contact/buffer layers in “all-oxide” solar cells. Additionally, simulations performed using Silvaco Atlas® and Solis also demonstrates the applicability of these films for “all-oxide” solar cells.

Keywords: Ultrasonic Spray Pyrolysis, Semiconductors, Zinc Oxide, Zinc Magnesium Oxide, Copper Oxide, Preparation, Thin Film, Structural Properties, Optical properties, Electrical properties, All-Oxide Solar Cell, Photovoltaics.

Résumé

Dans ce travail de recherche, sont présentés les résultats de l'élaboration de couches minces d'oxydes à base d'éléments abondants par la technique de spray pyrolyse ultrasonique. Cette technique est prometteuse pour élaborer des couches minces à bas coût. Trois matériaux constituant les briques de base de la cellule solaire « tout oxyde » ont été développés : l'oxyde de zinc (ZnO) comme couche fenêtre ; l'oxyde de zinc et de magnésium (ZnMgO) comme couche tampon et l'oxyde de cuivre (Cu_2O) comme couche absorbante. Un plan d'expériences précis a été mis en place pour chaque type d'élaboration afin de comprendre l'effet des paramètres d'élaboration sur les propriétés des films. Des caractérisations optiques, structurelles, morphologiques et électriques ont été utilisées pour étudier les propriétés du film et les résultats discutés et analysés en détail. Nous avons pu démontrer que l'approche utilisée permet d'obtenir des films de haute qualité avec un procédé maîtrisé. Ainsi, des films minces de ZnO avec une transparence élevée dans une large gamme d'épaisseurs ont été obtenus avec une température d'élaboration spécifique et un contrôle précis de la concentration des précurseurs. Le ZnMgO a été élaboré avec près de 30 % de miscibilité de Mg. Les films de ZnMgO présentaient une phase monocristalline avec une transparence élevée, comme montré par les caractérisations structurales et optiques. La limite de miscibilité du magnésium (près de 30 % dans notre cas) est supérieure à celle habituellement obtenue avec les méthodes d'élaboration sans vide. L'élaboration de l'absorbeur Cu_2O a été optimisée avec un contrôle efficace de la température d'élaboration et de la concentration d'un nouvel agent réducteur, le D-sorbitol. Pour élargir les perspectives de ce travail, deux autres matériaux, ZnAlO et ZnAlMgO, ont été élaborés. Nous avons ainsi mis en évidence le fait qu'avec de faibles concentrations d'aluminium, les propriétés optiques, électriques et structurales des films de ZnAlO pouvaient être modulées pour une utilisation en tant que couche fenêtre ou TCO dans les cellules solaires « tout-oxyde ». L'incorporation du magnésium (jusqu'à 7 %) a permis d'élaborer des films de ZnAlMgO avec énergies de gap et des propriétés électriques modulables permettant de les intégrer en tant que couches fenêtre, couche tampon, ou TCO dans la cellule solaire « tout-oxyde ». De plus, les simulations réalisées à l'aide des logiciels Silvaco Atlas® et Solis démontrent également le potentiel de ces films pour les cellules solaires « tout-oxyde ».

Mots-clés : Spray pyrolyse ultrasonique, Semi-conducteurs, Oxyde de zinc, Oxyde de zinc et de magnésium, Oxyde de cuivre, Élaboration, Couche mince, Propriétés structurales, Propriétés optiques, Propriétés électriques, Cellule solaire « tout-oxyde », Photovoltaïque.

Résumé étendu

Elaboration par spray pyrolyse ultrasonique et étude de couches minces à base d'oxydes d'éléments abondants pour le photovoltaïque

Dans la filière des couches minces, qui constitue l'une des technologies les plus importantes pour le photovoltaïque, l'objectif est de développer des procédés de fabrication permettant un compromis entre un rendement de conversion élevé et un coût faible. Une famille de matériaux utilisés dans cette filière et qui peuvent répondre à cet exigeant compromis sont les oxydes d'éléments abondants qui peuvent permettre de fabriquer une cellule solaire « tout-oxyde ».

Dans ce cadre, l'objectif de cette thèse était d'élaborer des couches minces à base d'oxydes d'éléments abondants en utilisant la technique polyvalente et peu coûteuse du spray pyrolyse ultrasonique (USP = Ultrasonic Spray Pyrolysis). Les procédés développés avec cette technique de croissance peuvent être facilement transférés à l'industrie pour l'élaboration sur de grandes surfaces. Les matériaux qui font l'objet de ce travail de recherche, les oxydes métalliques, sont une famille de semi-conducteurs à très fort potentiel pour le photovoltaïque : ils sont abondants dans la croûte terrestre, non toxiques et peuvent être élaborés aisément. La structure entière de la cellule solaire constituée de la couche de contact supérieure transparente, de la couche-fenêtre, de la couche tampon et de la couche absorbante, peut être fabriquée avec des oxydes métalliques en utilisant cette technique. Ce type de procédé de fabrication utilisant une seule méthode d'élaboration pour l'ensemble de la cellule solaire n'a pas été mis au point à ce jour.

Il s'agit dans ce travail de recherche d'optimiser les paramètres d'élaboration des couches minces, et en particulier l'optimisation de la solution précurseur, de la température de dépôt et du scan, pour obtenir des films minces d'oxyde métallique de haute qualité, homogènes et ayant les propriétés optoélectroniques requises pour l'application photovoltaïque. Ce travail d'optimisation est fait grâce notamment à l'utilisation de nombreuses techniques de caractérisation des propriétés morphologiques, optiques, structurales et électriques.

Nous avons démarré le travail de recherche en élaboration des oxydes à partir de rien, avec l'installation du nouvel équipement USP au laboratoire en juin 2019, quelques mois avant le début de la thèse. Tout était à faire, et les procédés devaient être mis au point et optimisés. Le travail de recherche a commencé par l'optimisation des solutions précurseurs et la conception et le choix des

matériaux pour le porte-substrat thermique qui a un impact important sur la qualité des matériaux élaborés. Tous les films ont été élaborés sur du verre sodé (SLG = Soda Lime Glass).
Pour chaque élaboration, pour un matériau donné, les paramètres ont été variés, et les propriétés morphologiques, optiques et structurales des films minces ont été étudiées en détail. L'analyse des résultats a permis de comprendre l'effet des paramètres d'élaboration, et les résultats ainsi obtenus ont été comparés à ceux des films minces optimaux obtenus par d'autres techniques d'élaboration. Les étapes expérimentales ont été rigoureusement suivies pour définir un ensemble de paramètres optimisés pour chaque type d'oxyde métallique, avec trois étapes essentielles : (i) la mise au point du procédé d'élaboration par USP ; (ii) la caractérisation morphologique, optique, structurale et électrique des films élaborés ; (iii) l'optimisation des couches pour préparer la réalisation d'un dispositif de cellule solaire « tout-oxyde ».

Ce travail est présenté dans ce manuscrit en **7 chapitres** résumés ci-dessous.

Le **chapitre 1** est une introduction générale sur le photovoltaïque et les oxydes semi-conducteurs. Le développement du photovoltaïque et son importance dans la demande énergétique moderne sont présentés. Le principe physique de fonctionnement des cellules solaires ainsi que les différents types de cellules (classés selon les avancées technologiques majeures) sont également abordés. Dans ce contexte, dans la deuxième partie du chapitre, les bases des semi-conducteurs à oxyde métallique sont abordées ainsi que la revue de la littérature des types de cellules solaires « tout-oxyde » en mettant l'accent sur les oxydes métalliques. Les détails sur les hétérostructures $Zn(Al)O/Cu_2O$ les plus recherchées pour les cellules solaires « tout-oxyde » sont discutés. En outre, la simulation numérique effectuée pour étudier les performances des cellules solaires « tout-oxyde » ainsi que le choix approprié des matériaux sont présentés. Dans la dernière partie, les objectifs et les défis du travail de thèse sont présentés ainsi que le plan du manuscrit.

Le **chapitre 2** est consacré aux principes de base du spray pyrolyse ultrasonique (USP) qui est utilisé pour l'élaboration des couches fenêtre, tampon et absorbante. Une présentation détaillée des paramètres d'élaboration USP est effectuée. Cela inclue la température de dépôt, la pression de la buse, la distance buse-substrat, le flux, la vitesse de scan, le nombre de scans, le temps d'arrêt, la puissance des ultrasons, et les propriétés de la solution de précurseurs (pH et concentrations). L'effet de ces paramètres est étudié grâce aux techniques de caractérisation des propriétés morphologiques, optiques, structurales et électriques des couches minces qui sont présentées dans ce chapitre.

Le **chapitre 3** concerne le développement et l'optimisation du ZnO utilisé comme couche fenêtre. Les propriétés du ZnO sont brièvement discutées. L'élaboration de ZnO avec une qualité optimale est discutée en détail. L'optimisation des paramètres d'élaboration est effectuée et leurs effets sur les propriétés morphologiques, optiques, structurales et électriques des films sont analysés.

L'ensemble du processus pour élaborer des films minces de ZnO de qualité optimale était difficile et long. Nous avons dû établir le plan d'expériences basé sur une vaste revue de l'état de l'art. La configuration du système d'élaboration par spray pyrolyse était la première tâche importante car tous les paramètres, y compris le support de substrat et le substrat lui-même, peuvent avoir un impact considérable sur les propriétés du film. La hauteur de la buse du spray par rapport au substrat et la vitesse de la buse ont été initialement calibrées et réglées en fonction des limites de sécurité du système. La durée de l'élaboration devait être fixée très soigneusement pour toutes les croissances. Au contact des gouttelettes atomisées, la température du substrat chute, et la durée de chaque cycle de spray et le temps d'arrêt entre deux cycles successifs permet au substrat à atteindre rapidement la température optimale. Pour vérifier la répétabilité et la fiabilité de notre procédé, chaque élaboration avec un ensemble donné de paramètres a été faite au moins trois fois. Les caractérisations optiques, morphologiques et structurales détaillées dans ce chapitre et leur analyse approfondie nous ont aidées à comprendre l'effet des paramètres sur la qualité du film. L'un des principaux objectifs de notre travail d'optimisation était de réduire drastiquement la formation d'hydroxydes durant l'élaboration, qui dégraderaient la qualité des films minces. Même de légers changements dans les conditions d'élaboration peuvent conduire à la formation d'hydroxydes, et c'est pourquoi un contrôle maximal de ces conditions d'élaboration est nécessaire. La compréhension du rôle des paramètres d'élaboration dans leur ensemble était importante car nous voulions développer des couches minces de ZnO avec des propriétés optoélectroniques compatibles avec leur utilisation comme couche-fenêtre dans les cellules solaires « tout oxyde ».

Ainsi ce travail a permis de développer des films avec une transparence très élevée dans le visible, avec une morphologie maîtrisée. La qualité cristalline mise en évidence par les mesures de diffraction de rayons X et spectroscopie Raman ont prouvé l'efficacité de notre procédé d'élaboration. Les paramètres d'élaboration optimaux dans ce procédé sont :

(i) La hauteur du de la buse du spray : 10 cm.

(ii) Vitesse de buse : 70 mm/seconde.

(iii) Temps d'arrêt entre deux cycles : 1 seconde.

(iv) Pression : 13,8 kPa.

Ces paramètres optimisés permettent de préparer des couches minces de ZnO qui remplissent les principaux critères d'utilisation comme couche fenêtre dans les cellules solaires « tout-oxyde » : (i)

vitesse de croissance rapide ; (ii) transparence élevée dans une large gamme d'épaisseurs allant de 100 nm à 800 nm ; (iii) orientation cristallographique selon l'axe c avec une grande taille de grain et des défauts minimisés ; (iv) une résistivité électrique relativement faible.

Le **chapitre 4** porte sur le développement et l'optimisation de la couche tampon. Le choix de $Zn_{1-x}Mg_xO$ pour la couche tampon est justifié en détail dans ce chapitre, avec notamment la possibilité de moduler les propriétés optoélectroniques pour les adapter à l'absorbeur. L'optimisation des paramètres d'élaboration ainsi que l'effet de l'ajout du magnésium sur les qualités du film sont détaillés.

Dans ce travail, nous avons développé un procédé d'élaboration de ZnMgO basé sur le spray pyrolyse ultrasonique en utilisant des solutions aqueuses dans la plage de composition en Mg allant jusqu'à 70 %. Pour les compositions de magnésium à partir de 30 %, une ségrégation de phase a été observée. Tous les films avaient une transmittance élevée d'environ 90 % dans le domaine visible, et variant très peu avec l'épaisseur, démontrant la maîtrise du procédé d'élaboration. Les variations de la largeur de la bande interdite et de l'énergie d'Urbach avec l'augmentation de la composition en magnésium ont été étudiées et corrélées aux caractéristiques structurales des films minces. Les caractéristiques structurales ont permis d'identifier la structure wurtzite comme la seule phase présente dans tous les films avec une composition en Mg inférieure à 30 %, tandis qu'une séparation de phase a été observée au-delà de cette composition. Lorsque la composition en Mg a été augmentée de 0 à 7 % en moles, les caractérisations électriques ont montré une chute significative de la concentration des porteurs. Lorsque la teneur en Mg dépasse 7 %, les films minces deviennent semi-isolants. Les résultats électriques impliquent qu'en plus de l'augmentation de la largeur de la bande interdite, un processus de compensation impliquant des défauts dans l'alliage joue un rôle clé dans la diminution de la concentration de porteurs. La mobilité augmente légèrement lorsque la teneur en magnésium augmente, indiquant que la qualité cristalline des films ne se détériore pas beaucoup lorsque la teneur en magnésium augmente dans la gamme étudiée. La grande transparence des films dans la région visible du spectre ainsi que la modulation de la largeur de la bande interdite et de la conductivité peuvent avoir des applications intéressantes pour la fabrication de cellules solaires, de photodétecteurs ultraviolets et d'autres composants optoélectroniques.

En résumé, l'élaboration par pyrolyse ultrasonique de ZnMgO à haute teneur en magnésium a été développée et des études structurales, optiques et électriques ont été menées avec une combinaison de propriétés optoélectroniques pouvant être exploitées pour les composants optoélectroniques. Les principales réalisations sont : (i) une limite de miscibilité du magnésium dans l'oxyde de zinc de 30 % ; (ii) une transparence dans le domaine visible supérieure à 90 % ; (iii) une largeur de la

bande interdite modulable de 3.26 eV à 3.65 eV ; (iv) diminution drastique de la concentration de porteurs avec l'augmentation de la teneur en Mg en raison de la modulation de la bande interdite et de l'inhibition des site interstitiels de Zn à l'origine des donneurs peu profonds.

Le **chapitre 5** concerne l'élaboration de la couche absorbante, l'oxyde de cuivre, élaborée et optimisée pour obtenir uniquement la phase Cu_2O. En effet, le Cu_2O s'oxyde rapidement en CuO, diminuant ainsi les performances des cellules solaires. Le rôle d'un nouvel agent réducteur, le D-sorbitol est analysé en détail.
Une étude structurale et optique détaillée a été réalisée pour évaluer la transition de phase dans des films minces d'oxyde de cuivre préparés par pyrolyse ultrasonique avec du D-sorbitol, avec un contrôle précis et poussée de la température d'élaboration. L'étude a permis de déterminer la plage de température dans laquelle seule la phase Cu_2O peut être formée, mais avec moins de défauts qu'avec l'agent réducteur classique, le glucose. En effet, l'étude en fonction de la concentration de D-sorbitol démontre que les caractéristiques optimales ont été atteintes sans l'utilisation excessive de D-sorbitol par rapport à l'acétate de cuivre, comme cela est courant lors de l'utilisation du glucose comme agent réducteur. L'utilisation d'une concentration plus faible d'agent réducteur entraîne moins de produits secondaires de pyrolyse, une diminution des défauts et une amélioration des caractéristiques électriques et optiques pour les applications optoélectroniques.
En résumé, l'élaboration par pyrolyse ultrasonique de couches minces d'oxyde de cuivre a été développée et optimisée à l'aide d'un nouvel agent réducteur, le D-sorbitol. Une étude optique et structurale complète a été réalisée. L'optimisation de la température d'élaboration à l'aide d'agent réducteur à faible concentration a été menée pour obtenir des films avec uniquement la phase Cu_2O ayant de bonnes propriétés optiques et structurales.

Le **chapitre 6** aborde les possibilités d'ajuster les propriétés optoélectroniques des alliages d'oxydes métalliques pour ouvrir la voie à la fabrication de l'ensemble de la cellule solaire « tout-oxyde ». Dans la première étape, l'alliage ZnAlO est élaboré pour une utilisation en tant que couche de contact supérieure (TCO pour « Transparent Conducting Oxide ») avec des paramètres de croissance optimisés. Dans la deuxième étape, et pour la première fois en utilisant le spray pyrolyse ultrasonique, un quaternaire d'oxyde d'aluminium, de magnésium et de zinc ($Zn_{1-x-y}Mg_xAl_yO$) a été élaboré. Le $Zn_{1-x-y}Mg_xAl_yO$ est polyvalent et peut être utilisé comme contact supérieur, couche-fenêtre ou encore comme couche-tampon. Enfin, un dispositif « tout oxyde » a été modélisé à l'aide du logiciel de simulation Solis pour montrer le potentiel de ces matériaux pour la réalisation du composant photovoltaïque.

Comme indiqué plus haut, le ZnAlO a été élaboré principalement pour être utilisé comme TCO en améliorant la conductivité avec l'incorporation d'Al. Avec des compositions molaires faibles en Al (1 et 2 %), la conductivité s'est révélée meilleure que celle du ZnO, mais cette conductivité a diminué au-delà de 2 % d'Al. De plus, en raison de la limite de solubilité extrêmement faible du précurseur d'aluminium, la transparence des films diminue lorsqu'ils sont élaborés avec une composition d'Al élevée. Ces résultats ont été très utiles dans le développement du quaternaire ZnMgAlO, avec la co-incorporation d'Al et de Mg. Ainsi la transparence des films de ZnMgAlO était optimale (supérieure à 90 %) avec une largeur de la bande interdite plus élevée. De façon corrélée, la qualité cristalline des films était meilleure qu'avec l'incorporation d'Al seul. Avec les différentes compositions Al et Mg, la structure wurtzite des cristaux a été conservée. Les propriétés électriques sont améliorées avec la co-incorporation d'Al et de Mg, en particulier pour les cas où les compositions de Mg sont élevées, notamment avec une mobilité plus élevée. La transparence élevée des films dans la région visible du spectre ainsi que la modulation de la largeur de la bande interdite et de la conductivité sont importantes pour des applications en tant que TCO, couche-fenêtres ou couche-tampon dans des cellules solaires « tout oxyde ». Le quaternaire ZnMgAlO peut aussi être utilisé dans les photodétecteurs ultraviolets et autres composants optoélectroniques.

Le **chapitre 7** est le chapitre de conclusion. Il met l'accent sur l'utilisation du spray pyrolyse ultrasonique pour l'élaboration de films minces d'oxydes métalliques de haute qualité. Tous les résultats importants obtenus sont résumés dans ce chapitre et les principales perspectives de ce travail de recherche sont présentées.

Acknowledgements

Pursuing the PhD at the **LMOPS laboratory** of the **Université de Lorraine** for 3 years has been an absolute privilege with lots of great learning experiences. I am immensely thankful to all the people for their co-operation, support and assistance which immensely contributed towards the success of this work.

In the first place, I would like to deeply thank my thesis director **Prof. Sidi OULD SAAD HAMADY** for always being there for me. His motivation, guidance, support and knowledge has helped in many different ways and has greatly contributed towards the successful completion of the thesis. He always showed immense faith in my abilities and his ideas, discussions, explanations, patience and encouragements throughout the duration of the thesis work needs to be cherished. The unparallel enthusiasm, positivity and energy helped me to better construct my research.

My sincere thanks go to my thesis co-director, **Prof. Nicolas FRESSENGEAS**, for his constant support and help. His knowledge, critical feedback, explanations and numerous discussions contributed greatly towards this thesis work. His help towards administrative matters also helped me a lot.

I am really very thankful to **Dr. Christyves CHEVALLIER**, for always being there for me. Christyves has helped me in all possible situations. From helping me to find an apartment, to speak in French to different persons on my behalf or in experimental and research work, Christyves has done it all. I owe a lot to him for a smooth stay in the beautiful city of Metz. Our friendly discussions, the fun during working together, nice dinners at French restaurants and car drives to Nancy while listening to Bollywood songs are some happy memories that will stay with me for a long long time.

Thanks a lot, to **Stéphanie VERGERIO**, for her pleasant behaviour and for always happily helping me in all the administrative tasks. Thanks a lot also to **Queny KIEFFER** and **Maryne CROUZET** for their assistance in laboratory technical matters, ordering of items and for chemical assistance. All of your help has contributed greatly towards my research work.

Merci Beaucoup Jean-Claude. **Jean-Claude PETIT** is a person from whom I have learnt positivity. Jean-Claude is not only my colleague, I consider him as one of my best friends. I can discuss anything and everything with him. Whatever, French I speak and understand is because of you. Jean-Claude

is my coffee partner. Starting the day at the lab, with some friendly discussions always helped me to start the work on a positive note. Your help towards my experiments and your immense knowledge in the technical aspects has helped my research in a great way. I will miss you.

Thanks to **Prof. David HORWAT** and **Prof. Jean-François PIERSON** for being actively involved in the research work. Their discussions, knowledge and support has contributed immensely towards the quality improvement of the thesis.

I would like to sincerely thank **Dr. Thomas KAUFFMANN** for always his help and discussions on Raman spectroscopy, X-ray fluorescence and FTIR.

I would also sincerely like to thank **Prof. Patrice BOURSON**, **Prof. Germano MONTEMEZZANI**, **Prof. Thierry AUBERT**, **Dr. David CHAPRON**, **Dr. Virginie CODA-BOUCHOT**, **Prof. Alain MAILLARD**, **Prof. Michel AILLERIE**, **Dr. Zhixue ZHENG** and **Dr. Laurent WEISS** for always their support and friendly discussions.

I am also thankful to **Dr. Brigitte VIGOLO-GREFFIER** and **Prof. Aotmane EN-NACIRI** for agreeing to be the members of "Comité de suivi" for my thesis. Insightful suggestions from both of them, help and support has motivated me a lot to continue my research in a positive way.

Thanks to **Stéphane MARCHAL** for always his friendly behavior, help and support.

I also want to thank **Dr. Pascal BOULET** and **Dr. Olivier PERROUD** for their help with XRD measurements, **Dr. Julien GUYON** for his help with the SEM, **Dr. Thomas GRIES** and **Dr. Montassar BILLEH BOUZOURÂA** for their help with AFM.

I am immensely thankful to **Mr. Laurent SCHMIDT** for always his help and support. He has always helped me a lot towards the visa procedures with detailed information. Also, I would like to thank **Mme. Nawal AQAIDI** for her help towards administrative matters.

I am thankful to **Mme. Christine SARTORI**, **Prof. Dominique DALOZ** and **Mr. Stéphane LEBRETON** for their help in matters related to ADUM, the doctoral studies and university registration procedures.

I am also exceptionally thankful to my friends from LMOPS and from Université de Lorraine: **Ahmad Sauffi BIN YUSOF** (also from Universiti Sains Malaysia)**, Rokaya EL OTMANI** (University of Casablanca – Morocco)**, Dr. Christy FADEL**, **Sadaqat ALI, Muhammad Waqar IQBAL, Dr. Yaya DOUMBIA, Rodolph ISKANDAR, Christelle HABIS, Carmen MOYA LOPEZ PELAEZ, Lucas OLIVERIO, Jordan MAUFAY, Nawal FERDI, Xin WANG, Dr. Rim ALRIFAI, Dr. Bachirou BOGNO, Dr. Luis Antonio García GUTIÉRREZ, David Javier Rincón ADARME, Dr. Dieudonné KIDMO KAOGA, Surya Nilamegam KUMARAN, Mohammad Iktiham Bin TAHER, Mohammed El ISMAILI, Dr. Ali ZAITER and Dr. Montassar BILLEH BOUZOURÂA** for their tremendous support, understanding and encouragement throughout the thesis period.

Thank you so much, my friend **Rohit GUPTA** for the constant encouragement, long friendly chats, and motivation. Much thanks go out to my friend, philosopher and guide **Dr. Aruanva PRADHAN** (Arunava da, as I call him) for his constant support, motivation and guidance.

I am really lucky to have friends like **Debopam BASU** and **Soumya BOSE**. They have supported me and cared for me whole-heartedly from overseas. I have received impeccable support and motivation from them during the thesis period.

A very special thanks and appreciation to my parents and my sister for their overwhelming and unending support that grew even stronger during this thesis period. Knowing the fact that I am being loved from far across was a vital motivation for the successful completion of the thesis. No words are enough to express my thanks to them. The love and support of my father, **Amit Kumar BOSE**, my mother **Krishna BOSE** and my sister **Arpita BOSE** is something that always kept me going. I miss my grandfather **Late Sri Hemendra Kumar BOSE**, I know that I am loved from high up in the skies.

Finally, I would like to thank each and every one for their support and help. My sincere apologies to all the people whom I could not mention in this small space. All of your support and assistance has been instrumental in the successes I have recorded thus far. I am forever grateful to all.

Thank you so much!
Sourav

Dedicated to my grandfather, my parents and my sister

"*Imagination is more important than knowledge. Knowledge is limited. Imagination encircles the world.*"
Albert Einstein

"*The sun, --the bright sun, that brings back, not light alone, but new life, and hope, and freshness to man-- burst upon the crowded city in clear and radiant glory. Through costly-coloured glass and paper-mended window, through cathedral dome and rotten crevice, it shed its equal ray.*"
Charles Dickens, Oliver Twist

Table of Contents

List of Figures

List of Tables

List of Abbreviations

4PP: four-point probe.

AALD: atmospheric atomic layer deposition.

ALD: atomic layer deposition.

AFM: atomic force microscopy.

ALD: atomic layer deposition.

AZO: aluminum (or *aluminum-doped*) zinc oxide (ZnAlO).

CPV: concentrator photovoltaics.

CVD: chemical vapor deposition.

ECD: electrochemical deposition.

FF: fill factor.

FTIR: Fourier transform infrared spectroscopy.

FTO: fluorine-doped tin oxide.

I_{SC}: short-circuit current.

ITO: indium tin oxide.

J_{SC}: short-circuit current density.

MOCVD: metal organic chemical vapor deposition.

MOVPE: metal organic vapor phase epitaxy.

PCE: power conversion efficiency.

PLD: pulsed laser deposition.

PV: photovoltaic.

RF sputtering: radio-frequency sputtering.

RMS: root mean square.

RPE-CVD: remote-plasma-enhanced chemical vapor deposition.

RTA: rapid thermal annealing.

SEM: scanning electron microscopy.

SLG: soda lime glass.

SMU: (electrical) source and measure unit.

TCM: transparent conducting (or conductive) material.

TCO: transparent conducting (or conductive) oxide.

USP: ultrasonic spray pyrolysis.

VAPE: vacuum arc plasma evaporation.

vdP: van der Pauw.

V_{OC}: open-circuit voltage.

XRD: X-ray diffraction.

XRF: X-ray fluorescence.

CHAPTER 1: Earth-Abundant Oxide Semiconductors for Photovoltaics: Current State and Challenges

1.1 General Introduction to Photovoltaics

The study of photovoltaics deals with the direct conversion of solar radiation to electricity. French physicist Alexandre Edmond Becquerel was the first who evidenced the photovoltaic effect in 1839 [1,2]. Few years later in 1873, Willoughby Smith found the photovoltaic effect in selenium [3]. In March 1905, Albert Einstein, in his paper "*Über einen die Erzeugung und Verwandlung des Lichtes betreffenden heuristischen Gesichttspunkt*" ("*On a Heuristic Viewpoint Concerning the Production and Transformation of Light")*, explained the photovoltaic effect and sent it to the famous German journal "Annalen der Physik" [4–6]. Research on the photovoltaic effect was carried forward at the Bell Laboratories and after several years in 1951 produced a photovoltaic solar cell made of germanium with an efficiency of 4.5 % [7,8]. Later, in 1954 Chapin *et al.* [9,10] from the same laboratory created an improved solar cell from silicon which produced a conversion efficiency of about 6 %. Soon after, in 1960, the efficiency reached 14 % for applications in space technologies [11]. Since 1970's not only the research, but even the production of photovoltaic modules increased enormously. Due to the inherent advantages commercial solar cells and modules were becoming more and more prominent as cheaper energy suppliers. In the ***Sections 1.1.1*** and ***1.1.2*** the importance and need for the photovoltaic technology and the physics of the solar cells are discussed respectively.

Figure 1.1: The Einstein's article on the photovoltaic effect published in "Annalen der Physik" in 1905. Right: Einstein in the same year, 1905 [12]**.**

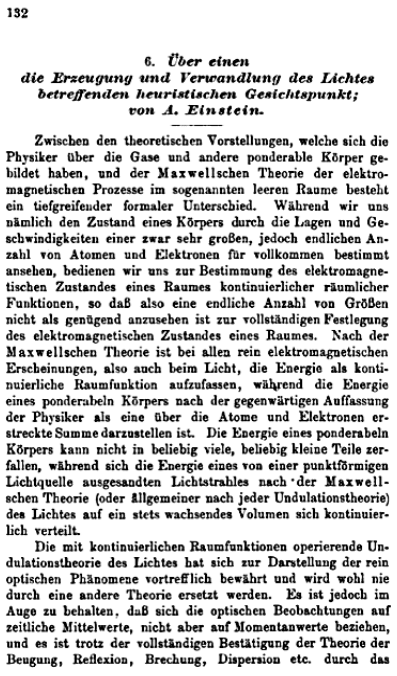

132

6. *Über einen die Erzeugung und Verwandlung des Lichtes betreffenden heuristischen Gesichtspunkt;* von A. Einstein.

Zwischen den theoretischen Vorstellungen, welche sich die Physiker über die Gase und andere ponderable Körper gebildet haben, und der Maxwellschen Theorie der elektromagnetischen Prozesse im sogenannten leeren Raume besteht ein tiefgreifender formaler Unterschied. Während wir uns nämlich den Zustand eines Körpers durch die Lagen und Geschwindigkeiten einer zwar sehr großen, jedoch endlichen Anzahl von Atomen und Elektronen für vollkommen bestimmt ansehen, bedienen wir uns zur Bestimmung des elektromagnetischen Zustandes eines Raumes kontinuierlicher räumlicher Funktionen, so daß also eine endliche Anzahl von Größen nicht als genügend anzusehen ist zur vollständigen Festlegung des elektromagnetischen Zustandes eines Raumes. Nach der Maxwellschen Theorie ist bei allen rein elektromagnetischen Erscheinungen, also auch beim Licht, die Energie als kontinuierliche Raumfunktion aufzufassen, während die Energie eines ponderabeln Körpers nach der gegenwärtigen Auffassung der Physiker als eine über die Atome und Elektronen erstreckte Summe darzustellen ist. Die Energie eines ponderabeln Körpers kann nicht in beliebig viele, beliebig kleine Teile zerfallen, während sich die Energie eines von einer punktförmigen Lichtquelle ausgesandten Lichtstrahles nach der Maxwellschen Theorie (oder allgemeiner nach jeder Undulationstheorie) des Lichtes auf ein stets wachsendes Volumen sich kontinuierlich verteilt.

Die mit kontinuierlichen Raumfunktionen operierende Undulationstheorie des Lichtes hat sich zur Darstellung der rein optischen Phänomene vortrefflich bewährt und wird wohl nie durch eine andere Theorie ersetzt werden. Es ist jedoch im Auge zu behalten, daß sich die optischen Beobachtungen auf zeitliche Mittelwerte, nicht aber auf Momentanwerte beziehen, und es ist trotz der vollständigen Bestätigung der Theorie der Beugung, Reflexion, Brechung, Dispersion etc. durch das

Figure 1.2: Gerald Pearson, Daryl Chapin and Calvin Fuller (from left to right), the inventors of the first silicon solar cell in 1954 [13].

1.1.1 Photovoltaic Technology for Green Energy

"**Our dependence on fossil fuels amounts to global pyromania, and the only fire extinguisher we have at our disposal is renewable energy.**" - Hermann Scheer, German statesman and entrepreneur.

In the past few decades, the world has witnessed the importance of energy usage in terms of human civilization. With the rapid population increase, the demand for energy is rising steeply. By the year 2050, the UN expects the world population to reach 9.3 billion [14]. The huge technological and economic developments, specifically in the developing countries, have also contributed to the enormous increase in energy demand. According to the recent statistics from International Energy Agency (IEA) it is estimated that from 2010 to 2040 there can be another one-third increase in the global energy use where countries like China and India could account for almost 50 % of the increased growth in demand [15,16]. The current energy supply will be insufficient towards the requirement if the demand continues in this rapid increasing trend.

Due to this huge demand of energy the production of non-renewable resources has increased rapidly. To satisfy the demand, the use of fossil fuels also soared up, although the usage cost is high too. Among the primary energy sources present, globally fossil fuels accounts for 74 % of total energy used [17]. It is an undisputed fact that the rampant use of the fossil fuels leads to the enormous quantities of greenhouse gases being released to the atmosphere which directly contributes to the rise of global temperature thereby contributing immensely to the earth's climate change. The shrinkage of the Arctic ice and the increase in sea levels are the direct consequences of global warming. Submergence of coastal and low-lying regions and salt-water intrusion to groundwater are inevitable due to rise of sea-levels [18–21]. So, to preserve the earth's ecosystem, the demand for a sustainable energy supply that serves our energy demands is ever so high.

Sustainable energy technologies such as hydropower, wind power, geothermal energy, solar energy etc. are some of the prominent options which can fulfill the energy demands better than fossil fuels. Nuclear energy too can be an option but in case of an accident its consequences could be dangerous as seen in cases of Chernobyl in 1986 and Fukushima ten years ago [22,23]. Biomass is another potent option for fuel source, but its extensive use without proper planning and management could lead to deforestation which in turn may result in the imbalance of the ecosystem [24,25]. Renewable energy generated from sun, wind and water are not only sustainable but also safe. But none of them can solely satisfy the criteria of meeting the global energy demands [26,27]. A recent review study from Lai *et al.* [28] and an extensive study by Sharifzadeh *et al.* [29], incorporates the concept of machine learning to the different renewable energy concepts and shows that both wind and solar energies would go a long way in satisfying the global energy demand but with solar energy taking a slender lead in this matter. So, we focus our attention to the details of solar PV energy production.
The earth receives about 173000 terawatts (trillions of watts) of solar energy over a span of 1 year which is approximately 10000 times the energy consumed worldwide [30,31].
Solar energy technology which incorporates photovoltaic (PV) solar cells works by directly converting the solar radiation into electricity. The worldwide PV electricity share is 3.2 % [32]. Based on the report from IRENA, it is predicted that the global share of solar PV power generation would reach up to 13 % by 2030 and to 25 % by 2050, thanks to the supporting policies and reductions in production costs [33]. Alongside, the decrease in the costs, in the last decade, the installation of PV systems has increased from 14 % to 18 % globally [33]. Thus, the price of electricity has also decreased considerably in most regions in the past decade [34,35]. Electricity generation from solar photovoltaics has been one of the cheapest among all the possible sources. Continuing in this trend, PV technology will not only be a key contributor to electricity generation

but also a major contributor to all the segments of the global energy system [36]. The global economy will also be benefitted by the fact that solar PV cost is expected to dramatically decrease in the coming decades [33].

Majority of the solar cells which are manufactured today globally, comprises of crystalline silicon as the base material. Silicon based solar cells can be called as the first-generation solar cells. The efficiency record for a silicon solar cell is 26.7 % in laboratory [37–39].

Solar cells based on thin film are also being fabricated. These solar cells have several advantages over traditional solar cells [40–43]. Recent research on solar cells is also focussed on developing advanced materials and processes to ramp up the conversion efficiencies along with reduction of production costs [44,45]. In the next section we will discuss about the basic working principles of solar cells.

1.1.2 Solar Cells

A solar cell is usually based on a p-n semiconductor junction device converting the incident sunlight into electric current. A typical p-n junction solar cell structure is shown in ***Figure 1.3***. To understand in depth about semiconductor properties literatures [46–53] can be looked upon.

Figure 1.3: Schematic of a typical solar cell structure.

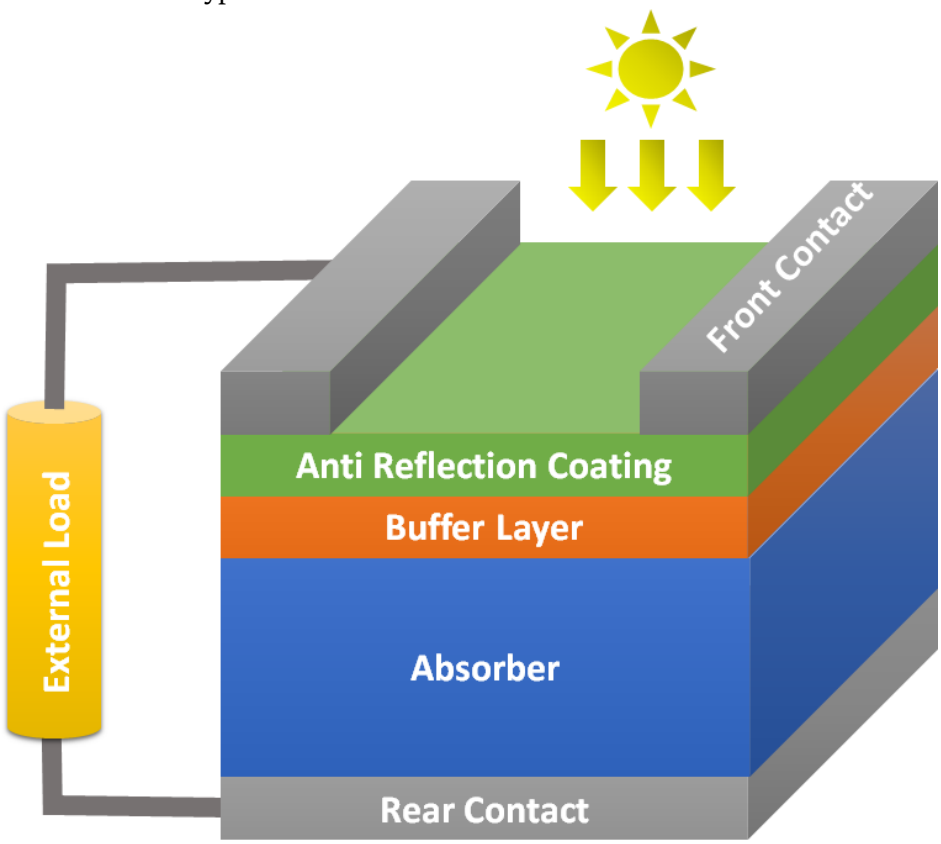

In semiconductors, Fermi energy lies in the forbidden energy zone and is related to the carrier concentration and can be controlled e.g., by doping [46,52,53]. The positioning of the valence and conduction bands along with the Fermi energy level will help us to understand the differences among insulations, semiconductors, and conductors (***Figure 1.4***). In insulators, the forbidden energy gap is too high (typically bandgap greater than 3 eV) so no free electrons are available in the conduction band and thus no conductivity. In semiconductors, the conductivity is between that of a conductor and insulator (0.5 to 3 eV typically), depending upon the temperature. At very low temperatures, semiconductors are insulators too, but with increasing temperature, electrons are excited to be promoted to the conduction band. Thus, conductivity increases. In conductors (for e.g., metals) there is no forbidden band, and the conductivity is very high in a wide range of temperature [52,53].

In a pure semiconductor material, the average number of free electrons and holes at a particular temperature is known as the intrinsic carrier concentration n_i [52,54,55]. The index "i" means *intrinsic* and indicates an undoped semiconductor. It is determined from the following equation:

Equation (1.1):

$$n_i = \sqrt{N_C N_V}\ exp\left(-\frac{E_G}{2\,k\,T}\right)$$

Where N_C, N_V, k, E_G and T stands for density of states respectively in the conduction and in the valence band; Boltzmann constant, Bandgap energy and temperature in Kelvin respectively.

Figure 1.4: Energy band diagram of the three types of material considering the electric conductivity. In a semiconductor, electron can absorb a photon and be promoted to from the valence band to the conduction band, leaving a hole in the valence band.

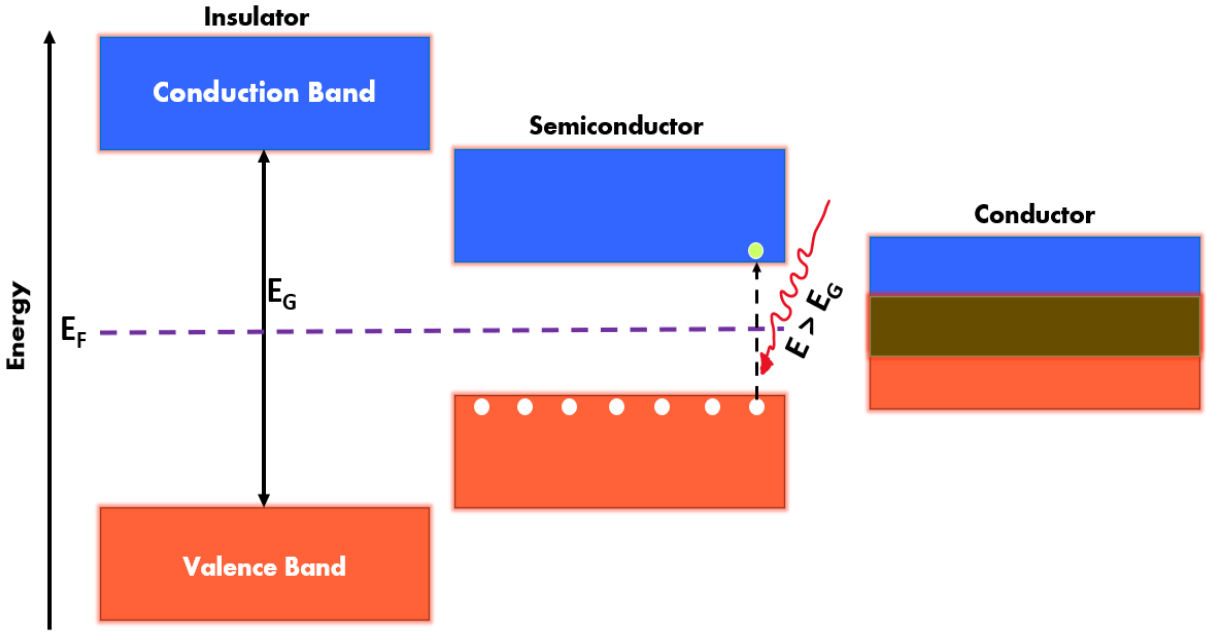

Figure 1.5: Schematic energy-band diagram showing the positioning of Fermi energy levels for n type, p type and intrinsic semiconductors.

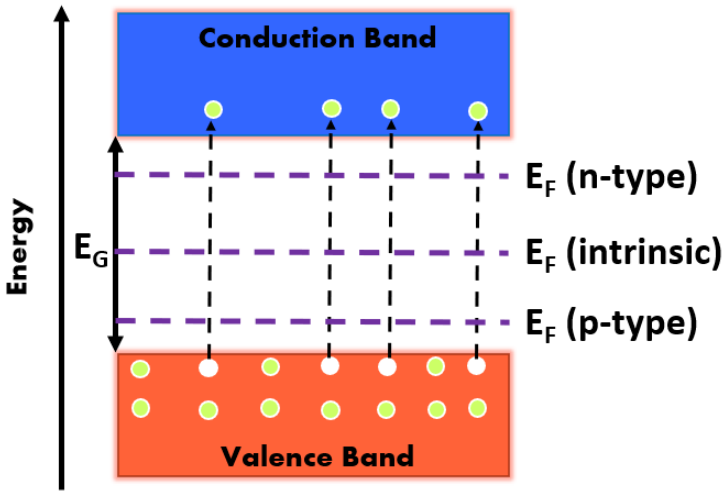

In n-doped semiconductors, the concentration of electrons is higher than the concentration of holes, and the Fermi level E_F is located near the conduction band. Similarly, for p-doped semiconductors E_F is located near the valence band since the concentration of holes is higher (***Figure 1.5***). More details about this phenomenon can be found in the literatures [46,52,54-57].

When a p-doped and a n-doped semiconductors are in contact, a diffusion phenomenon occurs to form the depletion region and induces the internal electric field in the p-n junction, shown in the ***Figure 1.6***. The corresponding potential $\mathbf{q \times V_D}$ that builds up in the junction can be written as:

Equation (1.2):

$$q \times V_D = E_G - k \times T * \ln\left(\frac{N_C N_V}{N_D N_A}\right)$$

In the above equations, N_C and N_V are respectively the density of states in the conduction band and in the valence band. E_G is the bandgap energy. N_D and N_A are respectively the donor and acceptor concentrations. The potential $\mathbf{q \times V_D}$ is shown in the ***Figure 1.7***.

Figure 1.6: Schematic diagram of p-n junction.

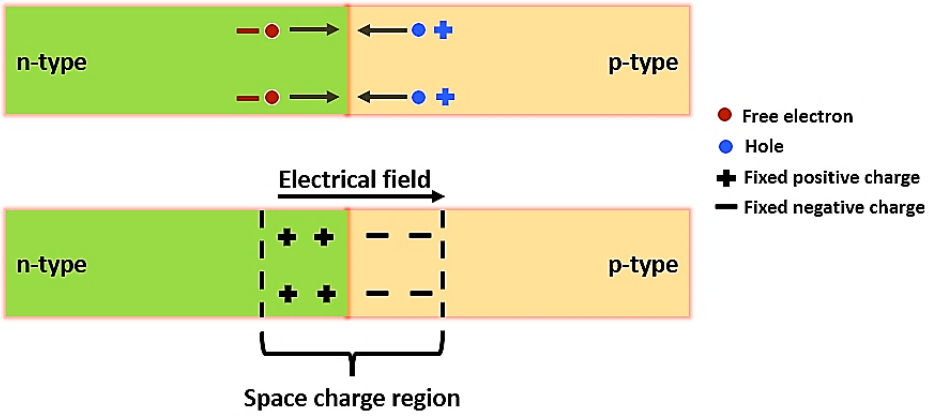

Figure 1.7: Diffusion potential V_D of a p-n junction [52].

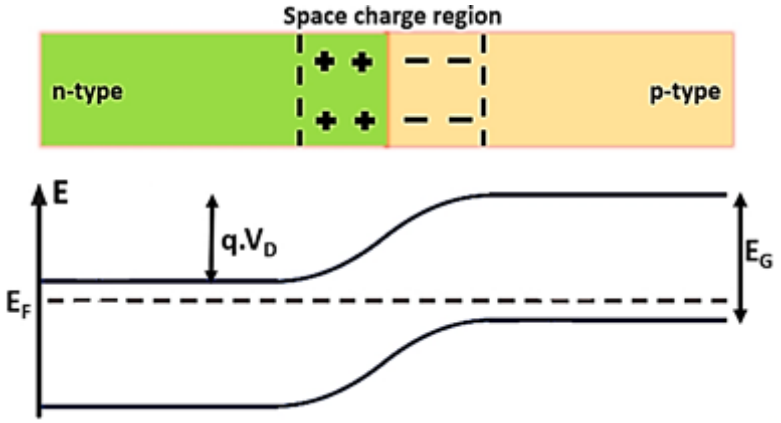

Under illumination, the carriers that are photogenerated in the depletion region and outside are extracted due to the action of the internal electric field and diffuses to the contacts. There are certain recombination centres known as mid-gap states, acts as nonradiative centers. There are some shallow traps too that hinders slightly the mobility of carriers but are much less detrimental as they keep the lifetime of carriers nearly unchanged. This is mostly the case for homojunctions. A diagram of a p-n junction under illumination is shown in the ***Figure 1.8***.

Figure 1.8: Energy diagram of a p-n junction under illumination showing the electron-hole photogeneration, the deep trap assisted recombination, the drift and diffusion of photocarriers [57].

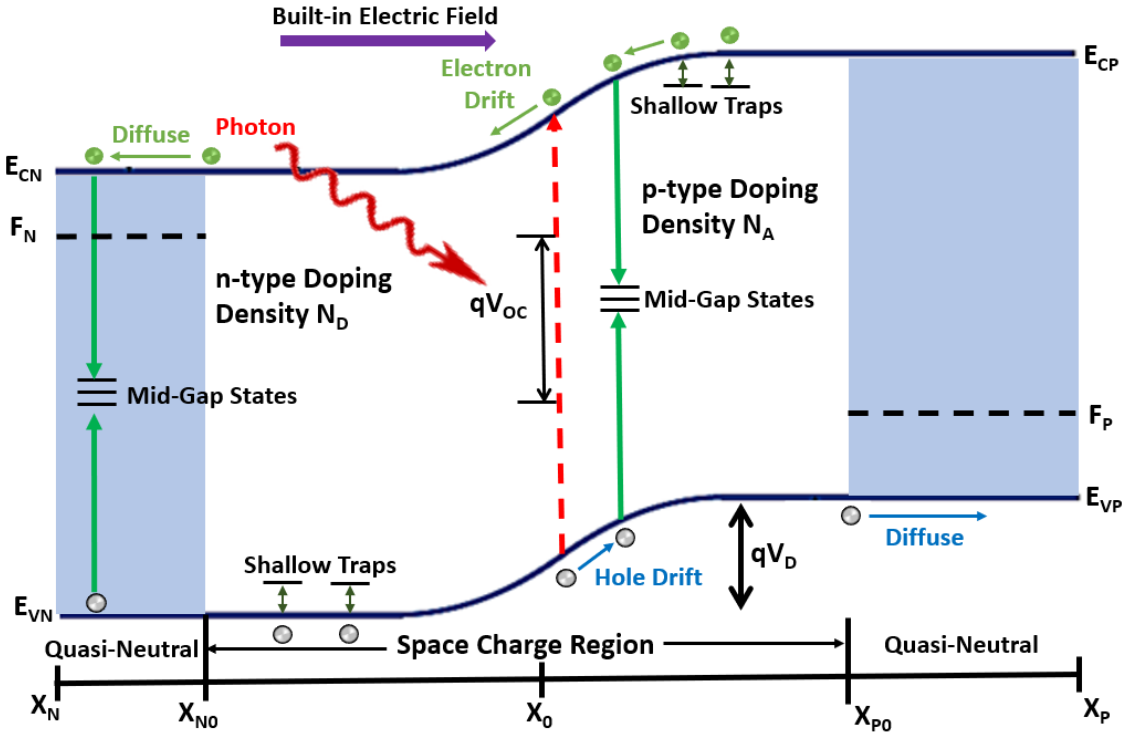

Under illumination, the absorption occurs for photons with energy higher than the bandgap. The additional energy of the electrons over the band gap is lost through thermalization loss. The wavelength at which the photons are just absorbed is the bandgap wavelength (λ_G). The solar spectrum which is above λ_G cannot be used for providing electrical energy and hence termed as transmission losses. A balance between the absorption while minimizing the thermalization losses defines the theoretical limit for power conversion efficiency (PCE). The theoretical limit of PCE has been calculated by the Shockley-Queisser model based on certain assumptions and considering an ideal p-n diode model estimated the optimal band gap for photovoltaics to be in the range of 1.1 eV to 1.4 eV [52,57-61] as illustrated in the ***Figure 1.9***. There are other factors too other than band gap energy that determines the PCE limit for various solar cell materials.

Figure 1.9: Solar spectrum outside (AM0) and inside the atmosphere (AM1.5G). The Shockley-Queisser limit zone corresponding to the optimal bandgap at around 1.3 eV is marked by orange lines [52]. An open-source implementation of the Shockley-Queisser model written in Python can be found here: https://github.com/sidihamady/Shockley-Queisser.

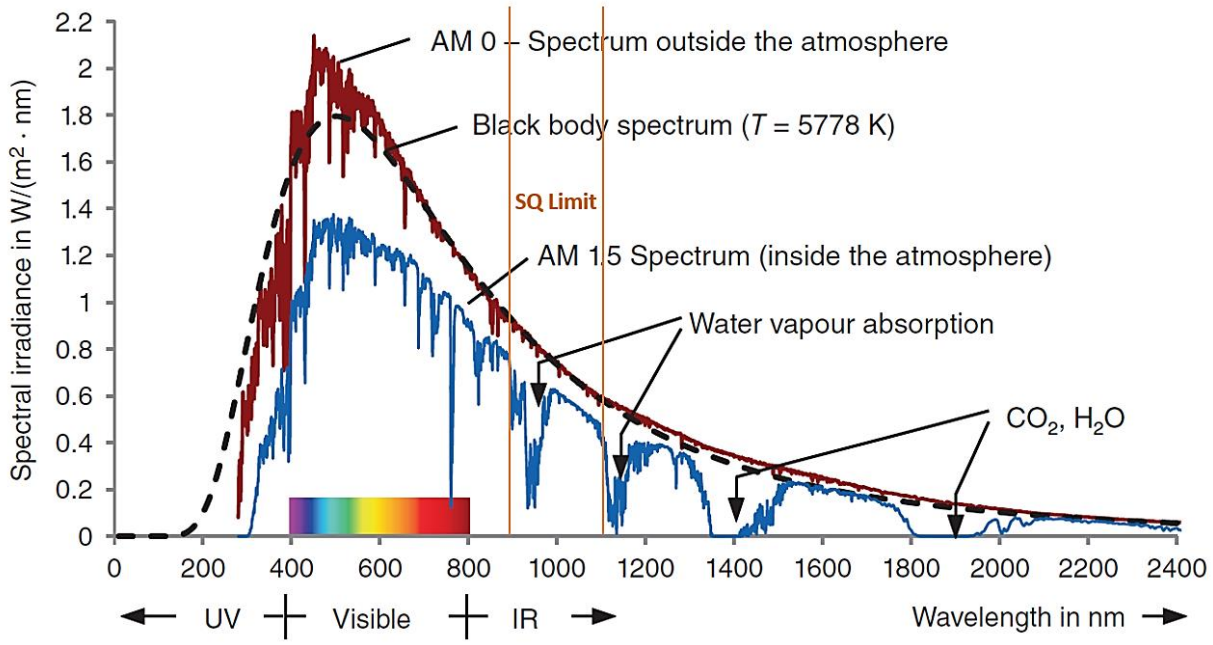

Figure 1.10: The bandgap wavelengths for some standard semiconductors with respect to the standard AM1.5G solar spectrum [57].

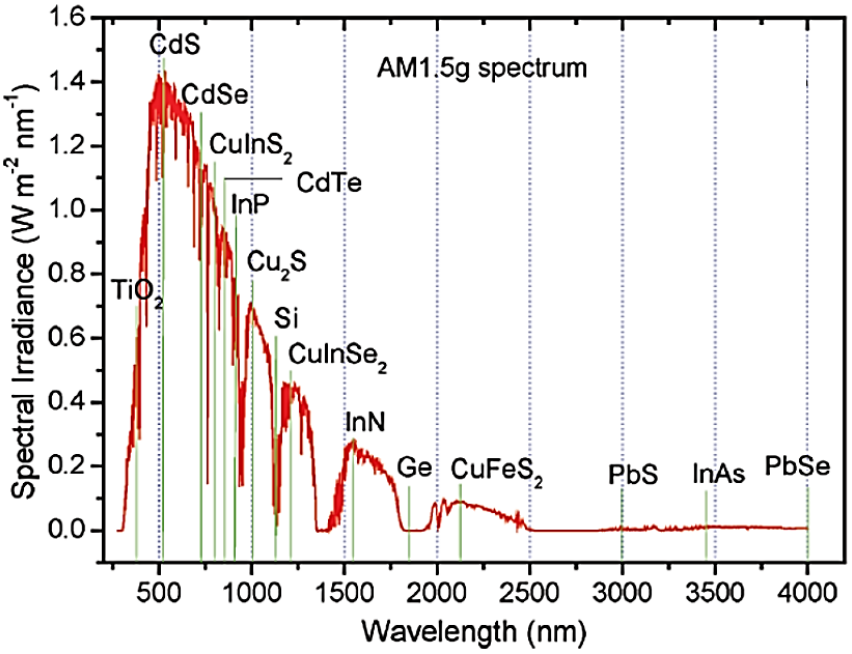

In general, the effect of light absorption in a semiconductor can be described by the following relation:

Equation (1.3):

$$\phi\,(x) = \phi_0\, e^{-\alpha x}$$

Where ϕ is the light irradiance at a certain depth; ϕ_0 is the irradiance at x=0, x is the position in the absorber and α is the absorption coefficient.

Solar cells absorber materials can have different bandgaps with different absorption coefficients. For indirect bandgap material like silicon, typically few dozen microns are required for light absorption and practically few hundred microns are required for the final solar module. Thin films based on direct bandgap materials required much lesser thickness of absorbers (less than few microns). They can be eco-friendly too with industrial compatible fabrication methods to reduce the overall cost of electricity production. Based, on the different absorber materials and different junction types of solar cells technologies can be categorized into different generations which is broadly discussed in the next section.

1.2 Overview of Different Technologies of Solar Cells

Solar cell technologies can be classified based on the diverse materials used to build up the device and their production types. Broadly, the solar cell technologies can be categorized into three types: (**i**) First Generation with crystalline silicon, (**ii**) Second Generation using thin films and (**iii**) Third Generation with heterojunctions and new concepts.

1.2.1 First Generation Solar Cell: Crystalline Silicon

The first generation of solar cells consists of crystalline silicon as the absorber material. To create a pn-junction silicon is often doped with p-type boron or n-type phosphorus. Now, silicon solar cells are a major player in the worldwide solar cell market. With very pure silicon qualities, silicon solar cells can produce very high conversion efficiencies considering a pn junction. But for high energy consuming processes for pure silicon production, the cost of solar cells is high too. Based on differences in crystallization, silicon solar cells can be of two types: monocrystalline solar cell and multi-crystalline (polycrystalline) solar cell. For monocrystalline solar cells, the entire wafer consists of a single crystal whereas, for multi-crystalline solar cells, the wafers consist of many fragments of crystal grains. Generally, the efficiency of monocrystalline solar cells is higher than multi-crystalline solar cells [62], but their production cost is higher due to wafer cutting process.

Kaneka Corporation using the real laboratory standards were able to achieve 26.7 % conversion efficiency for silicon solar cells. However, some of the most common drawbacks of silicon solar cells include the high bulk thickness of silicon absorber. Silicon being an indirect bandgap semiconductor, needs high thickness for light absorption. Hence, Auger charge-carrier recombination and bulk non-radiative recombination are dominant and causes loss of charge-carriers [37,64,65].

Figure 1.11: Three types of silicon wafers for solar cells: **(a)** 156-mm monocrystalline solar wafer and cell; **(b)** 156-mm multi-crystalline solar wafer and cell; and **(c)** 280-Wsolar cell module (from multi-crystalline wafers) [63].

1.2.2 Second Generation Solar Cell: Thin Films

The second generation of solar cells are mostly known as thin film solar cells. The absorber materials for these types of solar cells are only few micrometres thick. Typical absorber materials for thin film solar cells are amorphous silicon (a-Si), copper indium selenide (CIS), copper indium gallium sulfide/selenide (CIGS) [66-69], copper zinc tin sulfide/selenide (CZTS), cadmium telluride (CdTe) and gallium arsenide (GaAs). All these absorbers are direct band gap materials unlike silicon; hence the absorber thickness is considerably lower compared to silicon wafer absorbers. So, the production costs can also be considerably lower for thin film solar cells.

Figure 1.12: Some illustrations of thin film solar cells technologies [70].

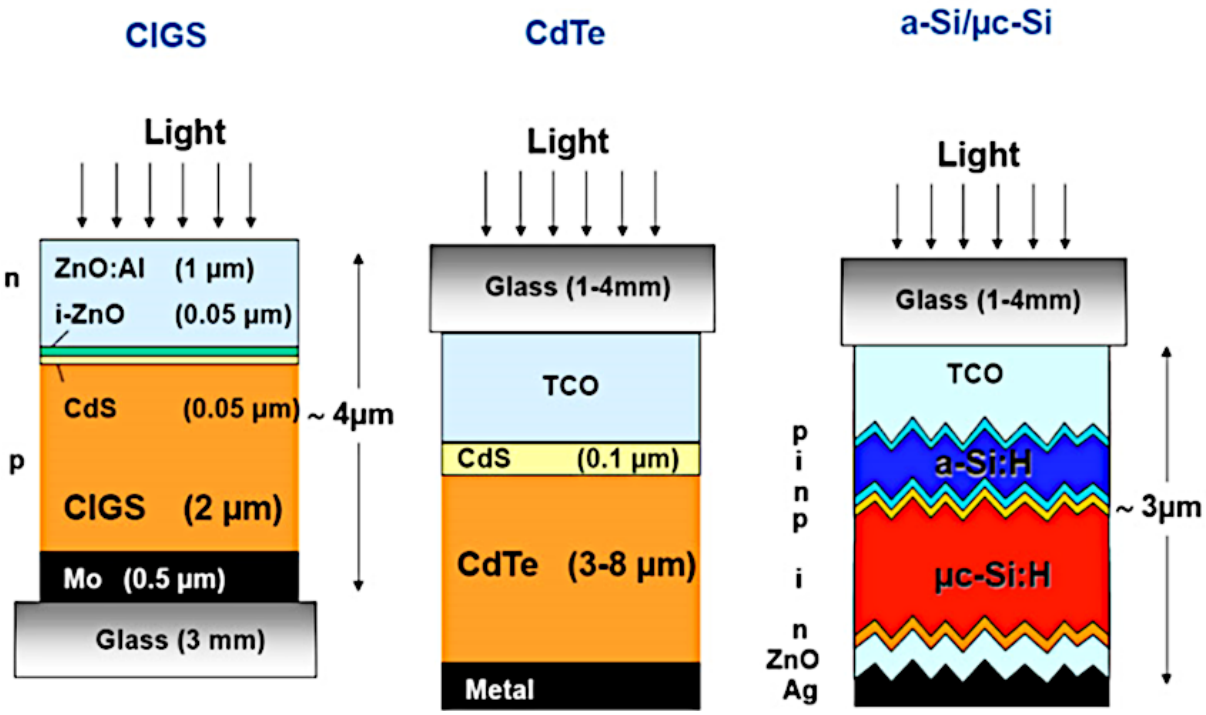

Mostly the thin film solar cells are fabricated on glass substrates, but flexible substrates are also used. Fabrication on flexible substrates allows thin films solar cells to be more lightweight, cost-effective, and usable on various types of surfaces and additionally with attractive looks [66, 71]. Typically, thin film solar cells achieve efficiencies of 7-14 %, but with recent high-end research the efficiencies have shot up to 23 % approx. [72–74]. CdTe solar cells based on single junctions reaches efficiencies up to 22 % but with major drawbacks including the non-abundancy of Te and the toxicity of Cd [75,76].

Figure 1.13: Some illustrations of thin film solar cells technologies: **(a)** CZTS solar cell [77,78], **(b)** GaAs solar cell [79,80].

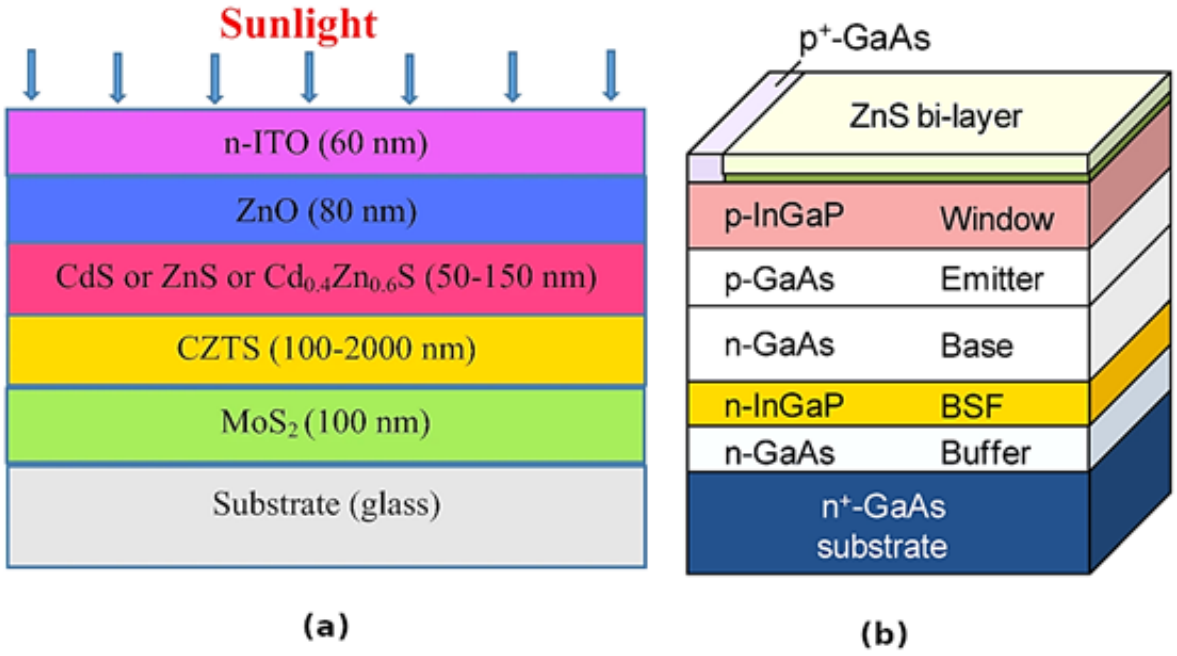

CIGS technology also has potential to reach high efficiencies, but most CIGS technologies use CdS used as a buffer layer which is a major source of toxicity [81]. Recently, Nakamura *et al.* [82] were able to fabricate Cd-free CIGS solar cells by a complicated process with double buffer layers to achieve record efficiency of 23 %. Recent research also puts focus on CZTS solar cells, which could be a possible replacement of CIGS solar cells due to the abundancy of zinc (as a replacement of the rare indium), the high absorption coefficient and the bandgap perfectly matching the Shockley-Queisser optimal one. CZTS solar cells have reached a maximum efficiency of 12.6 % using non-vacuum hydrazine-based solution process strategies. But one major drawback is the use of CdS as buffer layer which contributes to toxicity [83–85]. Amorphous Si (a-Si) solar cells can reach conversion efficiencies up to 10.2 % [86] but compared to crystalline solar cells or other thin film technologies the lifetime of the cells is much shorter in addition to the lower efficiency. This is due to the excess of recombination centres present in a-Si [87]. Single junction GaAs solar cells has achieved 29.1 % conversion efficiency [88] but with a high production cost and some toxicity [89]. The structure of the different second-generation solar cell types along with the solar cells fabricated on flexible substrates are illustrated in the ***Figures 1.12 & 1.13*** respectively.

1.2.3 Third Generation Solar Cell: Multijunction, Polymers, New Concepts

Third generation solar cells are being developed using polymers, dye sensitized materials, nanocrystal and multijunction solar cells [90-98].

Polymer solar cells reach a record power conversion efficiency (PCE) of 16.05 % [91]. The polymer technology suffers from two drawbacks: the poor absorption of the solar spectrum and the very low carrier mobility inducing a diffusion length as low as 10 nm [92]. Dye sensitized solar cells have a record PCE of 15 % with a structure with a perovskite [98].

Another promising technology being recently developed is the concentrator photovoltaics (CPV) for high efficiency and small area multijunction (mainly III-V materials and Ge) solar cells [99,103] with a concentration as high as 1000× corresponding to a solar density power of 100000 mW/cm² or 100 W/cm². The fabrication technique and the needed optics make the production cost of these solar cells very high. With control on the growth parameters lattice matched devices based on GaInP/GaAs/GaInAs materials are fabricated [104–108]. With nearly constant lattice parameter of ~3.2 Å InN/GaN/AlN based devices are also being investigated [109]. Highest conversion efficiency of 40.7 % (above 40 % for the first time) under 240 suns was possible to achieve by a GaInP/GaInAs/Ge metamorphic device (with strained lattice growth and flexible bandgap design) [110]. For these solar cells, as already stated, the main disadvantage is the very high cost of production of the epitaxial layers. Crystal imperfections and unwanted impurities severely affects the conversion efficiencies; hence, low-cost production methods cannot be used. Compared to silicon these materials are mechanically weaker. So, although the III-V tandem devices are suitable for space applications, but for terrestrial applications the high cost remains a matter of concern [111-113].

Another emerging technology is that of photovoltaics based on perovskites [114–116]. Based on the atomic/molecular arrangement in the structure, perovskite materials can have some interesting properties such as, ferroelectricity, superconductivity, ferromagnetism, piezoelectricity, etc. [116,117]. A PCE of 10.9 % was achieved by Lee *et al.*, by using super-structured organometal halide perovskites [118]. Even higher efficiency of 15.4 % was achieved by using a physical vapour deposited perovskite of the structure $CH_3NH_3PbX_3$, with compact TiO_2 as an electron selective layer [119]. However, perovskite solar cells face serious issues of stability, and, to a lesser extent, toxicity of lead used in the high-performance cells [120-123].

1.3 Next Generation Photovoltaics: Focus on "All-Oxide" Structures Based on Earth-abundant Semiconductors

As discussed in detail in the ***Section 1.1.1***, we have seen an exponential demand and growth in photovoltaic (solar cell) technology in the last two decades to fulfil the global energy demand. But there are some challenges that needs to be addressed for full-scale implementation of this technology. To this day, the cost of construction of photovoltaic modules remains very high and most technologies use either toxic or scarce elements in fabricating the solar cells. Some solar cells even require very high energy consuming and expensive techniques for their fabrication. To meet the energy demands in a sustainable and cost-effective way, the implementation of photovoltaic technology demands further price reductions. Upscaling of the technology could be made possible with the use of earth-abundant, non-toxic, easily available, and cheap materials with low deposition and fabrication costs. Metal oxides are the materials that most suitably fulfils these criteria and are suitable candidates to bring the production costs down thus allowing for upscaling of the photovoltaic technology with high conversion efficiency in ambient conditions. The typical structure of an all-oxide solar cell, as shown in the ***Figure 1.14***, consists of a TCO coated glass substrate, a p-type absorber layer, a buffer layer, a window layer, and a top contact that can be a TCO or an interdigitated metal contact. In the next sections the different solar cell technologies based on oxide semiconductors are presented.

Figure 1.14: Schematic representation of "all-oxide" solar cell.

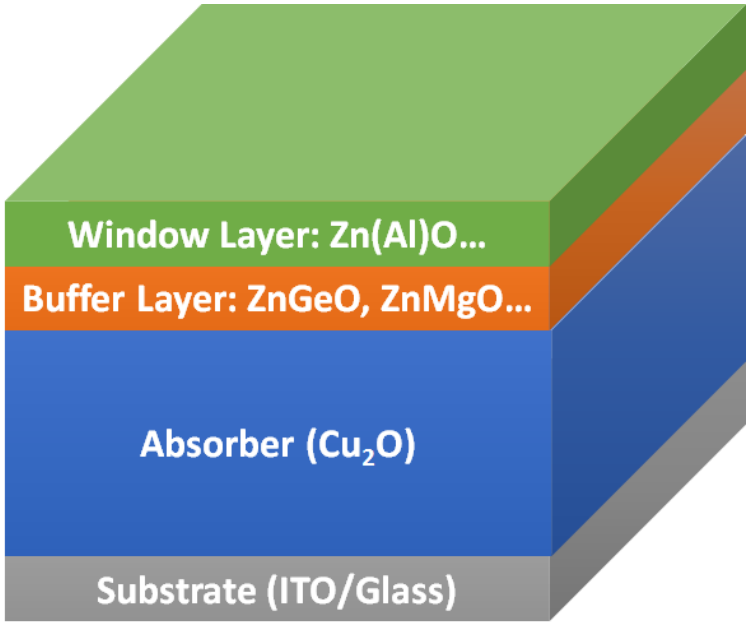

1.3.1 Spinel Oxide Solar Cells

Spinel oxide materials possessing the stoichiometry AB_2X_4, are also potential materials for all-oxide solar cells due to their light absorbing capacity. In the crystallite, X are anions, mostly chalcogens. A and B are cations which occupies most or all the octahedral and tetrahedral sites in the lattice [125–127]. With an optimal bandgap of around 1.5 eV, spinel oxide based solar cells could reach up maximum conversion efficiency theoretically [103,127]. Using $(Co_xFe_{1-x})_3O_4$ as a spinel oxide absorber in a multi-layered geometry, a better photovoltaic performance was achieved with J_{sc} of 53 mA/cm² and V_{oc} of 534 mV. The Co/(Co+Fe) composition ratio was maintained at approximately 55 % [126]. The structural stability of spinel oxides should be studied extensively as the distribution of cations and anions could seriously alter the material properties [127,128].

1.3.2 "All-Oxide" Structures using Metal Oxides

Using earth-abundant elements, oxides have a large oxygen electronegativity and thus can create stable compounds. Oxides can possess varied conductivity and can be insulators, semiconductors, or even conductors and can be used in photovoltaic devices in different ways [129-130]. The focus in this section is to summarize the basic properties of oxides for solar cells, to discuss about "all-oxide" solar cells using Cu_2O as an absorber.

1.3.2.1 ZnO and Related Materials

Zinc oxide has an optical bandgap of around 3.3 eV and is electrically conductive due to its non-intentional doping. It is very transparent in the visible region of the spectrum and can be used as a transparent conducting contact (TCO for transparent conducting oxide) [131,133]. Most often, in CIGS solar cells a stack of ZnO and ZnAlO layers are used as electron conducting layers for the front contacts [72,134]. In polymer based solar cells, for achieving a selective contact, ZnO has been used [135,136]. Beyond ZnO, other wide bandgap oxides, such as ITO (Indium Tin Oxide), TiO_2, NiO, V_2O_5, MoO_3 and WO_3 are commonly used in solar cells [137-141].

1.3.2.2 P-type Oxide Absorbers

P-type oxides forms with n-type transparent wide bandgap oxide the p-n junction with the built-in electric field necessary to separate the photogenerated electron-hole pairs [142].

It is an important criterion for all-oxide solar cells to have direct bandgap semiconductors for absorbers with an absorption coefficient higher than 10^4 cm^{-1} [113,143].

1.3.2.3 Cu_2O as an Absorber in "All-Oxide" Solar Cells

Cu_2O is among the most frequently investigated light absorber material for all-oxide photovoltaics with a bandgap near 2.2 eV and a theoretical photovoltaic efficiency of 20 % under AM1 solar illumination [103,113,144]. In addition, Cu_2O has relatively high hole mobility and high absorption coefficient and can be used with n-type wide oxides such as, ZnO, ZnAlO, Ga_2O_3 and TiO_2 [145–148]. In tandem solar cells, Cu_2O along with ZnO has been used as a sub cell [149] and with perovskite solar cells [150].

For Cu_2O based all-oxide devices, the efficiency values remain far below the theoretical value of 20 %. The solar cell figures of merit (V_{OC}, J_{SC}, FF and PCE) for Cu_2O based solar cell devices are mentioned in the ***Table 1.1***. As a starting point, Mittiga *et al.*, were able to achieve an overall conversion efficiency of 1 % and 2 % with Cu_2O/ITO and Cu_2O/ZnO/ITO based devices respectively under AM1.5G illumination. V_{OC}, J_{SC} and FF values of 0.595 mV, 6.78 mA/cm² and 50 % respectively were achieved for the best solar cell. The TCO films (ZnO and ITO) were grown by sputtering and the absorber Cu_2O thin films were prepared at high temperature by thermal oxidation of Cu. The low efficiency as pointed out by the authors, is partially due to the very high resistivity of Cu_2O, ≈ 1000 $\Omega \times cm$ [151]. An improved PCE of 4.12 % was reported by Nishi *et al.*, by introduction of a 50 nm ZnO buffer layer between the TCO (ZnAlO) and the Cu_2O absorber. With ZnO as buffer this is the highest PCE value as without the buffer the PCE was 2.19 %. Cu_2O was produced by thermally oxidising Cu sheets by PLD method. With the insertion of ZnO (which has a low carrier concentration than ZnAlO), not only the barrier height but also the width of the depletion region is increased. ZnO here not only acts as the buffer but an active layer.

The PCE was further improved by Minami *et al.* to 6.25 %, by a $(Ga_{0.975}Al_{0.025})_2O_3$ buffer layer, with a V_{OC} of 840 mV, a J_{SC} of 10.8 mA/cm², and an FF of 69 %. The Cu_2O here was also produced by thermally oxidising Cu sheets [153]. The improved efficiency is mainly due to the optimized n-type oxide and the lower resistivity of the Cu_2O film induced by the Na doping. Replacing $(Ga_{0.975}Al_{0.025})_2O_3$ with $Zn_{0.38}Ge_{0.62}O$ reduces the conduction band offset with Cu_2O and further improves the efficiency [154].

Cu_2O/TiO_2 solar cell structure was fabricated on FTO/glass substrates by using low-cost deposition technique of spray-pyrolysis, with V_{OC} of 350 mV and J_{SC} of 0.4 mA/cm². The very low photocurrent is partially due to the poor crystal quality of Cu_2O prepared by spray pyrolysis that might have enhanced recombination of charge carriers [148].

Winkler *et al.*, developed all-oxide solar cells by all-solution based processes. Here zinc magnesium oxide ($Zn_{1-x}Mg_xO$) of 50 nm with the stoichiometry of $Zn_{0.88}Mg_{0.12}O$ was used as a buffer layer on electrodeposited Cu_2O. A transparent top contact layer of indium-doped zinc oxide (IZO) was used.

$Zn_{0.88}Mg_{0.12}O$ and IZO were deposited using ultrasonic spray pyrolysis (USP). The highest conversion efficiency achieved was 0.67 %. These solar cells faced higher shunt resistance than with only ZnO as buffer layer, but series resistance was similar. V_{OC}, J_{SC} and FF of 0.34 V, 3.76 mA/cm² and 52.7 % respectively. High shunt resistance with low series resistance suggested better heterojunction interface quality of $Zn_{0.88}Mg_{0.12}O$ with Cu_2O. An improved conduction band alignment with $Zn_{0.88}Mg_{0.12}O$ buffer layer led to the improved V_{OC} and reduced optical losses improved the J_{SC} [155]. Ievskaya *et al.*, fabricated $Zn_{1-x}Mg_xO/Cu_2O$ heterojunction solar cells before Winkler *et al.* $Zn_{1-x}Mg_xO$ layer was deposited via a low temperature atmospheric atomic layer deposition (AALD) in open air on thermally oxidised Cu_2O. PCE of 2.2 % was achieved along with V_{OC}, J_{SC} and FF of 0.61 V, 7.55 mA/cm² and 48.5 % respectively with unannealed Cu_2O absorber. The authors point out the $Zn_{1-x}Mg_xO/Cu_2O$ defective heterointerface due in part to the formation of CuO before the deposition of $Zn_{1-x}Mg_xO$ [147].

Gallium oxide (Ga_2O_3) layer was used by Minami *et al.* [156] and Lee *et al.* [157], to fabricate heterostructures with Cu_2O. Minami *et al.* prepared a solar cell heterostructure using Ga_2O_3 as a buffer layer deposited on the Cu_2O absorber obtained by thermal oxidation of Cu and obtained an efficiency of 5.38 % with V_{OC} of 0.80 V, J_{SC} of about 10 mA/cm², and FF of 67 %. Leet *et al.*, used Ga_2O_3 as a buffer layer deposited on Cu_2O by ALD and achieved an enhanced V_{OC} of 1.2 V with J_{SC} of 7.37 mA/cm² and FF of 44.7 %. The Ga_2O_3 material has a perfect conduction band alignment with Cu_2O thereby reducing the interface recombination.

Figure 1.15: Power conversion efficiency by year of publication of oxide solar cells using Cu_2O as absorber. The corresponding references are shown with markers indicating the preparation technique conditions (vacuum or non-vacuum based).

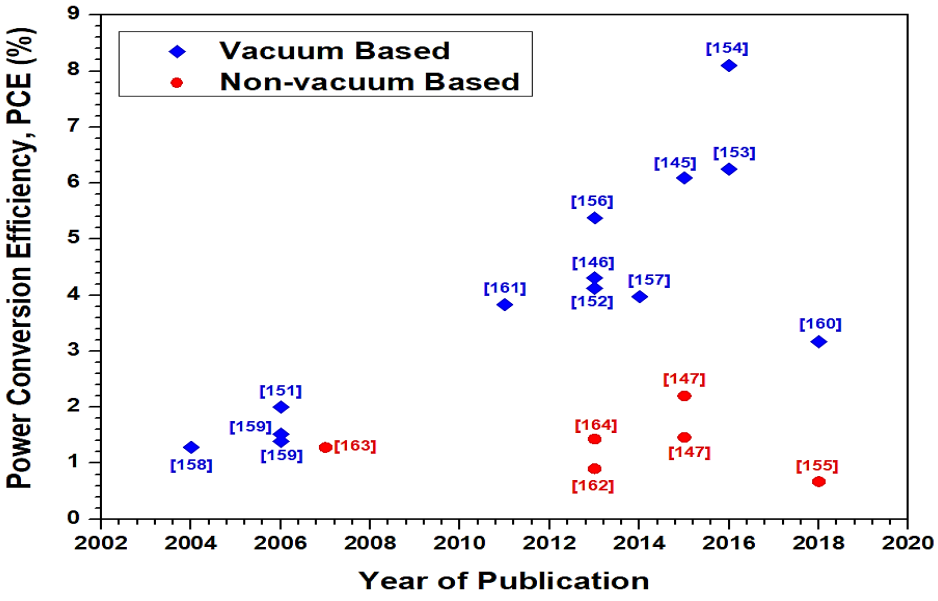

Table 1.1: Cu_2O solar cells state-of-the-art with increasing power conversion efficiency (PCE) values.

Solar Cell Structure	V_{OC} (V)	J_{SC} (mA/cm²)	FF (%)	**PCE (%)**	Ref.
Vacuum Based Methods					
ZnAlO/Cu_2O	0.4	7.1	40	**1.28**	[158]
ZnAlO /Cu_2O	0.4	6.91	50	**1.39**	[159]
ZnAlO:Ga/Cu_2O	0.41	6.94	53	**1.52**	[159]
ITO/ZnO/Cu_2O	0.59	6.78	50	**2**	[151]
ZnO/Cu_2O ***by CVD***	0.55	11.42	49.8	**3.17**	[160]
ZnAlO/ZnO/Cu_2O	0.69	10.1	55	**3.83**	[161]
ZnAlO/Ga_2O_3/Cu_2O ***by CVD***	1.2	7.37	44.7	**3.97**	[157]
ZnAlO/ZnO/Cu_2O	0.72	9.67	58	**4.12**	[152]
ZnAlO/$Zn_{0.91}Mg_{0.09}O$/Cu_2O	0.85	8	60	**4.31**	[146]
ZnAlO/Ga_2O_3/Cu_2O	0.8	9.99	67	**5.38**	[156]
ZnAlO/$Al_{0.025}Ga_{0.975}O$/Cu_2O:Na	0.84	10.95	66	**6.1**	[145]
ZnAlO/$(Al_{0.025}Ga_{0.975})_2O_3$/$Cu_2O$:Na	0.84	10.8	69	**6.25**	[153]
ZnAlO/$Zn_{0.38}Ge_{0.62}O$/Cu_2O:Na	1.1	11.1	62	**8.1**	[154]
Non-Vacuum Based Methods					
ZnO/$Zn_{0.88}Mg_{0.12}O$/Cu_2O ***by ECD***	0.34	3.76	52.7	**0.67**	[155]
ZnO/Cu_2O/Cu_2O ***by ECD***	0.32	6.32	45	**0.9**	[162]
ZnO/Cu_2O ***by ECD***	0.59	7.1	42	**1.28**	[163]
ZnO/Cu_2O ***by ECD***	0.54	4.47	59	**1.43**	[164]
ITO/ZnO/Cu_2O	0.49	7.5	40	**1.46**	[147]
ITO/$Zn_{0.79}Mg_{0.21}O$/Cu_2O	0.65	6.9	49.2	**2.2**	[147]

Cu_2O is prepared using **thermal oxidation** of Cu unless otherwise stated. **CVD**: chemical vapor deposition; **ECD**: electrochemical deposition.

1.3.2.4 Heterojunctions Based on ZnO/Cu_2O Structure

ZnO/Cu_2O heterojunctions have been widely studied towards their potential application in low-cost displays and photovoltaic devices. Cu_2O exhibits a bandgap value of about 2.2 eV, which makes it suitable to be used in combination with ZnO for applications mentioned above. A compromise between transparency and electrical performances is often needed depending on the type of application of the ZnO/Cu_2O heterojunction [165,166].

ZnO/Cu_2O heterojunctions have been successfully used for photodetectors with nanostructured architectures [167]. A fast response self-powered photo-detector device was designed using ZnO/Cu_2O core shell nanowires [168]. The use of nanostructured devices is being developed with the aim of enhancing the optical absorption without requiring thick absorbing layers thus enabling less material use. In most of the devices Cu_2O thin films are grown on nanostructured ZnO. ZnO possess the versatility to be produced in different shapes and sizes in the nanostructured (nanotubes, nanorods or nanowires) format. Hence with lower absorber (Cu_2O) thickness, charge carrier collection efficiency is enhanced too [167,169–171]. Attempts to fabricate nanostructured ZnO/Cu_2O solar cells yielded poor efficiencies with very long fabrication times. Yuhas *et al.* [172], used drop-cast method to deposit Cu_2O nanoparticles on ZnO nanowires array grown hydrothermally along with an intermittent 10 nm blocking layer of TiO_2. Under 1 sun illumination the highest PCE obtained was 0.053 %. According to the authors, the nanoparticle deposition process and conditions have affected the PCE severely. Baek *et al.* [173], used electrodeposition to prepare p-type Cu_2O layer on CVD grown ZnO nanowires. PCE obtained was 0.27 % due to limiting factors such as the low conductivity of ZnO nanowires and contamination during the long electrodeposition process. Hsueh *et al.* [174], used sputtering to deposit Cu_2O on vertical n-ZnO nanowires grown by a self-catalysed vapor–liquid–solid (VLS) method. PCE of around 0.1% was achieved. Authors point out low transmission of the ZnO nanowires and poor interface quality at the heterojunction as the limiting factors. Musselman *et al.* [171] fabricated Cu_2O/ZnO solar cells with the highest efficiency of 0.36 %. The bilayer of Cu_2O-ZnO resulting in the formation of heterojunctions was synthesized at near room temperatures by electrodeposition from solutions. Although charge collection remained a matter of concern, but reduction of the optical depth by nanowire architecture improved the solar cell performance.

In this thesis work, we will present the results of preparation of thin films of metal oxides using the very low-cost, versatile, low energy consuming and non-vacuum technique of Ultrasonic Spray Pyrolysis (USP). Achieving the optimum quality window, buffer and absorber layers are the main

objectives of the thesis. Material and electrical characterizations are performed to demonstrate the material quality towards their application in "all-oxide" solar cells.

Before proceeding towards the material preparation, we did a detailed study using numerical simulations to understand the choice of the different layers, their growth by USP and impacts on solar cell performances. The main findings from this first published numerical study of the ZnAlO/$Zn_{1-x}Ge_xO$/Cu_2O heterostructure are discussed in the following sub-section.

1.3.2.5 Numerical Investigations of "All-Oxide" Solar Cell Performances

To establish the potential of using metal oxide materials for future photovoltaic technologies, several studies have been performed in the past two decades. Among several materials, Cu_2O being the mostly researched material for the absorber layer. Studies on optimization of "all-oxide" solar cells are being performed to carefully select the window, buffer, and the absorber materials. The low electron affinity (χ = 2.1 eV) of Cu_2O creates a conduction band offset with the buffer layer, mostly ZnO (χ = 4.4 eV). Thus, to decrease the band offset, a layer of zinc germanium oxide with low electron affinity was introduced experimentally by Minami *et al.* [154]. In the first part, we performed numerical simulations based on the ZnAlO/$Zn_{1-x}Ge_xO$/Cu_2O heterojunction. Physical parameter values were carefully chosen from various literatures and the simulation results are compared with the solar cells obtained by Minami *et al.* [154]. For the extraction of the solar cell figures of merit, the modelling is performed by using Silvaco Atlas® simulator. To account for unwanted phases of copper oxide, at the interface of Cu_2O with the buffer layer an interface and defect layer is introduced in agreement with previous study [175]. The electrical parameters for Cu_2O are chosen from [154] with Hall mobility value of 100 cm^2/Vs and hole concentration of the order of 10^{15} cm^{-3}. The optical parameters are chosen from [176]. The electron affinity values can vary with respect to the experimental growth conditions. We chose a value of χ = 3.2 eV in accordance with experimental measurements of the literature [175]. For the top window layer, ZnAlO, the doping concentration ($7.64\times10^{20}cm^{-3}$) and electron mobility (30 cm^2/Vs) are chosen from [154,177] for a PLD deposition process. The optical parameters are selected from [178,179]. The experimental data, carrier lifetimes and defect concentrations are chosen in order of nanoseconds and 10^{18} cm^{-3} respectively [180,181]. As, for the buffer layer, $Zn_{1-x}Ge_xO$, experimental data is not available, so an estimation of bandgap energy, electron affinity and permittivity are done through linear interpolation, details of which can be found in our research article [182]. The estimated values of bandgap energy, electron affinity and permittivity for the compound $Zn_{0.38}Ge_{0.62}O$, are 4.97 eV,

3.11 eV and 6.18 respectively. The other parameter details for all the layers can be found in the ***Table 1*** of our article [182]. In the simulation model, the solar cell performances for different Ge compositions in the buffer layer are evaluated and compared with the results from Minami et al. [154]. Without the interface and defect layers, a maximum PCE of about 12 % was predicted (red curve in ***Figure 1.16*** with Ge composition x = 0.4). However, the experimental optimum (black dots in ***Figure 1.16***) was achieved for a Ge composition of x = 0.62 with PCE value at 6.68 %. Including interface layer with high density of defects makes the model more accurate and the simulated characteristics more coherent with the experimental results. The simulated PCE value reaches the experimental value of 6 % when x is between 0.5 and 0.65. The simulation results start to diverge when x is increased beyond 0.65, which might be due to the fact that the electrical properties of the buffer layer start to degrade with Ge increase (strong resistivity increase) and these are not included in the simulation model. The solar cell model thus developed with the simulations matches closely with the experimental values which can found in Table 2 in our article [182].

With the understanding of the performance of "all-oxide" solar cells from the simulation mentioned above, it is now important to assess the performance of "all-oxide" solar cells when the layers are grown by the method of ultrasonic spray pyrolysis (USP). As the photovoltaic performance is poor (PCE below 1 % [148,183]) when metal oxides are grown by USP, it is important to investigate the reasons for such low performance. One of the key reasons is the thickness reduction of the absorber layer (from 200 µm down to less than 1 µm) for USP process. The effect of such thickness reductions on the solar cell performances were investigated in our article [182].

A constant decrease in PCE (from 6.6 % to 3.65 %) is observed with the thickness reduction due to the loss in J_{SC} (shown in ***Figure 1.17***). Nevertheless, a PCE of 4.2 % is achieved for a 1 µm thick absorber layer. This value is although higher than most observed values for devices grown by USP (below 1 %) [148,183], which suggests that there are other factors involved for solution-based processed for the loss of PCE.

Figure 1.16: Photovoltaic characteristics simulated for ZnAlO/$Zn_{1-x}Ge_xO$/Cu_2O solar cell with respect to the germanium composition. Also given the conduction band offset χ_{ZnGeO} - χ_{Cu2O} [182]. The line curves show the simulation results with (blue) and without (red) the defect. The experimental data taken from [154] are also show (black dots).

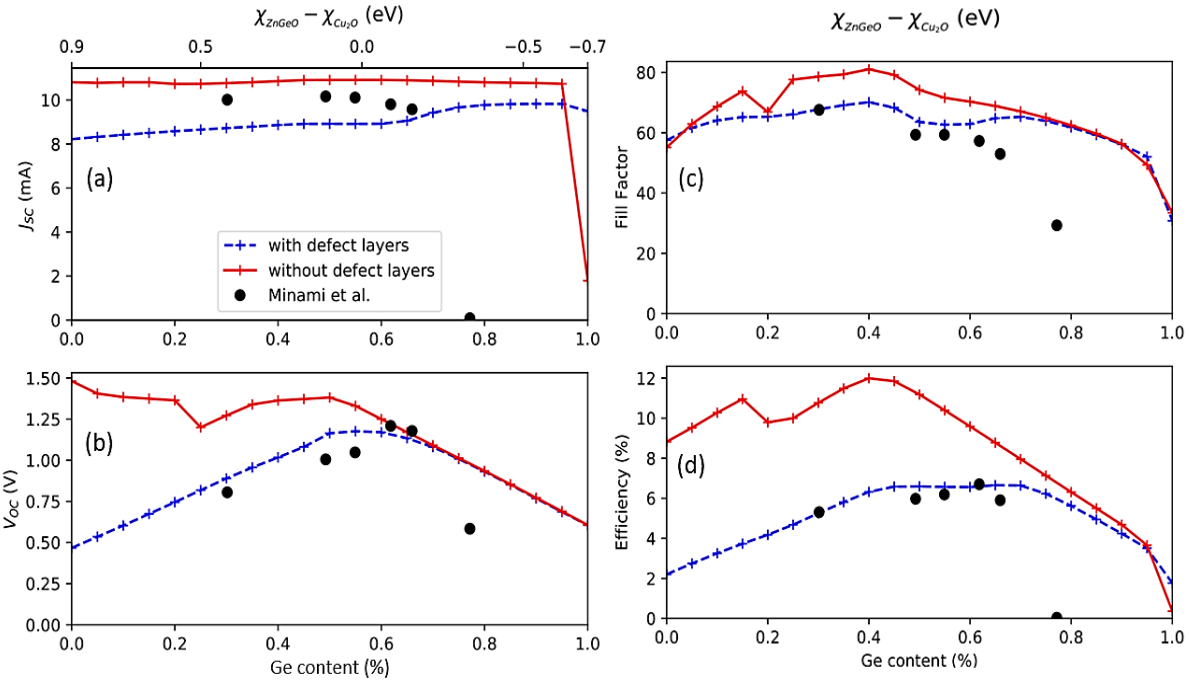

For ZnAlO grown by USP [184], the electrical properties are nearly like that grown by standard process of PLD. But, for Cu_2O, the properties of films grown by USP differs a lot from films grown by thermal oxidation. The electrical properties can even vary a lot depending upon the spray system, doping and other deposition conditions. The Hall mobilities can vary from 0.45 to 22 cm^2/Vs while carrier concentration varies from 2.68×10^{15} cm^{-3} to 2.1×10^{17} cm^{-3} [148,183,185,186]. To begin the evaluation, a typical hole mobility value of 5 cm^2/Vs was chosen along with a doping concentration of 10^{16} cm^{-3}. Details of other values can be looked up on our article [182]. With these values for Cu_2O, a PCE value of 3.6 % was obtained, which is not far below than previously obtained by us for a 1 µm thick Cu_2O. So, this does not account for all other loss factors which takes the experimental value to below 1 %. In the next part, some more factors for the loss analysis are investigated.

Figure 1.17: Variation of the solar cell performances with the absorber thickness [182].

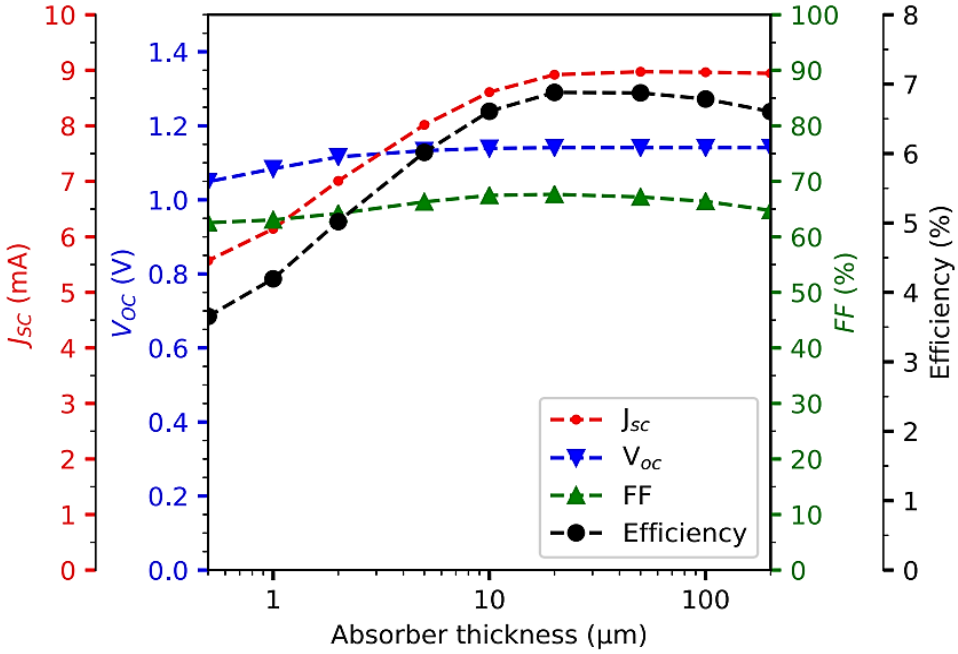

At first, the doping concentration in the absorber is varied in the range from 10^{18} cm^{-3} to a very minimal 10^{12} cm^{-3}. All other parameters as mentioned above are kept constant. Increasing the doping concentration beyond 10^{16} cm^{-3} reduces the V_{OC} and J_{SC} and the PCE as well. For lower doping concentration the effects are minimal. With higher doping, the decrease in the space charge region decreases the carrier collection efficiency while for lower doping, the space charge region (maximum 0.974 µm) is limited by the absorber thickness itself (1 µm). The effects of the variation of the absorber doping concentration are shown in the ***Figure 1.18***. Regarding the introduction of the defects of the absorber in the simulation model, it is seen that the J_{SC} is greatly impacted (reduced) when the defect concentration is increased beyond the doping concentration of 10^{16} cm^{-3}. Even the PCE rapidly drops below 1 % (shown in ***Figure 1.19***). Thus, it can be said that high defect concentration is a crucial factor for Cu_2O grown by USP. This factor was also hypothesized by the authors in [148] as they found a very low J_{SC} of 0.4 mA/cm^2.

Another important factor considered for our simulations is the carrier mobility. Mobility for Cu_2O could vary from 200 cm^2/Vs (for thermal oxidation) down to 1 cm^2/Vs (for USP). For our simulations, the hole mobility is varied between 0.1 cm^2/Vs and 200 cm^2/Vs while keeping the electron to hole mobility ratio to 2. The change of mobility does not show a pronounced effect on the solar cell performances. Even for very low mobility value of 1 cm^2/Vs the PCE is 2.4 %. The mobility variation effects are shown in the ***Figure 1.20***. From the analysis with all these parameters

it is proven that the high defect density of Cu_2O (both bulk and interfaces) combined with low thickness are the most detrimental factors towards low performance of the solar cells. Very importantly Plankensteiner *et al.* shows in their research [187] that impurities are incorporated in the absorbers due to incomplete pyrolysis of agents present in the precursor solution.

Figure 1.18: Variation of the solar cell performances with the doping concentration [182].

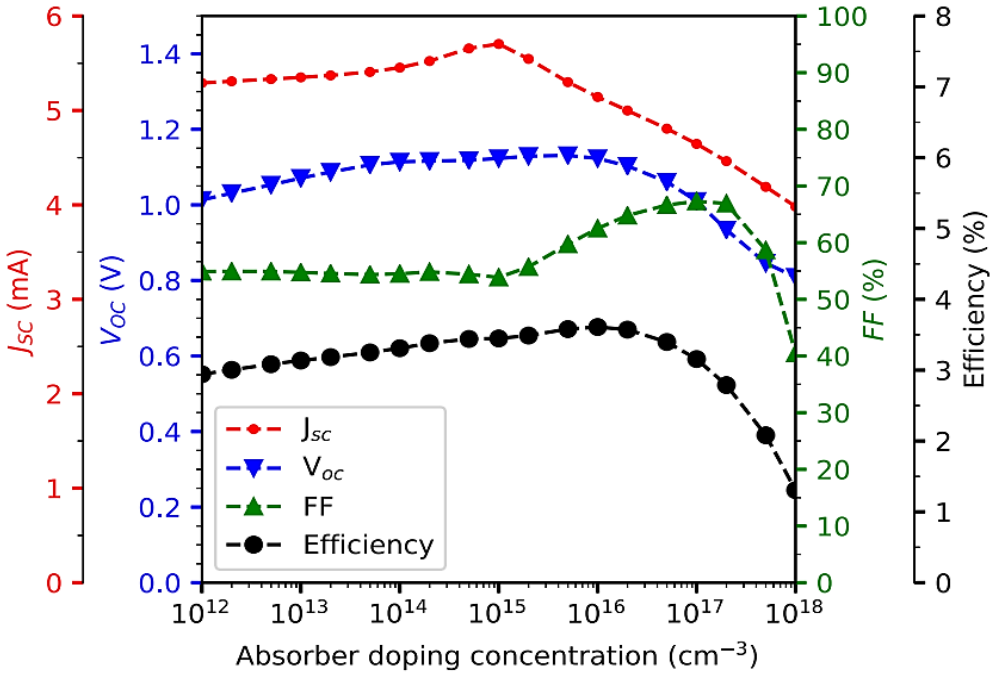

Figure 1.19: Variation of the solar cell performances with the defect concentration [182].

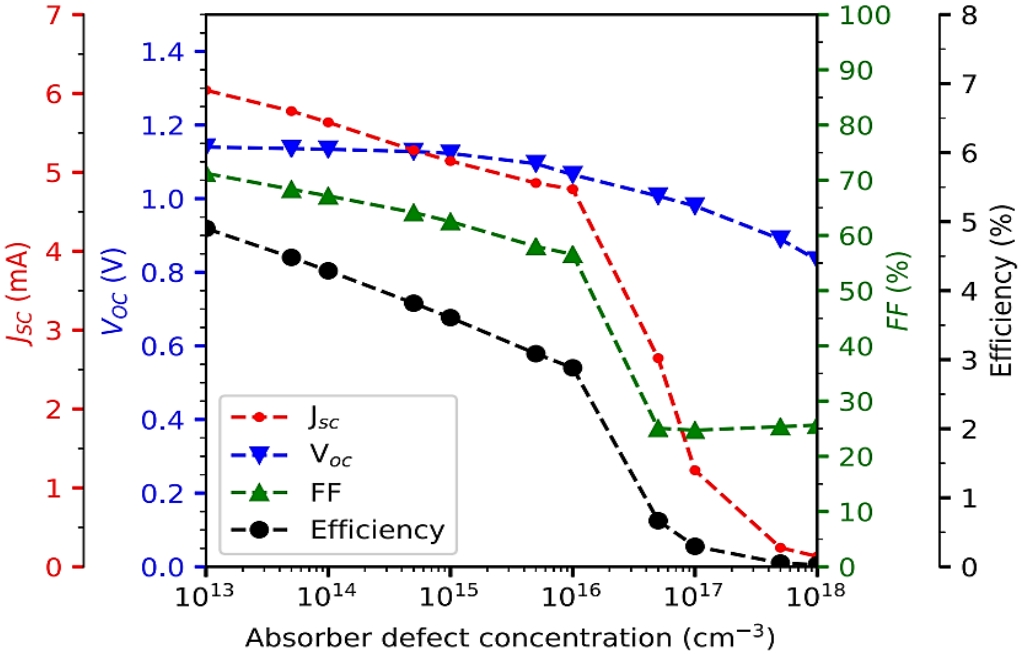

Figure 1.20: Variation of the solar cell performances with the carrier mobility [182].

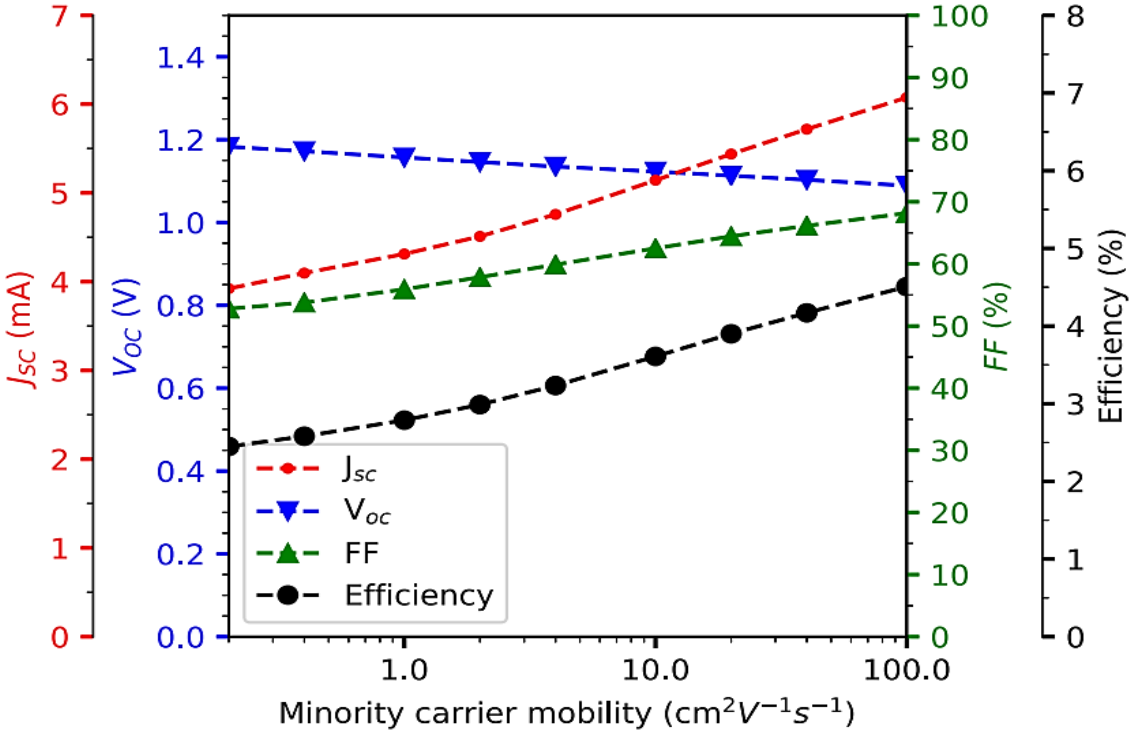

Figure 1.21: Variation of the solar cell performances with the germanium composition in $Zn_{1-x}Ge_xO$, the doping concentration in the absorber and the density of defects in the interfacial layer [182].

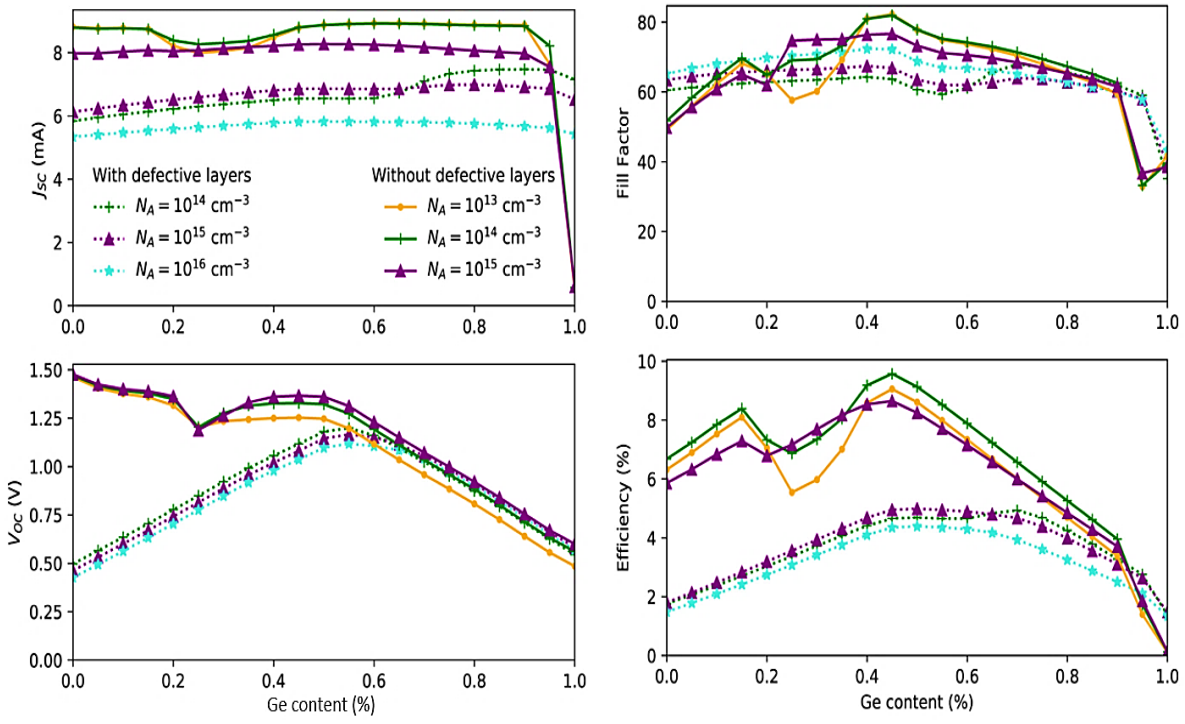

From the analysis above, we have understood the limiting factors for the performance of "all-oxide" solar cells. In this section we will discuss about the guidelines for the fabrication of "all-oxide" solar cells with USP. To improve the photovoltaic performance, we first estimate a 2 μm thick absorber with hole and electron mobility values of 25 cm^2/Vs and 50 cm^2/Vs, thereby maintaining the electron to hole ratio to 2. We keep some flexibility to select these values for USP, as these can be obtained for growth by sputtering [188]. We can further increase the absorber thickness beyond 2 μm but keeping the polycrystalline nature of the layer in mind, it would be very challenging to obtain such thickness by USP. Also, regarding the Ge composition in the buffer layer, the optimum might also depend on the optimal absorber layer parameters. The solar cell performance by varying the absorber doping and the Ge composition and keeping the other parameters fixed are shown in the ***Figure 1.21***.

With 2 μm absorber, a doping concentration of 10^{15} cm^{-3} can be used with Ge composition of x = 0.50 for the buffer. With these, the solar cells can reach a PCE of 4.98 %, which is relatively close to the experimental maximum 6.68 % [154]. Another slight modification to the simulation model is done without considering the interface defect layers at the buffer-absorber heterojunction. A doping concentration of 10^{14} cm^{-3} is chosen for the absorber with the Ge composition at x = 0.45, thus yielding a PCE of 9.57 %. We further assume that with an overall improvement of the "all-oxide" fabrication by USP like introduction of back surface field and anti-reflection coatings it is further possible to enhance the PCE.

1.4 Objectives and Challenges of the Present work

Based on the variety of applications of metal oxide thin films/layers, in this thesis the main objective was to prepare such thin films/layers by using the versatile and low-cost technique of Ultrasonic Spray Pyrolysis (USP). USP is being used for preparation purpose to reduce the production cost thus making it economically feasible. The USP can be easily integrated for industry standards for preparation on large areas. Metal oxides are a family of materials which have very high potential for photovoltaics: they are abundant in the earth's crust, are non-toxic and can be procured easily, as detailed in section 1.3. Moreover, preparation of metal oxides is compatible with low-cost techniques such as USP, thereby enabling the design and fabrication of an "all-oxide" solar cell. The entire solar cell structure consisting of transparent top contact layer, window layer, buffer layer and the absorber layer can be fabricated with metal oxides using the technique of USP. This type of fabrication using only one preparation equipment has not been realized till date.

The plan of the research work is to optimize the spray parameters, including the precursor solution optimization to obtain high-quality, homogenous, and stoichiometric metal oxide thin films applicable for solar cells and possible other optoelectronic applications. The thin-film processing technique thus forms the heart of this research work. Keeping the functionality in mind, each layer thus prepared are characterized in terms of their morphological, optical, structural, and electrical properties.

The versatility of the USP technique lies in the fact that, spray parameters can be tailored and carefully controlled for each individual layer with respect to their chemical functionality. This fact also adds to the challenges to obtain the high-quality films.

In our research work, we began the process of preparation from scratch with the USP equipment installed in the laboratory in June 2019, a few months before the start of the thesis. The entire process at the beginning was non-optimized. The research began with the optimization of the precursor solutions and the design and material choice for the substrate holder. These are very sensitive towards the prepared material quality. All the films were prepared on 1 mm thick soda lime glass (SLG).

The range of spray deposition parameters are manifold. The parameters include: the substrate temperature; substrate position; shaping air pressure of spray nozzle; solution flow rate; vertical

distance between the substrate and the spray nozzle; nozzle speed; nozzle power; number of spray scans (spray cycles) and dwell time (a pause or stopping time between each spray scan). Each of these spray parameters are intertwined.

For each spray preparation, for a particular film, the parameters were varied, and the resulting film was studied in terms of the morphological, optical, and structural characteristics. The analysis of the results helped to understand the effect of the spray parameters on the prepared film. The results thus obtained were compared to the best quality films obtained by other common preparation techniques with an aim to reach optimal quality for the films prepared by USP. Thus, a round-robin experimental steps were followed for each film and then a set of optimized spray parameters were finalized for a particular film.

Preparation of ternary and quaternary materials are not so common using USP. In our research we will develop both ternary and quaternary thin film with optimum quality to integrate them for usage in “all-oxide” solar cells. The preparation of quaternary thin films using USP will be quite unique as in most cases quaternary thin films are prepared using very expensive vacuum-based techniques like sputtering and pulsed laser deposition (PLD).

Keeping all the above-mentioned factors and challenges in mind, the thesis work will be based on three pillars: (**i**) the optimization of the ultrasonic spray preparation process; (**ii**) the morphological, optical, structural, and electrical characterization of the prepared films; (**iii**) towards realization of an “all-oxide” solar cell device.

As mentioned above, the preparation of all the films towards the realization of “all-oxide” solar cell device using only the cost-effective and versatile process of USP is unique. The expertise thus developed from this research work can be valued not only in academics but also in industry.

1.5 Thesis Organization

Overall, the research work in this thesis deals with the optimization of spray preparation parameters to produce thin films of earth-abundant and non-toxic metal oxides with optimal quality to be applicable for "all-oxide" solar cell devices. The manuscript is organized in total **7 chapters**.

Chapter 1 is a general introduction about photovoltaics and oxide semiconductors. The growth of photovoltaics and its importance in the modern-day energy demand scenario are discussed. The basics of solar cells along with the different types of solar cells (classified according to generations) are also discussed. In this context, in the second part of the chapter, the basics of metal oxide semiconductors are discussed along with the literature review of the types of "all-oxide" solar cells with focus on the metal oxides. The details about the mostly researched ZnO-Cu_2O heterostructures for "all-oxide" solar cells are discussed. Also, simulation performed for performance "all-oxide" solar cells along with the suitable choice of materials are discussed. In the last part, the objectives and challenges for the thesis work are mentioned along with the detailed literature survey.

Chapter 2 is dedicated to the basic principles of ultrasonic spray pyrolysis (USP). USP is employed for the preparation of the window, buffer, and absorber layers. The fundamental techniques of the characterization tools used for the morphological, optical, structural, and electrical characterizations are also discussed.

Chapter 3 is about the development and optimization of ZnO used as the window layer. The material properties of ZnO are discussed briefly. Preparation of ZnO with optimal quality is discussed in detail. The optimization of the spray parameters and their subsequent effect on the film quality are discussed. The morphological, optical, and structural characterizations are discussed with reference to the spray parameters. The electrical characterizations are done to analyze the conductive properties of the films.

Chapter 4 is about the development and optimization of the buffer layer. The choice of $Zn_{1-x}Mg_xO$ for the buffer layer is explained with brief literature review. The optimization of spray parameters along with the effect of addition of Mg on the film properties.

Chapter 5 is about the preparation of the absorber layer. Cuprous oxide (Cu_2O) is the absorber layer prepared with keeping few challenges in mind, the foremost one being the control of the spray

parameters to keep the "cuprous" phase (Cu_2O) intact. It has been seen that Cu_2O to quickly change to cupric phase (CuO) which can be detrimental to solar cell performances. The spray parameters are optimized to have the cuprous phase after preparation. Also, the role of a new reducing agent, D-sorbitol is analyzed in detail.

Chapter 6 focus on the possibilities to tune the optoelectronic properties of oxide alloys to pave the way to the fabrication of the entire "all-oxide" solar cell. In the first step, aluminium is doped with ZnO to prepare a top contact layer of ZnAlO with optimized spray parameters. In the second step, for the first time using USP, a quaternary film of Zinc Magnesium Aluminium Oxide ($Zn_{1-x-y}Mg_xAl_yO$) is prepared. $Zn_{1-x-y}Mg_xAl_yO$ can be of multi-purpose use, it can be designed to be used as a top contact/window/buffer layer. Lastly, an "all-oxide" device was modelled using the Solis simulation software.

Chapter 7 is the concluding chapter. It emphasizes the use of USP for preparing high-quality metal oxide thin films. All the important results obtained are summarized in this chapter. An outlook is written mentioning about the prospects of the research work.

1.6 References

[1] A.E. Becquerel, Recherches sur les effets de la radiation chimique de la lumière solaire au moyen des courants électriques, Comptes Rendus L'Académie Des Sciences. 9 (1839).

[2] A.E. Becquerel, Mémoire sur les effets électriques produits sous l'influence des rayons solaires, Ann. Der Physick Und Chemie. 54 (1841).

[3] W. Smith, Selenium: its Electrical Qualities, and the Effect of Light Thereon: Being a Paper Read Before the Society of Telegraph Engineers, 44 (1877) 21.

[4] A. Einstein, Über einen die Erzeugung und Verwandlung des Lichtes betreffenden heuristischen Gesichtspunkt, Ann. Phys. 322 (1905) 132–148. https://doi.org/10.1002/andp.19053220607.

[5] A. Pais, Einstein and the quantum theory, Rev. Mod. Phys. 51 (1979) 863–914. https://doi.org/10.1103/RevModPhys.51.863.

[6] A.B. Arons, M.B. Peppard, Einstein's Proposal of the Photon Concept—a Translation of the Annalen der Physik Paper of 1905, Am. J. Phys. 33 (1965) 367–374. https://doi.org/10.1119/1.1971542.

[7] M. Zeman, Solar Cells Theory, 2014.

[8] Pearson GL, PV founders award luncheon. Conference Record, 18th IEEE Photovolt. Spec. Conf. Las Vegas, IEEE, New York. (1985). https://www.worldcat.org/title/conference-record-of-the-eighteenth-ieee-photovoltaic-specialists-conference-1985-las-vegas-nevada-october-21-25-1985/oclc/13805157.

[9] D.M. Chapin, C.S. Fuller, G.L. Pearson, A New Silicon p-n Junction Photocell for Converting Solar Radiation into Electrical Power, J. Appl. Phys. 25 (1954) 676–677. https://doi.org/10.1063/1.1721711.

[10] Bell Laboratories Record, November, (1954) 436.

[11] B. Zaidi, Introductory Chapter: Introduction to Photovoltaic Effect, in: Sol. Panels Photovolt. Mater., InTech, 2018. https://doi.org/10.5772/intechopen.74389.

[12] Jørgen Veisdal, Einstein's 1905 paper on the Photoelectric Effect: The paper that earned Einstein the Nobel Prize, Priv. July 16th. (2021). https://www.privatdozent.co/p/einsteins-1905-paper-on-the-photoelectric-8e3 (accessed December 24, 2021).

[13] P. John, The silicon solar cell turns 50, J. Chem. Inf. Model. 53 (2013) 1689–1699.

[14] United Nations Population Division, World Population Prospects: The 2010 Revision, Popul. Dev. Rev. I (2011). https://doi.org/10.1553/populationyearbook2010s77.

[15] International Energy Agency IEA, World Energy Outlook, (2019) 810. https://iea.blob.core.windows.net/assets/98909c1b-aabc-4797-9926-35307b418cdb/WEO2019-free.pdf.

[16] S. Ahmed, M.T. Islam, M.A. Karim, N.M. Karim, Exploitation of renewable energy for sustainable development and overcoming power crisis in Bangladesh, Renew. Energy. 72 (2014) 223–235. https://doi.org/10.1016/j.renene.2014.07.003.

[17] S. Teske, G. Masson, Solar generation 6 Solar photovoltaic electricity empowering the world, (2011). http://www.epia.org/index.php?eID=tx_nawsecuredl&u=0&file=fileadmin/EPIA_docs/documents/Solar_Generation_6__2011_Full_report_Final.pdf&t=1304600305&hash=560a42b1538dac04a12781c7ffc251bf.

[18] R. Lindsey, Climate Change: Global Sea Level, (2021). https://www.climate.gov/news-features/understanding-climate/climate-change-global-sea-level (accessed December 26, 2021).

[19] R.K. Priestley, Z. Heine, T.L. Milfont, Public understanding of climate change-related sea-level rise, PLoS One. 16 (2021) e0254348. https://doi.org/10.1371/journal.pone.0254348.

[20] Climate Change Indicators: Arctic Sea Ice, United States Environ. Prot. Agency. (2021). https://www.epa.gov/climate-indicators/climate-change-indicators-arctic-sea-ice (accessed December 26, 2021).

[21] NASA (National Aeronautics and Space Administration). Scientific Visualization Studio, (2021). https://svs.gsfc.nasa.gov.

[22] S. Wheatley, B.K. Sovacool, D. Sornette, Reassessing the safety of nuclear power, Energy Res. Soc. Sci. 15 (2016) 96–100. https://doi.org/10.1016/j.erss.2015.12.026.

[23] L. Högberg, Root Causes and Impacts of Severe Accidents at Large Nuclear Power Plants, Ambio. 42 (2013) 267–284. https://doi.org/10.1007/s13280-013-0382-x.

[24] A. Freiberg, J. Scharfe, V.C. Murta, A. Seidler, The Use of Biomass for Electricity Generation: A Scoping Review of Health Effects on Humans in Residential and Occupational Settings, Int. J. Environ. Res. Public Health. 15 (2018) 354. https://doi.org/10.3390/ijerph15020354.

[25] Y. Wu, F. Zhao, S. Liu, L. Wang, L. Qiu, G. Alexandrov, V. Jothiprakash, Bioenergy production and environmental impacts, Geosci. Lett. 5 (2018) 14. https://doi.org/10.1186/s40562-018-0114-y.

[26] O. Demirtas, Evaluating the Best Renewable Energy Technology For Sustainable Energy Planning, Int. J. Energy Econ. Policy. 3 (2013) 23–33.

[27] D. Gielen, F. Boshell, D. Saygin, M.D. Bazilian, N. Wagner, R. Gorini, The role of renewable energy in the global energy transformation, Energy Strateg. Rev. 24 (2019) 38–50. https://doi.org/10.1016/j.esr.2019.01.006.

[28] J.-P. Lai, Y.-M. Chang, C.-H. Chen, P.-F. Pai, A Survey of Machine Learning Models in Renewable Energy Predictions, Appl. Sci. 10 (2020) 5975. https://doi.org/10.3390/app10175975.

[29] M. Sharifzadeh, A. Sikinioti-Lock, N. Shah, Machine-learning methods for integrated renewable power generation: A comparative study of artificial neural networks, support vector regression, and Gaussian Process Regression, Renew. Sustain. Energy Rev. 108 (2019) 513–538. https://doi.org/10.1016/j.rser.2019.03.040.

[30] DGS The German Energy Society (Deutsche Gesellshaft fur Sonnenenergie, BRB) Berlin, Planning and Installing Photovoltaic Systems A guide for installers, architects and engineers second edition, Earthscan, London, 2008.

[31] ChemViews, Renewable Energies: Wind, Solar, Biomass, ChemViews. (2012). https://doi.org/10.1002/chemv.201200005.

[32] Fraunhofer Institute for Solar Energy Systems, ISE with support of PSE Projects GmbH, Photovoltaics Report, Freiburg, 2021. www.ise.fraunhofer.de.

[33] IRENA, Future of solar photovoltaic: Deployment, investment, technology, grid integration and socio-economic aspects (A Global Energy Transformation: paper), 2019. https://www.irena.org/-/media/Files/IRENA/Agency/Publication/2019/Oct/IRENA_Future_of_wind_2019.pdf.

[34] International Renewable Energy Agency, Renewable Power Generation Costs in 2019, Abu Dhabi, 2020. https://www.irena.org/-/media/Files/IRENA/Agency/Publication/2018/Jan/IRENA_2017_Power_Costs_2018.pdf.

[35] Max Roser, Why did renewables become so cheap so fast?, Our World Data. (2021). https://ourworldindata.org/cheap-renewables-growth (accessed December 29, 2021).

[36] N.M. Haegel, H. Atwater, T. Barnes, C. Breyer, A. Burrell, Y.-M. Chiang, S. De Wolf, B. Dimmler, D. Feldman, S. Glunz, J.C. Goldschmidt, D. Hochschild, R. Inzunza, I. Kaizuka, B. Kroposki, S. Kurtz, S. Leu, R. Margolis, K. Matsubara, A. Metz, W.K. Metzger, M. Morjaria, S. Niki, S. Nowak, I.M. Peters, S. Philipps, T. Reindl, A. Richter, D. Rose, K. Sakurai, R. Schlatmann, M. Shikano, W. Sinke, R. Sinton, B.J. Stanbery, M. Topic, W. Tumas, Y. Ueda, J. van de Lagemaat, P. Verlinden, M. Vetter, E. Warren, M. Werner, M. Yamaguchi, A.W. Bett, Terawatt-scale photovoltaics: Transform global energy, Science (80-.). 364 (2019) 836–838. https://doi.org/10.1126/science.aaw1845.

[37] S. Bhattacharya, S. John, Beyond 30% Conversion Efficiency in Silicon Solar Cells: A Numerical Demonstration, Sci. Rep. 9 (2019) 12482. https://doi.org/10.1038/s41598-019-48981-w.

[38] K. Yoshikawa, H. Kawasaki, W. Yoshida, T. Irie, K. Konishi, K. Nakano, T. Uto, D. Adachi, M. Kanematsu, H. Uzu, K. Yamamoto, Silicon heterojunction solar cell with interdigitated back contacts for a photoconversion efficiency over 26%, Nat. Energy. 2 (2017) 17032. https://doi.org/10.1038/nenergy.2017.32.

[39] M.A. Green, Y. Hishikawa, E.D. Dunlop, D.H. Levi, J. Hohl-Ebinger, A.W.Y. Ho-Baillie, Solar cell efficiency

tables (version 51), Prog. Photovoltaics Res. Appl. 26 (2018) 3–12. https://doi.org/10.1002/pip.2978.

[40] H.W. Schock, Thin film photovoltaics, Appl. Surf. Sci. 92 (1996) 606–616. https://doi.org/10.1016/0169-4332(95)00303-7.

[41] S. Sladić, B. Barišić, M. Soković, Cost-effective power converter for thin film solar cell technology and improved power quality, J. Mater. Process. Technol. 201 (2008) 786–790. https://doi.org/10.1016/j.jmatprotec.2007.11.161.

[42] M. Dhankhar, O. Pal Singh, V.N. Singh, Physical principles of losses in thin film solar cells and efficiency enhancement methods, Renew. Sustain. Energy Rev. 40 (2014) 214–223. https://doi.org/10.1016/j.rser.2014.07.163.

[43] A. Shah, P. Torres, R. Tscharner, N. Wyrsch, H. Keppner, Photovoltaic Technology: The Case for Thin-Film Solar Cells, Science (80-.). 285 (1999) 692–698. https://doi.org/10.1126/science.285.5428.692.

[44] M.A. Green, E.D. Dunlop, J. Hohl-Ebinger, M. Yoshita, N. Kopidakis, A.W.Y. Ho-Baillie, Solar cell efficiency tables (Version 55), Prog. Photovoltaics Res. Appl. 28 (2020) 3–15. https://doi.org/10.1002/pip.3228.

[45] S. Sharma, K.K. Jain, A. Sharma, Solar Cells: In Research and Applications—A Review, Mater. Sci. Appl. 06 (2015) 1145–1155. https://doi.org/10.4236/msa.2015.612113.

[46] S.M. Sze, K.K. Ng, Physics of Semiconductor Devices, John Wiley & Sons, Inc., Hoboken, NJ, USA, 2006. https://doi.org/10.1002/0470068329.

[47] P. Würfel, Physics of Solar Cells, Wiley, 2005. https://doi.org/10.1002/9783527618545.

[48] K.L. Chopra, S.R. Das, Thin Film Solar Cells, Springer US, Boston, MA, 1983. https://doi.org/10.1007/978-1-4899-0418-8.

[49] A. Goetzberger, J. Knobloch, B. Voß, Crystalline Silicon Solar Cells, John Wiley & Sons, Ltd, Chichester, UK, 2014. https://doi.org/10.1002/9781119033769.

[50] N. Bohr, On the constitution of atoms and molecules, London, Edinburgh, Dublin Philos. Mag. J. Sci. 26 (1913) 1–25. https://doi.org/10.1080/14786441308634955.

[51] R.D.L. Kronig, W.G. Penney, R.H. Fowler, Quantum mechanics of electrons in crystal lattices, Proc. R. Soc. London. Ser. A, Contain. Pap. a Math. Phys. Character. 130 (1931) 499–513. https://doi.org/10.1098/rspa.1931.0019.

[52] K. Mertens, Photovoltaics: Fundamentals, Technology, and Practice, 2nd Edition, Chichester, West Sussex, UK : Wiley, 2018. https://www.wiley.com/en-us/9781119401339.

[53] T. Soga, Nanostructured Materials for Solar Energy Conversion, in: Elsevier, Amsterdam, 2006: pp. vii–ix. https://doi.org/10.1016/B978-044452844-5/50001-9.

[54] C.S. Solanki, Solar Photovoltaics: Fundamentals, Technologies And Applications, PHI Learning, 2015. https://books.google.fr/books?id=y1W2CAAAQBAJ.

[55] C.S. Solanki, B.M. Arora, J. Vasi, M.B. Patil, Solar Photovoltaics, Foundation Books, Delhi, 2013. https://doi.org/10.1017/9789382993254.

[56] A. Kiejna, K.F. Wojciechowski, Electrons in metals, in: Met. Surf. Electron Phys., Elsevier, 1996: pp. 53–76. https://doi.org/10.1016/B978-008042675-4/50004-9.

[57] J. Tang, E.H. Sargent, Infrared Colloidal Quantum Dots for Photovoltaics: Fundamentals and Recent Progress, Adv. Mater. 23 (2011) 12–29. https://doi.org/10.1002/adma.201001491.

[58] C.A. Gueymard, D. Myers, K. Emery, Proposed reference irradiance spectra for solar energy systems testing, Sol. Energy. 73 (2002) 443–467. https://doi.org/10.1016/S0038-092X(03)00005-7.

[59] A.R. Denton, N.W. Ashcroft, Vegard's law, Phys. Rev. A. 43 (1991) 3161–3164. https://doi.org/10.1103/PhysRevA.43.3161.

[60] S. Calnan, Applications of oxide coatings in photovoltaic devices, Coatings. 4 (2014) 162–202. https://doi.org/10.3390/coatings4010162.

[61] Solar Cells: A Guide to Theory and Measurement, Ossila (Enabling Mater. Sci. (2022). https://www.ossila.com/pages/solar-cells-theory (accessed February 12, 2022).

[62] J. Zhao, A. Wang, M.A. Green, F. Ferrazza, 19.8% efficient "honeycomb" textured multicrystalline and 24.4% monocrystalline silicon solar cells, Appl. Phys. Lett. 73 (1998) 1991–1993. https://doi.org/10.1063/1.122345.

[63] G. Fisher, M.R. Seacrist, R.W. Standley, Silicon Crystal Growth and Wafer Technologies, Proc. IEEE. 100 (2012) 1454–1474. https://doi.org/10.1109/JPROC.2012.2189786.

[64] A. Richter, M. Hermle, S.W. Glunz, Reassessment of the Limiting Efficiency for Crystalline Silicon Solar Cells, IEEE J. Photovoltaics. 3 (2013) 1184–1191. https://doi.org/10.1109/JPHOTOV.2013.2270351.

[65] A. Richter, S.W. Glunz, F. Werner, J. Schmidt, A. Cuevas, Improved quantitative description of Auger recombination in crystalline silicon, Phys. Rev. B. 86 (2012) 165202. https://doi.org/10.1103/PhysRevB.86.165202.

[66] M. Bojic, J. Radulovic, V. Rankovic, D. Nikolic, L. Bojic, J. Skerlic, Int. J. Eng. (2016) 37–40.

[67] What is amorphous silicon thin film solar cell?, Dev. Status Res. Types Sol. Pv Cells. (2021). http://www.gatewaysolarcoop.com/what-is-amorphous-silicon-thin-film-solar-cell.html (accessed March 27, 2022).

[68] B.M. Basol, B. McCandless, Brief review of cadmium telluride-based photovoltaic technologies, J. Photonics Energy. 4 (2014) 040996. https://doi.org/10.1117/1.JPE.4.040996.

[69] H.-J. Jeong, Y.-C. Kim, S.K. Lee, Y. Jeong, J.-W. Song, J.-H. Yun, J.-H. Jang, Ultrawide Spectral Response of CIGS Solar Cells Integrated with Luminescent Down-Shifting Quantum Dots, ACS Appl. Mater. Interfaces. 9 (2017) 25404–25411. https://doi.org/10.1021/acsami.7b08122.

[70] Photovoltaic solar power: technologies and their trajectory. https://www.encyclopedie-energie.org/en/photovoltaic-solar-power-technologies-trajectory/ (accessed March 27, 2022).

[71] H. Joël Tchognia Nkuissi, F. Kouadio Konan, B. Hartiti, J.-M. Ndjaka, Toxic Materials Used in Thin Film Photovoltaics and Their Impacts on Environment, in: Reliab. Ecol. Asp. Photovolt. Modul., IntechOpen, 2020. https://doi.org/10.5772/intechopen.88326.

[72] R. Kamada, T. Yagioka, S. Adachi, A. Handa, K.F. Tai, T. Kato, H. Sugimoto, New world record Cu(In, Ga)(Se, S)2 thin film solar cell efficiency beyond 22%, in: 2016 IEEE 43rd Photovolt. Spec. Conf., IEEE, 2016: pp. 1287–1291. https://doi.org/10.1109/PVSC.2016.7749822.

[73] X. Wu, High-efficiency polycrystalline CdTe thin-film solar cells, Sol. Energy. 77 (2004) 803–814. https://doi.org/10.1016/j.solener.2004.06.006.

[74] M. Konagai, Present Status and Future Prospects of Silicon Thin-Film Solar Cells, Jpn. J. Appl. Phys. 50 (2011) 030001. https://doi.org/10.1143/JJAP.50.030001.

[75] M. Gloeckler, I. Sankin, Z. Zhao, CdTe Solar Cells at the Threshold to 20% Efficiency, IEEE J. Photovoltaics. 3 (2013) 1389–1393. https://doi.org/10.1109/JPHOTOV.2013.2278661.

[76] M. Powalla, S. Paetel, E. Ahlswede, R. Wuerz, C.D. Wessendorf, T. Magorian Friedlmeier, Thin-film solar cells exceeding 22% solar cell efficiency: An overview on CdTe-, Cu(In,Ga)Se 2 and perovskite-based materials, Appl. Phys. Rev. 5 (2018) 041602. https://doi.org/10.1063/1.5061809.

[77] F.A. Jhuma, M.Z. Shaily, M.J. Rashid, Towards high-efficiency CZTS solar cell through buffer layer optimization, Mater. Renew. Sustain. Energy. 8 (2019) 6. https://doi.org/10.1007/s40243-019-0144-1.

[78] Y. Zhang, Q. Ye, J. Liu, H. Chen, X. He, C. Liao, J. Han, H. Wang, J. Mei, W. Lau, Earth-abundant and low-cost CZTS solar cell on flexible molybdenum foil, RSC Adv. 4 (2014) 23666–23669. https://doi.org/10.1039/C4RA02064B.

[79] J.W. Leem, D.-H. Jun, J. Heo, W.-K. Park, J.-H. Park, W.J. Cho, D.E. Kim, J.S. Yu, Single-material zinc sulfide bi-layer antireflection coatings for GaAs solar cells, Opt. Express. 21 (2013) A821. https://doi.org/10.1364/OE.21.00A821.

[80] H. Helmers, E. Lopez, O. Höhn, D. Lackner, J. Schön, M. Schauerte, M. Schachtner, F. Dimroth, A.W. Bett, 68.9% Efficient GaAs-Based Photonic Power Conversion Enabled by Photon Recycling and Optical Resonance, Phys. Status Solidi – Rapid Res. Lett. 15 (2021) 2100113. https://doi.org/10.1002/pssr.202100113.

[81] M. Powalla, S. Paetel, D. Hariskos, R. Wuerz, F. Kessler, P. Lechner, W. Wischmann, T.M. Friedlmeier, Advances in Cost-Efficient Thin-Film Photovoltaics Based on Cu(In,Ga)Se2, Engineering. 3 (2017) 445–451. https://doi.org/10.1016/J.ENG.2017.04.015.

[82] M. Nakamura, K. Yamaguchi, Y. Kimoto, Y. Yasaki, T. Kato, H. Sugimoto, Cd-Free Cu(In,Ga)(Se,S) 2 Thin-Film Solar Cell With Record Efficiency of 23.35%, IEEE J. Photovoltaics. 9 (2019) 1863–1867. https://doi.org/10.1109/JPHOTOV.2019.2937218.

[83] M. Kumar, A. Dubey, N. Adhikari, S. Venkatesan, Q. Qiao, Strategic review of secondary phases, defects and defect-complexes in kesterite CZTS–Se solar cells, Energy Environ. Sci. 8 (2015) 3134–3159. https://doi.org/10.1039/C5EE02153G.

[84] S.M. Bhosale, M.P. Suryawanshi, M.A. Gaikwad, P.N. Bhosale, J.H. Kim, A.V. Moholkar, Influence of growth temperatures on the properties of photoactive CZTS thin films using a spray pyrolysis technique, Mater. Lett. 129 (2014) 153–155. https://doi.org/10.1016/j.matlet.2014.04.131.

[85] W. Wang, M.T. Winkler, O. Gunawan, T. Gokmen, T.K. Todorov, Y. Zhu, D.B. Mitzi, Device Characteristics of CZTSSe Thin-Film Solar Cells with 12.6% Efficiency, Adv. Energy Mater. 4 (2014) 1301465. https://doi.org/10.1002/aenm.201301465.

[86] W. Qarony, M.I. Hossain, M.K. Hossain, M.J. Uddin, A. Haque, A.R. Saad, Y.H. Tsang, Efficient amorphous silicon solar cells: characterization, optimization, and optical loss analysis, Results Phys. 7 (2017) 4287–4293. https://doi.org/10.1016/j.rinp.2017.09.030.

[87] H. Kang, Crystalline Silicon vs. Amorphous Silicon: the Significance of Structural Differences in Photovoltaic Applications, IOP Conf. Ser. Earth Environ. Sci. 726 (2021) 012001. https://doi.org/10.1088/1755-1315/726/1/012001.

[88] M. Yamaguchi, High-Efficiency GaAs-Based Solar Cells, in: Post-Transition Met., IntechOpen, 2021. https://doi.org/10.5772/intechopen.94365.

[89] S. Flora, N. Dwivedi, A Toxicochemical Review of Gallium Arsenide, Def. Sci. J. 62 (2012) 95–104. https://doi.org/10.14429/dsj.62.1014.

[90] T. Xu, L. Yu, How to design low bandgap polymers for highly efficient organic solar cells, Mater. Today. 17 (2014) 11–15. https://doi.org/10.1016/j.mattod.2013.12.005.

[91] Y. Zhang, B. Wu, Y. He, W. Deng, J. Li, J. Li, N. Qiao, Y. Xing, X. Yuan, N. Li, C.J. Brabec, H. Wu, G. Lu, C. Duan, F. Huang, Y. Cao, Layer-by-layer processed binary all-polymer solar cells with efficiency over 16% enabled by finely optimized morphology, Nano Energy. 93 (2022) 106858. https://doi.org/10.1016/J.NANOEN.2021.106858.

[92] Y. Wang, W. Wei, X. Liu, Y. Gu, Research progress on polymer heterojunction solar cells, Sol. Energy Mater. Sol. Cells. 98 (2012) 129–145. https://doi.org/10.1016/j.solmat.2011.10.003.

[93] B. O'Regan, M. Grätzel, A low-cost, high-efficiency solar cell based on dye-sensitized colloidal TiO2 films, Nature. 353 (1991) 737–740. https://doi.org/10.1038/353737a0.

[94] K. Sharma, V. Sharma, S.S. Sharma, Dye-Sensitized Solar Cells: Fundamentals and Current Status, Nanoscale Res. Lett. 13 (2018) 381. https://doi.org/10.1186/s11671-018-2760-6.

[95] M. Sokolský, J. Cirák, Dye-Sensitized Solar Cells: Materials and Processes, Acta Electrotech. Inform. 10 (2010) 78–81.

[96] H.M. Upadhyaya, S. Senthilarasu, M.-H. Hsu, D.K. Kumar, Recent progress and the status of dye-sensitised solar cell (DSSC) technology with state-of-the-art conversion efficiencies, Sol. Energy Mater. Sol. Cells. 119 (2013) 291–295. https://doi.org/10.1016/j.solmat.2013.08.031.

[97] D. Vatansever, E. Siores, T. Shah, Alternative Resources for Renewable Energy: Piezoelectric and Photovoltaic Smart Structures, in: Glob. Warm. - Impacts Futur. Perspect., InTech, 2012.

https://doi.org/10.5772/50570.

[98] J. Burschka, N. Pellet, S.-J. Moon, R. Humphry-Baker, P. Gao, M.K. Nazeeruddin, M. Grätzel, Sequential deposition as a route to high-performance perovskite-sensitized solar cells, Nature. 499 (2013) 316–319. https://doi.org/10.1038/nature12340.

[99] S.P. Philipps, A.W. Bett, K. Horowitz, S. Kurtz, Current Status of Concentrator Photovoltaic (CPV) Technology, Natl. Renew. Energy Lab. (2015) 1–25. http://www.ise.fraunhofer.de/en/publications/veroeffentlichungen-pdf-dateien-en/studien-und-konzeptpapiere/current-status-of-concentrator-photovoltaic-cpv-technology.pdf.

[100] S. Kurtz, Opportunities and Challenges for Development of a Mature Concentrating Photovoltaic Power Industry Opportunities and Challenges for Development of a Mature Concentrating Photovoltaic Power Industry, Natl. Renew. Energy Lab. (2012) 35. http://www.nrel.gov/docs/fy13osti/43208.pdf.

[101] R. McConnell, V. Fthenakis, Concentrated Photovoltaics, in: Third Gener. Photovoltaics, InTech, 2012. https://doi.org/10.5772/39245.

[102] M. Lamonica, Solar Concentrator Borrows Water Cooling from IBM Supercomputer: Parabolic dish concentrates light 2,000 times to produce both electricity and high-temperature water, IEEE Spectr. IBM Res. (2014). https://spectrum.ieee.org/solar-concentrator-borrows-water-cooling-from-ibm-supercomputer (accessed April 2, 2022).

[103] W. Shockley, H.J. Queisser, Detailed Balance Limit of Efficiency of p-n Junction Solar Cells, J. Appl. Phys. 32 (1961) 510–519. https://doi.org/10.1063/1.1736034.

[104] G. Conibeer, Third-generation photovoltaics, Mater. Today. 10 (2007) 42–50. https://doi.org/10.1016/S1369-7021(07)70278-X.

[105] T. Takamoto, M. Kaneiwa, M. Imaizumi, M. Yamaguchi, InGaP/GaAs-based multijunction solar cells, Prog. Photovoltaics Res. Appl. 13 (2005) 495–511. https://doi.org/10.1002/pip.642.

[106] J.F. Geisz, S. Kurtz, M.W. Wanlass, J.S. Ward, A. Duda, D.J. Friedman, J.M. Olson, W.E. McMahon, T.E. Moriarty, J.T. Kiehl, High-efficiency GaInP⁄GaAs⁄InGaAs triple-junction solar cells grown inverted with a metamorphic bottom junction, Appl. Phys. Lett. 91 (2007) 023502. https://doi.org/10.1063/1.2753729.

[107] M. Yamaguchi, T. Takamoto, K. Araki, N. Ekins-Daukes, Multi-junction III–V solar cells: current status and future potential, Sol. Energy. 79 (2005) 78–85. https://doi.org/10.1016/j.solener.2004.09.018.

[108] A.W. Bett, F. Dimroth, G. Stollwerck, O.V. Sulima, III-V compounds for solar cell applications, Appl. Phys. A Mater. Sci. Process. 69 (1999) 119–129. https://doi.org/10.1007/s003390050983.

[109] E. Trybus, G. Namkoong, W. Henderson, S. Burnham, W.A. Doolittle, M. Cheung, A. Cartwright, InN: A material with photovoltaic promise and challenges, J. Cryst. Growth. 288 (2006) 218–224. https://doi.org/10.1016/j.jcrysgro.2005.12.120.

[110] R.R. King, D.C. Law, K.M. Edmondson, C.M. Fetzer, G.S. Kinsey, H. Yoon, R.A. Sherif, N.H. Karam, 40% efficient metamorphic GaInP⁄GaInAs⁄Ge multijunction solar cells, Appl. Phys. Lett. 90 (2007) 183516. https://doi.org/10.1063/1.2734507.

[111] R.W. Miles, G. Zoppi, I. Forbes, Inorganic photovoltaic cells, Mater. Today. 10 (2007) 20–27. https://doi.org/10.1016/S1369-7021(07)70275-4.

[112] K.A. Horowitz, T.W. Remo, B. Smith, A.J. Ptak, A Techno-Economic Analysis and Cost Reduction Roadmap for III-V Solar Cells, Golden, CO (United States), 2018. https://doi.org/10.2172/1484349.

[113] S. Rühle, A.Y. Anderson, H.-N. Barad, B. Kupfer, Y. Bouhadana, E. Rosh-Hodesh, A. Zaban, All-Oxide Photovoltaics, J. Phys. Chem. Lett. 3 (2012) 3755–3764. https://doi.org/10.1021/jz3017039.

[114] M.L. Moreira, E.C. Paris, G.S. do Nascimento, V.M. Longo, J.R. Sambrano, V.R. Mastelaro, M.I.B. Bernardi, J. Andrés, J.A. Varela, E. Longo, Structural and optical properties of $CaTiO_3$ perovskite-based materials obtained by microwave-assisted hydrothermal synthesis: An experimental and theoretical insight, Acta Mater. 57 (2009) 5174–5185. https://doi.org/10.1016/j.actamat.2009.07.019.

[115] Y. Mao, T.-J. Park, S.S. Wong, Synthesis of classes of ternary metal oxide nanostructures, Chem.

Commun. (2005) 5721. https://doi.org/10.1039/b509960a.

[116] F. Dogan, H. Lin, M. Guilloux-Viry, O. Peña, Focus on properties and applications of perovskites, Sci. Technol. Adv. Mater. 16 (2015) 020301. https://doi.org/10.1088/1468-6996/16/2/020301.

[117] E.A.R. Assirey, Perovskite synthesis, properties and their related biochemical and industrial application, Saudi Pharm. J. 27 (2019) 817–829. https://doi.org/10.1016/j.jsps.2019.05.003.

[118] M.M. Lee, J. Teuscher, T. Miyasaka, T.N. Murakami, H.J. Snaith, Efficient Hybrid Solar Cells Based on Meso-Superstructured Organometal Halide Perovskites, Science (80-.). 338 (2012) 643–647. https://doi.org/10.1126/science.1228604.

[119] M. Liu, M.B. Johnston, H.J. Snaith, Efficient planar heterojunction perovskite solar cells by vapour deposition, Nature. 501 (2013) 395–398. https://doi.org/10.1038/nature12509.

[120] W. Ke, C.C. Stoumpos, M.G. Kanatzidis, "Unleaded" Perovskites: Status Quo and Future Prospects of Tin-Based Perovskite Solar Cells, Adv. Mater. 31 (2019) 1803230. https://doi.org/10.1002/adma.201803230.

[121] X. Zhao, N.-G. Park, Stability Issues on Perovskite Solar Cells, Photonics. 2 (2015) 1139–1151. https://doi.org/10.3390/photonics2041139.

[122] D. Wang, M. Wright, N.K. Elumalai, A. Uddin, Stability of perovskite solar cells, Sol. Energy Mater. Sol. Cells. 147 (2016) 255–275. https://doi.org/10.1016/j.solmat.2015.12.025.

[123] Y. Rong, Y. Hu, A. Mei, H. Tan, M.I. Saidaminov, S. Il Seok, M.D. McGehee, E.H. Sargent, H. Han, Challenges for commercializing perovskite solar cells, Science (80-.). 361 (2018). https://doi.org/10.1126/science.aat8235.

[124] F. Shi, G. Fu, E.-C. Xiao, J. Li, Lattice vibrational characteristics and dielectric properties of pure phase $CaTiO_3$ ceramic, J. Mater. Sci. Mater. Electron. 31 (2020) 18070–18076. https://doi.org/10.1007/s10854-020-04357-9.

[125] A. Alizadeh, M. Roudgar-Amoli, S.-M. Bonyad-Shekalgourabi, Z. Shariatinia, M. Mahmoudi, F. Saadat, Dye sensitized solar cells go beyond using perovskite and spinel inorganic materials: A review, Renew. Sustain. Energy Rev. 157 (2022) 112047. https://doi.org/10.1016/j.rser.2021.112047.

[126] Z. Yan, D.A. Keller, K.J. Rietwyk, H.-N. Barad, K. Majhi, A. Ginsburg, A.Y. Anderson, A. Zaban, Effect of Spinel Inversion on $(Co_xFe_{1-x})_3O_4$ All-Oxide Solar Cell Performance, Energy Technol. 4 (2016) 809–815. https://doi.org/10.1002/ente.201500402.

[127] S.-H. Wei, Electronic Structure and Stability of Spinel Oxides, Jpn. J. Appl. Phys. 39 (2000) 251. https://doi.org/10.7567/JJAPS.39S1.251.

[128] C. Julien, A. Mauger, K. Zaghib, H. Groult, Comparative Issues of Cathode Materials for Li-Ion Batteries, Inorganics. 2 (2014) 132–154. https://doi.org/10.3390/inorganics2010132.

[129] N. Tsuda, K. Nasu, A. Fujimori, K. Siratori, Electronic conduction in oxides, Springer Science & Business Media, 2000.

[130] A. Pérez-Tomás, A. Mingorance, D. Tanenbaum, M. Lira-Cantú, Metal Oxides in Photovoltaics: All-Oxide, Ferroic, and Perovskite Solar Cells, in: Futur. Semicond. Oxides Next-Generation Sol. Cells, Elsevier, 2018: pp. 267–356. https://doi.org/10.1016/B978-0-12-811165-9.00008-9.

[131] C.G. Granqvist, Transparent conductors as solar energy materials: A panoramic review, Sol. Energy Mater. Sol. Cells. 91 (2007) 1529–1598. https://doi.org/10.1016/j.solmat.2007.04.031.

[132] K.L. Chopra, S. Major, D.K. Pandya, Transparent conductors—A status review, Thin Solid Films. 102 (1983) 1–46. https://doi.org/10.1016/0040-6090(83)90256-0.

[133] E. Fortunato, D. Ginley, H. Hosono, D.C. Paine, Transparent Conducting Oxides for Photovoltaics, MRS Bull. 32 (2007) 242–247. https://doi.org/10.1557/mrs2007.29.

[134] E. Wallin, U. Malm, T. Jarmar, O.L.M. Edoff, L. Stolt, World-record $Cu(In,Ga)Se_2$ -based thin-film sub-module with 17.4% efficiency, Prog. Photovoltaics Res. Appl. 20 (2012) 851–854. https://doi.org/10.1002/pip.2246.

[135] J. Bouclé, P. Ravirajan, J. Nelson, Hybrid polymer–metal oxide thin films for photovoltaic applications, J. Mater. Chem. 17 (2007) 3141. https://doi.org/10.1039/b706547g.

[136] P. Ravirajan, A.M. Peiró, M.K. Nazeeruddin, M. Graetzel, D.D.C. Bradley, J.R. Durrant, J. Nelson, Hybrid Polymer/Zinc Oxide Photovoltaic Devices with Vertically Oriented ZnO Nanorods and an Amphiphilic Molecular Interface Layer, J. Phys. Chem. B. 110 (2006) 7635–7639. https://doi.org/10.1021/jp0571372.

[137] J. Meyer, S. Hamwi, M. Kröger, W. Kowalsky, T. Riedl, A. Kahn, Transition Metal Oxides for Organic Electronics: Energetics, Device Physics and Applications, Adv. Mater. 24 (2012) 5408–5427. https://doi.org/10.1002/adma.201201630.

[138] E.L. Ratcliff, B. Zacher, N.R. Armstrong, Selective Interlayers and Contacts in Organic Photovoltaic Cells, J. Phys. Chem. Lett. 2 (2011) 1337–1350. https://doi.org/10.1021/jz2002259.

[139] R.J. Singh, Solid state physics, Pearson Education India (2012).

[140] A.R. Hutson, Hall Effect Studies of Doped Zinc Oxide Single Crystals, Phys. Rev. 108 (1957) 222–230. https://doi.org/10.1103/PhysRev.108.222.

[141] J.W. Orton, M.J. Powell, The Hall effect in polycrystalline and powdered semiconductors, Reports Prog. Phys. 43 (1980) 1263–1307. https://doi.org/10.1088/0034-4885/43/11/001.

[142] F. Wooten, S.P. Davis, Optical Properties of Solids, Am. J. Phys. 41 (1973) 939–940. https://doi.org/10.1119/1.1987434.

[143] S. Rühle, A. Zaban, CHAPTER 8. All-oxide Photovoltaics, in: n.d.: pp. 258–286. https://doi.org/10.1039/9781849739955-00258.

[144] S. Rühle, Tabulated values of the Shockley–Queisser limit for single junction solar cells, Sol. Energy. 130 (2016) 139–147. https://doi.org/10.1016/j.solener.2016.02.015.

[145] T. Minami, Y. Nishi, T. Miyata, Heterojunction solar cell with 6% efficiency based on an n-type aluminum–gallium–oxide thin film and p-type sodium-doped Cu_2O sheet, Appl. Phys. Express. 8 (2015) 022301. https://doi.org/10.7567/APEX.8.022301.

[146] T. Minami, Y. Nishi, T. Miyata, S. Abe, Photovoltaic Properties in Al-doped ZnO/non-doped Zn1-XMgXO/Cu2O Heterojunction Solar Cells, ECS Trans. 50 (2013) 59–68. https://doi.org/10.1149/05051.0059ecst.

[147] Y. Ievskaya, R.L.Z. Hoye, A. Sadhanala, K.P. Musselman, J.L. MacManus-Driscoll, Fabrication of ZnO/Cu2O heterojunctions in atmospheric conditions: Improved interface quality and solar cell performance, Sol. Energy Mater. Sol. Cells. 135 (2015) 43–48. https://doi.org/10.1016/j.solmat.2014.09.018.

[148] M. Pavan, S. Rühle, A. Ginsburg, D.A. Keller, H.-N. Barad, P.M. Sberna, D. Nunes, R. Martins, A.Y. Anderson, A. Zaban, E. Fortunato, TiO_2/Cu_2O all-oxide heterojunction solar cells produced by spray pyrolysis, Sol. Energy Mater. Sol. Cells. 132 (2015) 549–556. https://doi.org/10.1016/j.solmat.2014.10.005.

[149] Ø. Nordseth, R. Kumar, K. Bergum, L. Fara, S.E. Foss, H. Haug, F. Drăgan, D. Crăciunescu, P. Sterian, I. Chilibon, C. Vasiliu, L. Baschir, D. Savastru, E. Monakhov, B.G. Svensson, Optical Analysis of a ZnO/Cu_2O Subcell in a Silicon-Based Tandem Heterojunction Solar Cell, Green Sustain. Chem. 07 (2017) 57–69. https://doi.org/10.4236/gsc.2017.71005.

[150] C. Zuo, L. Ding, Solution-Processed Cu_2O and CuO as Hole Transport Materials for Efficient Perovskite Solar Cells, Small. 11 (2015) 5528–5532. https://doi.org/10.1002/smll.201501330.

[151] A. Mittiga, E. Salza, F. Sarto, M. Tucci, R. Vasanthi, Heterojunction solar cell with 2% efficiency based on a Cu_2O substrate, Appl. Phys. Lett. 88 (2006) 163502. https://doi.org/10.1063/1.2194315.

[152] Y. Nishi, T. Miyata, T. Minami, The impact of heterojunction formation temperature on obtainable conversion efficiency in n-ZnO/p-Cu_2O solar cells, Thin Solid Films. 528 (2013) 72–76. https://doi.org/10.1016/j.tsf.2012.09.090.

[153] T. Minami, Y. Nishi, T. Miyata, Cu2O-based solar cells using oxide semiconductors, J. Semicond. 37 (2016) 014002. https://doi.org/10.1088/1674-4926/37/1/014002.

[154] T. Minami, Y. Nishi, T. Miyata, Efficiency enhancement using a $Zn_{1-x}Ge_xO$ thin film as an n-type window layer in Cu_2O-based heterojunction solar cells, Appl. Phys. Express. 9 (2016) 052301. https://doi.org/10.7567/APEX.9.052301.

[155] N. Winkler, S. Edinger, J. Kaur, R.A. Wibowo, W. Kautek, T. Dimopoulos, Solution-processed all-oxide solar cell based on electrodeposited Cu_2O and ZnMgO by spray pyrolysis, J. Mater. Sci. 53 (2018) 12231–12243. https://doi.org/10.1007/s10853-018-2482-2.

[156] T. Minami, Y. Nishi, T. Miyata, High-Efficiency Cu_2O-Based Heterojunction Solar Cells Fabricated Using a Ga_2O_3 Thin Film as N-Type Layer, Appl. Phys. Express. 6 (2013) 044101. https://doi.org/10.7567/APEX.6.044101.

[157] Y.S. Lee, D. Chua, R.E. Brandt, S.C. Siah, J. V. Li, J.P. Mailoa, S.W. Lee, R.G. Gordon, T. Buonassisi, Atomic Layer Deposited Gallium Oxide Buffer Layer Enables 1.2 V Open-Circuit Voltage in Cuprous Oxide Solar Cells, Adv. Mater. 26 (2014) 4704–4710. https://doi.org/10.1002/adma.201401054.

[158] H. Tanaka, T. Shimakawa, T. Miyata, H. Sato, T. Minami, Electrical and optical properties of TCO–Cu_2O heterojunction devices, Thin Solid Films. 469–470 (2004) 80–85. https://doi.org/10.1016/j.tsf.2004.06.180.

[159] T. Minami, T. Miyata, K. Ihara, Y. Minamino, S. Tsukada, Effect of ZnO film deposition methods on the photovoltaic properties of ZnO–Cu_2O heterojunction devices, Thin Solid Films. 494 (2006) 47–52. https://doi.org/10.1016/j.tsf.2005.07.167.

[160] Z. Zang, Efficiency enhancement of ZnO/Cu_2O solar cells with well oriented and micrometer grain sized Cu2O films, Appl. Phys. Lett. 112 (2018) 042106. https://doi.org/10.1063/1.5017002.

[161] T. Minami, Y. Nishi, T. Miyata, J. Nomoto, High-Efficiency Oxide Solar Cells with ZnO/Cu_2O Heterojunction Fabricated on Thermally Oxidized Cu_2O Sheets, Appl. Phys. Express. 4 (2011) 062301. https://doi.org/10.1143/APEX.4.062301.

[162] A.T. Marin, D. Muñoz-Rojas, D.C. Iza, T. Gershon, K.P. Musselman, J.L. MacManus-Driscoll, Novel Atmospheric Growth Technique to Improve Both Light Absorption and Charge Collection in ZnO/Cu_2O Thin Film Solar Cells, Adv. Funct. Mater. 23 (2013) 3413–3419. https://doi.org/10.1002/adfm.201203243.

[163] M. Izaki, T. Shinagawa, K.-T. Mizuno, Y. Ida, M. Inaba, A. Tasaka, Electrochemically constructed p-Cu_2O/n-ZnO heterojunction diode for photovoltaic device, J. Phys. D. Appl. Phys. 40 (2007) 3326–3329. https://doi.org/10.1088/0022-3727/40/11/010.

[164] K. Fujimoto, T. Oku, T. Akiyama, Fabrication and Characterization of ZnO/Cu_2O Solar Cells Prepared by Electrodeposition, Appl. Phys. Express. 6 (2013) 086503. https://doi.org/10.7567/APEX.6.086503.

[165] S. Nandy, A. Banerjee, E. Fortunato, R. Martins, A Review on Cu_2O and CuI-Based p-Type Semiconducting Transparent Oxide Materials: Promising Candidates for New Generation Oxide Based Electronics, Rev. Adv. Sci. Eng. 2 (2013) 273–304. https://doi.org/10.1166/rase.2013.1045.

[166] C.J. Traverse, R. Pandey, M.C. Barr, R.R. Lunt, Emergence of highly transparent photovoltaics for distributed applications, Nat. Energy. 2 (2017) 849–860. https://doi.org/10.1038/s41560-017-0016-9.

[167] M. Deo, S. Mujawar, O. Game, A. Yengantiwar, A. Banpurkar, S. Kulkarni, J. Jog, S. Ogale, Strong photo-response in a flip-chip nanowire p-Cu_2O/n-ZnO junction, Nanoscale. 3 (2011) 4706. https://doi.org/10.1039/c1nr10665a.

[168] P. Ghamgosar, F. Rigoni, S. You, I. Dobryden, M.G. Kohan, A.L. Pellegrino, I. Concina, N. Almqvist, G. Malandrino, A. Vomiero, ZnO-Cu_2O core-shell nanowires as stable and fast response photodetectors, Nano Energy. 51 (2018) 308–316. https://doi.org/10.1016/j.nanoen.2018.06.058.

[169] K.P. Musselman, A. Marin, L. Schmidt-Mende, J.L. MacManus-Driscoll, Incompatible Length Scales in Nanostructured Cu_2O Solar Cells, Adv. Funct. Mater. 22 (2012) 2202–2208. https://doi.org/10.1002/adfm.201102263.

[170] M. Abd-Ellah, J.P. Thomas, L. Zhang, K.T. Leung, Enhancement of solar cell performance of p-Cu_2O/n-ZnO-nanotube and nanorod heterojunction devices, Sol. Energy Mater. Sol. Cells. 152 (2016) 87–93. https://doi.org/10.1016/j.solmat.2016.03.022.

[171] K.P. Musselman, A. Wisnet, D.C. Iza, H.C. Hesse, C. Scheu, J.L. MacManus-Driscoll, L. Schmidt-Mende, Strong Efficiency Improvements in Ultra-low-Cost Inorganic Nanowire Solar Cells, Adv. Mater. 22 (2010) E254–E258. https://doi.org/10.1002/adma.201001455.

[172] B.D. Yuhas, P. Yang, Nanowire-Based All-Oxide Solar Cells, J. Am. Chem. Soc. 131 (2009) 3756–3761. https://doi.org/10.1021/ja8095575.

[173] S.K. Baek, K.R. Lee, H.K. Cho, Oxide p-n Heterojunction of Cu_2O/ZnO Nanowires and Their Photovoltaic Performance, J. Nanomater. 2013 (2013) 1–7. https://doi.org/10.1155/2013/421371.

[174] T.-J. Hsueh, C.-L. Hsu, S.-J. Chang, P.-W. Guo, J.-H. Hsieh, I.-C. Chen, Cu_2O/n-ZnO nanowire solar cells on ZnO:Ga/glass templates, Scr. Mater. 57 (2007) 53–56. https://doi.org/10.1016/j.scriptamat.2007.03.012.

[175] Y. Takiguchi, S. Miyajima, Device simulation of cuprous oxide heterojunction solar cells, Jpn. J. Appl. Phys. 54 (2015) 112303. https://doi.org/10.7567/JJAP.54.112303.

[176] C. Malerba, F. Biccari, C. Leonor Azanza Ricardo, M. D'Incau, P. Scardi, A. Mittiga, Absorption coefficient of bulk and thin film Cu2O, Sol. Energy Mater. Sol. Cells. 95 (2011) 2848–2854. https://doi.org/10.1016/j.solmat.2011.05.047.

[177] T. Minami, T. Miyata, J. Nomoto, Impurity-doped ZnO Thin Films Prepared by Physical Deposition Methods Appropriate for Transparent Electrode Applications in Thin-film Solar Cells, IOP Conf. Ser. Mater. Sci. Eng. 34 (2012) 012001. https://doi.org/10.1088/1757-899X/34/1/012001.

[178] K. Postava, H. Sueki, M. Aoyama, T. Yamaguchi, K. Murakami, Y. Igasaki, Doping effects on optical properties of epitaxial ZnO layers determined by spectroscopic ellipsometry, Appl. Surf. Sci. 175–176 (2001) 543–548. https://doi.org/10.1016/S0169-4332(01)00145-3.

[179] H. ElAnzeery, O. El Daif, M. Buffière, S. Oueslati, K. Ben Messaoud, D. Agten, G. Brammertz, R. Guindi, B. Kniknie, M. Meuris, J. Poortmans, Refractive index extraction and thickness optimization of $Cu_2ZnSnSe_4$ thin film solar cells, Phys. Status Solidi. 212 (2015) 1984–1990. https://doi.org/10.1002/pssa.201431807.

[180] S. Lettieri, L. Santamaria Amato, P. Maddalena, E. Comini, C. Baratto, S. Todros, Recombination dynamics of deep defect states in zinc oxide nanowires, Nanotechnology. 20 (2009) 175706. https://doi.org/10.1088/0957-4484/20/17/175706.

[181] M. Kubota, T. Onuma, A. Tsukazaki, A. Ohtomo, M. Kawasaki, T. Sota, S.F. Chichibu, Recombination dynamics of excitons in $Mg_{0.11}Zn_{0.89}O$ alloy films grown using the high-temperature-annealed self-buffer layer by laser-assisted molecular-beam epitaxy, Appl. Phys. Lett. 90 (2007) 141903. https://doi.org/10.1063/1.2719168.

[182] C. Chevallier, S. Bose, S. Ould Saad Hamady, N. Fressengeas, Numerical investigations of the impact of buffer germanium composition and low cost fabrication of Cu_2O on AZO/ZnGeO/Cu_2O solar cell performances, EPJ Photovoltaics. 12 (2021) 3. https://doi.org/10.1051/epjpv/2021003.

[183] R. David Prabu, S. Valanarasu, V. Ganesh, M. Shkir, A. Kathalingam, S. AlFaify, Effect of spray pressure on optical, electrical and solar cell efficiency of novel Cu_2O thin films, Surf. Coatings Technol. 347 (2018) 164–172. https://doi.org/10.1016/j.surfcoat.2018.04.084.

[184] K. Ravichandran, N. Jabena Begum, S. Snega, B. Sakthivel, Properties of Sprayed Aluminum-Doped Zinc Oxide Films—A Review, Mater. Manuf. Process. 31 (2016) 1411–1423. https://doi.org/10.1080/10426914.2014.930961.

[185] S. Santhosh Kumar Jacob, I. Kulandaisamy, S. Valanarasu, A.M.S. Arulanantham, M. Shkir, A. Kathalingam, N. Soundaram, Improving the conductivity of cuprous oxide thin film by doping Calcium via feasible nebulizer spray technique for solar cell (FTO/ZnO/Ca-Cu_2O), Mater. Res. Express. 6 (2019) 046405. https://doi.org/10.1088/2053-1591/aafb18.

[186] K. Kardarian, D. Nunes, P. Maria Sberna, A. Ginsburg, D.A. Keller, J. Vaz Pinto, J. Deuermeier, A.Y. Anderson, A. Zaban, R. Martins, E. Fortunato, Effect of Mg doping on Cu_2O thin films and their behavior on the TiO_2 /Cu_2O heterojunction solar cells, Sol. Energy Mater. Sol. Cells. 147 (2016) 27–36. https://doi.org/10.1016/j.solmat.2015.11.041.

[187] N. Plankensteiner, W. Kautek, T. Dimopoulos, Aqueous Spray Pyrolysis of Cu_2O Films: Influence of

Reducing Agent and Acetic Acid Addition, ChemNanoMat. 6 (2020) 663–671. https://doi.org/10.1002/cnma.202000006.

[188] K. Akimoto, S. Ishizuka, M. Yanagita, Y. Nawa, G.K. Paul, T. Sakurai, Thin film deposition of Cu_2O and application for solar cells, Sol. Energy. 80 (2006) 715–722. https://doi.org/10.1016/j.solener.2005.10.012.

CHAPTER 2: Preparation Process Using Ultrasonic Spray Pyrolysis and Characterization Techniques

2.1 Introduction to Spray Pyrolysis

Material preparation systems comprising of solution-based techniques are becoming more and more attractive for material production related industries due to their simplicity combined with high throughputs with reduced costs. Solution-based techniques include spray pyrolysis, spray painting, sol-gel, spin coating, spray casting, slot-die coating, doctor-blading, knife-over-edge coating, screen printing, pad printing, offset printing, flexographic printing, gravure printing and others [1]. Spray pyrolysis techniques gained a lot of popularity during the last decade due to their flexibility to deposit a wide variety of thin film materials. Thin films metal oxides (both binary and ternary), metallic spinel oxides, chalcogenides (binary, ternary, and quaternary), kesterites (quaternary) and superconducting oxides among others [2]. Not only the process of spray pyrolysis is simple, but it is also attractive due to its cost-effectiveness. Many studies have been done on spray pyrolysis towards the preparation of thin films but Chamberlin *et al.* [3] first reported a CdS thin film prepared by spray pyrolysis.

Despite being a cost-effective and simple process, spray pyrolysis has another major advantage due to its tuneable parameters. These parameters in turn makes the spray process widely flexible for preparation purpose without requiring high quality targets or substrates. Even the temperature range of 100 °C to 600 °C (depends on the specific tool set-up) is ample. The deposited rate can be controlled by adjusting the flow rate and the speed of the nozzle, but with a limit on the thickness of the films. Control of the film is important as with higher thickness there is a tendency for the film quality to deteriorate, especially without control and optimization of the spray parameters. So, spray conditions need to suitably be tailored based on the type of the substrate and the thickness of film desired. Basically, with lower financial investments needed and subsequently with lower production costs spray pyrolysis is an interesting thin film deposition technique. Nonetheless, there are some drawbacks such as, the grain sizes in the films are relatively small [4,5], presence of unwanted impurity phases in the films resulting from incomplete pyrolysis which are hard to remove [5–7] and often films have high surface roughness [5,8].

In the first half of the chapter different aspects of spray pyrolysis for preparation of thin films are discussed. Types of spray pyrolysis with a focus on ultrasonic spray pyrolysis (USP) is discussed with description of the actual spray system used. All the spray parameters involved in the preparation process are also discussed. The physical processes involved in the USP technique are discussed in detail. The characterization techniques used to investigate the prepared thin films are detailed in the last part of the chapter.

The deposition technique using spray can be known by various names: chemical spray [9], spray coating [9], spray [9,10], spray pyrolysis [11] and combinations of all these. Generally, the different names are given based on the source of the precursors and the processes involved in the formation of the films. More specific names are assigned to this deposition technique based on the methods of atomization. Each atomization technique is unique in terms of the control of the sizes of the generated droplets and their distribution and decomposition across the pre-heated substrates. Depending on the atomization technique, the types can be named as: corona spray pyrolysis [12], electrostatic spray pyrolysis [13,14], nebulized spray pyrolysis [15], ultrasonic spray pyrolysis [4,16] and pneumatic spray pyrolysis [17]. The spray systems can be further classified in two more categories according to the relative direction of the droplets: horizontal and vertical configurations [11]. The horizontal configuration permits a separation of the droplets/particles according to their size, while in the vertical configuration the droplets/particles possess a certain velocity provided by the carrier gas and thus undergo a free fall motion [11,18]. Spray systems can even be names on the process of substrate heating. When the hot walls of the vertical or horizontal reactor heats up the substrate, then the system is called hot-wall spray. If the heating of the substrate happens by the direct contact with the heat source (hot-plate or tin-bath) then the spray system is called cool-wall spray.

Research has been carried on for decades to understand and explain all the physical and chemical processes that leads to the formation of films by spray pyrolysis; but the understanding is not yet complete. To understand the underlying physics of the droplets transport process there are both empirical [19] and theoretical [20] models. Considering some factors such as the extremely large number of atomized droplets in a spray process with high and varying velocity, very differing droplet sizes along with the change in time due to coalescence and evaporation, the temperature gradient, the regions with gas between the neighbouring droplets etc., are typically very complex to understand. Depending solely on computational resources are insufficient. All the dynamical and thermal interactions coupled with the large system of equations cannot be solved by only computation. This is the reason why the theoretical explanation of the spray deposition become extremely important. The theoretical explanations consider ideal bounded conditions to simplify the hypothesis thus revealing the level of complexity of the spray process. In this thesis an attempt has been done to explain the parameters leading to the formation of high-quality metal oxide thin films suitable to photovoltaics.

Perednis *et al.* in their review article [19] compiled important experimental results as a guidance for understanding in detail the plethora of spray parameters from the perspective of film quality. They mentioned about the importance of the process optimization for each change of spray parameter for each different kind of film with different material. According to Perednis *et al.* [19], different processes for spray preparation of a material, occur either sequentially or simultaneously. Understanding of each of the process is essential to improve the film quality.

From the studies by Perednis *et al.* [19], Filipovic *et al.* [20] and others, a general agreement can be reached regarding the steps followed in the deposition and growth of thin films by spray pyrolysis. The steps are mostly deduced from experimental observations following a logic sequence. Following the logic, the entire process can be broadly classified into three main steps:

(**i**) Spray of the atomized precursor solution.

(**ii**) Transport of the aerosol (resultant droplets).

(**iii**) Pyrolysis (decomposition) of the atomized precursor solution droplets.

Step (i): Spray of the atomized precursor solution:

In the first step, droplets are generated from the precursor solution by the process of atomization and then forms a spray. Hence, the spray in this step can be explained as: formation of very tiny droplets by breaking up a liquid (precursor solution). The droplets are then blown or forced through the air. This forms a classical definition of spray [21]. A typical cross-section of a spray generation system is shown in the ***Figure 2.1***. The entire process of spray pyrolysis is schematically shown in the ***Figure 2.2***.

Figure 2.1: Ultrasonic nozzle cross-section showing the generation of spray [22].

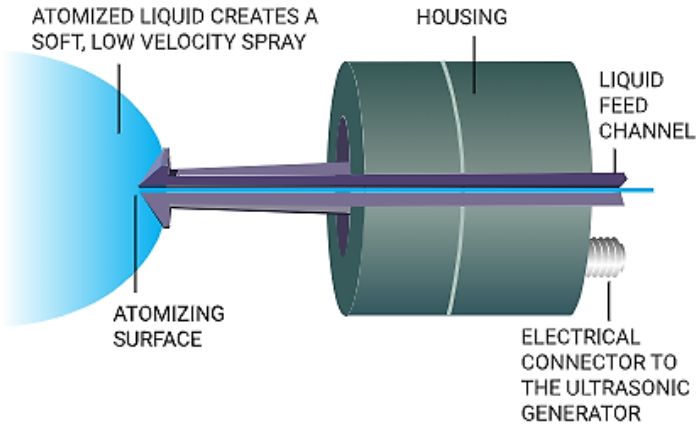

Figure 2.2: Schematic representation of the complete spray pyrolysis process. Concept adapted and modified from [19].

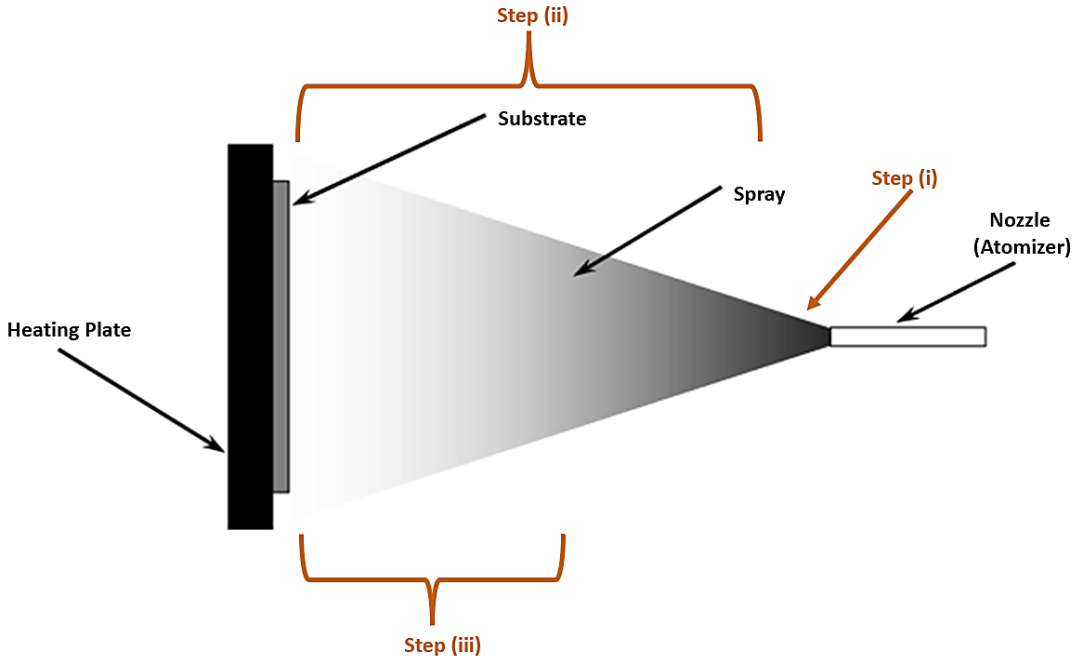

In ***Step (i)*** the atomized droplets are generated from the nozzle, and it happens very rapidly, while ***Steps (ii)*** and ***(iii)*** takes more time. The ***Step (iii)*** starts even before the ***Step (ii)*** is complete. The pressure of the compressed carrier gas (system's shaping air pressure) determines the duration of ***Step (ii)***. The start of ***Step (iii)*** is determined by the liquid droplet size and the set temperature of the heating plate and the substrate temperature which is in direct contact with the heating plate. The spray pattern is entirely dependent on the nozzle as different nozzles generates different droplet sizes with differing velocity, spray shape and coverage area.

For our preparations we have implemented ultrasonic nozzles in which the high frequency sound waves are converted into mechanical energy which is then transferred into the liquid (precursor solution). With the transfer of the mechanical energy to the liquid, a standing wave is created and as the liquid exits the surface of the nozzle it gets atomized, i.e., it gets broken into fine mist of uniform micron sized droplets. Unlike pressure-based nozzles, in ultrasonic nozzles the liquid flows through the nozzle center (with a large orifice) without pressure and the atomization happens only due to the ultrasonic vibrations in the nozzle. The median droplet size depends on the specific resonant frequency of the nozzle. The mist of droplets thus created (also known as aerosol) are guided towards the substrate by a low velocity spray shaping air (compressed carrier gas). The shaping air controls the shape/pattern of the spray which can be fine lines, conical patterns or wide flat fan shaped [2,22,23].

Step (ii): Transport of the aerosol (resultant droplets):

This step concerns the transport of the generated droplets. During the transport, the droplets will experience physico-chemical changes. The changes are dependent on the location, velocity, and size of the generated atomized droplets and on the temperature of the substrate. As the droplets travel, four forces can act upon them simultaneously: gravitational, electrical, Stokes and thermophoretic [24].

As the droplets travel their size will be reduced. It happens as the solvent undergoes evaporation and the rate of which also determines the droplet trajectory. The evaporation rate is higher when the temperature of the substrate is higher than the boiling point of the solvent. The unevaporated droplets will experience a gravitational force pulling them downward vertically towards the substrate [19]. In the titanium nozzles, a generator is vibrated at ultrasonic frequencies resulting in smaller droplet sizes with a force that is much higher than the gravitational force [2,24].

The thermophoretic force acts mostly near the substrate surface. It acts as a retarding force by pushing the droplets away from the substrate's hot surface and ultimately decreasing their velocity. The important factors that determine the thermophoretic force are heat conductivity and the heat absorption rate of the droplets in addition to the size and viscosity of the droplets. The magnitude of the temperature gradient is also directly proportional to the force. When the droplets are approaching the preheated substrate, they acquire thermal energy from the hot air atmosphere in the direction of motion. On touching the substrate, the hotter side of the droplets gets rebounded with a higher kinetic energy than compared to the cooler side. This is a forced convection mechanism [19,20,24].

The Stokes forces are dominant in ***Step (ii)*** and they are caused as friction happens between the droplets and the air molecules. So, the Stokes force can be defined as a drag force that the droplets experience against the air molecules. The magnitude of the Stokes force is directly dependent upon the size of the droplets, the viscosity of the air molecules (air vapour) and the relative velocity between the air molecules and the droplets [20,24].

A schematic of the process of transport of aerosols is shown in the ***Figure 2.3***.

Figure 2.3: A view of the transport of the aerosols during the spray operation [19].

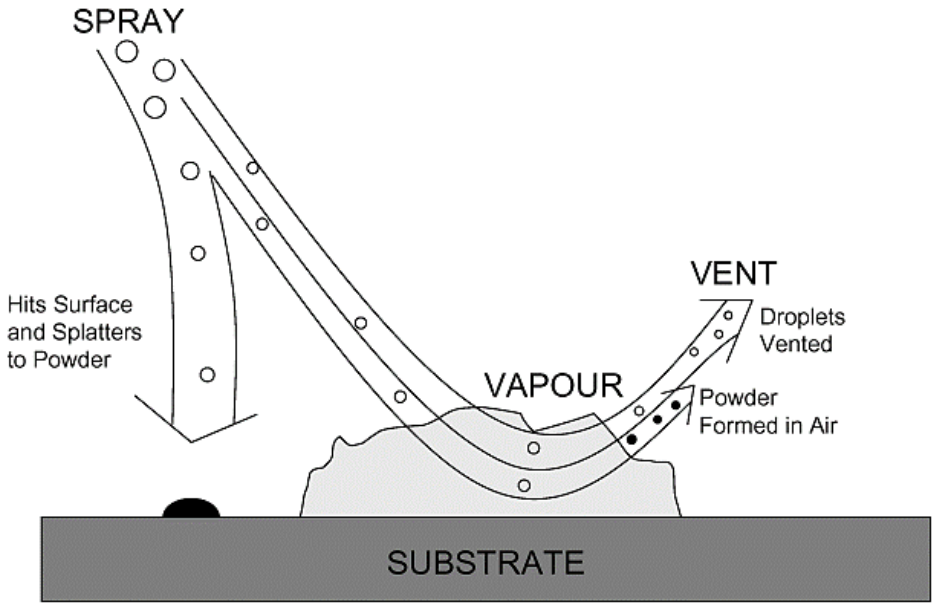

Step (iii): Pyrolysis (decomposition) of the atomized precursor solution droplets:

From the ***Figure 2.2***, we see that ***Step (iii)*** commence even before the ***Step (ii)*** is over. ***Step (ii)*** is generally complete before reaching the heated substrate. The ***Step (iii)*** begins when the solvent is evaporated. In this step it is expected that due to the action of the heat the droplets will undergo transformation. For each individual droplet, the starting point of ***Step (iii)*** will be dependent upon few factors: size of the droplet, the position (proximity) of the droplet with the substrate and the substrate temperature. To precisely define the ***Step (iii)***, we can think of four different types in which the atomized droplets might interact with the heated substrate.

Process 1: If all the solvent does not vaporize due to the temperature not being high enough, then unevaporated solvent droplet splatters on the substrate. After the droplet is on the substrate, then the vaporization starts leaving a dry precipitate and then the decomposition starts [19,25].

Process 2: The size of the droplet gets reduced with an increase in the temperature. The solvent gradually evaporates which leads to not only the reduction in size but also a concentration gradient within the droplet. The precursor tends to precipitate on the droplet surface when the concentration exceeds the solubility limit of the solvent. Eventually, a dry precipitate reaches the substrate which leads to the formation of unwanted particles in the sprayed films. The particles are not desired as they tend to remain on the substrate surface while adding to the roughness and loss of texture of the thin films [19,25–27].

Process 3: When the hot atmosphere of the spray system causes the droplets to evaporate then a precipitate will form. A sublimation (vaporization) process takes place when the precipitate is in the proximity of the hot substrate. The vapor thus generated, diffuses to the substrate top and undergoes a complete heterogeneous reaction. This results in high quality depositing of a film with a high sticking probability. This process is comparable to a chemical vapor deposition (CVD) process [19,25–28].

Process 4: If a droplet is too far from the substrate or if the droplet size is too small then it quickly forms a precipitate. Precipitate of the droplet can even form when the droplet is closer to the substrate if the substrate temperature is too high. When the precipitate is in the proximity of the hot substrate, vaporization happens. In this vapor phase a chemical reaction starts which is homogenous in nature. The reaction leads to the formation of crystallites by condensation. So, the crystallites get a form of powder precipitate and ultimately this powder without any further reaction reaches the substrate surface and sticks to it [19,24,25,27].

The condition for an ideal deposition is that the solvent gets completely removed (vaporized) because of the temperature as the droplet approaches the substrate surface (similar situation to process 3). However, the atomization of the precursor solution results in droplets of differing sizes, so all the four processes mentioned above occurs simultaneously. When the droplets are larger, they tend to carry most of the solvent salts and for these droplets the substrate temperature needs to be more optimized. For these droplets the powder formation during transportation is improbable. If the droplet size distribution is homogenous, it will be more compatible to have a deposition as in process 3. When the larger droplets will reach the substrate surface they may splash, stick, rebound or spread on the surface. Usually, dense films or rings form when the droplets spread on the surface. Rings are formed when the droplet velocity is high. Due to the thermophoretic force, the smaller droplets tend to rebound. If they are too fast in the movement, they might splash otherwise they can stick to the surface. The droplets which spread fast leads to high viscosity and dense films with the necessary heat from the substrate so that the solvent evaporates, and the salt completely decomposes. Without proper decomposition, even for viscous films cracks can happen due to stress build up [19,20,24,29]. The different types of droplet impact on heated substrates are shown in the ***Figure 2.4***.

Figure 2.4: Schematic representation of the impact of the droplets on heated surface of substrate. Designed and modified from reports of [19,20,24].

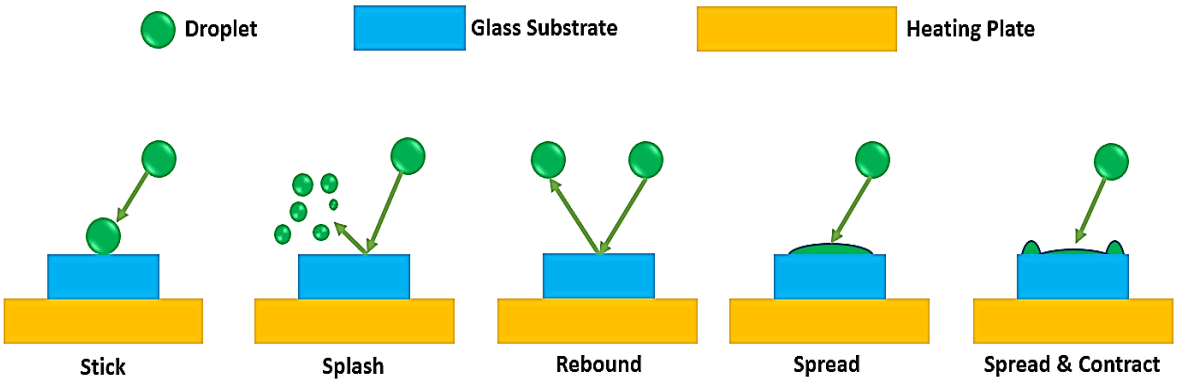

In ***Figure 2.5***, is shown the possible modifications that a droplet can experience in the ***Steps (ii)*** and ***(iii)***. The temperature axes represent the substrate temperature. The four physical forms in which the droplet possible interacts with the substrate is shown the cubic diagram of ***Figure 2.5***. The four processes explained above is according to the hypothesis proposed by Perednis *et al.* [19], Viguie *et al.* [25] with some modifications. Also, research by Rajan *et al.* [23], Cloupeau *et al.* [26], Sears *et al.* [28] and Albin *et al.* [27] have been considered while describing the four processes. The complete process of deposition can be schematically designed from the hypothesis of Viguie *et al.* [25]. The four processes have been named by them as A, B, C and D, but with our modifications we named the four processes as 1, 2, 3 and 4.

Figure 2.5: The modifications in the droplet size during the transport is shown with the increase of temperature and time. Designed and modified from the reports of [19,20,24–29].

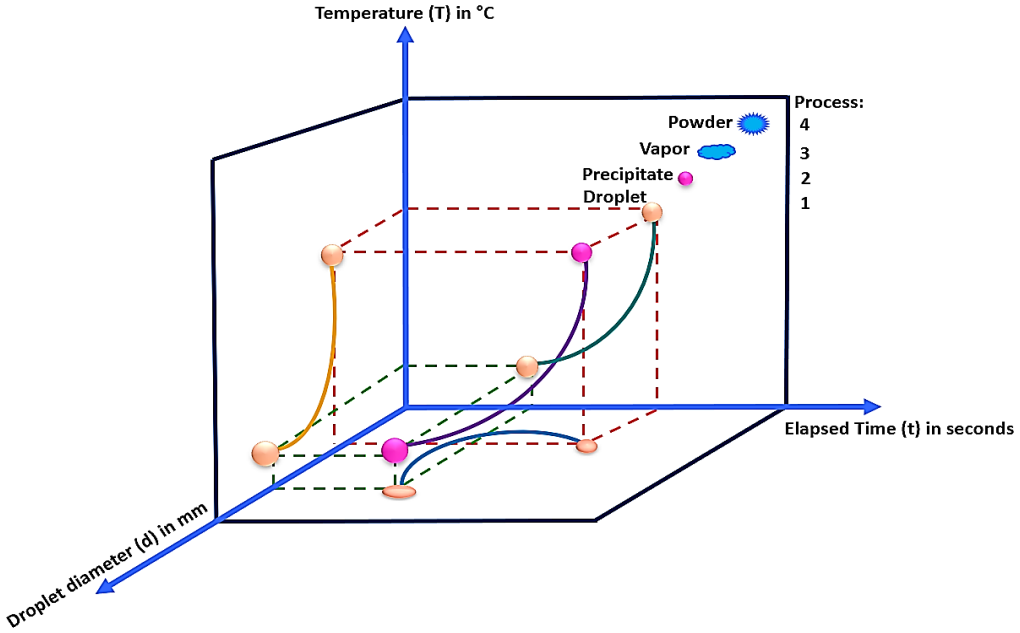

2.2 Experimental System Setup

Like typical ultrasonic spray systems, our spray pyrolysis equipment consists of the following arrangements: ultrasonic spray nozzle, precursor solution, substrate heater with a temperature controller, liquid flow meter, air pressure controller and others [29]. Parameters can be changed for each material deposition process. The flexibility to change the parameters allows to determine the required conditions to deposit a film of high quality. The set-up of the entire spray system along with the characteristics of the precursor solution will have a significant impact on the preparation of the film. For preparation of different materials, always the parameters are adapted to have a high-quality film of that material. A schematic of the spray system setup used in this thesis is shown in the ***Figure 2.6***. The gas pressure control and the liquid flow meter are not shown for simplicity. The precursor solution container and the central command computer (microcontroller system) is outside of the closable stainless-steel chamber. All other equipment is inside the chamber. The gases generated due to the pyrolysis are extracted from the chamber using a suction pump. So, all the films are prepared under controlled atmosphere.

Figure 2.6: Simplified schematic representation of the ultrasonic spray system used in this thesis.

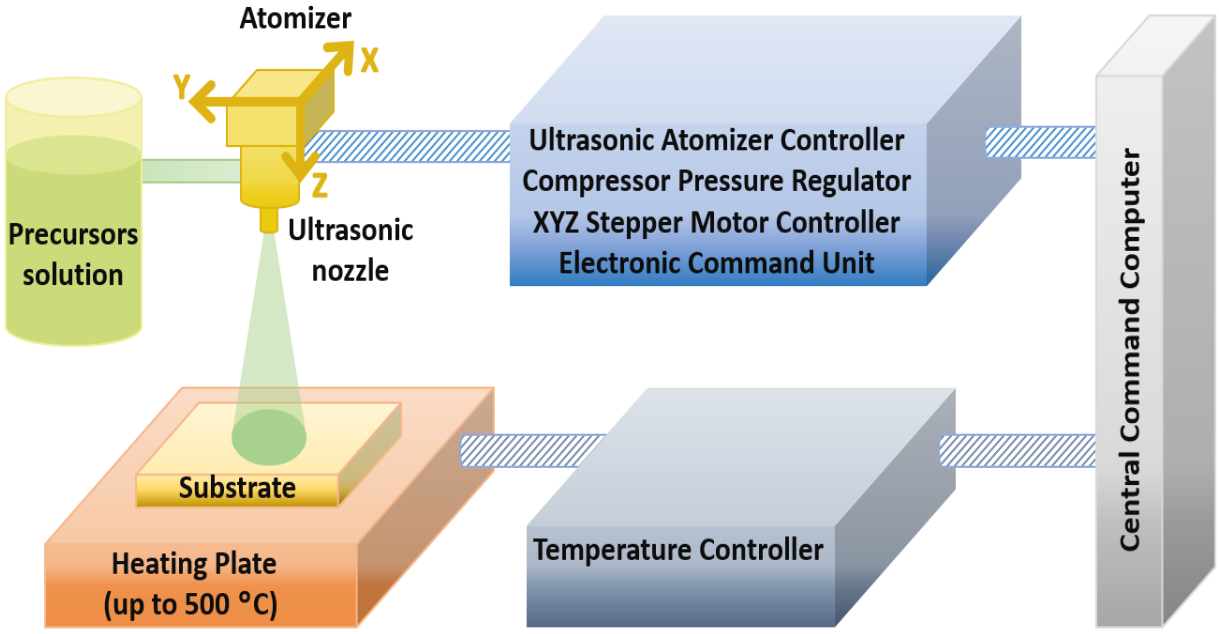

A picture of the ExactaCoat ultrasonic spray system from Sono-Tek used for preparation of all the thin films is shown in the ***Figure 2.7***.

Figure 2.7: ExactaCoat ultrasonic spray system from Sono-Tek (available at LMOPS laboratory) used in this thesis.

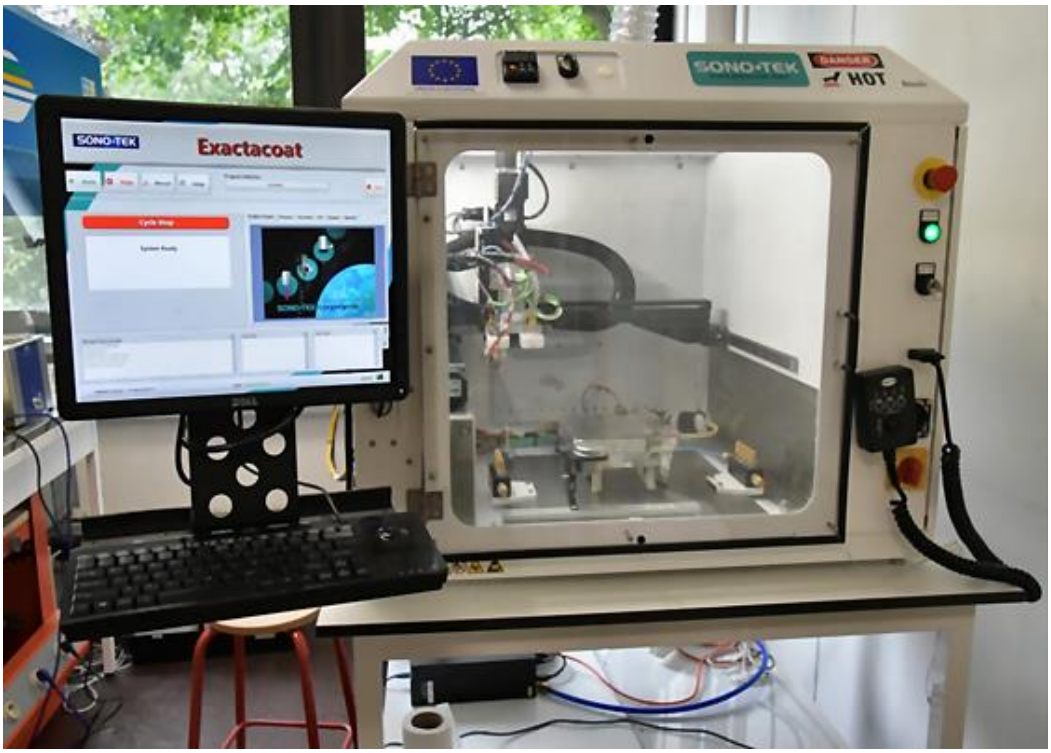

We have used ultrasonic nozzles from Sono-Tek for all our spray preparations. Under normal spray conditions these nozzle does not clog or wear out. The spray generated is soft without any overspray and thus the process and atmospheric contaminations are reduced. The body of the nozzles are fabricated from titanium because of high tensile strength, corrosion resistance and good acoustical properties. The atomizing happens in the nozzles at frequencies beyond those of human hearing, i.e., more than 20 kHz. In our work, the nozzles were operated at 120 kHz. The atomized spray droplets are produced from the breakup of the unstable capillary waves developed in the liquid (the precursor solution) introduced onto the atomizing surface of the nozzle which vibrates rapidly and constantly. The process of ultrasonic atomization is solely a surface phenomenon. The quantity of the liquid droplets produced by atomization depends exclusively on the rate at which the liquid is introduced onto the vibrating surface. The spray nozzle requires high frequency electrical energy which is provided by the Broadband Ultrasonic Controller [22,30,31]. The formation of atomized droplets in the nozzle is shown in the ***Figure 2.8***. The specific resonant frequency of each ultrasonic nozzle also determined the median droplet size. With higher frequencies the droplet sizes are smaller. As an example, the variation of median droplet sizes with ultrasonic frequencies are shown

in the ***Figure 2.9***. The liquid considered is isopropyl alcohol (IPA). It must be noted that for different liquids the droplet sizes with frequencies will be different.

Figure 2.8: Nozzle droplet formation [31].

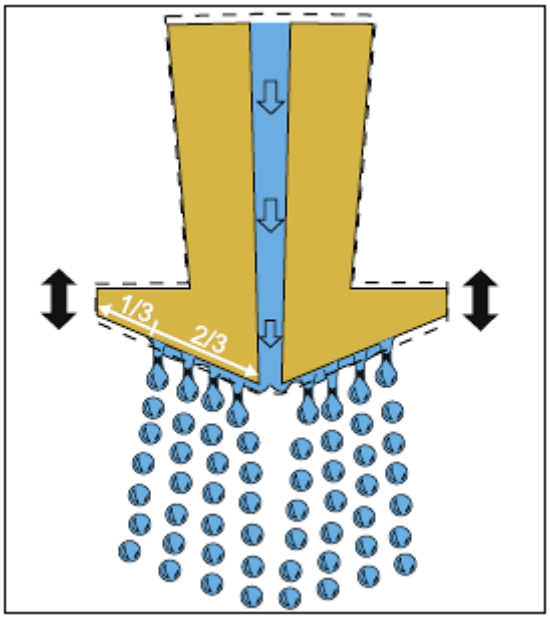

Figure 2.9: The evolution of median drop sizes with different ultrasonic frequencies for IPA [22].

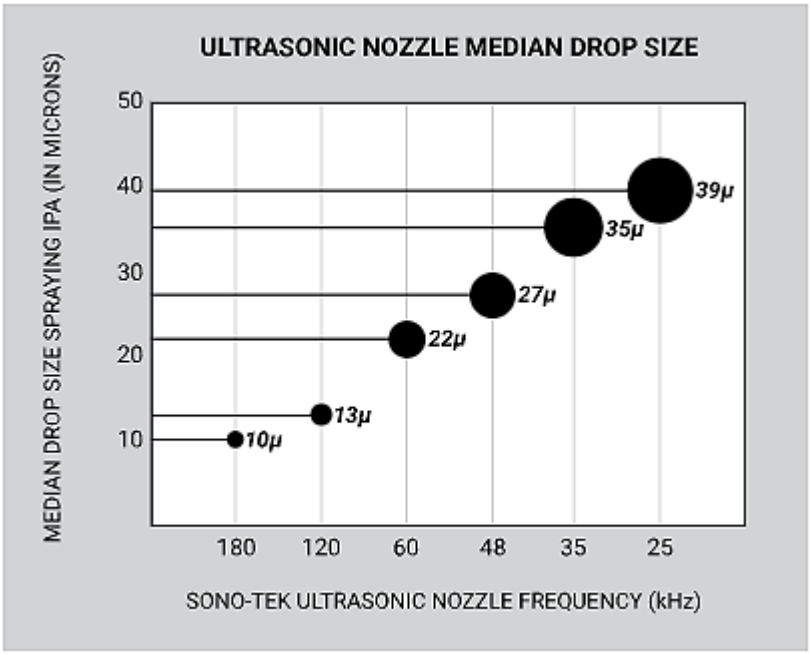

In the thesis, for the preparations of the different films we have used two different types of ultrasonic nozzles: Accumist and Impact. Both operate at 120 kHz frequency. For the Accumist nozzle, the droplets first converge at a focal point and then diverges out. This spray shape with an

adjustable focus region allows complete control on the spray width. The spray envelope is very narrow and hourglass-shaped. By adjusting the nozzle-to-substrate height, the width of the spray shape can be controlled. Typically, the width varies between 2 and 25 mm. For the Impact nozzle, the atomized spray droplets are entrained in the air stream at the nozzle's atomizing surface creates a fan-shaped spray pattern. The velocity of the air stream can be controlled to have low or high impacts of the atomized spray droplets onto the substrate. This versatile system can generate spray patterns up to 15 cm depending on the height between the nozzle and the substrate. The Impact nozzle is mostly required for wide area applications. For the air/gas inflow to the nozzle to have the desired spray shape is controlled by a pressure flow regulator. The movement of the spray nozzles according to the desired spray pattern can be controlled using specific machine-oriented programs. The spray systems employ robust ball-screw slides driven by brushless DC servo motors for this purpose. Typical structures of Accumist and Impact nozzles along with their spray patterns are shown in the ***Figure 2.10***.

Figure 2.10: Ultrasonic spray pyrolysis nozzle with its spray shape. Accumist: Left (top & bottom); Impact: Right (top & bottom) [22,32–34].

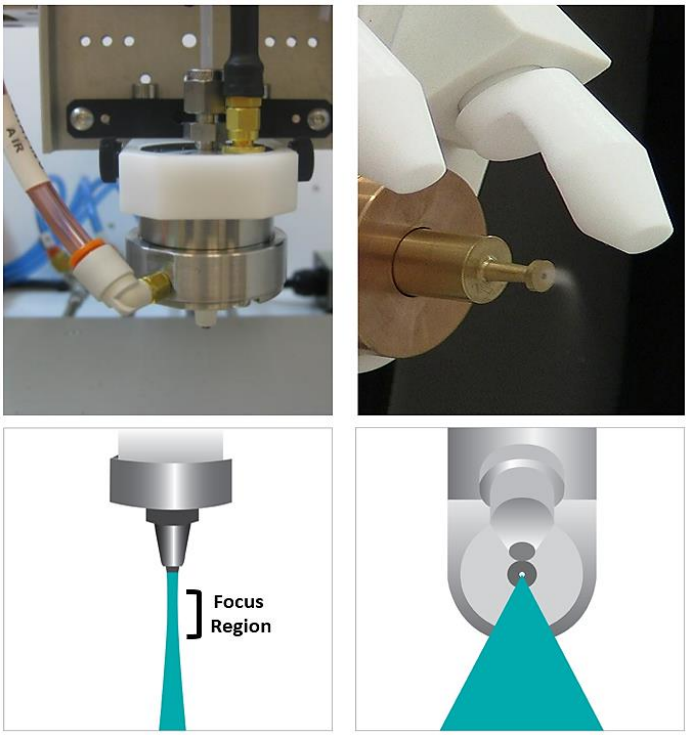

For the spray preparation, the precursor solution is loaded into a syringe. A SonicSyringe Ultrasonic Controller (operating at 120 kHz) is connected to the syringe to keep the liquid inside homogenized without formation of any agglomerates. The pump-in and pump-out of the solution are controlled

by a peristaltic syringe pump TI and the flow movement performance is controlled by a small angle stepper motor.

The temperature of the heating plate (above which the substrate holder is placed) is measured by a K-type thermocouple and monitored using a PID controller. The thermal inertia of the heater and the dynamic temperature control helps in minimum temperature decrease at the start of the spray and during the entire preparation process. The heating plate was always heated to the specific desired temperature prior to the start of the preparation. During the preparation, the temperature was measured precisely using a N-type thermocouple which was placed in contact with the glass substrate. To protect the heating plate from the chemicals, a substrate holder of 3 mm thickness was placed above covering it. Copper and ceramic substrate holders were used so that the heat distribution to the glass substrate was uniform. 1 mm thick Soda lime glass (SLG) substrates were used for all our preparations as mostly in research cases thin films solar cells are fabricated on SLG substrates. SLG substrates are cheap, hard, chemically stable, easily transmits visible light and with a very high melting point of ≈ 1000 °C.

2.3 Spray Parameters

To successfully prepare a thin film a precise control on all the spray parameters is necessary. The optimization of these parameters plays a key role in the quality of the prepared film. All these parameters work in tandem to produce a high-quality film. The parameters that we optimized for our preparations are as follows: Substrate temperature; shaping air pressure; nozzle-substrate height; solution flow rate; nozzle speed; dwell time; nozzle power; spray cycles; spray position; substrate choice; precursor solution concentration.

(i) Substrate Temperature: This parameter is important for preparation. Different substrate temperatures produce different film morphologies. Usually, when the temperature is below 200 °C, the deposited droplets are rich in solvent. A thin wet layer is thus present on top of the film during deposition. If the drying is too fast, then it adds to stresses in the film and causes cracking. At high temperatures of more than 350 °C, the droplets are devoid of the solvent and almost dry. These discrete particles are deposited on the substrate which might add to the roughness. It must be kept in mind that, for the pyrolysis reaction to be complete and to avoid formation any unnecessary byproducts certain temperature needs to be maintained throughout the preparation process. For different material preparations the temperature of the substrate needs to be adjusted.

(ii) Shaping air pressure: Adjusting the shaping air pressure is important to have a smooth thin film. The range of air pressure in the system is 0.5 to 3.5 psi (35 to 245 mbar). Using too high pressure, results in a high velocity spray that results in overspray (incomplete pyrolysis) and loss of material. The spray shapes for the two nozzle types are shown in the ***Figure 2.10***. For Accumist nozzle, the uniformly distributed droplets first merge at a focal point and then diverges uniformly. Higher shaping air pressure brings the focal point down and closer to the substrate which gives incomplete pyrolysis. The pressure needs to be such that the flow of the droplets is complete along with the reaction. For Impact nozzle, the conical spray shape and hence the spray width will be directly related to the shaping air pressure. It needs to be adjusted with respect to the nozzle-substrate height for a complete pyrolysis reaction to happen.

(iii) Nozzle-substrate height: The height between the nozzle and the substrate such that the droplets can reach the substrate surface without any over-spray. The height must be adjusted in conjunction to the shaping air pressure. The height also determines the area coated. With a high deposition rate, if the height is too small then the coated area is also small. Sufficient height must be allowed for the droplets to converge and then to diverge (for Accumist nozzle) to be deposited on the substrate with the complete pyrolysis.

(iv) Solution flow rate: The solution flow rate (in mL/min) determines the rate at which the precursor solution from the syringe is fed to the nozzle at a constant atomization rate. A high flow rate results in overspray while lower rate results in under-spray. With lower rate, the droplets even before reaching the surface get vaporized and the shaping air pressure drives out the particles before reaching the substrate. With a higher rate, higher number of droplets reaches the substrate without undergoing pyrolysis reaction resulting in over-spray and formation of agglomerates. This also gives rise to pores in the film. The flow rate is also directly linked (proportional) to the thickness of the film but with excessive rates films result to rougher morphologies with pores in the films as observed by Chen *et al*. [35]. Films with moderate flow rates gives more uniform morphology, contains less agglomerates and are also compact and dense.

(v) Nozzle speed: During the spray the nozzle speed (mm/sec) becomes an important factor. When the spray is happening, the nozzle is equipped to move along x and y axes respectively. The nozzle speed is inversely proportional to the thickness of the film. With very low nozzle speeds, the nozzle scans the substrate very slowly at the fixed flow rate, thus more material is deposited. Also, at this condition, the film experiences the substrate temperature for a longer time which builds up stresses

in the film leading to cracks. Too high nozzle speeds are not suitable for the spray system, as the system experiences a vibration due to the fast mechanical movement of the motor connected to the nozzle. This vibration leads to poor quality films and at these high speeds the films are extremely thin with high roughness. So, based on the material to be prepared and on the type of nozzle being used an intermediate speed should be maintained.

(vi) Dwell time: The dwell time is the stopping time (in seconds) between each spray cycle (spray scan). During the to-and-fro movement of the nozzle during preparation, the nozzle can be set to stop for a few seconds. This time is necessary for the droplets to crystalize towards film formation. The remaining solvent is usually vaporized in this time. But the time should not be long enough otherwise the already hot substrate will dry out the film rapidly leading to stress in the films. This duration depending on the material to be prepared should be set between 0.5 s to 1 s.

(vii) Nozzle power: For achieving best atomization, the nozzle power should be set to 1 watt above the stall point. Stall point is a critical power level below which the atomization process ceases. Below the stall point there is only cavitation where the liquid only wets out without forming atomized droplets. Setting the nozzle power 1 Watt above the stall point produces perfect atomization of the solution without any clogging or wetting. Too high power above the stall point can also cause cavitation. So, the stall point should be checked for each type of precursor solution and then the nozzle power should be set 1 watt above that value. The nozzle power is directly linked to the viscosity, concentration, and surface tension of the precursor solution.

(viii) Spray cycles: The number of spray cycles should be adjusted in conjunction with the other parameters as mentioned above. With more spray cycles we will achieve a film of higher thickness. The number of cycles should be set according to the desired thickness. However, it must be noted that too high thickness (beyond 1 μm) may lead to high stress and delamination in films. With very high thickness the heat distribution in the film microlayers is not even which probably can lead to delamination.

From the references [36,37], a relation has been deduced about the expected solid film thickness for each spray cycle. The relation is given below:

Equation (2.1):

$$t = \frac{q \cdot x_0}{w_a \cdot \mu_n}$$

Where, t is the film thickness, x_o is the mass fraction of the solute, q is the flow rate, w_a is the diameter of the spray and μ_n is the nozzle speed.

(ix) Spray position: The spray position should be adjusted according to the size of the substrate with reference to the pattern of the spray. For our experiments, a rectangular shaped glass substrate was used with a to-and-fro movement of the nozzle. So, the length of the spray cycle should cover the entire length of the substrate so that a uniform film is obtained covering the entire substrate.

(x) Precursor solution concentration: the main requirement of a precursor is to be able to form the oxide at a given substrate temperature. The main used precursors are based on acetate salts, or chlorides, or nitrates. Keeping in mind the drawbacks of chlorides and nitrates (toxicity, corrosive, impurities) only acetate-based salts are used for all our preparations. Also, most of the acetate-based salts are easily soluble in water without requiring any alcohols. Alcohols have toxic effects, evaporate quickly and are also flammable at high temperatures. So, the use of alcohols to dissolve precursor salts are avoided in our preparations. The solubility, viscosity, use of additives to reduce surface tension are important factors to consider when preparing the precursor solution. Solubility in relation to the concentration is important. It allows to control the concentration of the precursor to be used. For our preparations, de-ionized water is preferred as a solvent as it has high vapor pressure. The concentration (in mol/L) refers to the proportion of the salts dissolved in the solvent. The concentration should be carefully chosen such that it maintains the solution stability over time (does not hydrolyze, does not form segregated phases, does not conglomerate or precipitate) and at the end of the pyrolysis it produces the required stoichiometry in the prepared films. The number of spray cycles needed to reach the desired film thickness will also depend on the solution concentration.

The selection of the precursor solution and its optimization must be done before the optimization of all the other spray parameters as detailed above. To conclude about the precursor solutions, it can be rightly said that the solvent, the concentration of the precursor and the solution flux in varying degrees will have major impact on the film formation characteristics. The precursors along with their concentration finally selected to prepare the thin films are explained in the corresponding individual chapters dedicated for specific films.

2.4 Summary

In summary we can say that to obtain a film of optimal qualities many parameters have to be considered with a precise control over them. With a specific set of parameters, the films need to be prepared a few times in order not only to understand the film formation better but also to check for the reproducibility. In this thesis, the films are prepared by repeating the process a few times. To establish a co-relation between the system-related and the solution-related parameters ***Figure 2.11*** is drawn schematically. The parameters can be co-related with two main characteristics of the spray prepared high-quality films: the thickness and the composition. These parameters will have an influence on the final device characteristics. However, the final film properties will also depend on some post preparation conditions such as rapid thermal annealing which will be discussed in the experimental chapters of this thesis.

Figure 2.11: Schematic representation of the spray preparation parameters and their relationship with the composition and the thickness of the prepared films. Designed based on the reports of [19,22,24–27].

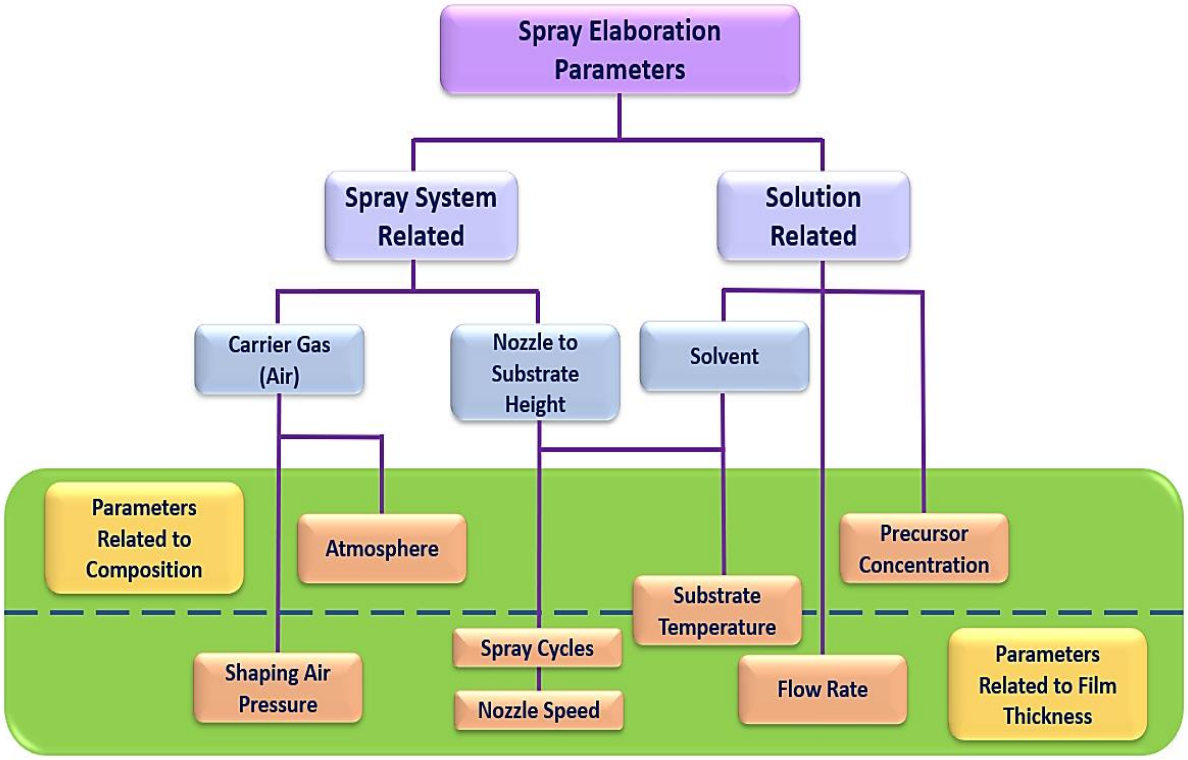

2.5 Characterization of the Spray Prepared Thin Films

All the different types of thin films prepared in this thesis work are characterized in terms of their thickness, morphology, optical, structural, and electrical properties. In the following sub-sections, all the tools used for the characterizations are discussed along with the analytical methods.

2.5.1 Thickness and Morphological Measurements

Mechanical and optical profilometers were used to measure the thickness and the roughness of the prepared thin films and their morphology was analyzed by AFM and SEM.

2.5.1.1 Mechanical and Optical Profilometers

A mechanical profilometer is an equipment that uses as a diamond tip to scan through the surface of a sample by taking each position its vertical coordinate. The profilometer can be used to measure step height and the roughness of the surface profiles. It can also be used to measure stress of thin films deposited on a wafer. The profile which is obtained is a convolution between the real profile and the stylus shape. The minimum width of a laterally measured point is the maximum hole depth that can be measured. Therefore, it is very difficult and often inaccurate to measure hole depths if the lateral dimensions are too short [38]. With the help of digital acquisition, the trace of the surface profile is obtained. Even for thin films this method can be applied to precisely measure thickness down to few nanometres. The roughness of the surface profiles gives additional information about the topography the films.

The system possesses some inherent advantages such as, it is independent of the optical or electrical properties of the material of the film. It can ignore the effects of the pollution as it does not require a vacuum environment or vacuum chamber for its operation. However, we must pay attention to some of its disadvantages. The pressure exerted by the stylus on the sample surface can easily scratch the sample. The force which the stylus exerts on the sample must be calibrated according to nature of the specific sample to avoid any damage to the stylus tip and as well the sample surface. On the contrary, the sample surface also must be solid enough for the tip so that it can measure the profile without sinking too much into the sample.

In our study, we have used a Dektak XT profilometer from Bruker [39] with a 2 μm tip (picture in ***Figure 2.12***). The analysis of the profiles was done using the Vision64 software which is equipped with a camera along with a pointer for scaling, plotting and analysis tools and therefore allows a quick measurement and an easy qualitative analysis.

Figure 2.12: Dektak XT mechanical profilometer from Bruker available at LMOPS laboratory.

Optical profilometry measurements are done using Filmetrics Profilm3D optical profilometer [40] based on the principle of vertical scanning interferometry (VSI). Surface topographies can be quantified with a vertical resolution of ≈0.1 nm and a lateral resolution of around 500 nm. The topography of the sample surface including step heights from the interference signal was analyzed by Profilm software. Even the roughness parameters such as arithmetic roughness, total roughness, and the root mean square (RMS) roughness can be (roughly) estimated.

2.5.1.2 Atomic Force Microscope (AFM)

AFM is used to analyzed the surface morphology of almost any material [43,44,45]. A tip with a nanometric radius of curvature scans the sample surface and the analysis of the deflection of a laser beam on the tip cantilever makes it possible to reproduce the surface topography. The tip can be in contact with the surface (contact mode) or near the surface (non-contact and tapping mode), depending on the material.

In this thesis, Nano-Observer atomic force microscope developed by CSInstruments [46] and

available at Institute Jean Lamour Campus Artem was used in tapping mode with an oscillation frequency of 323 kHz with a scan rate of 0.75 Hz. Also, Park NX10 atomic force microscope [47] developed by Park Systems and available at LCP-A2MC Laboratory was used in non-contact mode with an oscillation frequency of 336 kHz with a scan rate of 0.74 Hz.

2.5.1.3 Scanning Electron Microscopy (SEM)

SEM can be a complementary technique to AFM. With this technique, we can obtain high resolution surface images and their analysis can make it possible to study the phases (and possibly the chemical composition) and the surface morphology. In addition, we can measure the film thickness and analyze the growth of the thin film with a cross-sectional study [48, 49].

In this work, to understand the morphology and the growth of thin films, top-view and cross-section scanning electron micrographs were acquired. A FIB-SEM system of the Auriga series from Zeiss [50] with an In-lens detector available at LEM3 Laboratory has been used to acquire the micrographs at an acceleration voltage of 20 kV. The In-lens has been used as it has a very resolution for surface imaging in SE imaging. It is located just above the objective lens and can directly detect the low energy secondary electrons in the beam path [51,52].

2.5.2 Optical Measurements

A UV-VIS-NIR spectrophotometer has been used to measure the transmittance of the prepared thin films. The optical bandgap energy of the thin films was calculated using the Tauc model. Urbach energies of the thin films were also studied to estimate the crystalline lattice disorders.

UV-VIS-NIR spectroscopy is mainly used to characterize the optical transmission of a thin film to determine the optical bandgap, the refractive index, the absorption coefficient and to investigate the sub-bandgap defects. The film is shined with a monochromatic light and the intensity of the transmitted light is measured. The transmittance of the film is defined as the ratio of the transmitted to the incident light intensities. In our work, we have used the glass substrate as a reference and therefore the measured transmittance directly gives the transmittance of the film deposited on the glass. In our setup, the effects of the film-substrate interface (including reflection) are neglected. In this way we found that the film transmittance measurements are very accurate. The principle of UV-VIS-NIR spectroscopy is shown schematically in the ***Figure 2.13***. UV-VIS-NIR Perkin-Elmer Lambda 900 spectrophotometer used for our measurements is shown in the ***Figure 2.14*** along with the inset showing the placement positions of the glass reference and the actual sample.

Figure 2.13: Principle of UV-VIS-NIR spectroscopy is shown schematically.

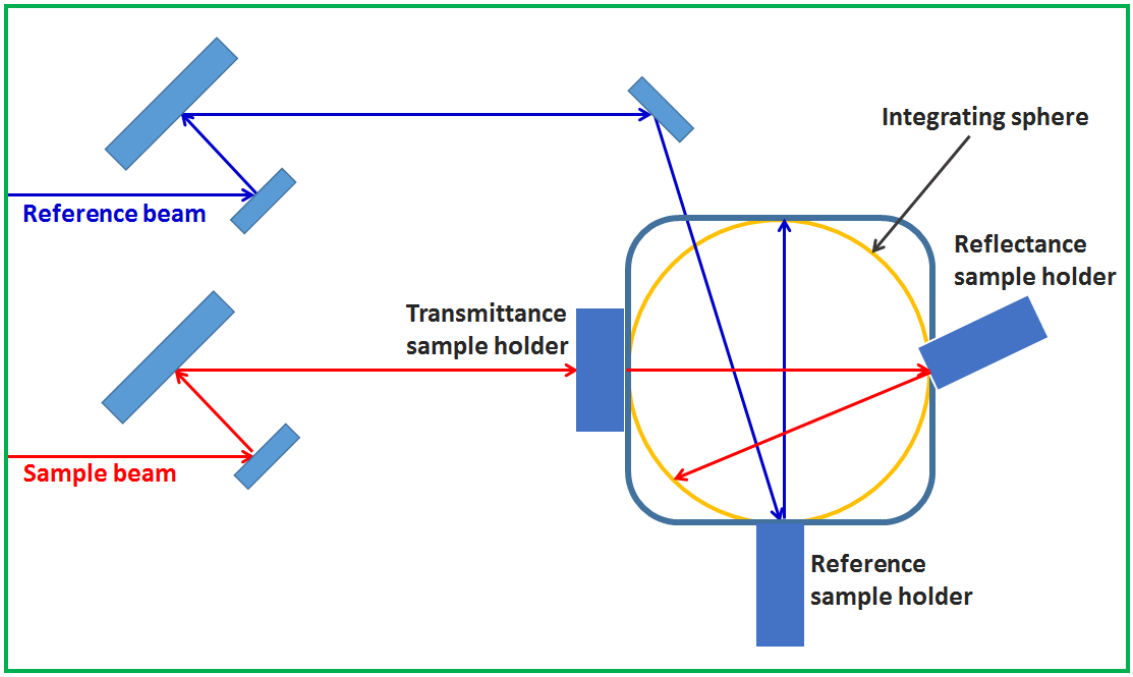

Figure 2.14: UV-VIS-NIR Perkin-Elmer Lambda 900 spectrophotometer available at LMOPS laboratory.

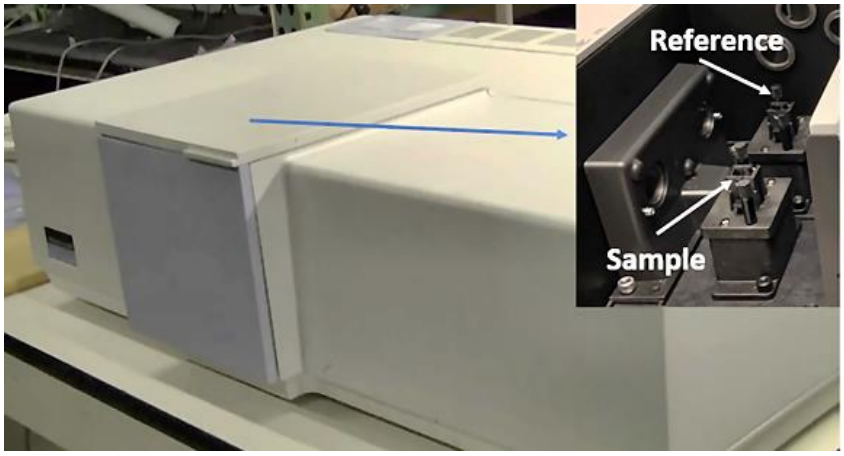

As an example, transmittance spectra of a Zinc Oxide (ZnO) thin film of thickness approx. 200 nm along with a glass reference spectrum are shown in the ***Figure 2.15***.

In the transmittance spectra is often seen the appearance of a modulation of intensity. This is seen in the form of maxima and minima appearing in the spectra. The analysis of these spectra makes it possible to determine the bandgap and the modulation can give an estimation of the thickness of the thin film [53,54].

Figure 2.15: Transmittance spectra of a ZnO thin film with glass substrate as reference.

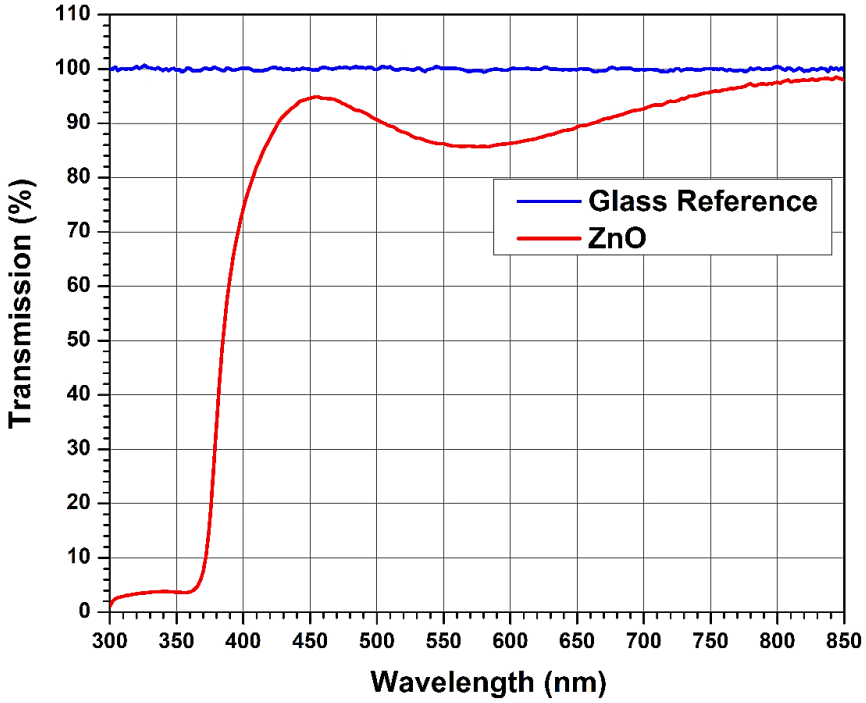

To determine the absorption coefficient (α) the standard Lambert-Beer's law [55] is used:

Equation (2.2):

$$\alpha = \frac{1}{t} \times \ln\left(\frac{1-R}{T}\right)$$

Where, T is the transmittance, R the reflectance, and t is the thickness of the film.

For semiconductor materials having a direct bandgap, the optical bandgap (E_g) can be determined from the Tauc plot [56]. In the Tauc method, the relation between the absorption coefficient and the direct bandgap E_g can be written as:

Equation (2.3):

$$(\alpha\, h\nu)^{1/n} = B \times (h\nu - E_g)$$

Where B is a constant and $h\nu$ the photon energy. n = 2 for an indirect bandgap such as CuO. For Cu_2O, the direct forbidden process is considered to affect the absorption and n is taken to be equal to 3/2 [57]. For ZnO and related alloys n = 1/2 as usually done for direct bandgap materials.

The absorption coefficient from the ***Equation (2.2)*** is also used to estimate the Urbach energy of thin films. Urbach energy is related to the crystalline lattice disorder in the thin films and the values of the Urbach energy of the thin films was obtained from the inverse of the slope of $ln(\alpha)$ versus photon energy ($h\nu$) [58]. It is expressed as:

Equation (2.4):

$$\alpha = \alpha_0 \, exp\left(\frac{h\nu}{E_u}\right)$$

Where E_u is the Urbach energy and α_o is a constant.

The determination of the optical bandgap energy and the Urbach energy is shown in the ***Figures 2.16 (a & b)*** respectively.

It should be noted that the Urbach energy is a qualitative indicator and does not allow to quantify the disorder in the material, and, moreover, it is not sensitive to any type of disorder. It should therefore be used as one indicator among others.

Figure 2.16: **(a)** Bandgap calculation of a ZnO thin film using Tauc plot method; **(b)** Urbach energy calculation of a ZnO thin film.

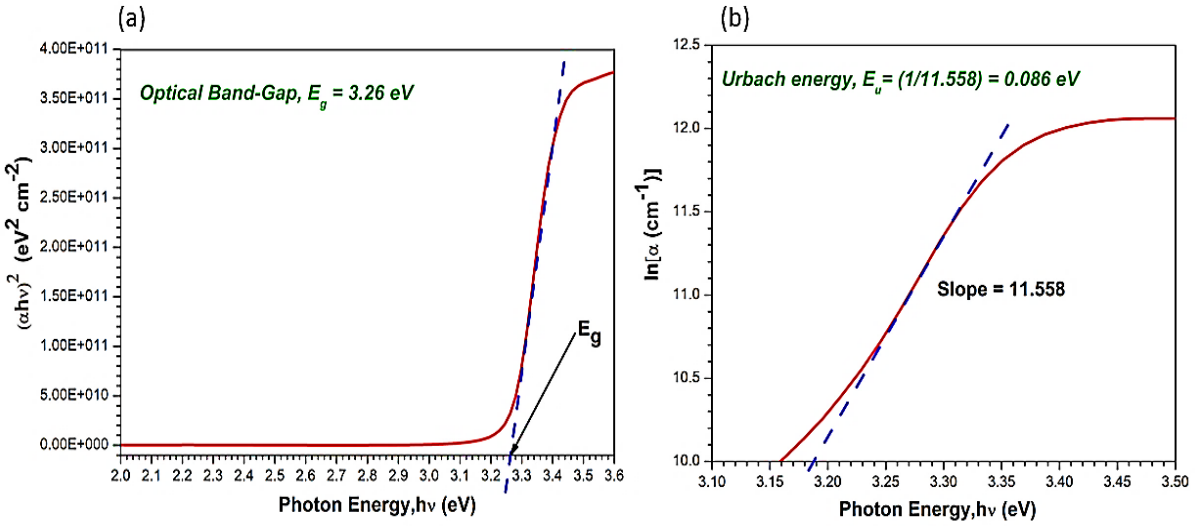

2.5.3 Structural and Chemical Analysis

The crystalline structure of the prepared thin films is studied by X-ray diffraction (XRD) and by Raman spectroscopy. The chemical analysis of the films has been done by using X-ray fluorescence (XRF) and Fourier Transform Infrared Spectroscopy (FTIR).

2.5.3.1 X-Ray Diffraction (XRD)

X-ray diffraction is the standard characterization technique used to investigate the structural properties of thin film materials and to determine the crystal type, the lattice parameters, the preferred orientation, the composition, the crystallites size, the defects properties, etc. Generally, XRD setups use wavelengths between of 0.1 and 0.2 nm. The most used wavelength in our topic is 0.15406 nm (CuKα). The basic principle is to measure the diffraction pattern of the thin film and to

analyze it, using simulations and crystallographic databases, to identify and study the crystalline phases [59]. Using the classical Bragg's law [60], one can extract the interatomic distance of a particular plane d_{hkl} as a function of the wavelength of the incident radiation (λ) and the position of the diffraction peaks (θ) [59,60]:

Equation (2.5):

$$2\, d_{hkl}\, sin(\theta_{hkl}) = m\, \lambda$$

Where m is the order of diffraction.

All the measurements done in this work used the Bragg Brentano θ-2θ configuration, as shown in the ***Figure 2.17***. in which the sample is rotated by an angle of θ and the detector is rotated by an angle of 2θ in order to detect only the crystallographic planes that are parallel to the sample surface. In our polycrystalline samples, peaks corresponding to different the crystallographic planes are detected.

Figure 2.17: Schematic of the Bragg-Brentano configuration used in XRD. Modified from [61].

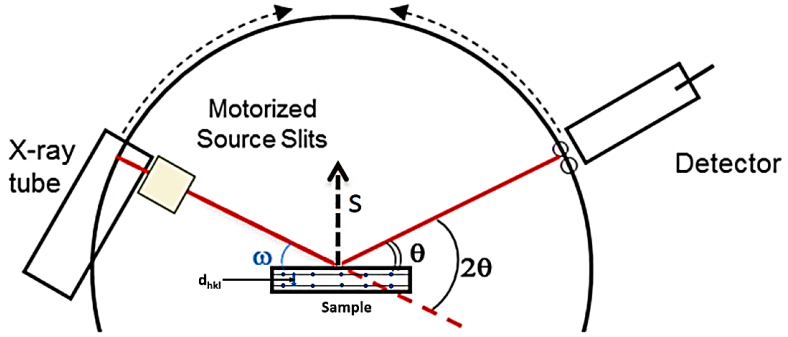

In our polycrystalline films, the size of the crystallites can be estimated by using the Scherrer's equation [62]:

Equation (2.6):

$$D_{hkl} = \frac{K\,\lambda}{\beta\,\cos(\theta)}$$

Where, D_{hkl} is the average size (in nm) of crystallite in a direction of plane (hkl), λ is the X-ray wavelength (in nm), K is a dimensionless shape factor with value of 0.94, β is the full width at half maximum (FWHM) of the diffraction peak (radian), after correction for instrumental broadening, and θ is the Bragg diffraction angle. It should be noted that K can have different values depending on the particle geometry. The Scherrer's equation is limited by the fact it supposes the crystallites to have spherical shape with diameters relatively small, usually less than 100 nm. The average diameter is usually determined by measuring the width of the diffraction peak with the highest intensity in the diffractogram.

In our work, we have used a modified Scherrer method developed by Monshi *et al.* [63]. In the modified method all the identified crystallite peaks are used to estimate the crystallite size by linearly fitting *ln(β)* against *ln(1/cos(θ))* and taking the value of *D* from its intercept (shown in the ***Figure 2.12***).

Figure 2.18: Modified Scherrer equation plot by Monshi *et al.* [63].

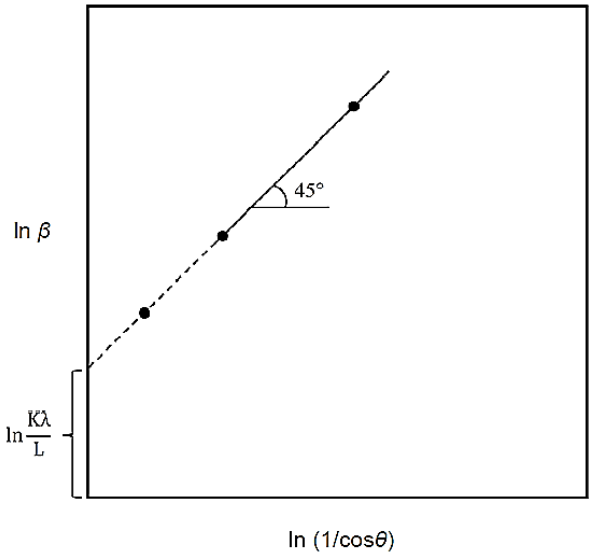

In addition, we have also estimated the texture factor for our thin films. The texture factor is important for polycrystalline films to determine the preferred orientation in the film [64,65]. The texture factor is given by [66]:

Equation (2.7):

$$F_{(xyz)} = \frac{I^{exp}_{(xyz)}/I^{ref}_{(xyz)}}{\frac{1}{N}\sum I^{exp}_{(hkl)}/I^{ref}_{(hkl)}}$$

Where, $I^{exp}_{(xyz)}/I^{ref}_{(xyz)}$ is the peak integrated peak intensity relatively to the reference one and N is the total number of peaks.

In this thesis, Bragg-Brentano configuration was used for collecting the X-rays diffractograms. Two Bruker D8 Advanced diffractometers with CuKα1 radiation (λ = 0.15406 nm) available at IJL laboratory and LEM3 laboratory respectively were used. The XRD reference for determining the crystalline structure of the prepared thin films was determined using the JCPDS data provided by Bruker and the RRUFF project database [67].

2.5.3.2 Raman Spectroscopy

Raman spectroscopy is another technique used for the determination of the crystal structure of materials. The Raman spectra are different for each material as the spectra mainly depend upon the atomic bonds in the material and the mass of the neighbouring atoms. So, it can be said that for known materials the Raman spectra are unique fingerprints towards material characteristics but for unknown complex materials suitable references should be required [68–72].

Raman spectrometry was performed at 100x confocal magnification using a green laser with an excitation wavelength of 532 nm under $z(y\text{-})\bar{z}$ configuration to focus the laser light onto the thin film. LabRAM Aramis system from Horiba Jobin-Yvon (Spectroscopies platform of LMOPS laboratory) was used for all the Raman measurements (***Figure 2.19***).

Figure 2.19: LabRAM Aramis system from Horiba Jobin-Yvon available at LMOPS laboratory, Spectroscopies platform.

2.5.3.3 X-Ray Fluorescence (XRF)

When a material is bombarded with high-energy X-rays or gamma rays then there is an emission of characteristic “secondary” (fluorescent) X-rays from the material. This emission can be defined as the X-ray fluorescence (XRF) and this phenomenon can be used widely for the elemental analysis. When the electrons in the material make transitions between the atomic energy levels then only the characteristic X-rays of the element are emitted. If an electron makes a transition from a level with energy E_1 to another level with energy E_2, then the emitted X-ray has an energy $E = E_1 - E_2$. Each element possesses a unique set of atomic energy levels, so based on the element’s characteristic it emits a unique set of X-rays [73–75]. X-ray fluorescence system from Horiba Jobin-Yvon (model

XGT 7000) [76] available at LMOPS laboratory, Spectroscopies platform, with a controlled X-ray beam diameter ranging from 10 μm to 100 μm was used for the elemental analysis of our prepared thin films on glass substrates.

The XRF technique has some advantages such as: with calibrations the analysis is accurate, it is a fast process with each measurement taking about 10 minutes, non-expensive process and the process is non-destructive but with a limit of acceptable detection range.

2.5.3.4 Fourier Transform Infrared Spectroscopy (FTIR)

Infrared (IR) spectroscopy is method by which the structure of molecules can be determined using infrared light. The principle of this technique is that it records the changes in the vibrational energy of the molecule. At first, the sample (thin film in our case), absorbs the IR radiation. On absorption, an alteration of the dipole moment of the molecular bond happens and so the vibrational energy level changes from ground state to excited state and this change (gap) in turn determines the absorption frequency. For each molecule type the IR spectrum in unique as each molecule has unique atomic bonds. This property of the molecules makes the qualitative and quantitative analysis of various types of samples possible. In the IR spectra, the unique peak frequency determines the presence of the different functional groups and the quantity of the presence of the groups is determined from the intensity of the peaks. A major advantage of IR spectroscopy is that it can analyze solid, liquid and even gas samples [77–79].

The Fourier Transform Infrared (FTIR) spectrometers belongs to the third generation of IR spectrometers. In the FTIR systems instead of a monochromator, a Michelson interferometer is used. In the spectrum, energy of all the wavelengths versus time are represented. The Fourier transform algorithm is used to interpret the data by translating the spectrum in a way that correlates the signal intensities to the wavelengths [77–79].

In our measurements on thin films attenuated total reflection (ATR) mode [80] was used. All the measurements were done using a commercial Agilent FTIR 680 spectrometer available at LMOPS laboratory, Spectroscopies platform. A reference spectrum before each acquisition was acquired to determine the absorption spectra in ambient conditions. To improve the signal-to-noise ratio, each measurement in continuous mode was averaged over 200 scans. With a spectral resolution of 4 cm^{-1}, all the spectra were acquired in the range of 4000-600 cm^{-1}.

2.5.4 Electrical Measurements

The resistivity of the prepared thin films is measured using four-point probe method using a manual probe station. The van der Pauw technique is used to measure the resistivity and a Hall Effect setup is used to measure the carrier concentration. Equipment available at LMOPS laboratory, Carel platform, were used, including Keithley source and measure units (SMU) models 2602, 2636B and 236 and a home-made Hall setup with a permanent magnet at 0.55 T.

Prior to the electrical measurements, some of the films were annealed using a rapid thermal annealing AS-Micro system from Annealsys (picture in ***Figure 2.20***). For some films, using a specific mask, metal contacts were deposited by thermal vacuum evaporation technique prior to the measurements. An example of the used shadow mask and the contact evaporation setup are shown in ***Figure 2.21***.

Figure 2.20: Rapid thermal annealing (RTA) system available at LMOPS laboratory.

Figure 2.21: **(a)** Example of an aluminum mask used for contact deposition; **(b)** Thermal vacuum evaporation system available at LMOPS Laboratory.

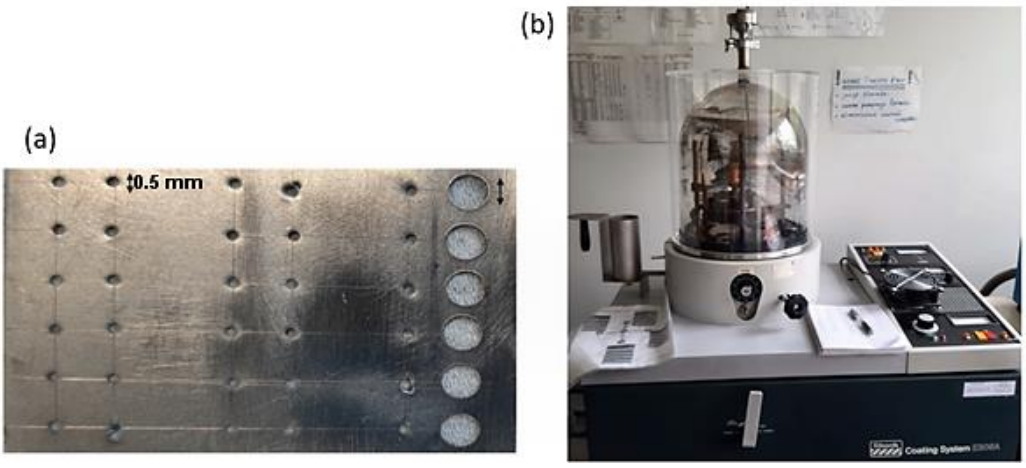

2.5.4.1 Four-Point Probe (4PP) Method

To measure the thin film resistivity, the standard four-point probe (4PP) method was used. Four contacts A, B, C and D are uniformly aligned in the middle of the sample. The current is injected between the external contacts A and D, and the voltage is measured between internal contacts B and C. The semiconductor thin film resistivity ρ is determined as follows:

Equation (2.8):

$$\rho = R_S \, t = \left(\frac{\pi}{\ln(2)}\right)\left(\frac{V_{BC}}{I_{AD}}\right) t \approx 4.53 \left(\frac{V_{BC}}{I_{AD}}\right) t$$

Where, R_S is the semiconductor resistance and t the film thickness.

The actual probe station used for the measurements in shown in the ***Figure 2.22***.

Figure 2.22: Probe station used for 4PP measurements available at LMOPS Laboratory, Carel platform.

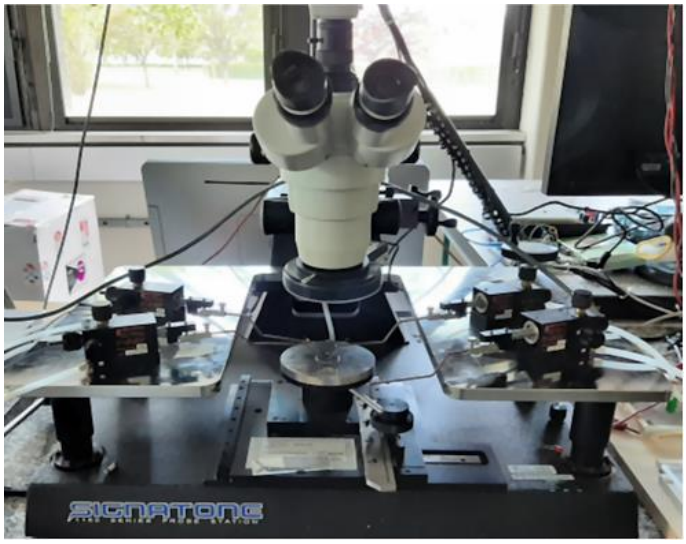

2.5.4.2 Van der Pauw Method

In this method, as with the four-point method, the resistivity of the sample is analyzed by applying a current to the layer and measuring the voltage. However, this technique allows a more accurate determination of the resistivity of the material. The van der Pauw configuration shown in the ***Figure 2.23*** requires four small ohmic contacts placed at the corners of a square on the top of the sample. The extraction of the sheet resistance R_S is based on the measurement of two different characteristic resistances: R_1 measured by applying the current between two contacts (C and D) and measuring the resulting voltage between the other two contacts (A and B); and R_2 measured by applying the current between D and A and measuring the voltage between B and C.

Figure 2.23: Representation of the van der Pauw measurements.

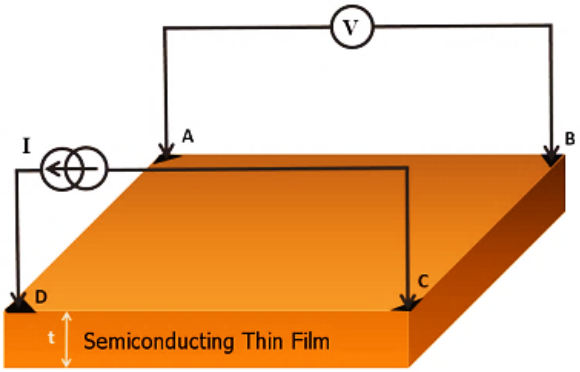

The two measured resistances are related to R_S by the following relation (van der Pauw theorem):

Equation (2.9):

$$\exp\left(-\pi\frac{R_1}{R_S}\right) + \exp\left(-\pi\frac{R_2}{R_S}\right) = 1$$

The numerical solution of this equation provides the resistance R_S and therefore the resistivity:

$$\rho = R_S\, t$$

2.5.4.3 Hall Effect Method

In addition to the van der Pauw (vdP) measurements, Hall Effect measurements were conducted to determine the charge carrier concentration and combined with vdP, the mobility in the sample in the configuration shown in ***Figure 2.24***. The Hall Effect is based on the accumulation of charges in a medium under the effect of the magnetic Lorentz force F_L. This force can be expressed as follows:

Equation (2.10):

$$F_L = q\, v\, B$$

Where q is the elementary charge (1.602×10^{-19} C), v is the charge velocity and B is the magnetic field.

The Lorentz force driver movement of the charges creates an electric field and therefore a voltage V_H in transverse direction to the carrier's flow. This voltage which can be represented as follows:

Equation (2.11):

$$V_H = \frac{I\,B}{n\,q\,t}$$

Where, V_H is the Hall voltage, I is the current in the longitudinal direction, t is the film thickness, n the charge carrier concentration and q is the electron charge. For different types of charge carriers V_H has different polarity. So, this technique is useful for the determination of the type of conductivity (p or n) for a semiconductor as given by:

Equation (2.12): The material is of n-type if (in the used convention):

$$V_H = -\frac{I\,B}{n\,q\,t} < 0$$

Equation (2.13): The material is of p-type if (in the used convention):

$$V_H = \frac{I\,B}{p\,q\,t} > 0$$

The mobility is given by the following relationship:

Equation (2.14):

$$\mu = \frac{t}{n\,q\,\rho}$$

Figure 2.24: Schematic of Hall-effect measurements.

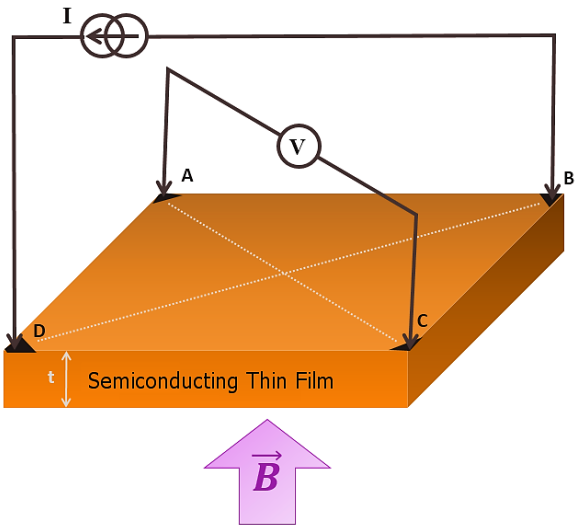

A detailed description of the van der Pauw / Hall Effect technique can be found in [81].

2.6 References

[1] F.C. Krebs, Fabrication and processing of polymer solar cells: A review of printing and coating techniques, Sol. Energy Mater. Sol. Cells. 93 (2009) 394–412. https://doi.org/10.1016/j.solmat.2008.10.004.

[2] P.S. Patil, Versatility of chemical spray pyrolysis technique, Mater. Chem. Phys. 59 (1999) 185–198. https://doi.org/10.1016/S0254-0584(99)00049-8.

[3] R.R. Chamberlin, J.S. Skarman, Chemically sprayed thin film photovoltaic converters, Solid. State. Electron. 9 (1966) 819–823. https://doi.org/10.1016/0038-1101(66)90121-3.

[4] W. Daranfed, M.S. Aida, N. Attaf, J. Bougdira, H. Rinnert, Cu2ZnSnS4 thin films deposition by ultrasonic spray pyrolysis, J. Alloys Compd. 542 (2012) 22–27. https://doi.org/10.1016/j.jallcom.2012.07.063.

[5] T. V. Gavrilović, D.J. Jovanović, M.D. Dramićanin, Synthesis of Multifunctional Inorganic Materials, in: Nanomater. Green Energy, Elsevier, 2018: pp. 55–81. https://doi.org/10.1016/B978-0-12-813731-4.00002-3.

[6] O. Vigil-Galán, M. Espíndola-Rodríguez, M. Courel, X. Fontané, D. Sylla, V. Izquierdo-Roca, A. Fairbrother, E. Saucedo, A. Pérez-Rodríguez, Secondary phases dependence on composition ratio in sprayed Cu_2ZnSnS_4 thin films and its impact on the high power conversion efficiency, Sol. Energy Mater. Sol. Cells. 117 (2013) 246–250. https://doi.org/10.1016/j.solmat.2013.06.008.

[7] M.E. Rodriguez, D. Sylla, Y. Sanchez, S. López-Marino, X. Fontané, J. López-García, M. Placidi, A. Pérez-Rodríguez, O. Vigil-Galán, E. Saucedo, Pneumatically sprayed Cu_2ZnSnS_4 films under Ar and Ar–H_2 atmosphere, J. Phys. D. Appl. Phys. 47 (2014) 245101. https://doi.org/10.1088/0022-3727/47/24/245101.

[8] M. Espindola-Rodriguez, M. Placidi, O. Vigil-Galán, V. Izquierdo-Roca, X. Fontané, A. Fairbrother, D. Sylla, E. Saucedo, A. Pérez-Rodríguez, Compositional optimization of photovoltaic grade Cu_2ZnSnS_4 films grown by pneumatic spray pyrolysis, Thin Solid Films. 535 (2013) 67–72. https://doi.org/10.1016/j.tsf.2012.12.082.

[9] S. Abermann, Non-vacuum processed next generation thin film photovoltaics: Towards marketable efficiency and production of CZTS based solar cells, Sol. Energy. 94 (2013) 37–70. https://doi.org/10.1016/j.solener.2013.04.017.

[10] A. Rothwarf, K.W. Böer, Direct conversion of solar energy through photovoltaic cells, Prog. Solid State Chem. 10 (1975) 71–102. https://doi.org/10.1016/0079-6786(75)90007-2.

[11] M.S. Tomar, F.J. Garcia, Spray pyrolysis in solar cells and gas sensors, Prog. Cryst. Growth Charact. 4 (1981) 221–248. https://doi.org/10.1016/0146-3535(81)90004-6.

[12] W. Siefert, Corona spray pyrolysis: A new coating technique with an extremely enhanced deposition efficiency, Thin Solid Films. 120 (1984) 267–274. https://doi.org/10.1016/0040-6090(84)90241-4.

[13] B.N. Joshi, H. Yoon, S.-H. Na, J.-Y. Choi, S.S. Yoon, Enhanced photocatalytic performance of graphene–ZnO nanoplatelet composite thin films prepared by electrostatic spray deposition, Ceram. Int. 40 (2014) 3647–3654. https://doi.org/10.1016/j.ceramint.2013.09.060.

[14] J.P. Liu, K.L. Choy, M. Placidi, J. López-García, E. Saucedo, D. Colombara, E. Robert, Fabrication and characterization of kesterite Cu_2ZnSnS_4 thin films deposited by electrostatic spray assisted vapour deposition method, Phys. Status Solidi. 212 (2015) 135–139. https://doi.org/10.1002/pssa.201431374.

[15] P. Usha Rajalakshmi, R. Oommen, C. Sanjeeviraja, V. Ganesan, Effect of composition on structural and optical characteristics of nebulised spray pyrolysed $(Bi_{1-x}Sb_x)_2S_3$ thin films, Superlattices Microstruct. 57 (2013) 158–165. https://doi.org/10.1016/j.spmi.2013.01.003.

[16] J. Denayer, P. Aubry, G. Bister, G. Spronck, P. Colson, B. Vertruyen, V. Lardot, F. Cambier, C. Henrist, R. Cloots, Improved coloration contrast and electrochromic efficiency of tungsten oxide films thanks to a surfactant-assisted ultrasonic spray pyrolysis process, Sol. Energy Mater. Sol. Cells. 130 (2014) 623–628. https://doi.org/10.1016/j.solmat.2014.07.038.

[17] M. García-Hipólito, R. Martínez, O. Alvarez-Fregoso, E. Martínez, C. Falcony, Cathodoluminescent and photoluminescent properties of terbium doped ZrO_2 films prepared by pneumatic spray pyrolysis technique, J. Lumin. 93 (2001) 9–15. https://doi.org/10.1016/S0022-2313(01)00168-5.

[18] D.S. Jung, S. Bin Park, Y.C. Kang, Design of particles by spray pyrolysis and recent progress in its application, Korean J. Chem. Eng. 27 (2010) 1621–1645. https://doi.org/10.1007/s11814-010-0402-5.

[19] D. Perednis, L.J. Gauckler, Thin Film Deposition Using Spray Pyrolysis, J. Electroceramics. 14 (2005) 103–111. https://doi.org/10.1007/s10832-005-0870-x.

[20] L. Filipovic, S. Selberherr, G.C. Mutinati, E. Brunet, S. Steinhauer, A. Köck, J. Teva, J. Kraft, J. Siegert, F. Schrank, Methods of simulating thin film deposition using spray pyrolysis techniques, Microelectron. Eng. 117 (2014) 57–66. https://doi.org/10.1016/j.mee.2013.12.025.

[21] WordReference. in: Random House Learner's Dictionary of American English, (2022). https://www.wordreference.com/definition/spray (accessed April 20, 2022).

[22] Sono-Tek Corporation, Ultrasonic Atomization, (2018). https://www.sono-tek.com/ultrasonic-coating/how-ultrasonic-nozzles-work/ (accessed April 22, 2022).

[23] R. Rajan, A.B. Pandit, Correlations to predict droplet size in ultrasonic atomisation, Ultrasonics. 39 (2001) 235–255. https://doi.org/10.1016/S0041-624X(01)00054-3.

[24] L. Filipovic, Dissertation: Topography Simulation of Novel Processing Techniques, Technischen Universität Wien, 2012. https://www.iue.tuwien.ac.at/phd/filipovic/.

[25] J.C. Viguié, J. Spitz, Chemical Vapor Deposition at Low Temperatures, J. Electrochem. Soc. 122 (1975) 585–588. https://doi.org/10.1149/1.2134266.

[26] M. Cloupeau, B. Prunet-Foch, Electrostatic spraying of liquids: Main functioning modes, J. Electrostat. 25 (1990) 165–184. https://doi.org/10.1016/0304-3886(90)90025-Q.

[27] D.S. ALBIN, S.H. RISBUD, Spray Pyrolysis Processing of Optoelectronic Materials, Adv. Ceram. Mater. 2 (1987) 243–252. https://doi.org/10.1111/j.1551-2916.1987.tb00089.x.

[28] W.M. Sears, M.A. Gee, Mechanics of film formation during the spray pyrolysis of tin oxide, Thin Solid Films. 165 (1988) 265–277. https://doi.org/10.1016/0040-6090(88)90698-0.

[29] R.R. Chamberlin, J.S. Skarman, Chemical Spray Deposition Process for Inorganic Films, J. Electrochem. Soc. 113 (1966) 86. https://doi.org/10.1149/1.2423871.

[30] Sono-Tek Corporation;, LICO Electronics GmbH, Ultrasonic Spray Nozzle Systems Sono-Tek Corporation Precision Counts … Spectrum of Industry, (1997). www.lico.at.

[31] G. Ferrari, P. Cardillo, Ultrasonic control, Concr. Eng. Int. 6 (2002) 69–72.

[32] Sono-Tek Corporation, Impact Array, (2018). https://www.sono-tek.com/product/impact-array/ (accessed April 25, 2022).

[33] Sono-Tek, AccuMist Fact Sheet, AccuMist Fact Sheet. (2003).

[34] S. Nathanael, Spray Coater: Standard Operating Procedure, (2014) 1–15. www.4dlabs.ca.

[35] C.H. Chen, E.M. Kelder, J. Schoonman, Unique porous LiCoO2 thin layers prepared by electrostatic spray deposition, J. Mater. Sci. 31 (20) (1996) 5437-5442. https://repository.tudelft.nl/islandora/object/uuid:155b4fcc-b555-47d1-8939-2bbda267e892?collection=research.

[36] Y. Xie, S. Gao, M. Eslamian, Fundamental Study on the Effect of Spray Parameters on Characteristics of P3HT:PCBM Active Layers Made by Spray Coating, Coatings. 5 (2015) 488–510. https://doi.org/10.3390/coatings5030488.

[37] M. Eslamian, J. Newton, Spray-on PEDOT:PSS and P3HT:PCBM Thin Films for Polymer Solar Cells, Coatings. 4 (2014) 85–97. https://doi.org/10.3390/coatings4010085.

[38] C. Villeneuve, L. Mazenq, Profilometres Mecaniques P15 Et P16 +, (n.d.) 15–16. http://www.laas.fr/images/TEAM/RTB/carac/Profilometre_mecanique.pdf.

[39] Bruker, Stylus Profilometer: Dektak XTL, (2022). https://www.bruker.com/en/products-and-solutions/test-and-measurement/stylus-profilometers/dektak-xtl.html (accessed April 26, 2022).

[40] KLA Corporation, The World's First Affordable 3D Profilometer: The Profilm3D, (2022). https://www.filmetrics.com/profilometers/profilm3d (accessed April 27, 2022).

[41] I. Pignatelli, A. Kumar, K. Shah, M. Balonis, M. Bauchy, B. Wu, G. Sant, Vertical scanning interferometry: A new method to quantify re-/de-mineralization dynamics of dental enamel, Dent. Mater. 32 (2016) e251–e261. https://doi.org/10.1016/j.dental.2016.07.004.

[42] O. V. Lyulko, G. Randers-Pehrson, D.J. Brenner, Immersion Mirau interferometry for label-free live cell imaging in an epi-illumination geometry, in: D.L. Farkas, D. V. Nicolau, R.C. Leif (Eds.), 2010: p. 756825. https://doi.org/10.1117/12.855651.

[43] S. Sinha Ray, Techniques for characterizing the structure and properties of polymer nanocomposites, in: Environ. Friendly Polym. Nanocomposites, Elsevier, 2013: pp. 74–88. https://doi.org/10.1533/9780857097828.1.74.

[44] M. Farré, D. Barceló, Introduction to the Analysis and Risk of Nanomaterials in Environmental and Food Samples, in: 2012: pp. 1–32. https://doi.org/10.1016/B978-0-444-56328-6.00001-3.

[45] NanoAndMore GmbH, What is Atomic Force Microscopy (AFM), (2022). https://www.nanoandmore.com/what-is-atomic-force-microscopy (accessed April 27, 2022).

[46] CSI Atomic Force Microscopes, Nano-Observer AFM, (2022). https://www.csinstruments.eu/nano-observer-afm-microscope/ (accessed April 27, 2022).

[47] Park Systems, Park NX10 Atomic force Microscope, (2022). https://www.parksystems.com/products/small-sample-afm/park-nx10/overview (accessed April 27, 2022).

[48] O. Jon, Handbook of Charged Particle Optics, CRC Press, 2017. https://doi.org/10.1201/9781420045550.

[49] A.J. Garratt-Reed, D.C. Bell, P. Nicholson, Energy-dispersive X-ray analysis in the electron microscope. Bios Scientific Publishers, Ltd., Oxford, U.K. 2003 ISBN 1859961096; paperback; 160 pages; $38.50, Scanning. 25 (2006) 162–162. https://doi.org/10.1002/sca.4950250309.

[50] Carl Zeiss NTS GmbH, Instruction manual AURIGA series, Modular CrossBeam® workstation, (2010). http://www.rochester.edu/urnano/assets/pdf/sem_fib_zeiss_auriga_manual.pdf.

[51] Nanoscience Instruments, Scanning Electron Microscopy, (2022). https://www.nanoscience.com/techniques/scanning-electron-microscopy/ (accessed April 27, 2022).

[52] Matsusada Precision, Electron Microscope and Elemental Analysis - Electron Microscope (SEM) Technical Explanation Series (3), (2021). https://www.matsusada.com/column/sem-tech3.html (accessed April 28, 2022).

[53] M. Ohring, Materials Science of Thin Films, Elsevier, 2002. https://doi.org/10.1016/B978-0-12-524975-1.X5000-9.

[54] C. de Melo, S. Larramendi, V. Torres-Costa, J. Santoyo-Salazar, M. Behar, J. Ferraz Dias, O. de Melo, Enhanced ZnTe infiltration in porous silicon by Isothermal Close Space Sublimation, Microporous Mesoporous Mater. 188 (2014) 93–98. https://doi.org/10.1016/j.micromeso.2013.12.036.

[55] H. Fujiwara, Spectroscopic ellipsometry : principles and applications, John Wiley & Sons, Chichester, England; Hoboken, NJ, 2007.

[56] E.A. Davis, N.F. Mott, Conduction in non-crystalline systems V. Conductivity, optical absorption and photoconductivity in amorphous semiconductors, Philos. Mag. 22 (1970) 0903–0922. https://doi.org/10.1080/14786437008221061.

[57] G. Martínez-Saucedo, R. Castanedo-Pérez, G. Torres-Delgado, A. Mendoza-Galván, O. Z. Ángel. Cuprous oxide thin films obtained by dip-coating method using rapid thermal annealing treatments. Materials Science in Semiconductor Processing 68 (2017), 133-139. https://doi.org/10.1016/j.mssp.2017.06.017.

[58] S. Bose, C. Chevallier, S. Ould Saad Hamady, D. Horwat, J.-F. Pierson, P. Boulet, T. Gries, T. Aubert, N. Fressengeas, Elaboration of high-transparency ZnO thin films by ultrasonic spray pyrolysis with fast growth rate, Superlattices Microstruct. 156 (2021) 106945. https://doi.org/10.1016/j.spmi.2021.106945.

[59] Vitalij K. Pecharsky, Peter Y. Zavalij, Fundamentals of Powder Diffraction and Structural Characterization of, Springer, New York, 2008.

[60] W.H. Bragg, W.L. Bragg, The reflection of X-rays by crystals, Proc. R. Soc. London. Ser. A, Contain. Pap. a Math. Phys. Character. 88 (1913) 428–438. https://doi.org/10.1098/rspa.1913.0040.

[61] Y. Fleming, J. Bour, Xrd: Structural Analysis At List, Luxemb. Inst. Sci. Technol. (n.d.) 1–22.

[62] P. Scherrer, Bestimmung der inneren Struktur und der Größe von Kolloidteilchen mittels Röntgenstrahlen, in: Kolloidchem. Ein Lehrb., Springer Berlin Heidelberg, Berlin, Heidelberg, 1912: pp. 387–409. https://doi.org/10.1007/978-3-662-33915-2_7.

[63] A. Monshi, M.R. Foroughi, M.R. Monshi, Modified Scherrer Equation to Estimate More Accurately Nano-Crystallite Size Using XRD, World J. Nano Sci. Eng. 02 (2012) 154–160. https://doi.org/10.4236/wjnse.2012.23020.

[64] H.J. Bunge, Influence of Texture on Powder Diffraction, Textures Microstruct. 29 (1997) 1–26. https://doi.org/10.1155/tsm.29.1.

[65] D. Maurya, Y. Zhou, Y. Wang, Y. Yan, J. Li, D. Viehland, S. Priya, Giant strain with ultra-low hysteresis and high temperature stability in grain oriented lead-free K0.5Bi0.5TiO3-BaTiO3-Na0.5Bi0.5TiO3 piezoelectric materials, Sci. Rep. 5 (2015) 8595. https://doi.org/10.1038/srep08595.

[66] D. Ariosa, F. Elhordoy, E.A. Dalchiele, R.E. Marotti, C. Stari, Texture vs morphology in ZnO nano-rods: On the x-ray diffraction characterization of electrochemically grown samples, J. Appl. Phys. 110 (2011) 124901. https://doi.org/10.1063/1.3669026.

[67] R. T. Downs, The RRUFF Project: An Integrated Study of the Chemistry, Crystallography, Raman and Infrared Spectroscopy of Minerals, Proceedings of the 19th General Meeting of the International Mineralogical Association, Kobe, 23-28 July 2006, pp. 3-13, (2006).

[68] A. Chaichi, A. Prasad, M. Gartia, Raman Spectroscopy and Microscopy Applications in Cardiovascular Diseases: From Molecules to Organs, Biosensors. 8 (2018) 107. https://doi.org/10.3390/bios8040107.

[69] G.S. Bumbrah, R.M. Sharma, Raman spectroscopy – Basic principle, instrumentation and selected applications for the characterization of drugs of abuse, Egypt. J. Forensic Sci. 6 (2016) 209–215. https://doi.org/10.1016/j.ejfs.2015.06.001.

[70] P. Larkin, Chapter 1 - Introduction: Infrared and Raman Spectroscopy, in: P.B.T.-I. and R.S. Larkin (Ed.), Elsevier, Oxford, 2011: pp. 1–5. https://doi.org/https://doi.org/10.1016/B978-0-12-386984-5.10001-1.

[71] K.W. Kho, U.S. Dinish, M. Olivo, Biomedicine with surface enhanced Raman scattering (SERS), in: Biophotonics Med. Appl., Elsevier, 2015: pp. 101–134. https://doi.org/10.1016/B978-0-85709-662-3.00005-1.

[72] E. V. Efremov, F. Ariese, C. Gooijer, Achievements in resonance Raman spectroscopy, Anal. Chim. Acta. 606 (2008) 119–134. https://doi.org/10.1016/j.aca.2007.11.006.

[73] B. Beckhoff, habil. B. Kanngießer, N. Langhoff, R. Wedell, H. Wolff, eds., Handbook of Practical X-Ray Fluorescence Analysis, Springer Berlin Heidelberg, Berlin, Heidelberg, 2006. https://doi.org/10.1007/978-3-540-36722-2.

[74] K. Ariyama, X-ray Fluorescence Analysis (XRF), Nippon Shokuhin Kagaku Kogaku Kaishi. 61 (2014) 150–150. https://doi.org/10.3136/nskkk.61.150.

[75] T.D.T. Oyedotun, X-ray fluorescence (XRF) in the investigation of the composition of earth materials: a review and an overview, Geol. Ecol. Landscapes. 2 (2018) 148–154. https://doi.org/10.1080/24749508.2018.1452459.

[76] HORIBA Scientific, What is X-ray Fluorescence (XRF)?, (2022). https://www.horiba.com/int/what-is-x-ray-fluorescence-xrf/ (accessed April 29, 2022).

[77] N. Birkner, Q. Wang, How an FTIR Spectrometer Operates, Chem. Libr. (2022). https://chem.libretexts.org/Bookshelves/Physical_and_Theoretical_Chemistry_Textbook_Maps/Supplemental_Modules_(Physical_and_Theoretical_Chemistry)/Spectroscopy/Vibrational_Spectroscopy/Infrared_Spectroscopy/How_an_FTIR_Spectrometer_Operates (accessed April 29, 2022).

[78] W.D. Perkins, Topics in chemical instrumentation: Fourier transform infrared spectroscopy: Part III. Applications, J. Chem. Educ. 64 (1987) 5–10. https://doi.org/10.1021/ed064pa296.

[79] A.A. Ismail, F.R. van de Voort, J. Sedman, Chapter 4 Fourier transform infrared spectroscopy: Principles and applications, in: 1997: pp. 93–139. https://doi.org/10.1016/S0167-9244(97)80013-3.

[80] M.-M. Blum, H. John, Historical perspective and modern applications of Attenuated Total Reflectance - Fourier Transform Infrared Spectroscopy (ATR-FTIR), Drug Test. Anal. 4 (2012) 298–302. https://doi.org/10.1002/dta.374.

[81] A. S. Yusof, S. Ould Saad Hamady, C. Chevallier, N. Fressengeas, Z. Hassan, S. S. Ng, M. A. Ahmad, W. F. Lim, and M. A. Che Seliman. Analysis using a two-layer model of the transport properties of InGaN epilayers grown on GaN template substrate. Materials Science in Semiconductor Processing 144 (2022), p. 106614. https://doi.org/10.1016/j.mssp.2022.106614

CHAPTER 3: Preparation of Zinc Oxide: Optimization for Use as a Window Layer

3.1 Introduction to Zinc Oxide (ZnO)

ZnO is an inorganic II-VI binary semiconductor compound. It is mostly available as a white powder in the Earth's crust as mineral zincite. The commercially used ZnO as an additive is produced synthetically. ZnO is a compound semiconductor with an ionicity that falls in between covalent and ionic semiconductors. ZnO crystal structures can have three forms as schematically shown in ***Figure 3.1***: rock salt (B1, relatively rare, obtained at high pressure), zinc blende (B3) and wurtzite (B4). The most thermodynamically stable phase is wurtzite even at room temperatures while the zinc blende structure can only be stabilized by growing them on cubic substrates.

The hexagonal lattice in ZnO is defined by two interconnecting Zn^{2+} and O^{2-} sublattices, with each Zn^{2+} ion surrounded by a tetrahedron of O^{2-} ions, and vice versa. The tetrahedral coordination thus results in a non-central symmetric structure, which leads to significant piezoelectric, pyroelectric, and spontaneous polarization effects, all of which are important in crystal growth, etching, and defect generation [1,2]. This coordination is typically of sp^3 covalent bonding nature. The materials in the ZnO group also tend to possess substantial ionic character that results in increasing the bandgap beyond the values generally expected from the covalent bonding.

Figure 3.1: ZnO Crystal structures **(a)** cubic rocksalt, **(b)** cubic zinc blende and **(c)** Hexagonal wurtzite. Zn atoms are shown as small black spheres and the O atoms are shown as large white spheres [3].

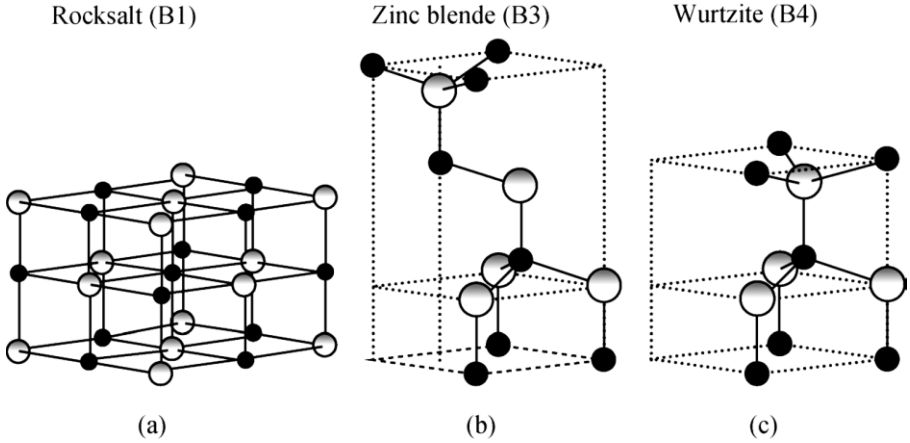

In the hexagonal wurtzite structure of ZnO that interests us, the c-axis, which is parallel to z (0001), is a polar hexagonal axis. The zinc atoms are almost in a hexagonal close packing configuration. Typically, each sublattice in the wurtzite structure has four atoms per unit cell, and each atom of one kind (group II) is surrounded by four atoms of the other kind (group VI), or vice versa, at the tetrahedron's borders with a ratio of the lattice parameters (c/a) of about 1.66 [4].

3.2 Properties of ZnO

For applications in semiconductor devices, the properties of ZnO can be classified into three different types: optical, chemical, and electrical.

3.2.1 Optical Properties

(i) Bandgap: ZnO exhibits a large bandgap value of about 3.44 eV at low temperatures, whereas at room temperatures, it is close to 3.37 eV, corresponding to the emission in the UV region [5]. In comparison, wurtzite gallium nitride (GaN) can have values of 3.44 eV to 3.5 eV [6] very close to those of ZnO. The bandgap of ZnO is perfectly suited to applications in UV optoelectronics, such as light-emitting diodes, laser diodes, solar cells (as a window layer) and "solar-blind" photodetectors [3,7–10]. Due to the favourable optical properties ZnO can be used in different forms such as platelets [11], nanowires [12], nanocrystals [13], thin-films [14] and even in p-n homojunctions [15–17].

(ii) Binding energy: In comparison to GaN, the free-exciton binding energy of ZnO is quite large. For ZnO it is 60 meV while GaN has a value of 25 meV [6,11,14]. Because of the high exciton binding energy, efficient excitonic emission in ZnO can be maintained at room temperature and above [11]. The strong exciton binding energy makes ZnO a potential material for optical devices based on excitonic effects, as the oscillator strength of excitons is often significantly higher than that of direct electron–hole transitions in direct gap semiconductors [18].

(iii) Luminescence: ZnO is a suitable material for phosphor applications because of its intense luminosity in the green–white region of the spectrum. The induced emission spectrum exhibits a broad peak at 495 nm [half-width of 0.4 eV] [19]. Because of its n-type conductivity, ZnO is suitable for use in vacuum fluorescent displays and field emission displays. The origin of the luminescence center and its mechanism is unknown, and it is commonly attributed to oxygen vacancies or zinc interstitials despite the lack of evidence [19]. It's been proposed that green luminescence is most likely caused by zinc vacancies.

3.2.2 Chemical Properties

(i) Wet chemical etching: The capacity to use "low-temperature wet chemical etching" in semiconductor device fabrication methods is extremely beneficial. ZnO thin films have been reported to be etched using acidic, alkaline, and combination solutions. The ability to manufacture,

develop, and integrate electrical and optoelectronic devices using low-temperature chemical etching gives a lot of flexibility [20–22].

(ii) Thermal conductivity: This feature makes ZnO a useful additive (for example, ZnO is added to rubber to improve tyre thermal conductivity). This also makes ZnO a more appealing substrate for homoepitaxy or heteroepitaxy (for example, growth of GaN, which has a comparable lattice constant) [23,24]. Excellent thermal conductivity corresponds to high heat removal efficiency while the device is in use.

(iii) Radiation hardness: For applications at high altitudes or in space, radiation hardness is critical. ZnO has been found to have a very high radiation hardness, much higher than GaN, the cause of which is yet unknown [25,26].

(iv) Surface conductivity: The conductivity of ZnO thin films is highly dependent on the surface's exposure to various gases. Due to its great sensitivity to trimethylamine contained in the odour, it can be employed as a “cheap smell sensor” capable of detecting the freshness of foods and drinks [27]. Sensor action mechanisms are poorly understood. In vacuum-annealed single crystals, recent tests have revealed the presence of a surface electron accumulation layer that disappears when exposed to ambient air. This layer could also play a function in sensor action [28–30]. It's been claimed that the presence of this conducting surface channel is linked to some perplexing type-conversion effects found when attempting to generate p-type ZnO.

3.2.3 Electrical Properties

Because of two factors, much research has been conducted on the electrical characteristics of ZnO films to better understand the conduction behaviour. For practical TCOs with rather large carrier concentrations, carrier concentration (n) and mobility (μ) cannot be separately increased. Ionized impurity scattering, or the Coulomb interactions between electrons and dopants, limits carrier transport at high electron densities. Higher levels of doping restrict carrier mobility to the degree where conductivity cannot be enhanced.

Even in the absence of intentional doping, mostly ZnO has an n-type character. Although native defects such as oxygen vacancies and zinc interstitials are frequently considered to be the cause, an alternate explanation based on theoretical calculations has been proposed: unintentional substitutional hydrogen impurities are to be responsible [31].

By replacing Zn with group-III elements Al, Ga, and In, controllable n-type doping can be easily achieved; then, according to most reports about ZnO films deposited using various methods, resistivity and mobility were, to a large extent, independent of the deposition method and limited to about 2×10^{-4} Ω×cm and 50 cm^2/Vs, respectively [32,33]. Furthermore, it is difficult to fabricate p-type ZnO due to the limited solubility of p-type dopants and their compensation by abundant n-type impurities. This fact is analogous to materials like GaN and ZnSe. Due to inhomogeneity, it is often difficult to measure p-type behaviour in an "intrinsically" doped n-type material. High levels of p-type conductivity are dubious and needs to be experimentally verified. Additionally, it reduces optical transmission at the near-infrared edge. The resistivity approaches a lower limit as the dopant concentration rises, beyond which it cannot decrease [34].

3.3 Applications of ZnO in Solar Cells

The recent years witnessed massive research and development towards transparent oxides for solar cells. These oxides, used as transparent conducting materials (TCM, in our case: transparent conducting oxides (TCO)), as absorbers or window layers, allow for the development of solar cells with performance characteristics that are suitable for large-scale terrestrial applications. Because of the following advantages, TCO are very successful in solar cell applications: (i) the conducting transparent layer allows direct transmission of solar radiation to the absorber with little or no attenuation; (ii) the p-n junction formation temperature is lower and thus it is easier to fabricate and (iii) can act as both a low-resistance junction contact and an anti-reflective layer. ZnO as a material satisfies all these criteria.

Aranovich *et al.* [35] studied the electrical and photovoltaic properties of a heterojunction fabricated from spray pyrolyzed ZnO films on single crystal p-type CdTe. The optimum cell yielded an efficiency of 8.8 %. A $CuInS_2$/ZnO heterojunction solar cell fabricated by Tiwari *et al.* [36] using spray pyrolysis produced 2 % conversion efficiency. The ZnO conductivity increased post annealing thus improving the junction behaviour. Tomar *et al.* [37] prepared a heterojunction ZnO/$CuInSe_2$ solar cell using chemical spray pyrolysis with more than 2 % efficiency. Kao *et al.* [38] used sol-gel spin coating technique to fabricate a ZnO nano-crystalline thin film on fluorine doped tin oxide (FTO) coated glass substrate for dye sensitized solar cells. Using pre-annealed ZnO at 300 °C, 2.5 % conversion efficiency was possible. For CIGS solar cells, Campa *et al.* [39] reported that ZnO placed between the CIGS and molybdenum back contact shows increased reflectance thereby enhancing the J_{SC}. Rau *et al.* [40] shows that in CIGS solar cells, intrinsic ZnO layer prevents electrical inhomogeneities from dominating the device's open circuit voltage. ZnO has been used extensively

for heterojunctions with Cu_2O absorber in "all-oxide" solar cells. The interested readers can look into the ***Sections 1.3.2.3*** and ***1.3.2.4*** of ***Chapter 1*** where it is discussed thoroughly.

3.4 Preparation of ZnO by Ultrasonic Spray Pyrolysis

The preparation of ZnO films was done using an ExactaCoat system from Sono-Tek. For the ultrasonic atomization of the precursor solution an Accumist nozzle operating at 120 kHz was employed. A detailed description of the ultrasonic spray pyrolysis process is included in ***Chapter 2***. Soda lime glass (SLG) slides ($76\times26\times1$ mm^3) were used as substrates. Prior to the deposition, the soda lime glass was cleaned ultrasonically with solutions such as acetone, isopropanol and distilled water for 15, 10 and 5 minutes respectively to remove any organic residues. A 3 mm thick and uniform copper plate was used as a substrate holder on top the heating block of the spray system to protect it and to supply maximum heat to the glass substrate. The temperature on the heating plate was regulated by an in-built PID temperature controller. The temperatures of the substrate holder and the glass substrate were measured using N-type thermocouples. The substrate was pre-heated to the desired spray temperature. A suction pump was operated constantly during the spray preparation process continuously to extract the gaseous by-products and vapours of the solvent. The set temperature of the heating plate in the spray system was kept constant during the entire spray preparation process. The height between the spray nozzle and the glass substrate was fixed to 10 cm. Air as carrier gas was used to maintain the shaping air pressure of 13.8 kPa to the Accumist nozzle so that the resulting droplets (aerosols) from the nozzle is guided with a good control and uniformity towards the heated substrate. Zinc acetate dihydrate, $Zn(Ac)_2.2H_2O$ was used as the source precursor salt dissolved in deionized water. For simplicity henceforth, in this thesis we will always refer it as only $Zn(Ac)_2$. Always 50 mL of precursor solution was prepared before the start of the spray. Acetic acid was added to the solution of $Zn(Ac)_2$ to reduce the formation of zinc hydroxide, $Zn(OH)_2$. Zinc ions could actually get precipitated in the pyrolysis process on the form of a milky textured $Zn(OH)_2$. Thus, the acetic acid quantity added to the precursor solution becomes an important study point in this chapter.

3.4.1 Chemicals Used and Chemical Reactions Involved for ZnO Preparation

All the chemicals used for the preparation of ZnO thin films are listed in the ***Table 3.1***.

Table 3.1: Chemicals with high purity used for spray pyrolysis deposition of ZnO.

Name	Formula	Supplier
Zinc acetate dihydrate	$Zn(CH_3COO)_2 \cdot 2H_2O$	Merck 108802
Acetic acid	CH_3COOH	Alfa Aesar 10994-AE
Deionized water	H_2O	Avantor-VWR

The pH of the precursor solution is monitored using acetic acid. Zn^{2+} is transformed into complexes, $Zn(Ac)^+$ and $Zn(Ac)_2$, depending on the pH of the solution. The concentration of these species is significant in the development of the film. In order to achieve film deposition, it is preferable to have neutral zinc acetate [written as $Zn(CH_3COO)_2$ or $Zn(Ac)_2$] in solution. Addition of acetic acid, keeps the solution pH in the range of 4-5, which actually makes $Zn(Ac)_2$ the dominating species in the solution and thereby the film deposition process in enhanced. Possible pyrolytic reactions taking place in the formation of ZnO thin films are discussed by Paraguay *et al.* [41] and shown in our own work [42] as:

$$Zn(CH_3COO)_2 \xrightarrow{Heat} 4Zn(CH_3COO)_2 + H_2O \xrightarrow{Adsorption} Zn_4O(CH_3COO)_6 + 2CH_3COOH$$

Solid near substrate *Gas near substrate* *Adsorbed on surface* *Gas*

$$Zn_4O(CH_3COO)_6 + 3H_2O \xrightarrow{yields} 4ZnO\ (Film) + 6CH_3COOH\ \text{(Gas)}$$

Adsorbed on surface

In our study [42], as we already pre-heat the substrate to a very high temperature in ambient air conditions and with $Zn(CH_3COO)_2$ as the dominating complex we can write the pyrolytic reaction as:

$$Zn(CH_3COO)_2 + 4O_2 \xrightarrow{Heat} ZnO\ (film) + 4CO_2\ (Gas) + 3H_2O\ (Vapour) \uparrow$$

The formation of zinc hydroxide can be written as:

$$Zn(CH_3COO)_2 + 2H_2O \xrightarrow{Heat} 4Zn(OH)_2 + 2CH_3COOH\ (Gas) \uparrow$$

Generally, the droplets that are larger than 50 μm in diameter reacts with the Zn^{2+} ions and the atmospheric water vapour present inside the spray chamber to form the hydroxide. Adding acetic acid in the precursor solution allows the ionization of zinc acetate. A subsequent reaction facilitates the production of a zinc-based complex, $ZnCH_3COO^+$ and thereby preventing the formation of $Zn(OH)_2$. The reactions are written below:

$$CH_3COOH \xleftrightarrow{yields} CH_3COO^- + H^+$$

$$Zn^{2+} + CH_3COO^- \overset{yields}{\longleftrightarrow} ZnCH_3COO^+$$

In our study, the pH of the solution along with the variation of the spray parameters along with their subsequent effect on the film quality was studied in detail with the help of a design of experiments as discussed in the next sub-section.

The effects of the $Zn(Ac)_2$ precursor solution concentration on the ZnO film quality have been discussed later in this chapter. The quantity of the $Zn(Ac)_2$ powder required in the solution to reach a particular solution concentration is calculated using the relation:

Equation (3.2):

$$m = C \times V \times M$$

Where, m is the mass (in g) of $Zn(Ac)_2$ powder; C is the ultimate solution concentration in mol/L; V is the solution volume in litres (L) and M is the molar mass of $Zn(Ac)_2$ (in g/mol).

So, for example, mass of $Zn(Ac)_2$ needed for preparing a 50 mL solution with concentration of 0.10 mol/L is: m = 0.10 × 0.05 × 219.49 = 1.09 g.

3.4.2 Design of Experiment

Many parameters are involved in the spray pyrolysis preparation process for depositing high-quality thin films, as detailed in ***Chapter 2***. Variation in each parameter impacts the resulting film quality. This is the reason to set up the design of experiments, so that we can understand and analyze the nature and degree of impact of the parameters towards the prepared film quality. The list below shows the variation of spray parameters along with range of their variation.

1. The hot plate set temperature, varied in the range from 350 °C to 450 °C.
2. The spray flow rate, which was varied in the range from 0.3 to 0.7 mL/min.
3. A precursor solution concentration ranging from 0.03 to 0.10 mol/L.
4. The pH of the precursor solution was adjusted between 4 and 5.
5. The number of spray cycles, which ranged from 10 to 60. The duration of each preparation is determined by this parameter.

When one spray parameter was varied, all the other parameter remained fixed to a particular value. This helped in understanding the effect of the variation of the parameter on the film's quality. Some parameters such as, the height between the spray nozzle and the substrate and the scan speed movement of the spray nozzle were fixed before according to the system's safety measures to achieve high transparency thin films with a fast growth rate across a wide thickness range. The repeatability

of the ultrasonic spray pyrolysis method was rigorously verified by preparing each sample at least three times with the parameters listed above. For better understanding, the design of experiment to select the optimal ultrasonic spray pyrolysis parameters is shown in the ***Table 3.2***.

Table 3.2: Design of experiment to select the optimal spray parameters for ZnO preparation.

Preparation Parameter	Range
Preparation temperature	[350 °C ; 450 °C]
Spray flow rate	[0.3 ; 0.7]
Precursor solution concentration	[0.03 ; 0.10]
pH of precursor solution	[4 ; 5]
Number of spray cycles	[10 ; 60]

3.5 Results and Discussions on the Preparation of ZnO

The design of experiments scheme mentioned above was used for the preparation of ZnO thin films. Various characterization techniques were used to understand the variation of the spray parameters on the growth, morphological, optical, and structural characteristics of the ZnO thin films.

3.5.1 Growth of the ZnO Thin Films

The thickness of the spray zone was systematically measured at three sites by the mechanical Dektak XT profilometer and then averaged. ***Figure 3.2*** depicts the relationship between ZnO film thickness and the number of spray cycles. The growth of the ZnO films is shown to be linear in relation to the number of spray cycles. The fitted line does not cross the origin, indicating that there is an incubation period when grains coalesce and grow to form the ZnO thin film. In spray pyrolysis and sol-gel procedures, this nucleation/coalescence duration is commonly reported [43–45].

By preparing many samples (up to four) in the same process and by regularly preparing new samples with the same previously employed settings, the procedure's reproducibility and stability were tested. The growth rate was around 120 nm per minute, or 14 nm every spray cycle. We set the number of spray cycles to 20 based on this calibration, which corresponds to a ZnO film thickness of roughly 200 nm. With thicknesses of the ZnO films, ranging from around 100 nm to almost 800 nm, a growth rate of roughly 120 nm/min was achieved from our spray process.

The growth rate achieved in our spray preparation process was higher than reported values in known studies. Kenanakis *et al.* [46] reports a growth rate of 1 nm/min, Mata *et al.* [47] reaches up to 42 nm/min, Ergin *et al.* [48] could reach 55 nm/min, and Ynineb *et al.* [49] recently reported a

growth rate of 80 nm/min. We were able to sustain this high growth rate of 120 nm/min while also maintaining a fast nozzle scan speed of 70 mm/sec with good reproducibility. The set substrate temperature was 450 °C for the depositions with a solution concentration of 0.10 mol/L and pH 4. Flow rate was constant at 0.5 mL/min.

Figure 3.2: ZnO thickness variation with the number of spray cycles.

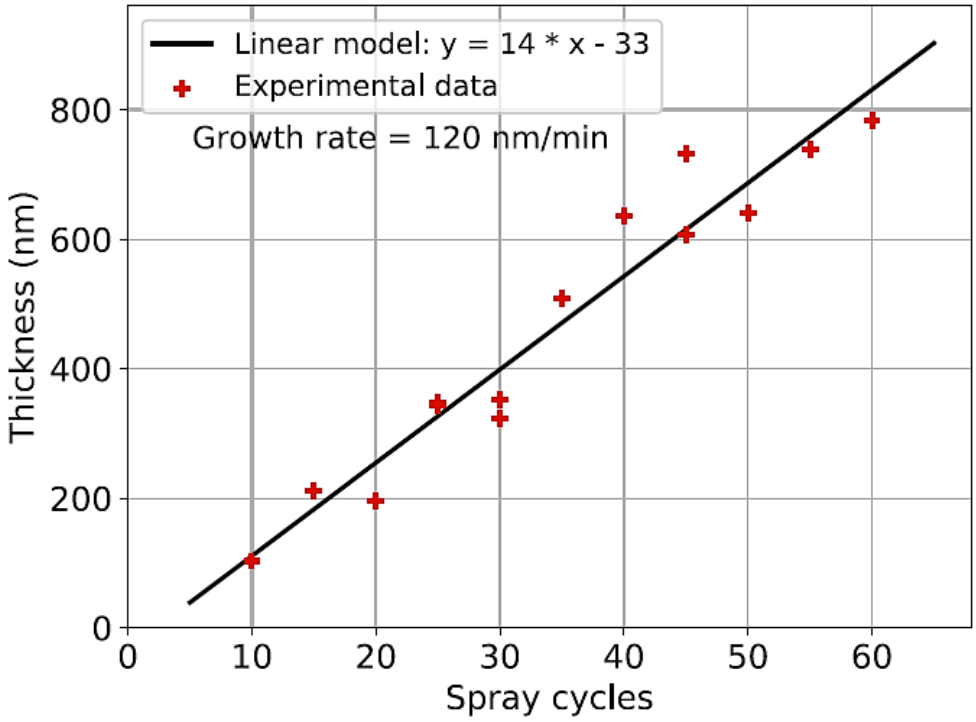

3.5.2 Optical Properties of the ZnO Thin Films

To investigate the optical characteristics of the ZnO thin films, the transmission of the films was assessed in relation to deposition conditions. The experimental details of the technique are given in **Section 2.7.2** of **Chapter 2**. In the first step, the set substrate temperature was varied from 350 °C to 450 °C (in three different experimental steps of 50 °C each). The spray parameters which are kept fixed for these preparations are: number of spray cycles: 20, solution flow rate: 0.5 mL/min; precursor solution concentration and pH: 0.1 mol/L and 4 respectively; dwell time: 1 sec for each spray cycle. The resulting transmission spectra's is shown in the ***Figure 3.3***.

Figure 3.3: Transmission spectra for ZnO films prepared at different temperatures.

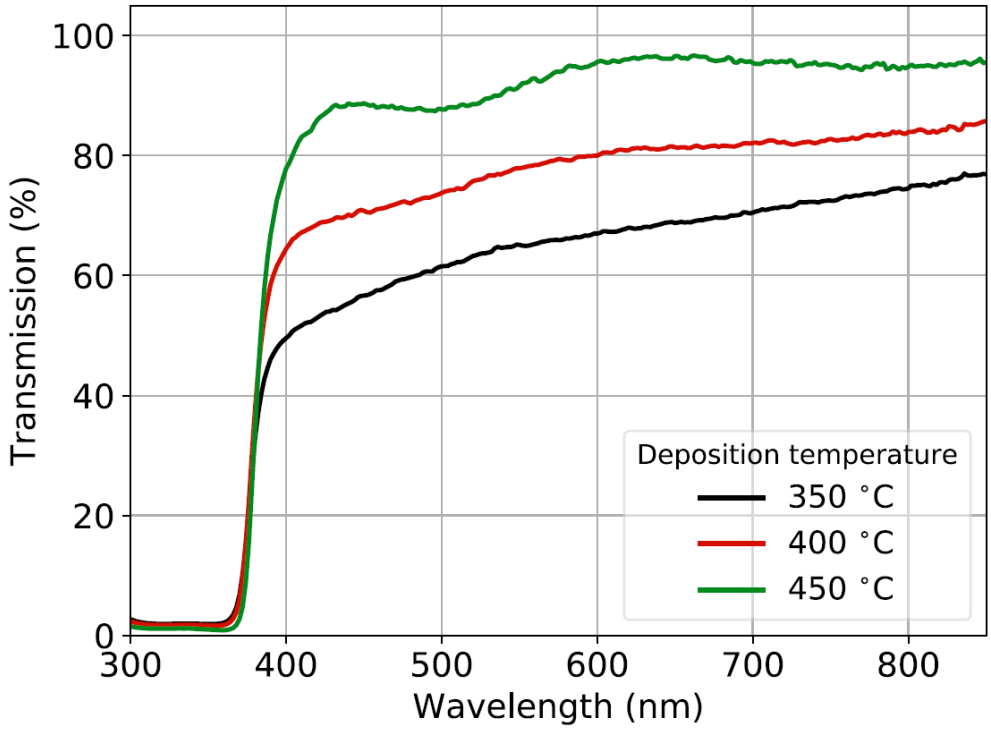

The loss of transparency can be attributed to the fact that at lower temperatures the pyrolysis reaction is incomplete (also observed in [50]), which means that production of $Zn(OH)_2$, will dominate in the film along with presence of other carbon related by-products, which is discussed by showing the related reactions in the ***Section 3.4.1***. $Zn(OH)_2$ has a milky white texture, which absorbs much more than normal transparent ZnO films. This interpretation is confirmed by the FTIR measurements which will be presented later.

In the next step, keeping the temperature fixed to 450 °C, the solution flow rate was varied from 0.03 to 0.10 mol/L. The number of spray cycles was kept to 20 with the precursor solution concentration and pH was fixed at to 0.1 mol/L and 4 respectively and the dwell time was set to 1 second for each spray cycle. With the increase in the flow rate, it is seen that the transmission gradually decreases (shown in the ***Figure 3.4***).

Figure 3.4: Transmission spectra for ZnO films prepared at different flow rates.

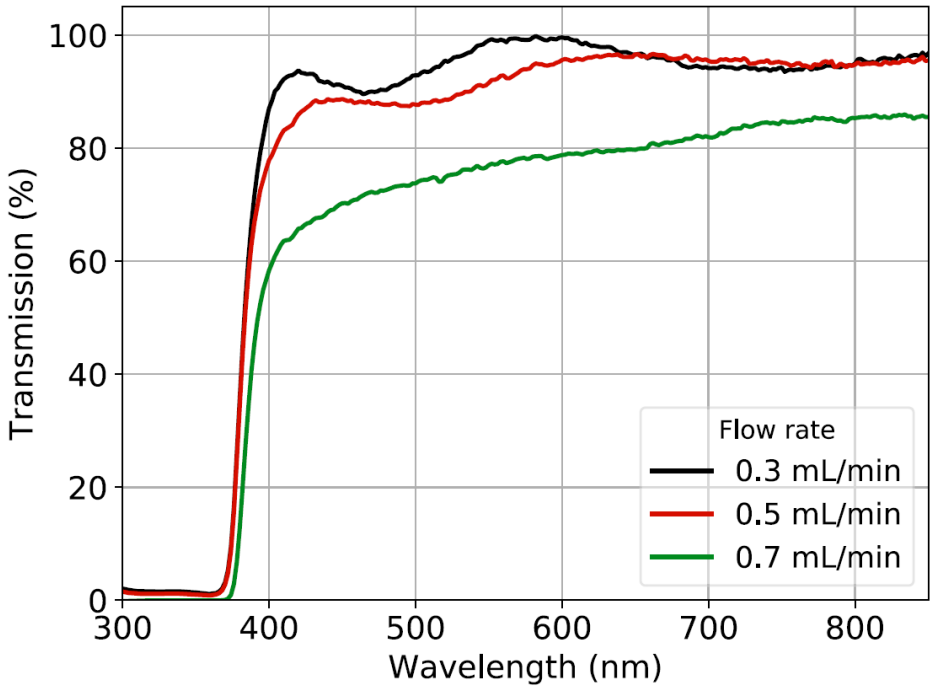

A large decrease in transmission at the high flow rate is mostly due to the fact that, at this high flow rate, the atomization of the precursor solution is incomplete, which in turn, results to larger droplets being deposited on the substrate. These large droplets do not contribute to the pyrolysis reaction and generally forms $Zn(OH)_2$, thereby reducing the film transparency. The loss of the transparency for the highest flow rate could be explained from another perspective: in this case the main cause is the oxygen-zinc stoichiometry, as with the high flow rate, the atomic ratio of Zn/O is relatively high. The high Zn/O ratio makes the reaction of pyrolysis not only incomplete but also ambiguous which directly impacts the growth mechanism of the ZnO films and presents a disrupted surface morphology. Similar evidence with the high Zn/O ratio can also be seen in ZnO films prepared by sputtering [51–53]. We need to maintain the flow rate to an optimum value of the flow rate with respect to the shaping air pressure so that a complete pyrolysis takes place. With very low rates the process results in under-spray as the major portion of droplets vaporize even before reaching the hot substrate surface. For this reason, the prepared films are too thin with high surface roughness, so although we achieve high transparency with a low flow rate it is advisable to use the moderate flow rate of 0.5 mol/L to have nearly similar transparency (as shown in the ***Table 3.3***) with good film qualities.

Now, with the substrate temperature and flow rate values fixed to 450 °C and 0.5 mol/L respectively, we studied the effect of the variation of the precursor solution concentration on the film transparency. As usual, the number of spray cycles, the solution pH and the dwell times were kept

same as before. The concentration was varied from 0.03 mol/L to 0.10 mol/L. But, in this case, we do not see major variations in the transparency of the films (cf. ***Figure 3.5***) as the concentration changes are not major themselves and the pyrolysis reaction is complete in all cases resulting in the desired stoichiometry of the ZnO films. All the films exhibited high average transmission of more than 90 %. But, to choose the exact value of the solution concentration we will show and discuss in the subsequent sections the structural analysis of the films with varying concentrations.

Figure 3.5: Transmission spectra for ZnO films prepared at different solution concentrations.

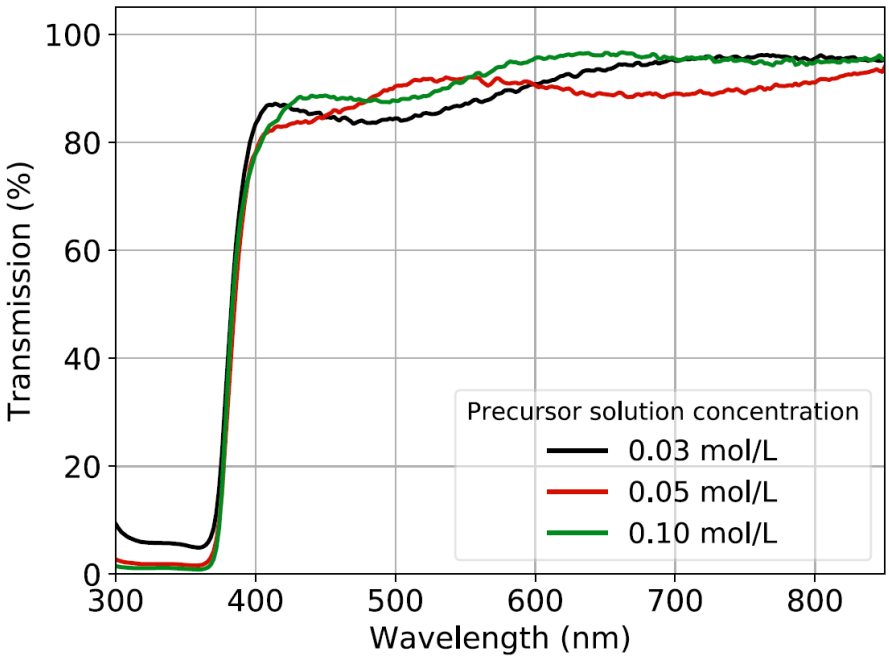

For the next preparation step, we only vary the pH of the precursor solution from 4 to 5. We chose the solution concentration to be 0.10 mol/L. To have complete pyrolysis, the substrate temperature was set to 450 °C and the solution flow rate of 0.5 mL/min was chosen. The other parameters were kept same as before. Different quantities of acetic acid were added to the precursor solutions to have different pH values in the final solutions. In 50 mL solutions, the volume percentages of acetic acid were 1.2 % and 0.4 % respectively for solutions with pH 4 and 5 respectively. The transmission spectra for ZnO films prepared with these solutions are shown in the ***Figure 3.6***. A dramatic decrease in transparency (from 93.5 % to 80.3 %) is seen for the film prepared with pH 5. With pH 5, the less quantity of acetic acid does not completely help in the ionization process which of the $Zn(Ac)_2$, thus formation of $Zn(OH)_2$ dominates during the pyrolysis process and agglomerates are also noticed in the film. Importantly, adding acetic acid to the solution also reduces the surface tension of water, thereby assisting in the process of droplet atomization and creation of uniform

solution droplets which ultimately forms a compact, dense, and uniform film of ZnO. So, it is better to have a pH value of 4 of the precursor solution. The reduction of the formation of $Zn(OH)_2$ with acetic acid is also found in the research by Edinger *et al.* [54] and Li *et al.* [55]. Edinger *et al.* [54] and Winkler *et al.* [56] also reported the reduction of surface tension with addition of acetic acid.

Figure 3.6: Transmission spectra for ZnO films prepared with different pH of the precursor solutions.

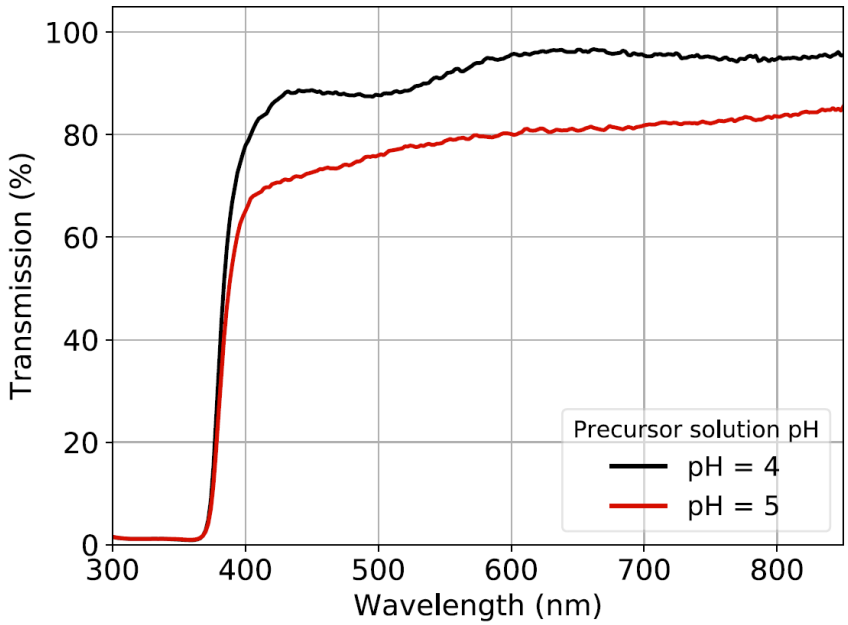

From the above discussions, we can clearly understand the reasons for the loss in transparency along the effects of the changes of the spray parameters on the ZnO films. The ***Table 3.3*** below shows the measured values of transmission in all prepared ZnO films along with the details of the varied spray parameters. Also, the optical bandgap of the films is calculated along with the corresponding Urbach energies. The method of calculation of the optical bandgap and the Urbach energy are already discussed is details in the ***Section 2.7.2*** of ***Chapter 2***.

Now, with all the spray parameters varied and their effect on the film transparency analyzed, another additional analysis was performed. Taking the best spray parameters from the ***Table 3.3***, we varied the number of spray cycles to understand the change in the transmission with increasing thickness of the ZnO films. The spray parameters chosen for these preparations are substrate temperature: 450 °C, solution flow rate: 0.5 mL/min; precursor solution concentration and pH: 0.1 mol/L and 4 respectively; dwell time: 1 sec for each spray cycle. The Transmission spectra and the optical bandgap estimation by the Tauc model of the films are shown in the ***Figure 3.7 (a & b)***.

Table 3.3: Spray pyrolysis preparation parameters of ZnO with 20 spray cycles**.** Measured optical parameters values are provided for all the films.

Temperature (°C)	Precursor Solution Concentration (mol/L)	Precursor Solution pH	Solution Flow Rate (mL/min)	Average Transmission (%) in [450-800] nm range	Bandgap (eV) ± 0.01 eV	Urbach Energy (meV) ± 5 meV
350	0.10	4	0.5	68.3	3.26	96
400	0.10	4	0.5	79.9	3.28	84
450	0.10	4	0.5	93.5	3.26	63
450	0.10	4	0.3	95.4	3.28	69
450	0.10	4	0.7	80.0	3.29	67
450	0.03	4	0.5	91.5	3.28	77
450	0.05	4	0.5	90.0	3.26	78
450	0.10	5	0.5	80.3	3.26	77

Figure 3.7: Transmission spectra for ZnO films prepared with different spray cycles **(a)** and Tauc plots for 20 and 50 cycles **(b)**.

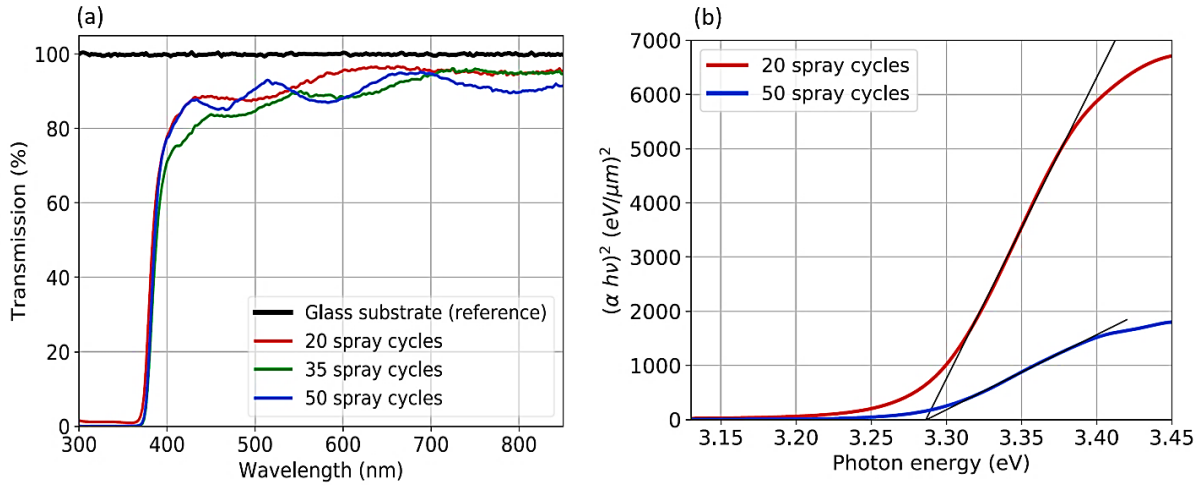

From the figure above, we see that the transparency of the films remains almost similar with the increase in thickness of the prepared films. This result suggests the effective control of the spray parameters in our preparation process, and we see in the films uniform and smooth surface without any porosity or any grain pockets (also confirmed later by the AFM and SEM measurements). This is the reason that the transparency remains almost similar even with increasing thickness. To establish the success of our spray process, we compare our results with those of the state-of-the-art results which are detailed in the ***Table 3.4***.

It is observed that the transparency of the films remains in the range of 90-95 % in the wavelength regime of 400-850 nm. The thickness of the ZnO films varies from ≈ 200 nm (for 20 spray cycles) up to ≈ 640 nm (for 50 spray cycles). As seen from the ***Table 3.4***, our values can well be compared

with the state-of-the-art values for ZnO thin films prepared with different processes. The values of Urbach energies for the films with the best spray parameters lies between 63-78 meV (shown in ***Tables 3.3 & 3.4***) which are also comparable with good quality ZnO films prepared with other processes [57,58]. Low Urbach energy values, indicate that the optical quality of the films improved during the spray preparation process. The transmission values for our ZnO thin films also stands out when compared with other high-quality films from other preparation processes. Usually, the reported average transmission values for ZnO films lies in the range of 80-85 % in the visible region of the spectrum [41,54,59–62]. A recent study produced highly transparent ZnO film (95 % transmission) with a thickness of 30 nm by using custom made spray pyrolysis and CVD systems for the preparation [63]. Using ultrasonic spray pyrolysis 90 % transmission in ZnO was achieved by Mokhtari *et al.* [64] for use as a window layer in solar cell applications. It is also shown that an anneal process after the deposition can further increase the transparency beyond 90 % [65]. But with an effective control on the spray parameters, we were able to prepare conformal ZnO films with high precision, such that even without a post-annealing treatment on the ZnO films we were able to achieve transparencies as high as 95 %. All the mentioned spray parameters work in unison to provide excellent atomization of the precursor solution to achieve highly conformal, uniform, compact and dense ZnO films.

Overall, by studying the optical characteristics of the ZnO thin films with respect to the variation of the spray preparation parameters, we can say that that the films prepared with the optimized set of parameters (mentioned in ***Table 3.6***) can be applied as window layers for “all-oxide” solar cells. The slight improvement (widening) in the bandgap energy of the films prepared at higher temperature can be explained by the Burstein–Moss effect [72], in which case, with an increase in the carrier concentration, the Fermi level merges into the conduction band. Also, due to high level of crystallinity, as shown later in the XRD measurements, the Urbach energies are the lowest, as at high temperature the concentration of the oxygen vacancies is low as also shown by Othmane *et al.* [73]. At a higher temperature, the Zn–O–Zn bonds gets weaker causing the loss of oxygen atoms. In turn, the O 1s binding energy in lowered with lowering of Urbach energies. Hence, the band-tail width is lowered with less disorders in the films, which also causes the increase in the optical bandgap energy.

Table 3.4: Spray pyrolysis preparation parameters of ZnO with varying spray cycles. Measured optical parameters values are provided for all the films along with comparison of the state-of-the-art values.

Preparation Technique on Different Substrates along with References	**Deposition Temperature (°C)**	**Number of Spray Cycles**	**Film Thickness (nm) ± 10 nm**	**Average Transmission (%)**	**Bandgap (eV) ± 0.01 eV**	**Urbach Energy (meV) ± 5 meV**
Our work [42]	450	20	196	93.5	3.28	63
Our work [42]	450	35	508	92.4	3.25	72
Our work [42]	450	50	640	90.6	3.26	61
USP: ZnO/Glass [60]	400	N.M.	N.M.	86	3.25	N.M.
USP: ZnO/Glass [57]	400	N.M.	N.M.	84; 90	3.24	N.M.
USP: ZnO/Glass [66]	365 ; 465	N.M.	N.M.	83; 91	3.35 ; 3.40	N.M.
USP: ZnO/Glass [61]	350 ; 450	N.M.	N.M.	85	3.29 ; 3.31	N.M.
EB: ZnO/Sapphire [67]	600	N.A.	N.M.	N.M.	N.M.	74 ; 99
SC: ZnO/Glass [68]	450 (Anneal 1 hour)	N.A.	N.M.	84	3.24 ; 3.33	N.M.
RFS: ZnO/Si [69]	RT	N.A.	N.M.	80 ; 92	3.24 ; 3.29	N.M.
PLD: ZnO/Glass [70]	550	N.A.	N.M.	N.M.	3.34	N.M.
PLD: ZnO/Glass [71]	300	N.A.	N.M.	70	3.83	120

USP: Ultrasonic spray pyrolysis; **EB**: e-beam; **SC**: Spin-coating; **RFS**: Radio-frequency sputtering; **PLD**: Pulsed laser deposition; **RT**: room temperature; **N.M.**: Not mentioned in literature; **N.A.**: Not applicable

3.5.3 Morphological Properties of the ZnO Thin Films

To follow-up the optical properties, morphological analysis of the films was performed with the help of atomic force microscopy (AFM). The measurements were done in the tapping (resonant) mode with an oscillation frequency of 323 kHz with a scan rate of 0.75 Hz. The images thus obtained are shown in the ***Figure 3.8 (a-d)***. For all the preparations, the precursor solution concentration and flow rate were maintained at 0.1 mol/L and 0.5 mL/min.

Figure 3.8: AFM images of ZnO films prepared with pH 4 at substrate temperatures **(a)** 350 °C, **(b)** 400 °C, **(c)** 450 °C and **(d)** with pH 5 at substrate temperature 450 °C.

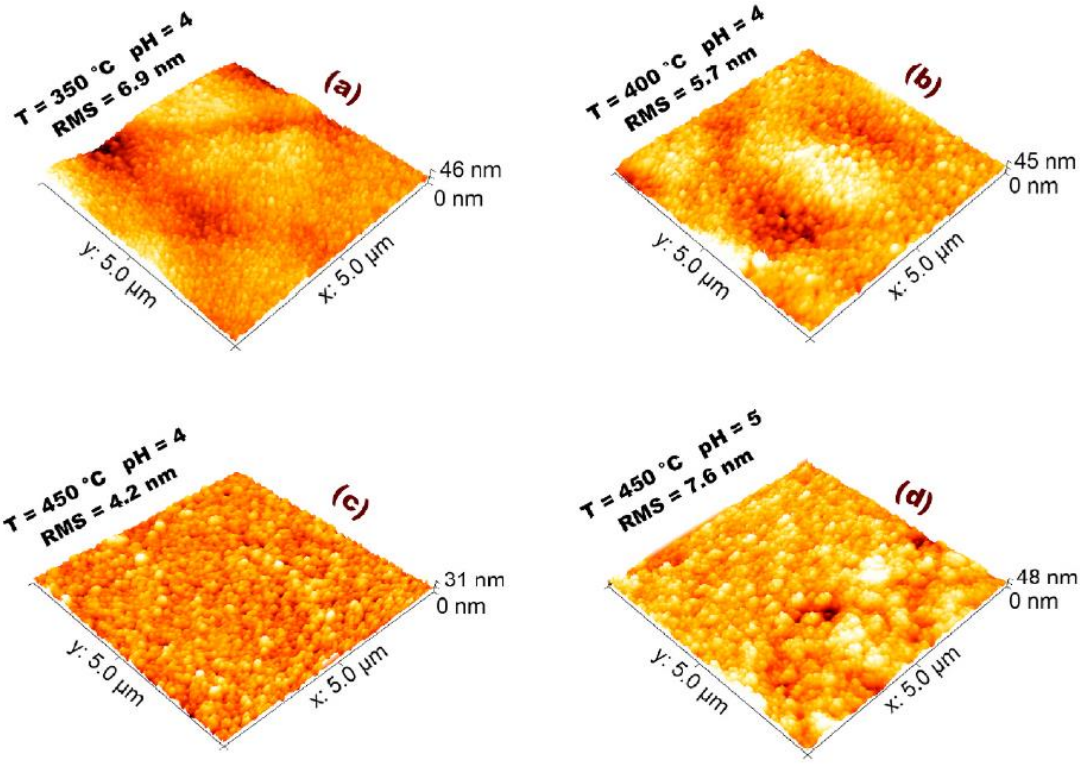

When ZnO is sprayed at a higher temperature, the micrographs demonstrate a granular and polycrystalline morphology with an increase in grain size. The average grain diameter measured from surface micrographs was roughly 40 nm. The best morphology is obtained for the ZnO film prepared at 450 °C with a precursor solution pH of 4. The surface is very uniform with a very low RMS roughness of 4.2 nm (***Figure 3.8c***). Furthermore, the high growth temperature of 450 °C aids to the reduction of surface mechanical stress, resulting in a more uniform surface. For the preparation done at lower temperatures (below 450 °C) and with precursor solution pH of 5, grain agglomerates were noticed on the films. Generally, at lower temperatures the pyrolysis reactions are not complete which tends to form hydroxides as seen in the case for optical study of the films (***Figure 3.3***) in the above section. Similarly, when the pH is 5, the less acetic acid quantity in the

precursor solution does not contribute towards full ionization of the $Zn(Ac)_2$, which helps in the cause of the formation of $Zn(OH)_2$. The formation of $Zn(OH)_2$ is quite detrimental towards the film quality as can be seen in the micrographs of the ***Figure 3.8 a, b and d***. For these reasons, the RMS roughness are higher than the films prepared at 450 °C with pH of 4. This result is consistent with the optical studies which also show similar effects towards the film's optical quality. Prasada Rao *et al*. reported similar temperature effects in their AFM analysis [61]. The RMS roughness of ZnO thin films grown by ultrasonic spray pyrolysis at 450 °C from a pH 4 solution compares favourably to RMS roughness values achieved by more complex techniques such as ion-beam or RF magnetron sputtering [74,75].

To support the results from AFM analysis, SEM micrographs were also captured for the ZnO films. The SEM micrographs are shown in the ***Figure 3.9 (a-d)***. Similar to the AFM micrograph, we can see the polycrystalline nature of the ZnO film with a smooth and uniform surface (***Figure 3.9c***) with no porosity for the preparation done at 450°C. Preparations done at lower temperature (***Figure 3.9 a, b***) shows surface roughness with the presence of agglomerates proving the fact of incomplete pyrolysis at lower substrate temperatures. A rough surface morphology is also evidenced for the film prepared with pH of 5 (***Figure 3.9d***).

Figure 3.9: SEM micrographs for ZnO films prepared with pH 4 at substrate temperatures **(a)** 350 °C, **(b)** 400 °C, **(c)** 450 °C and (d) with pH 5 at substrate temperature 450 °C.

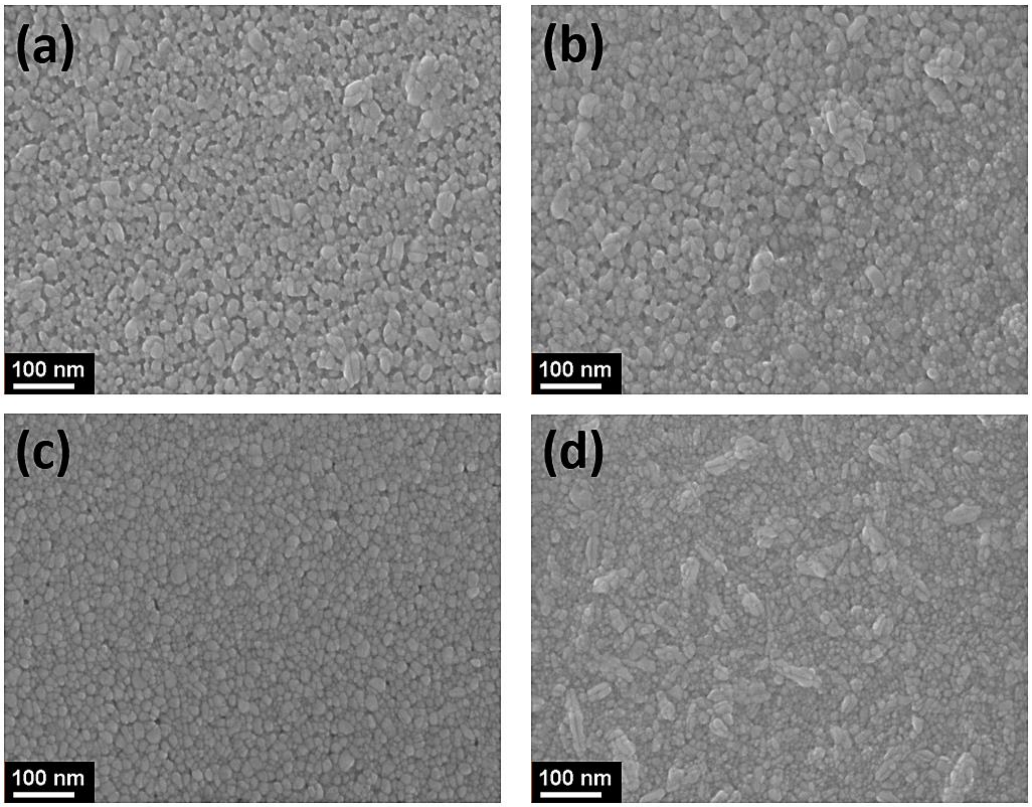

From the morphological analysis, we can surely conclude that preparations done at higher substrate temperature of 450 °C and with a precursor solution pH 4 is a much better choice for the preparation of high-quality ZnO films.

3.5.4 Chemical Properties of the ZnO Thin Films

A chemical analysis was performed on the ZnO films to identify the presence of the hydroxides (O-H bands). With Fourier Transform Infrared Spectroscopy (FTIR) analysis we could detect the presence of the O-H bands. Our analysis was performed in accordance with some previous studies [76,77]. The bands corresponding to the oscillating vibrations O–H (≈ 3400 cm^{-1}), symmetric and asymmetric valence bands C–H (3000 cm^{-1} and 1500 cm^{-1}), stretching vibrations Zn–OH (≈ 1400 cm^{-1}) and Zn–O (≈ 900 cm^{-1}) are visible in the spectra illustrated in ***Figure 3.10 (a & b)***. The presence of O–H bands is more prominent for ZnO sprayed at lower substrate temperatures and with a precursor solution of pH 5, as expected. This behaviour is strongly connected with the production of agglomerates observed with AFM and SEM studies and the resulting decrease of the transmission and it could be the result of hydroxide formation coupled with an incomplete spray pyrolytic reaction. It is consistent with the findings of Edinger *et al.* [54] and Li *et al.* [55], which imply that acetic acid in the precursor solution aids in the reduction of $Zn(OH)_2$ precipitation. The reduction mechanism of $Zn(OH)_2$ precipitation by acetic acid is shown in the ***Section 3.4.1***.

Figure 3.10: FTIR spectra for ZnO prepared with pH 4 **(a)** at different preparation temperatures and **(b)** with precursor solution pH 4 and 5 at substrate temperature 450 °C.

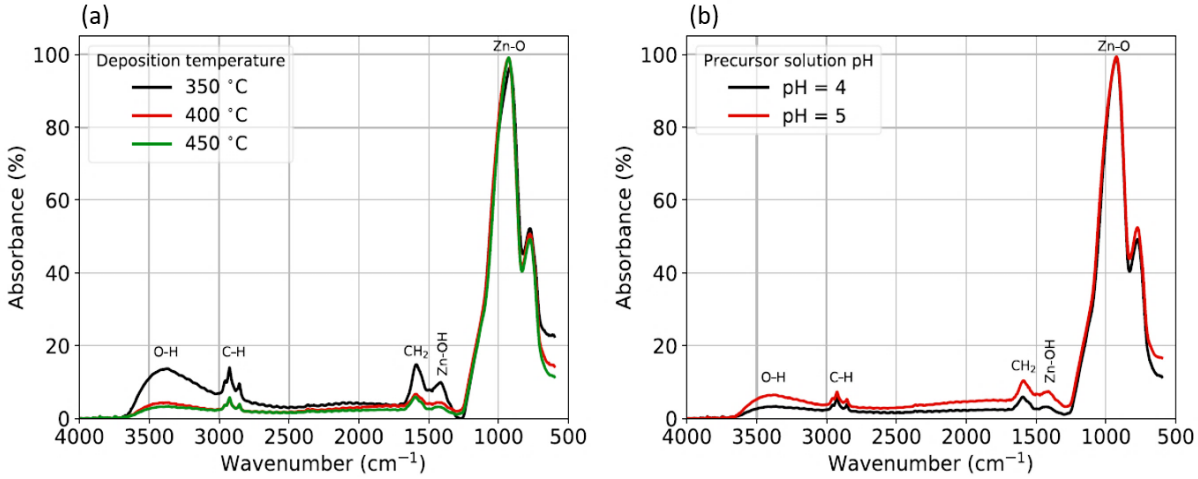

3.5.5 Structural and Electrical Properties of the ZnO Thin Films

X-ray diffraction (XRD) was used to examine the structural properties of the sprayed ZnO films, to determine the deposited material structure and to assess the crystalline quality of the films. ***Figures 3.11*** and ***3.12*** illustrates the X-ray diffractograms of the spray prepared ZnO films. The hexagonal wurtzite phase with space group $P6_3mc$ features four ZnO peaks in the (100), (002), (101), and (110) planes, according to the diffractograms. The Lorentzian structure of X-ray diffractograms is commonly attributed to size-induced peak widening, whereas strain-induced broadening is better characterized by Gaussian or Voigt functions [78]. The shape of the X-ray peak is affected by other factors like as stoichiometry and defects. A least squares fitting procedure was utilized to precisely calculate peak position and full width at half maximum [79,80]. The detailed procedure is given in the ***Section 2.7.3.1*** of ***Chapter 2***.

Figure 3.11: X-Ray diffractograms for ZnO thin films with different precursor solution concentrations but with fixed pH 4. The preparations done at substrate temperature 450 ◦C with 20 spray cycles at a spray flow rate of 0.5 mL/min.

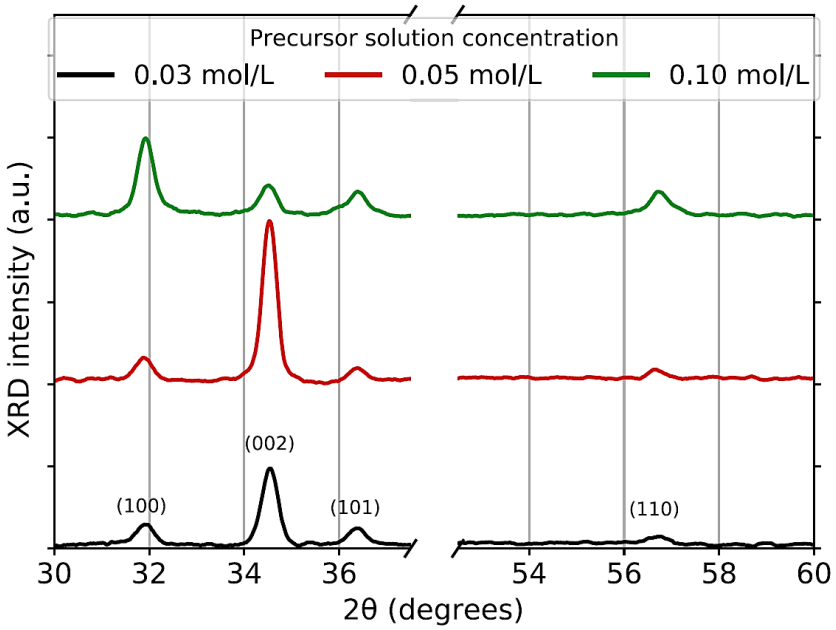

The texture coefficient and crystallite size for the prepared ZnO films, as well as state-of-the-art results for various deposition processes, are determined and summarized in the ***Table 3.5***. As seen in the table, the computed lattice parameters are quite near to the values a = 0.32503 nm and c = 0.52074 nm for pure and stoichiometric ZnO from the RRUFF database [81].

Figure 3.12: X-Ray diffractograms for ZnO thin films prepared at different substrate temperatures. The preparations done with a precursor solution concentration of 0.1 mol/L with pH 4. Number of spray cycles were always 20 with a spray flow rate of 0.5 mL/min.

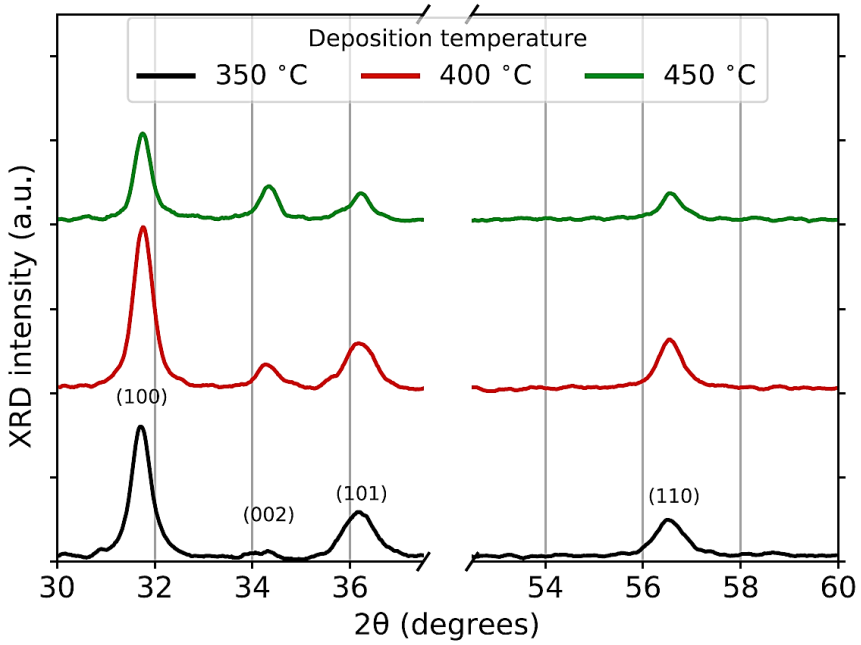

The crystallite dimensions, as calculated using the modified Scherrer method [82], range from 15 to 39 nm, with the maximum obtained for the film prepared at substrate temperature of 450 °C and 0.05 mol/L precursor solution concentration. This crystallite dimension (39 nm) is higher than those obtained previously in similar deposition conditions by de Godoy *et al.* [83], and comparable to or better than similar thin films described in the literature, as shown in ***Table 3.5***. The obtained crystallite dimension agrees with the values obtained from the AFM analysis.

From the diffractograms in the ***Figure 3.11***, it is seen that for films prepared at a deposition temperature of 450 °C and precursor solution concentrations of 0.03 mol/L and 0.05 mol/L, the high value of the texture factors, F_{002} indicates that growth proceeds preferentially with the (002) orientation plane parallel to the substrate in these conditions.

These findings are consistent with prior findings [57,83], which imply that ZnO films with c-axis orientation have the lowest surface energy, uniformly aligned crystallites, and few defects and trapping sites. The c-axis orientation is mostly dominating because of a faster growth rate along this direction during the spray preparation. With a lower concentration of precursor solution, the Zn atoms present in the solution easily finds an O atom to get bonded. The availability of an O atom generally does not depend on the precursor solution concentration. The Zn atoms gets significant mean free path to get bonded to an O atom and thus the crystallization gets optimized in the c-axis

direction. While contrarily, when the concentration of the precursor solution is higher, then the abundance of the Zn atoms favours a random orientation as can be usually seen in the case of a powder diffraction pattern. This effect with the change in concentrations is also seen in [84].

In the diffractograms of the ***Figure 3.12***, the F_{002} values are close to unity or lower than unity. The films in this case, are prepared at lower deposition temperatures of 350 °C and 400 °C, but with precursor solution concentration of 0.10 mol/L. The growth pattern of ZnO indicates that the growth has lost its (002) preferential orientation and the film now has a preferential a-axis orientation along the (100) plane.

Table 3.5: Structural parameters of ZnO extracted from XRD measurements in this work and a comparison with the state-of-the-art.

Preparation Technique on Different Substrates along with References	**Deposition Temperature (°C)**	**Precursor Concentration (mol/L)**	**Texture Factor F_{002}**	**Crystallite Size (nm) ± 5 nm**	**Lattice Parameters c;a (nm) ± 0.00010 nm**
Our work [42]	350	0.10	0.18	16	0.52434 ; 0.32532
Our work [42]	400	0.10	0.45	15	0.52227 ; 0.32513
Our work [42]	450	0.10	0.83	21	0.51955 ; 0.32379
Our work [42]	450	0.05	2.48	39	0.51905 ; 0.32417
Our work [42]	450	0.03	1.96	35	0.51896 ; 0.32418
ZnO powder [81]	N.A.	N.A.	1.00	N.A.	0.52074 ; 0.32503
USP: ZnO/Glass [60]	400	N.M.	N.M.	25	0.51980 ; 0.31830
USP: ZnO/Glass [83]	300 (cycles)	0.03 ; 0.10	160 ; 2.60	12 ; 17	N.M.
USP: ZnO/Glass [66]	365 ; 465	0.03 ; 0.20	N.M.	2 ; 4	N.M.

USP: ZnO/Glass [61]	350 ; 450	0.10	N.M.	13 ; 18	0.52100 ; 0.32480
SC: ZnO/Glass [68]	450 (anneal 1h)	N.A.	N.M.	7 ; 33	0.52109 ; N.M.
SC: ZnO/Glass [85]	500 (anneal 2h)	N.A.	N.M.	19 ; 23	0.52098 ; 0.32387
RFS: ZnO/Sapphire [51]	RT	N.A.	N.M.	27 ; 52	0.52620 ; N.M.
RFS: ZnO/Si [69]	N.M.	N.A.	N.M.	N.M.	N.M.; 0.32527
PLD: ZnO/Quartz [70]	550	N.A.	N.M.	24	0.51460 ; N.M.
PLD: ZnO/Sapphire [86]	675	N.A.	N.M.	21	N.M. ; N.M.

USP: Ultrasonic spray pyrolysis; **SC**: Spin-coating; **RFS**: Radio-frequency sputtering; **PLD**: Pulsed laser deposition; **RT**: room temperature; **N.M.**: Not mentioned in literature; **N.A.**: Not applicable.

To support the findings from the XRD measurements and complete the structural analysis, Raman spectroscopy measurements were performed on our prepared ZnO thin films. The Raman spectra of the ZnO films prepared with different substrate temperatures of 350 °C, 400 °C and 450 °C are shown in the ***Figure 3.13***. All the spectra are shown after a Lorentzian fit of the obtained peaks.

Figure 3.13: ZnO Lorentzian fitted Raman spectra.

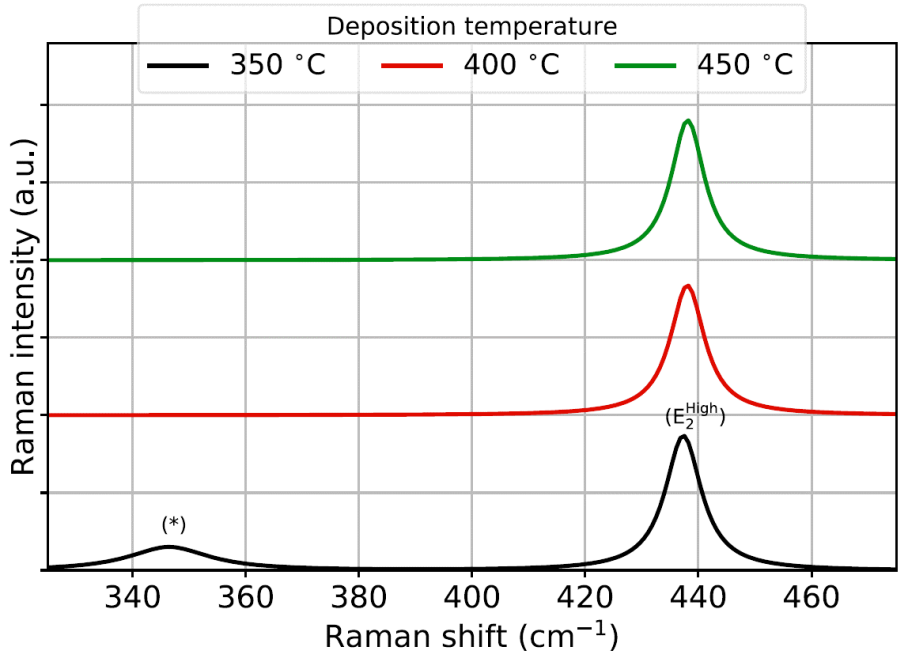

For ZnO films the E_2 modes are directly linked to the quality of the crystal and for textured polycrystalline films the E_2 modes will be dominant. We generally do not see any E_1(TO) mode as it only prominent for films grown at lower substrate temperatures of around 150 °C. We also do not see any A_1(LO) modes, as they are prominent at very high substrate temperatures of 600 °C [87]. The dominant peak at a Raman shift of 438 cm^{-1} is recognized as the E_2^{High} ZnO Raman phonon vibration of the wurtzite structure in all samples obtained by fitting the spectra. In addition, for the lowest deposition temperature of 350 °C, another broad peak develops at a Raman shift around 350 cm^{-1}, but, due to its position and width, which are too different from the known values for this ZnO mode, this peak could not be identified as the ($E_2^{High} - E_2^{Low}$) ZnO mode, which is commonly observed in ZnO [88]. The peak presents a relatively broad nature which could be co-related to change of textures as observed in the XRD diffractograms and could induced by defects in ZnO partially due to an incomplete spray pyrolytic reaction. The E_2^{High} peak full width at half maximum is roughly 8 cm^{-1} at low deposition temperature, which is similar to the values commonly reported for ZnO thin films deposited by sputtering [89]. According to [90], the dominance of the E_2^{High} mode in our thin films without the appearance of the A_1(LO) and E_1(LO) modes suggest very good crystallinity with very less formation of zinc interstitial defect states and oxygen vacancies.

The electrical characteristics of very transparent ZnO thin films were investigated using the four probes technique. An annealing treatment has been performed on the samples, using a rapid thermal annealing system (shown in ***Section 2.7.4, chapter 2***) to obtain semiconducting films since all deposited films were highly resistive before annealing. The resistivity variation with respect to the annealing temperature is shown in the ***Figure 3.15*** while the voltage-current characteristics in the four-point probe configuration are shown in the ***Figure 3.14***. The optimum annealing temperature obtained is 300 °C. This temperature makes it possible both to obtain a low resistivity and to remain below the preparation temperature.

After the post-annealing at 300 °C for 30 minutes, samples deposited at 450 °C with an optimum solution concentration of 0.05 mol/L, spray flow rate of 0.5 mL/min, number of cycles of 50, and pH of 4 were evaluated. The average resistivity was found to be 1.5 Ω×cm. The relatively low resistivity due to the background n-type doping in ZnO is usually attributed to interstitial Zn (Zn_i) which acts as a shallow donor in ZnO with a low formation energy both in Zn-rich and O-rich preparation conditions [91]. This origin of the n-doping in ZnO related to Zn_i is far more probable than oxygen vacancy (V_O) as it is supported by both theoretical studies (using the local density approximation) [91] and experimental results [92] evidencing the fact that Zn_i, acting as a shallow

donor in ZnO, is predicted to be far more abundant than other defects, including V_O. It can be noted that the resistivity values measured in this work are comparable to results recently obtained in identical conditions for non-intentionally doped ZnO produced by spray pyrolysis [93].

Figure 3.14: Voltage-current characteristics of ZnO thin films in the four-point probe (4PP) configuration for the measurement of resistivity. The 4PP technique is presented in **section 2.7.4.1** of **chapter 2**. I_{AD} (in µA) is the current passed through the outer two probes (A & D) and the V_{BC} (in V) is the voltage between the inner two probes (B & C).

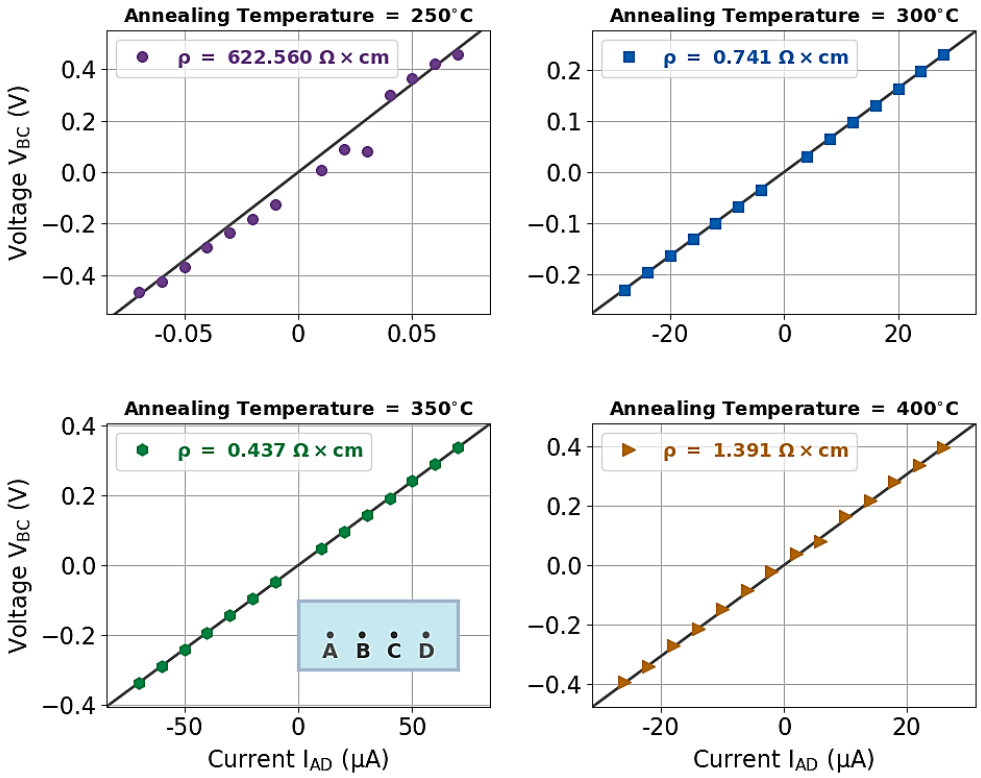

Figure 3.15: Resistivity of ZnO thin films with respect to the annealing temperature.

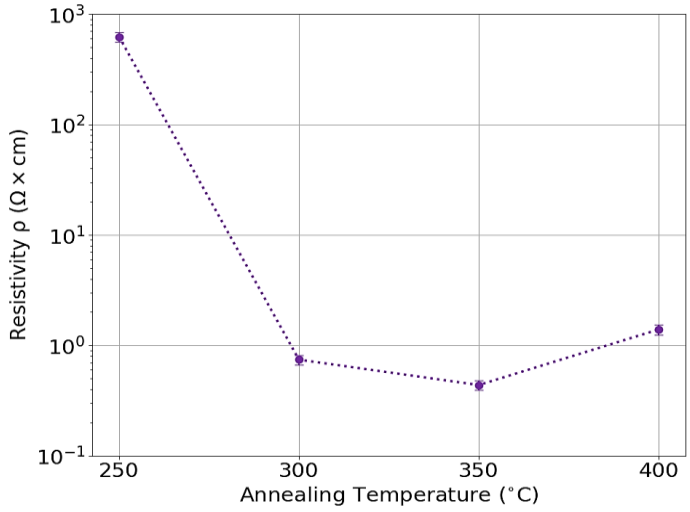

3.6 Challenges Faced Towards the Preparation of ZnO

The entire process to successfully prepare ZnO thin films of optimum quality was not only challenging but also time consuming. We had to make the design of experiments based on an extensive literature survey. Setting up the spray system was the first important task as all parameters including the substrate holder and the substrate itself can impact the film properties a lot. After a lot of tries, a scheme was found using a copper substrate holder with the substrate on it to ensure a uniform heat distribution. The substrate to spray nozzle height and the nozzle speed were initially calibrated and set according to the safely limitations of the spray system. The dwell time had to be fixed for all the preparations very carefully. With the contact of the atomized droplets the substrate temperature can fall up to 50 °C, the dwell time which is a stopping time between the spray cycles helps the substrate to quickly reach the set temperature again. The pre-heated copper plate with a high heat conductivity also helps in this purpose. For the design of experiments, to check the effectivity of our process each preparation of each film with a fixed set of parameters were repeated at least 3 times. The detailed optical, morphological, and structural characterizations (in sequence) and their in-depth analysis helped us to understand the effect of the parameters on the film quality. The analysis of the characterizations with one set of spray parameters helped us to proceed with the next preparation process. One of the major targets of our work was to prevent the formation of the hydroxides. The formation of hydroxides was detrimental in terms of the quality of the thin films as we have seen. Even slight changes in the spray conditions can lead to the formation of hydroxides, so utmost control on the spray parameters is needed to avoid the formation of hydroxides. The understanding of the control of the spray parameters as a whole were important as we wanted to prepare the ZnO thin films with high precision so that they could be utilized as a window layer for “all-oxide” solar cells. So, uniform, and compact ZnO films with a smooth surface along with high transmission and high crystalline quality is crucial.

3.7 Chapter Conclusions

To conclude, we can rightly mention that through the detailed design of experiment we have successfully prepared ZnO thin films of optimum quality to be used as a window layer for “all-oxide” solar cells. The films with the optimized set of spray parameters were highly transparent with excellent morphology. The crystalline qualities as evidenced from the XRD and Raman measurements proved the success of our preparation process.

Fixed spray parameters based on system safety requirements set prior to creating the design of

experiments are listed as:

(i) Substrate to spray nozzle height: 10 cm.

(ii) Nozzle speed: 70 mm/sec.

(iii) Dwell time: 1 sec for each spray cycle.

(iv) Shaping air pressure: 13.8 kPa.

The values of the optimized spray parameters that can be implemented for preparation of ZnO to be used as window layer for "all-oxide" solar cells are mentioned in the ***Table 3.6*** below.

Table 3.6: Optimized spray preparation parameters along with their values.

Spray Preparation Parameters	**Optimized Parameter Values**
Set substrate/deposition temperature	450 ^{o}C
Solution flow rate	0.5 mL/min
Number of spray cycles	20
Precursor solution concentration	0.05 mol/L
Precursor solution pH	4

These optimized parameters make it possible to prepare ZnO thin films which fulfill the main criteria for use in all-oxide solar cells as window layer: **(i)** fast growth rate; **(ii)** high transparency in a wide range of thickness from 100 nm up to 800 nm; **(iii)** c-axis preferred orientation with large grain size and minimized defects; **(iv)** relatively low electrical resistivity.

3.8 References

[1] Z.L. Wang, Zinc oxide nanostructures: growth, properties and applications, J. Phys. Condens. Matter. 16 (2004) R829–R858. https://doi.org/10.1088/0953-8984/16/25/R01.

[2] R.W. Whatmore, Pyroelectric devices and materials, Reports Prog. Phys. 49 (1986) 1335–1386. https://doi.org/10.1088/0034-4885/49/12/002.

[3] C. Jagadish, S. Pearton, eds., Zinc Oxide Bulk, Thin Films and Nanostructures, Elsevier, 2006. https://doi.org/10.1016/B978-0-08-044722-3.X5000-3.

[4] E.H. Kisi, M.M. Elcombe, u parameters for the wurtzite structure of ZnS and ZnO using powder neutron diffraction, Acta Crystallogr. Sect. C Cryst. Struct. Commun. 45 (1989) 1867–1870. https://doi.org/10.1107/S0108270189004269.

[5] A. Mang, K. Reimann, S. Rübenacke, Band gaps, crystal-field splitting, spin-orbit coupling, and exciton binding energies in ZnO under hydrostatic pressure, Solid State Commun. 94 (1995) 251–254. https://doi.org/10.1016/0038-1098(95)00054-2.

[6] O. Madelung, Semiconductors: Data Handbook, Springer Berlin Heidelberg, Berlin, Heidelberg, 2004. https://doi.org/10.1007/978-3-642-18865-7.

[7] D.C. Look, Recent advances in ZnO materials and devices, Mater. Sci. Eng. B. 80 (2001) 383–387. https://doi.org/10.1016/S0921-5107(00)00604-8.

[8] Ü. Özgür, Y.I. Alivov, C. Liu, A. Teke, M.A. Reshchikov, S. Doğan, V. Avrutin, S.-J. Cho, H. Morkoç, A comprehensive review of ZnO materials and devices, J. Appl. Phys. 98 (2005) 041301. https://doi.org/10.1063/1.1992666.

[9] S.B. Ogale, Thin Films and Heterostructures for Oxide Electronics, Springer-Verlag, New York, 2005. https://doi.org/10.1007/b136780.

[10] N.H. Nickel, E. Terukov, eds., Zinc Oxide — A Material for Micro- and Optoelectronic Applications, Springer Netherlands, Dordrecht, 2005. https://doi.org/10.1007/1-4020-3475-X.

[11] D.C. Reynolds, D.C. Look, B. Jogai, Optically pumped ultraviolet lasing from ZnO, Solid State Commun. 99 (1996) 873–875. https://doi.org/10.1016/0038-1098(96)00340-7.

[12] M.H. Huang, S. Mao, H. Feick, H. Yan, Y. Wu, H. Kind, E. Weber, R. Russo, P. Yang, Room-Temperature Ultraviolet Nanowire Nanolasers, Science (80-.). 292 (2001) 1897–1899. https://doi.org/10.1126/science.1060367.

[13] H. Cao, Y.G. Zhao, S.T. Ho, E.W. Seelig, Q.H. Wang, R.P.H. Chang, Random Laser Action in Semiconductor Powder, Phys. Rev. Lett. 82 (1999) 2278–2281. https://doi.org/10.1103/PhysRevLett.82.2278.

[14] D.M. Bagnall, Y.F. Chen, Z. Zhu, T. Yao, S. Koyama, M.Y. Shen, T. Goto, Optically pumped lasing of ZnO at room temperature, Appl. Phys. Lett. 70 (1997) 2230–2232. https://doi.org/10.1063/1.118824.

[15] A. Tsukazaki, A. Ohtomo, T. Onuma, M. Ohtani, T. Makino, M. Sumiya, K. Ohtani, S.F. Chichibu, S. Fuke, Y. Segawa, H. Ohno, H. Koinuma, M. Kawasaki, Repeated temperature modulation epitaxy for p-type doping and light-emitting diode based on ZnO, Nat. Mater. 4 (2004) 42–46. https://doi.org/10.1038/nmat1284.

[16] Y.R. Ryu, T.S. Lee, J.H. Leem, H.W. White, Fabrication of homostructural ZnO p–n junctions and ohmic contacts to arsenic-doped p-type ZnO, Appl. Phys. Lett. 83 (2003) 4032–4034. https://doi.org/10.1063/1.1625787.

[17] S. Chu, M. Olmedo, Z. Yang, J. Kong, J. Liu, Electrically pumped ultraviolet ZnO diode lasers on Si, Appl. Phys. Lett. 93 (2008) 181106. https://doi.org/10.1063/1.3012579.

[18] P.Y. Yu, M. Cardona, Fundamentals of Semiconductors, Springer Berlin Heidelberg, Berlin, Heidelberg, 2010. https://doi.org/10.1007/978-3-642-00710-1.

[19] S. Shionoya, W.M. Yen, H. Yamamoto, eds., Phosphor Handbook, CRC Press, 2018. https://doi.org/10.1201/9781315222066.

[20] X.-G. Han, Y.-Q. Jiang, S.-F. Xie, Q. Kuang, X. Zhou, D.-P. Cai, Z.-X. Xie, L.-S. Zheng, Control of the Surface of ZnO Nanostructures by Selective Wet-Chemical Etching, J. Phys. Chem. C. 114 (2010) 10114–10118. https://doi.org/10.1021/jp101284p.

[21] H. Zheng, X.L. Du, Q. Luo, J.F. Jia, C.Z. Gu, Q.K. Xue, Wet chemical etching of ZnO film using aqueous acidic salt, Thin Solid Films. 515 (2007) 3967–3970. https://doi.org/10.1016/j.tsf.2006.09.017.

[22] D.-G. Yoo, S.-H. Nam, M.H. Kim, S.H. Jeong, H.-G. Jee, H.J. Lee, N.-E. Lee, B.Y. Hong, Y.J. Kim, D. Jung, J.-H. Boo, Fabrication of the ZnO thin films using wet-chemical etching processes on application for organic light emitting diode (OLED) devices, Surf. Coatings Technol. 202 (2008) 5476–5479. https://doi.org/10.1016/j.surfcoat.2008.06.064.

[23] D.I. Florescu, L.G. Mourokh, F.H. Pollak, D.C. Look, G. Cantwell, X. Li, High spatial resolution thermal conductivity of bulk ZnO (0001), J. Appl. Phys. 91 (2002) 890–892. https://doi.org/10.1063/1.1426234.

[24] Ü. Özgür, X. Gu, S. Chevtchenko, J. Spradlin, S.-J. Cho, H. Morkoç, F.H. Pollak, H.O. Everitt, B. Nemeth, J.E. Nause, Thermal conductivity of bulk ZnO after different thermal treatments, J. Electron. Mater. 35 (2006) 550–555. https://doi.org/10.1007/s11664-006-0098-9.

[25] F. Tuomisto, K. Saarinen, D.C. Look, G.C. Farlow, Introduction and recovery of point defects in electron-irradiated ZnO, Phys. Rev. B. 72 (2005) 085206. https://doi.org/10.1103/PhysRevB.72.085206.

[26] D.C. Look, J.W. Hemsky, J.R. Sizelove, Residual Native Shallow Donor in ZnO, Phys. Rev. Lett. 82 (1999) 2552–2555. https://doi.org/10.1103/PhysRevLett.82.2552.

[27] H. Nanto, H. Sokooshi, T. Usuda, Smell sensor using zinc oxide thin films prepared by magnetron sputtering, in: TRANSDUCERS '91 1991 Int. Conf. Solid-State Sensors Actuators. Dig. Tech. Pap., IEEE, n.d.: pp. 596–599. https://doi.org/10.1109/SENSOR.1991.148948.

[28] O. Schmidt, P. Kiesel, D. Ehrentraut, T. Fukuda, N.M. Johnson, Electrical characterization of ZnO, including analysis of surface conductivity, Appl. Phys. A. 88 (2007) 71–75. https://doi.org/10.1007/s00339-007-3949-1.

[29] O. Schmidt, A. Geis, P. Kiesel, C.G. Van de Walle, N.M. Johnson, A. Bakin, A. Waag, G.H. Döhler, Analysis of a conducting channel at the native zinc oxide surface, Superlattices Microstruct. 39 (2006) 8–16. https://doi.org/10.1016/j.spmi.2005.08.056.

[30] D.C. Look, Quantitative analysis of surface donors in ZnO, Surf. Sci. 601 (2007) 5315–5319. https://doi.org/10.1016/j.susc.2007.09.030.

[31] C.G. Van de Walle, Hydrogen as a Cause of Doping in Zinc Oxide, Phys. Rev. Lett. 85 (2000) 1012–1015. https://doi.org/10.1103/PhysRevLett.85.1012.

[32] K. Ellmer, Magnetron sputtering of transparent conductive zinc oxide: relation between the sputtering parameters and the electronic properties, J. Phys. D. Appl. Phys. 33 (2000) R17–R32. https://doi.org/10.1088/0022-3727/33/4/201.

[33] K. Ellmer, Resistivity of polycrystalline zinc oxide films: current status and physical limit, J. Phys. D. Appl. Phys. 34 (2001) 3097–3108. https://doi.org/10.1088/0022-3727/34/21/301.

[34] D.C. Look, B. Claflin, Y.I. Alivov, S.J. Park, The future of ZnO light emitters, Phys. Status Solidi. 201 (2004) 2203–2212. https://doi.org/10.1002/pssa.200404803.

[35] J.A. Aranovich, D. Golmayo, A.L. Fahrenbruch, R.H. Bube, Photovoltaic properties of ZnO/CdTe heterojunctions prepared by spray pyrolysis, J. Appl. Phys. 51 (1980) 4260–4268. https://doi.org/10.1063/1.328243.

[36] A.N. Tiwari, D.K. Pandya, K.L. Chopra, Fabrication and analysis of all-sprayed CuInS2/ZnO solar cells, Sol. Cells. 22 (1987) 263–273. https://doi.org/10.1016/0379-6787(87)90056-1.

[37] M.S. Tomar, F.J. Garcia, A ZnO/p-CuInSe2 thin film solar cell prepared entirely by spray pyrolysis, Thin Solid Films. 90 (1982) 419–423. https://doi.org/10.1016/0040-6090(82)90551-X.

[38] M.C. Kao, H.Z. Chen, S.L. Young, Effects of preannealing temperature of ZnO thin films on the performance of dye-sensitized solar cells, Appl. Phys. A. 98 (2010) 595–599. https://doi.org/10.1007/s00339-

009-5467-9.

[39] A. Čampa, J. Krč, J. Malmström, M. Edoff, F. Smole, M. Topič, The potential of textured front ZnO and flat TCO/metal back contact to improve optical absorption in thin Cu(In,Ga)Se_2 solar cells, Thin Solid Films. 515 (2007) 5968–5972. https://doi.org/10.1016/j.tsf.2006.12.093.

[40] U. Rau, M. Schmidt, Electronic properties of ZnO/CdS/Cu(In,Ga)Se_2 solar cells — aspects of heterojunction formation, Thin Solid Films. 387 (2001) 141–146. https://doi.org/10.1016/S0040-6090(00)01737-5.

[41] F. Paraguay D., W. Estrada L., D.R. Acosta N., E. Andrade, M. Miki-Yoshida, Growth, structure and optical characterization of high quality ZnO thin films obtained by spray pyrolysis, Thin Solid Films. 350 (1999) 192–202. https://doi.org/10.1016/S0040-6090(99)00050-4.

[42] S. Bose, C. Chevallier, S. Ould Saad Hamady, D. Horwat, J.-F. Pierson, P. Boulet, T. Gries, T. Aubert, N. Fressengeas, Elaboration of high-transparency ZnO thin films by ultrasonic spray pyrolysis with fast growth rate, Superlattices Microstruct. 156 (2021) 106945. https://doi.org/10.1016/j.spmi.2021.106945.

[43] A. Palafox, G. Romero-Paredes, A. Maldonado, R. Asomoza, D.R. Acosta, J. Palacios-Gomez, Physical properties of CdS and CdS:In thin films obtained by chemical spray over different substrates, Sol. Energy Mater. Sol. Cells. 55 (1998) 31–41. https://doi.org/10.1016/S0927-0248(98)00044-0.

[44] K. Murakami, K. Nakajima, S. Kaneko, Initial growth of SnO2 thin film on the glass substrate deposited by the spray pyrolysis technique, Thin Solid Films. 515 (2007) 8632–8636. https://doi.org/10.1016/j.tsf.2007.03.128.

[45] M.W. Zhu, J.H. Xia, R.J. Hong, H. Abu-Samra, H. Huang, T. Staedler, J. Gong, C. Sun, X. Jiang, Heat-activated structural evolution of sol-gel-derived ZnO thin films, J. Cryst. Growth. 310 (2008) 816–823. https://doi.org/10.1016/j.jcrysgro.2007.11.074.

[46] G. Kenanakis, N. Katsarakis, Ultrasonic spray pyrolysis growth of ZnO and ZnO:Al nanostructured films: Application to photocatalysis, Mater. Res. Bull. 60 (2014) 752–759. https://doi.org/10.1016/j.materresbull.2014.09.060.

[47] V. Mata, A. Maldonado, M. de la Luz Olvera, Deposition of ZnO thin films by ultrasonic spray pyrolysis technique. Effect of the milling speed and time and its application in photocatalysis, Mater. Sci. Semicond. Process. 75 (2018) 288–295. https://doi.org/10.1016/j.mssp.2017.11.038.

[48] B. Ergin, E. Ketenci, F. Atay, Characterization of ZnO films obtained by ultrasonic spray pyrolysis technique, Int. J. Hydrogen Energy. 34 (2009) 5249–5254. https://doi.org/10.1016/j.ijhydene.2008.09.108.

[49] F. Ynineb, D.E. Guitoume, D. Mendil, N. Attaf, M.S. Aida, H. Farh, ZnO Nanorods Prepared by Ultrasonic Spray Pyrolysis: Effect of Deposition Time on the Structural Morphological and Optical Properties, Defect Diffus. Forum. 397 (2019) 88–100. https://doi.org/10.4028/www.scientific.net/DDF.397.88.

[50] T.G. Silva, E. Silveira, E. Ribeiro, K.D. Machado, N. Mattoso, I.A. Hümmelgen, Structural and optical properties of ZnO films produced by a modified ultrasonic spray pyrolysis technique, Thin Solid Films. 551 (2014) 13–18. https://doi.org/10.1016/j.tsf.2013.11.011.

[51] W. Chamorro, D. Horwat, P. Pigeat, P. Miska, S. Migot, F. Soldera, P. Boulet, F. Mücklich, Near-room temperature single-domain epitaxy of reactively sputtered ZnO films, J. Phys. D. Appl. Phys. 46 (2013) 235107. https://doi.org/10.1088/0022-3727/46/23/235107.

[52] D. Horwat, A. Billard, Effects of substrate position and oxygen gas flow rate on the properties of ZnO: Al films prepared by reactive co-sputtering, Thin Solid Films. 515 (2007) 5444–5448. https://doi.org/10.1016/j.tsf.2006.12.188.

[53] M. Jullien, D. Horwat, F. Manzeh, R. Escobar Galindo, P. Bauer, J.F. Pierson, J.L. Endrino, Influence of the nanoscale structural features on the properties and electronic structure of Al-doped ZnO thin films: An X-ray absorption study, Sol. Energy Mater. Sol. Cells. 95 (2011) 2341–2346. https://doi.org/10.1016/j.solmat.2011.04.003.

[54] S. Edinger, J. Bekacz, M. Richter, R. Hamid, R.A. Wibowo, A. Peić, T. Dimopoulos, Influence of the acetic acid concentration on the growth of zinc oxide thin films prepared by spray pyrolysis of aqueous solutions,

Thin Solid Films. 594 (2015) 238–244. https://doi.org/10.1016/j.tsf.2015.04.027.

[55] Y. Li, Y. Liu, Z. Liu, X. Xie, E.-C. Lee, Improvement of inverted organic solar cells using acetic acid as an additive for ZnO layer processing, AIP Adv. 8 (2018) 025204. https://doi.org/10.1063/1.5018382.

[56] N. Winkler, S. Edinger, W. Kautek, T. Dimopoulos, Mg-doped ZnO films prepared by chemical bath deposition, J. Mater. Sci. 53 (2018) 5159–5171. https://doi.org/10.1007/s10853-017-1959-8.

[57] J.K. Saha, R.N. Bukke, N.N. Mude, J. Jang, Significant improvement of spray pyrolyzed ZnO thin film by precursor optimization for high mobility thin film transistors, Sci. Rep. 10 (2020) 8999. https://doi.org/10.1038/s41598-020-65938-6.

[58] X. Zhang, S. Ma, F. Li, F. Yang, J. Liu, Q. Zhao, Effects of substrate temperature on the growth orientation and optical properties of ZnO:Fe films synthesized via magnetron sputtering, J. Alloys Compd. 574 (2013) 149–154. https://doi.org/10.1016/j.jallcom.2013.04.055.

[59] N. Kalyani, Y.C. Ching, N. Azizi, Structural and optical properties of ZnO thin films obtained by spray pyrolysis, Mater. Res. Innov. 18 (2014) S6-126-S6-130. https://doi.org/10.1179/1432891714Z.0000000001013.

[60] P. Singh, A. Kumar, Deepak, D. Kaur, Growth and characterization of ZnO nanocrystalline thin films and nanopowder via low-cost ultrasonic spray pyrolysis, J. Cryst. Growth. 306 (2007) 303–310. https://doi.org/10.1016/j.jcrysgro.2007.05.023.

[61] T. Prasada Rao, M.C. Santhosh Kumar, A. Safarulla, V. Ganesan, S.R. Barman, C. Sanjeeviraja, Physical properties of ZnO thin films deposited at various substrate temperatures using spray pyrolysis, Phys. B Condens. Matter. 405 (2010) 2226–2231. https://doi.org/10.1016/j.physb.2010.02.016.

[62] S. Jongthammanurak, M. Witana, T. Cheawkul, C. Thanachayanont, The effects of carrier gas and substrate temperature on ZnO films prepared by ultrasonic spray pyrolysis, Mater. Sci. Semicond. Process. 16 (2013) 625–632. https://doi.org/10.1016/j.mssp.2012.11.009.

[63] C. Biswas, Z. Ma, X. Zhu, T. Kawaharamura, K.L. Wang, Atmospheric growth of hybrid ZnO thin films for inverted polymer solar cells, Sol. Energy Mater. Sol. Cells. 157 (2016) 1048–1056. https://doi.org/10.1016/j.solmat.2016.08.022.

[64] H. Mokhtari, M. Benhaliliba, A. Boukhachem, M.S. Aida, Y.S. Ocak, Nanostructured device based on coated ZnO layer as a window in solar cell applications, Mater. Sci. 36 (2018) 570–583. https://doi.org/10.2478/msp-2018-0090.

[65] M. Qu, J. Wu, G. Zhao, Y. Zhang, Nanostructured Surfaces, Coatings, and Films: Fabrication, Characterization, and Application, J. Nanomater. 2013 (2013) 1–2. https://doi.org/10.1155/2013/492646.

[66] N. Kumari, S. Patel, J. Gohel, Optical and structural properties of ZnO thin films prepared by spray pyrolysis for enhanced efficiency perovskite solar cell application, Opt. Quantum Electron. 50 (2018).

[67] R.C. Rai, Analysis of the Urbach tails in absorption spectra of undoped ZnO thin films, J. Appl. Phys. 113 (2013) 153508. https://doi.org/10.1063/1.4801900.

[68] V. Kumar, N. Singh, R.M. Mehra, A. Kapoor, L.P. Purohit, H.C. Swart, Role of film thickness on the properties of ZnO thin films grown by sol-gel method, Thin Solid Films. 539 (2013) 161–165. https://doi.org/10.1016/j.tsf.2013.05.088.

[69] B. Abdallah, A.K. Jazmati, R. Refaai, Oxygen Effect on Structural and Optical Properties of ZnO Thin Films Deposited by RF Magnetron Sputtering, Mater. Res. 20 (2017) 607–612. https://doi.org/10.1590/1980-5373-mr-2016-0478.

[70] V. Kumar, S.K. Singh, H. Sharma, S. Kumar, M.K. Banerjee, A. Vij, Investigation of structural and optical properties of ZnO thin films of different thickness grown by pulsed laser deposition method, Phys. B Condens. Matter. 552 (2019) 221–226. https://doi.org/10.1016/j.physb.2018.10.004.

[71] G. Wisz, I. Virt, P. Sagan, P. Potera, R. Yavorskyi, Structural, Optical and Electrical Properties of Zinc Oxide Layers Produced by Pulsed Laser Deposition Method, Nanoscale Res. Lett. 12 (2017) 253. https://doi.org/10.1186/s11671-017-2033-9.

[72] A.P. Roth, J.B. Webb, D.F. Williams, Absorption edge shift in ZnO thin films at high carrier densities, Solid

State Commun. 39 (1981) 1269–1271. https://doi.org/10.1016/0038-1098(81)90224-6.

[73] M. Othmane, A. Attaf, H. Saidi, F. Bouaichi, N. Lehraki, M. Nouadji, M. Poulain, S. Benramache, Modulation of Physical Properties of Sprayed ZnO Thin Films by Substrate Temperature for Optical Applications, Int. J. Nanosci. 15 (2016) 1650007. https://doi.org/10.1142/S0219581X16500071.

[74] G.-X. Liang, P. Fan, X.-M. Cai, D.-P. Zhang, Z.-H. Zheng, The Influence of Film Thickness on the Transparency and Conductivity of Al-Doped ZnO Thin Films Fabricated by Ion-Beam Sputtering, J. Electron. Mater. 40 (2011) 267–273. https://doi.org/10.1007/s11664-010-1503-y.

[75] D. Mendil, F. Challali, T. Touam, A. Chelouche, A.H. Souici, S. Ouhenia, D. Djouadi, Influence of growth time and substrate type on the microstructure and luminescence properties of ZnO thin films deposited by RF sputtering, J. Lumin. 215 (2019) 116631. https://doi.org/10.1016/j.jlumin.2019.116631.

[76] A. Kołodziejczak-Radzimska, E. Markiewicz, T. Jesionowski, Structural Characterisation of ZnO Particles Obtained by the Emulsion Precipitation Method, J. Nanomater. 2012 (2012) 1–9. https://doi.org/10.1155/2012/656353.

[77] S. Gayathri, O.S.N. Ghosh, S. Sathishkumar, S. Sudhakara, J. Jayaramudu, S.S. Ray, A.K. Viswanath, Investigation of physicochemical properties of Ag doped ZnO nanoparticles prepared by chemical route, (n.d.). http://hdl.handle.net/10204/8553.

[78] D. Balzar, Voigt-function model in diffraction line-broadening analysis, Microstruct. Anal. from Diffraction, Int. Union Crystallogr. 10 (1999) 94–126. https://www.semanticscholar.org/paper/Voight-Function-Model-in-Diffraction-Line-Analysis-Balzar/9d95b352ccb0b65040d436d60ed4e773ca943d13.

[79] W.I.F. David, Powder diffraction: Least-squares and beyond, J. Res. Natl. Inst. Stand. Technol. 109 (2004) 107. https://doi.org/10.6028/jres.109.008.

[80] C.R. Houska, T.M. Smith, Least-squares analysis of x-ray diffraction line shapes with analytic functions, J. Appl. Phys. 52 (1981) 748–754. https://doi.org/10.1063/1.328757.

[81] R. T. Downs, The RRUFF Project: An Integrated Study of the Chemistry, Crystallography, Raman and Infrared Spectroscopy of Minerals, Proceedings of the 19th General Meeting of the International Mineralogical Association, Kobe, 23-28 July 2006, pp. 3-13, (2006).

[82] A. Monshi, M.R. Foroughi, M.R. Monshi, Modified Scherrer Equation to Estimate More Accurately Nano-Crystallite Size Using XRD, World J. Nano Sci. Eng. 02 (2012) 154–160. https://doi.org/10.4236/wjnse.2012.23020.

[83] M.P.F. de Godoy, L.K.S. de Herval, A.A.C. Cotta, Y.J. Onofre, W.A.A. Macedo, ZnO thin films design: the role of precursor molarity in the spray pyrolysis process, J. Mater. Sci. Mater. Electron. 31 (2020) 17269–17280. https://doi.org/10.1007/s10854-020-04281-y.

[84] I. Sugihartono, E. Handoko, V. Fauzia, A. Arkudato, L. Permata Sari, Structural and Photoluminescence Properties of ZnO Thin Films Deposited by Ultrasonic Spray Pyrolysis, Makara J. Technol. 22 (2018) 13. https://doi.org/10.7454/mst.v22i1.3423.

[85] K.L. Foo, M. Kashif, U. Hashim, W.-W. Liu, Effect of different solvents on the structural and optical properties of zinc oxide thin films for optoelectronic applications, Ceram. Int. 40 (2014) 753–761. https://doi.org/10.1016/j.ceramint.2013.06.065.

[86] M. Mosca, R. Macaluso, C. Calì, R. Butté, S. Nicolay, E. Feltin, D. Martin, N. Grandjean, Optical, structural, and morphological characterisation of epitaxial ZnO films grown by pulsed-laser deposition, Thin Solid Films. 539 (2013) 55–59. https://doi.org/10.1016/j.tsf.2013.04.146.

[87] P. Ghosh, A.K. Sharma, Optical Characterization and Growth Mechanism of Combination of Zinc Oxide Nanowires and Nanorods at Various Substrate Temperatures, J. Nanomater. 2013 (2013) 1–9. https://doi.org/10.1155/2013/480164.

[88] C.F. Klingshirn, B.K. Meyer, A. Waag, A. Hoffmann, J. Geurts, Zinc Oxide, Springer Berlin Heidelberg, Berlin, Heidelberg, 2010. https://doi.org/10.1007/978-3-642-10577-7.

[89] M. Gabás, P. Díaz-Carrasco, F. Agulló-Rueda, P. Herrero, A.R. Landa-Cánovas, J.R. Ramos-Barrado, High

quality ZnO and Ga:ZnO thin films grown onto crystalline Si (100) by RF magnetron sputtering, Sol. Energy Mater. Sol. Cells. 95 (2011) 2327–2334. https://doi.org/10.1016/j.solmat.2011.04.001.

[90] C.P. Li, J. Zhang, H.M. Yu, L.Z. Zhang, Raman and Photoluminescence Properties of ZnO Nanorods with Wurtzite Structure, Key Eng. Mater. 538 (2013) 50–53. https://doi.org/10.4028/www.scientific.net/KEM.538.50.

[91] S.B. Zhang, S.H. Wei, A. Zunger, Intrinsic n-type versus p-type doping asymmetry and the defect physics of ZnO, Physical Review B 63 (2001) 075205. https://doi.org/10.1103/PhysRevB.63.075205.

[92] A. Janotti, C.G. Van de Walle, Native point defects in ZnO, Physical Review B 76 (2007) 165202. https://doi.org/10.1103/PhysRevB.76.165202.

[93] S. Edinger, N. Bansal, M. Bauch, R.A. Wibowo, G. Újvári, R. Hamid, G. Trimmel, T. Dimopoulos, Highly transparent and conductive indium-doped zinc oxide films deposited at low substrate temperature by spray pyrolysis from water-based solutions, J. Mater. Sci. 52 (2017) 8591–8602. https://doi.org/10.1007/s10853-017-1084-8.

CHAPTER 4: Zinc Magnesium Oxide as a Buffer Layer: Modulation of Optoelectronic Properties by Mg

4.1 Introduction to Zinc-Magnesium Oxide (ZnMgO)

Zinc-magnesium oxide ($ZnMgO/Zn_{1-x}Mg_xO$) is obtained by incorporating magnesium in zinc oxide (ZnO) to form a broad bandgap semiconductor with wurtzite structure and a higher conduction band energy level than ZnO [1,2]. As detailed in ***Chapter 2***, ZnO can possess three types of crystal structures: zinc blende, wurtzite and rocksalt [3]. MgO can have only a stable rocksalt structure like NaCl with a lattice constant of 4.215 Å. The crystal structure can be described as a face-centred cubic (fcc) lattice of O^{2-} ions with Mg^{2+} ions filling all octahedral positions or vice versa. Because the tetrahedral ionic radius of Mg^{2+} (0.57 Å) is similar to that of Zn^{2+} (0.60 Å), Mg atoms are expected to replace a considerable portion of Zn atoms [4]. The MgO crystal structure is shown in the ***Figure 4.1***. The solubility of Mg in the ZnO wurtzite structure, on the other hand, has been a contentious issue. The solid solution limit of MgO in wurtzite ZnO is less than 4 % at 1800 °C, according to the MgO-ZnO binary system phase diagram described by Segnit and Holland [5], and this limit is further decreased at lower temperatures. Bergstein *et al.* [6] later used ultra-fine MgO source powder to produce a small portion of the (Zn,Mg)O phase diagram to clarify the solubility limit of MgO . The solubility limits for samples sintered at 1500 °C, 1400 °C, and 1200 °C are approximately 18, 17 and 15 atomic %.

Figure 4.1: Rocksalt crystal structure of MgO [7].

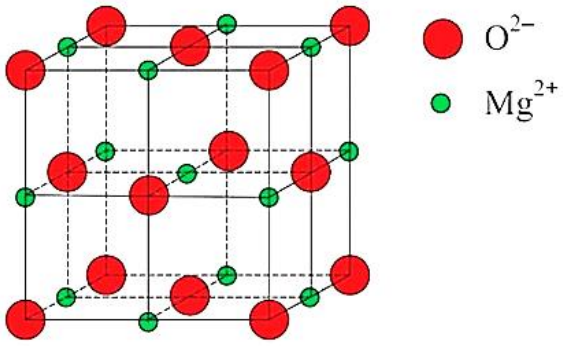

Single-phase wurtzite ZnMgO thin films with Mg concentration greater than 33 atomic% have been reported repeatedly in experiments [8,9]. Using metalorganic vapor-phase epitaxial growth, Park *et al.* [10] increased the Mg content in hexagonal ZnMgO films to 49 atomic% Mg.

Based on experimental data, the crystal structure of ZnMgO may be separated into three zones as a function of Mg concentration, as illustrated in ***Figure 4.2***. Although the specific values of the Mg content boundaries that separate these three zones vary depending on deposition technique and conditions, the overall phase evolution trend from hexagonal to cubic with increasing Mg

concentration remains consistent. When the Mg percentage in the films is less than 35 %, the alloy has a wurtzite structure, but when the Mg content is greater than 50 %, the alloy has a rocksalt structure. Between these two points, a mixed phase zone exists.

Since 1997, thin films of ZnMgO have been formed under vacuum, originally by pulsed-laser deposition onto sapphire substrates at 600 °C [8,9]. Molecular beam epitaxy (MBE) was used to deposit heterojunctions between ZnO and $Zn_{1-x}Mg_xO$, which were then annealed at 1,000°C and showed no Mg diffusion across the interface with $x \leq 0.15$ [11], despite an anticipated solubility limit of $x = 0.04$ [5]. ZnMgO metastable phases allow for an adjustable bandgap between 3.4 and 4.1 eV with a stable solid solution up to $x = 0.4$ [12,13].

ZnMgO depositions by means of aqueous solution has been achieved through ultrasonic spray pyrolysis (USP) [14–16] and sol-gel techniques [17]. Mostly nanoparticle formations [14,17] have been reported but recent works also showed formation of thin films by USP [15,16].

Some research groups tried to deposit ZnMgO at very low temperatures of 50 °C [18] and 70 °C [19]. Miyazaki *et al.* [18] used an aqueous solution consisting of zinc acetate ($Zn(CH_3COO)_2$), magnesium acetate ($Mg(CH_3COO)_2$) and ammonia (NH_3), with a pH of 8-9 to deposit thin films. At this lower tempearuture, they found no evidence of Mg in the ZnO films. Gayen *et al.* [19] were able to produce $Zn_{1-x}Mg_xO$ nanofibers with $0 \leq x \leq 0.2$. They used an aqueous solution of zinc nitrate ($Zn(NO_3)_2$), magnesium nitrate ($Mg(NO_3)_2$) and sodium hydroxide (NaOH), with a pH > 13.

Figure 4.2: The bandgap energy of $Zn_{1-x}Mg_xO$ as a function of Mg concentration is summarized. Ohtomo *et al.* [8] (circle) provided Mg-poor wurtzite structure data; Choopun *et al.* [20] provided Mg-rich rocksalt structure data (triangle and square).

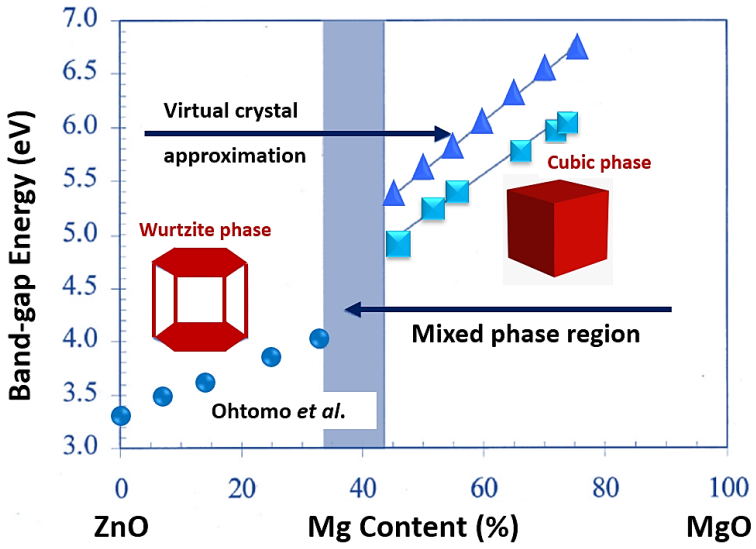

4.2 Understanding the Energy Band Structure of ZnMgO

Many studies have indicated that the relationship between the bandgap and Mg content is nearly linear [8,20,21]. Wenckstern *et al.* [22] compiled experimental values for the basic bandgap energy E_g from the absorption edges from over 30 research articles. They discovered that Vegard's law [23,24], which includes a bowing parameter, can accurately represent the composition evolution of the energy of the basic absorption edge as shown below:

Equation (4.1):

$$\boldsymbol{E_g\ (Zn_{1-x}Mg_xO) = 3.339 + 1.24x + 1.89x^2}\ \text{(For wurtzite phase)}$$

Equation (4.2):

$$\boldsymbol{E_g\ (Zn_{1-x}Mg_xO) = 3.679 + 1.516x + 2.48x^2}\ \text{(For cubic rocksalt phase)}$$

The Bloch theorem, which states that the bond strength determines the band gap, can qualitatively explain this characteristic. A greater bandgap is expected because Mg-O has a stronger bond than Zn-O. The Molecular Orbital Theory can be used to make similar conclusions. Zhang *et al.* [25] investigated the electron exchange correlation in ZnMgO utilizing a first-principles total energy investigation using the generalized gradient approximation (GGA). They concluded that increasing Mg concentration causes bandgap widening in ZnMgO via lowering the Zn 4s states.

The energy difference between the conduction band edge (E_{CB}) and the valence band edge (E_{VB}) of ZnMgO widens as the band gap increases with increasing Mg concentration. The displacement of the band edge relative to the vacuum energy level has been investigated through experiments. To study the relative band alignment between ZnO and ZnMgO, Rao *et al.* [26] used photoelectron spectroscopy to investigate the electronic characteristics of CdS/ZnO and CdS/$Zn_{0.85}Mg_{0.15}O$ interfaces. The valence band edge E_{VB} and vacuum level E_{VAC} of ZnO and $Zn_{0.85}Mg_{0.15}O$ remained unchanged when compared to CdS (shown in ***Figure 4.3***). The variation in band gap between ZnO and $Zn_{0.85}Mg_{0.15}O$ could thus be ascribed entirely to a shift in the conduction band edge ECB. Olson *et al.* [27] measured the work function of ZnMgO films (shown in ***Figure 4.4***) and came to the same conclusion. With increasing Mg concentration from 0 to 25 atomic % of Mg, the absolute value of the work function of ZnMgO decreases. They assumed the Fermi energy of the layers they found was close to E_{CB} since they were n-type semiconductors. However, due to the influence of other parameters such as carrier concentration and surface states, it should be emphasized that the E_{CB} could not be retrieved clearly from work function measurement. Nonetheless, the lower work function supports the general pattern of the conduction band edge moving upward to vacuum as Mg concentration increases.

Figure 4.3: Band alignment at the CdS/ZnO and CdS/$Zn_{0.85}Mg_{0.15}O$ interfaces as determined by Rao *et al.* [26]. All measurements are in eV.

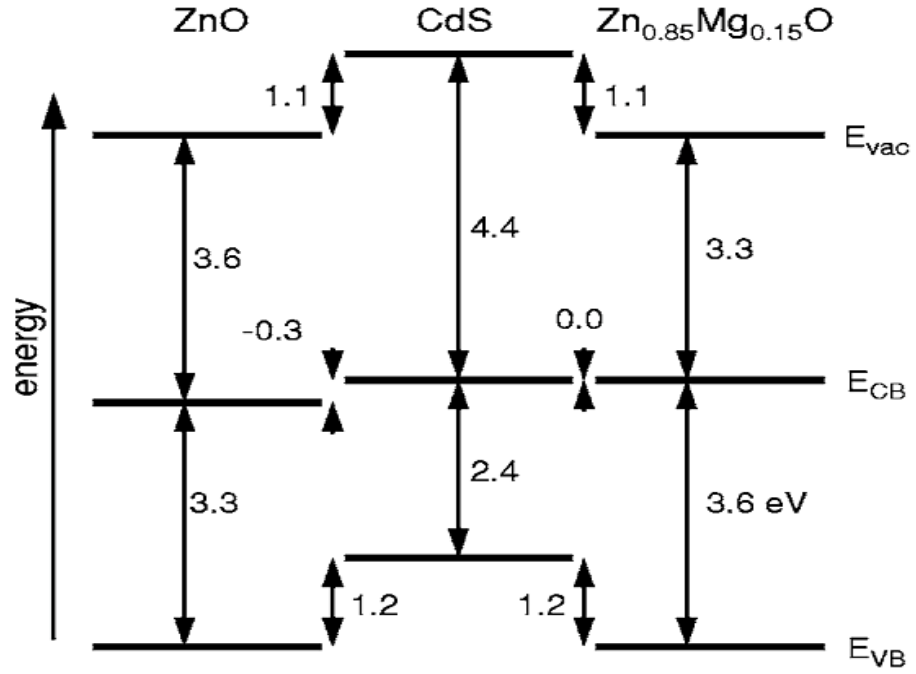

Figure 4.4: Work function versus Mg content for ZnMgO films coated on Indium Tin Oxide (ITO) as measured by Olson *et al.* [27].

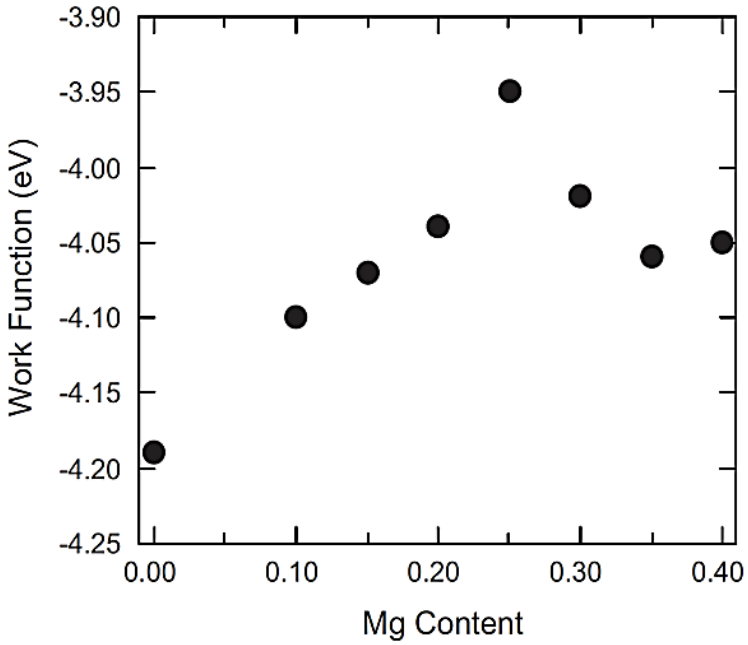

4.3 Properties of ZnMgO

For applications in semiconductor-based devices, the properties of ZnMgO can be classified into three different types: thermal, optical, and electrical.

4.3.1 Thermal Stability

According to the solubility limits, incorporating 30 atomic % Mg in wurtzite-ZnMgO is a metastable state. Because thermal stability is critical for device applications, Ohtomo *et al.* [11] examined the thermal stability of supersaturated $Zn_{1-x}Mg_xO$ thin films and ZnMgO/ZnO bilayers. Laser molecular beam epitaxy (LMBE) was used to deposit the $Zn_{1-x}Mg_xO$ thin films on sapphire at 550 °C. The as-deposited films were annealed at temperatures from 700 °C to 1000 °C. MgO segregation occurred at 850 °C in films with Mg concentration of more than 15 atomic %. However, even at annealing temperatures as high as 1000 °C, films with a Mg concentration of 15 atomic % or less showed no MgO segregation. Furthermore, Mg thermal diffusion across the ZnMgO/ZnO interface was only seen after annealing at temperatures exceeding 700 °C. As a result, Ohtomo *et al.* [11] determined that MgO has a thermodynamic solubility of around 15 atomic % in wurtzite ZnMgO epitaxial films, and ZnO-based alloy films and heterointerfaces are stable enough to fabricate highly crystalline heterostructures at high temperatures.

4.3.2 Optical Properties

ZnMgO has different optical characteristics than ZnO. The reasons are as follows: First, due to a greater bandgap (than ZnO), the absorption in ZnMgO thin films is at a lower wavelength. ZnMgO is thus more UV-transparent than ZnO [8,20,21]. This shift of the absorption edge towards the lower wavelengths in the UV region is due to the Burstein-Moss shift [28]. Second, because the plasma wavelength of ZnMgO shifts to a greater wavelength, it is more IR transparent [29]. This is primarily due to the doping effect and the large effective mass of ZnMgO [30]. Thirdly, as explained by Lu *et al.* [31], in the presence of free carriers, the effective mass of electrons increases with the Mg content. In ZnMgO, this phenomenon has a big impact on electron conduction. With same quantity of free carriers in ZnO and ZnMgO, the bandgap widening effect in ZnO is slightly higher than ZnMgO.

4.3.3 Electrical Properties

The major causes that affect the electrical properties of ZnMgO can be classified into two groups.

The first category is linked to changes in crystal quality (extended defects), while the second is linked to changes in quasi-bulk characteristics due to higher Mg incorporation in the alloy. The first is not intrinsic to ZnMgO and can be addressed by enhancing crystal quality, whereas the second is directly tied to ZnMgO's material qualities.

While it is relatively simple to partially substitute Mg atoms for Zn atoms in the ZnO wurtzite structure to increase the bandgap and elevate the conduction band edge of ZnO [20,21,32], it has been widely discovered that the highest obtained free carrier concentration (n) and mobility (μ) achieved in $Zn_{1-x}Mg_xO$ ($x > 0.2$) rapidly decreases as a function of Mg [29,30,33–36].

There is currently a lack of clarity on the mechanisms that cause the inferior electrical characteristics of wide-bandgap ZnMgO. Various theories based on their observations have been given in previous publications. The decrease in carrier concentration has been attributed to both a decrease of active donors due to composition enrichment [30] and an increase in donor activation energy, which can be induced by either a greater effective mass [30,31,33] or a change in the band structure [37]. Strong alloy disorder scattering [31,34], a larger effective mass [30,33,35], enhanced impurity scattering [30], and/or stronger grain boundary scattering due to fewer carriers have all been proposed as reasons for the reduced mobility with increasing Mg content in ZnMgO. As plausible as several of these theories are, none of them have been thoroughly investigated.

Furthermore, the impact of intrinsic defects such as zinc vacancy (V_{Zn}) on the electrical characteristics of ZnMgO has not been discussed in detail in prior research. Recent studies have found that intrinsic acceptors, particularly V_{Zn} and its complexes, have a significant impact on the electrical characteristics of ZnO [38–41]. However, there is no equivalent explanation about ZnMgO, including if its weaker electrical properties are owing to a stronger compensation.

4.4 Applications of ZnMgO

For solar cells, ZnMgO is mostly used as buffer layers (placed in between the window and the absorber layers). Unintentionally, ZnO is always an n-type material. As a result, ZnO and n-doped equivalents are good choices for p-n junction buffer layers. The conduction band maximum (CBM) of the p-type absorber should be aligned with an ideal n-type buffer layer. The difference in CBM is measured as the band offset. An optimal conduction band-offset (CBO) should be “flat” and not create a “cliff” or “spike” cases and must vary in accordance with the absorber/buffer-layer combination [42]. The possible band-alignments are shown in the ***Figure 4.5***.

Figure 4.5: Possible pn-heterojunction conduction band alignments [42].

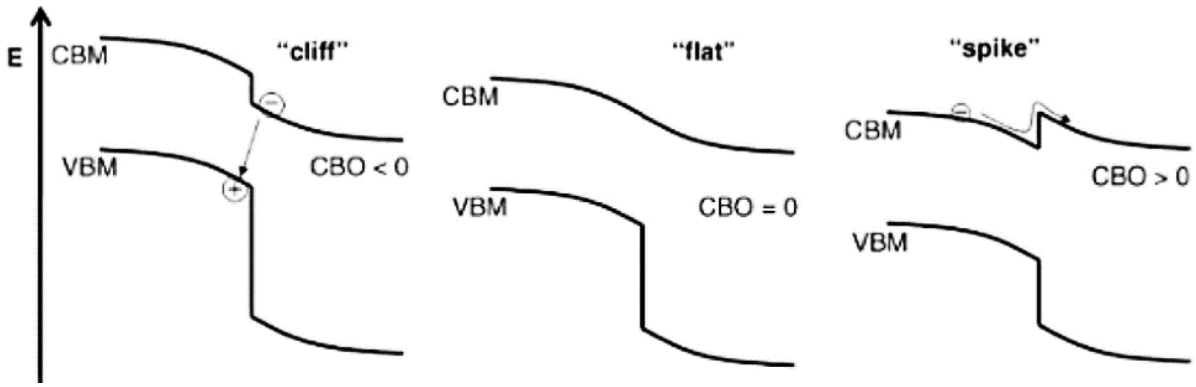

The bandgap of $Zn_{1-x}Mg_xO$ can be tuned in response to the content of Mg added to ZnO and thus making it an interesting candidate for buffer layers in photovoltaic devices.

In thin-film solar cells such as those based on CIGS, CdS which is the usual buffer layer is being replaced due to the cadmium high toxicity and CdS relatively low bandgap of 2.4 eV. The loss of current due to absorption in CdS cannot be avoided and a larger bandgap material like ZnMgO can reduce this loss and thereby increase the cell efficiency. The light-soaking behaviour of the ZnMgO layer is another unseen benefit. With light soaking, the fill factor of cells with CIGS absorber and ZnMgO buffer layer increased [43]. Using a ZnS/ZnMgO buffer layer combination in CIGS solar cells yielded an efficiency of 18 % for solar cells under laboratory conditions while for mini modules the efficiency was 15.2 % [44]. ZnMgO was deposited by RF magnetron sputtering. For ALD deposited ZnMgO, the efficiency of CIGS solar cells reached 16 % [45]. $Zn_{1-x}Mg_xO$ with specific stoichiometries has been used in "all-oxide" solar cells with Cu_2O as the absorber layer. The properties of these solar cells have been discussed in detail in the ***Section 1.3.2*** of ***Chapter 1***.

Beyond the photovoltaic application that interests us in this research work, ZnMgO is also an interesting candidate for ultraviolet (UV) photodetectors. Because of their well-developed technology, silicon photodiodes have dominated the market so far. Because Si's band gap is only 1.1 eV, UV detection takes additional filters to prevent the long-wavelength response. Due to the reflection of these filters, the photoresponsivity is poor. Due to these concerns, the band gap adjustable ZnMgO is being investigated as a possible substitute [46]. ZnMgO can be employed for deep UV detection because its absorption edge is abrupt and can be adjusted to the deep UV region. Fabrication of a metal-semiconductor-metal (MSM) device with a peak responsivity of 270 nm was done by Liu *et al.* [47].

ZnMgO layers can also be used to make thin-film transistors (TFTs). TFTs are utilized in a variety of applications, including liquid crystal displays (LCDs) and organic light-emitting displays (OLEDs). The hexagonal-ZnMgO can be employed as a channel, whereas the cubic-ZnMgO can be used as a gate insulator [48].

Biosensing is another conceivable application for ZnMgO because it is a non-toxic compound. An ion-sensitive ZnO/ZnMgO heterojunction field-effect transistor (HFET) was fabricated by [49] using an amine-modified gate electrode.

Fabricating a laser with a certain wavelength is difficult. Such applications are made possible through band gap engineering. Stimulated emission from ZnMgO alloy nanowires at ambient temperature was reported by [50]. This behaviour can be employed in applications involving light-emitting devices.

4.5 Preparation of ZnMgO by Ultrasonic Spray Pyrolysis

The preparation of ZnMgO films was done using an ExactaCoat system from Sono-Tek. Accumist nozzle operating at 120 kHz. Details about the USP system are given in the ***Section 2.4*** and ***2.5*** of ***Chapter 2*** and in the ***Section 3.4*** of ***Chapter 4***. Zinc acetate dihydrate [$Zn(Ac)_2.2H_2O$] and Magnesium acetate tetrahydrate [$Mg(Ac)_2.4H_2O$] were used as the source precursor salts dissolved in deionized water. For simplicity henceforth, in this thesis we will always refer the salts as $Zn(Ac)_2$ and $Mg(Ac)_2$ only. Always 50 mL of precursor solution was prepared before the start of the spray. Acetic acid was added to the precursor solution to reduce the formation and precipitation of hydroxides.

4.5.1 Chemicals Used and Chemical Reactions Involved for ZnMgO Preparation

All the chemicals used for the preparation of ZnMgO thin films are listed in the ***Table 4.1***.

Table 4.1: Chemicals with high purity used for spray pyrolysis deposition of ZnMgO.

Name	Formula	Supplier
Zinc acetate dihydrate	$Zn(CH_3COO)_2 \cdot 2H_2O$	Merck 108802
Magnesium acetate tetrahydrate	$Mg(CH_3COO)_2 \cdot 4H_2O$	SigmaAldrich M5661
Acetic Acid	CH_3COOH	Alfa Aesar 10994-AE
Deionized water	H_2O	Avantor-VWR

The pH of the precursor solution was regulated using the acetic acid. The pH of the solution can also play a role in the film morphology which can vary from nanorods to compact films. We monitored the pH value in collaboration with other spray parameters to have dense, uniform, and compact films. Generally, the acetic acid can reduce the formation of the volatile Zn and Mg species in the solution, thereby reducing the chances of them further reacting to form respective hydroxides. Further, the acetic acid addition helps to have a lower surface tension of the water-based precursor solution so that during the atomization uniform sized droplets are generated from the spray nozzle. But, when compared to the effect of the Mg concentration in the solution, the effect of acetic acid concentration on the morphology of the spray prepared films is less pronounced.

In our published study [51], as we already pre-heat the substrate to a very high temperature of 470 °C in ambient air conditions and with $Zn(CH_3COO)_2$ and $Mg(CH_3COO)_2$ as the dominating complexes we can write the pyrolytic reaction as:

$$Zn(CH_3COO)_2 + Mg(CH_3COO)_2 + \frac{15}{2}O_2 \xrightarrow{Heat} ZnMgO\ (film) + 8CO_2\ (Gas) + 6H_2O\ (Vapour) \uparrow$$

Adding acetic acid to the precursor solution allows the ionization of zinc acetate and magnesium acetate. Subsequent reactions tentatively facilitate production of zinc and magnesium-based complexes, $ZnCH_3COO^+$ and $MgCH_3COO^+$, thereby preventing the formation of hydroxide complexes. The probable reactions are written below:

$$CH_3COOH \overset{yields}{\longleftrightarrow} CH_3COO^- + H^+$$

$$Zn^{2+} + CH_3COO^- \overset{yields}{\longleftrightarrow} ZnCH_3COO^+$$

$$Mg^{2+} + CH_3COO^- \overset{yields}{\longleftrightarrow} MgCH_3COO^+$$

If some precursor solution droplets are larger than 50 μm in diameter, then there is a possibility that they will not undergo a complete pyrolysis reaction thus forming hydroxides by reacting with the atmospheric water vapour present inside the spray chamber.

The effects of the increase of the $Mg(Ac)_2$ concentration while keeping the $Zn(Ac)_2$ concentration fixed in the precursor solution on the ZnMgO film quality have been discussed later in this chapter. The calculation procedure to select the concentrations of $Zn(Ac)_2$ and $Mg(Ac)_2$ along with the quantities of $Zn(Ac)_2$ and $Mg(Ac)_2$ powder needed is discussed below.

Based on the preparation experience of ZnO, as detailed in the ***Section 3.4.1*** of ***Chapter 3***, we select for $Zn(Ac)_2$ always a concentration of 0.05 mol/L. The chemical protocol for preparation of ZnMgO is based on 3 types of solutions: Solution 1 (S1), Solution 2 (S2) and solution 3 (S3). The final alloy of ZnMgO film will be of the stoichiometry $Zn_{1-x}Mg_xO$, with *x* being the Mg content in mol%.

The solution S1 of 100 mL is only a solution of $Zn(Ac)_2$ which is dissolved only in deionized water. The quantity of $Zn(Ac)_2$ powder needed is given by the equation below:

Equation (4.3):

$$m_{Zn(Ac)_2} = C \times V \times M$$

Where, m is the mass (in g) of $Zn(Ac)_2$ powder; C is the $Zn(Ac)_2$ solution concentration in mol/L; V is the solution volume in litres (L) and M is the molar mass of $Zn(Ac)_2$ (in g/mol).

So, $m_{Zn(Ac)_2}$ = 0.05 (mol/L) × 0.1 (L) × 219.49 (g/mol) = 1.09 g ≈ 1.1 g.

The solution S2 of 100 mL is a solution of both $Zn(Ac)_2$ and $Mg(Ac)_2$. Both the precursor salts are dissolved only in deionized water. The mass of $Zn(Ac)_2$ remains the same as in S1, 1.1 g. Initially, we choose x = 0.3, corresponding to Mg doping of 30 mol%. This value is taken as a base or reference for preparing solutions with other Mg doping mol%. The value corresponding to 30 mol% is selected after an extensive literature survey about the best values Mg concentrations required for ultrasonic spray pyrolysis process for preparation of ZnMgO films and keeping in mind the low solubility limit of $Mg(Ac)_2$ in only water-based solutions. The concentration for 30 % Mg doping with a corresponding constant concentration of $Zn(Ac)_2$ is given by:

Equation (4.4):

$$C_{Mg(Ac)_2} = \left(\frac{x}{1-x}\right) \times C_{Zn(Ac)_2}$$

So, for x =0.3:

$$C_{Mg(Ac)_2} = \left(\frac{0.3}{1-0.3}\right) \times 0.05 = 0.0214 \text{ mol/L}$$

Therefore, the quantity of $Mg(Ac)_2$ powder needed corresponding to the concentration of 0.0214 mol/L is given by the equation below:

Equation (4.5):

$$m_{Mg(Ac)_2} = C \times V \times M$$

Where, m is the mass (in g) of $Mg(Ac)_2$ powder; C is the desired concentration of $Mg(Ac)_2$ in mol/L;

V is the solution volume in litres (L) and M is the molar mass of $Mg(Ac)_2$ (in g/mol).

So, $m_{Mg(Ac)_2}$ = 0.0214 (mol/L) × 0.1 (L) × 214.45 (g/mol) = 0.4589 g ≈ 0.46 g.

Finally, the 100 mL solution S2 consists of 1.1 g of $Zn(Ac)_2$ and 0.46 g of $Mg(Ac)_2$ dissolved completely in deionized water.

Now let us assume that $C_{Mg(Ac)2}$ = 0.0214 mol/L is the initial concentration. Using the ***Equation 4.5***, we can calculate the different values of concentration corresponding to different Mg content %. The values are shown in the ***Table 4.2***.

Table 4.2: Calculation for different concentrations of $Mg(Ac)_2$.

Mg content values (mol%)	$C_{Zn(Ac)2}$ (mol/L)	$C_{Mg(Ac)2}$ (mol/L)
0	0.05	0.0000
3	0.05	0.0015
5	0.05	0.0026
7	0.05	0.0037
10	0.05	0.0056
13	0.05	0.0074
15	0.05	0.0088
20	0.05	0.0125
25	0.05	0.0167
30	0.05	0.0214
50	0.05	0.0500
70	0.05	0.1167

Now, we need to prepare the solution S_3. It should be noted that S_3 will be the final solution that will be used for the actual preparation. For preparing the solution S_3, we need to mix different proportions of S_1 and S_2. Basically we, will collect a certain volume of S_2 based on the desired Mg content % value and we will dilute it by adding S_1. The final volume "V_3" of S_3 will be 50 mL. Volume of S_1 needed is "V_1". The volume "V_2" of S_2 to be collected is given by:

Equation (4.6):

$$V_2 = \frac{Desired\ Mg(Ac)_2\ concentration}{Initial\ Mg(Ac)_2\ concentration} \times V_3$$

The different volumes of V1 and V2 are given in the ***Table 4.3***.

Table 4.3: Calculation for volumes of S_1 and S_2 to prepare the final precursor solution S_3.

Mg content values (mol%)	$C_{Mg(Ac)2}$ (mol/L)	Final stoichiometry of ZnMgO	Volume V_2 of S_2 (mL)	Volume V_1 of S_1 (mL)
0	0.0000	ZnO	0	50
3	0.0015	$Zn_{0.97}Mg_{0.03}O$	3.6	46.4
5	0.0026	$Zn_{0.95}Mg_{0.05}O$	6.074	43.926
7	0.0037	$Zn_{0.93}Mg_{0.07}O$	8.65	41.35
10	0.0056	$Zn_{0.90}Mg_{0.10}O$	13.084	36.916
13	0.0074	$Zn_{0.87}Mg_{0.13}O$	17.29	32.71
15	0.0088	$Zn_{0.85}Mg_{0.15}O$	20.560	29.44
20	0.0125	$Zn_{0.80}Mg_{0.20}O$	29.205	20.795
25	0.0167	$Zn_{0.75}Mg_{0.25}O$	39.019	10.981
30	0.0214	$Zn_{0.70}Mg_{0.30}O$	50	0

For Mg doping beyond 30 %, the dominant salt in the precursor solution is $Mg(Ac)_2$. The concentration values of $Mg(Ac)_2$ for 50 % and 70 % doping are shown in the ***Table 4.2***. Final precursor solutions of volume 50 mL each prepared separately for the preparations of Mg 50 % and 70 % are named as S4 and S5 respectively. The quantities of $Zn(Ac)_2$ and $Mg(Ac)_2$ powders are calculated using the ***Equations (4.3 & 4.5)*** respectively and shown in the ***Table 4.4***.

Table 4.4: Calculation for quantities of $Zn(Ac)_2$ and $Mg(Ac)_2$ powders needed to prepare precursor solutions S_4 and S_5.

Mg content values (mol%)	$C_{Mg(Ac)2}$ (mol/L)	Final stoichiometry of ZnMgO	Precursor solution	Mass of $Mg(Ac)_2$ (g)	Mass of $Zn(Ac)_2$ (g)
50	0.0500	$Zn_{0.50}Mg_{0.50}O$	S4	0.536	0.55
70	0.1167	$Zn_{0.30}Mg_{0.70}O$	S5	1.251	0.55

Based on the experimental details mentioned in the ***Chapter 2*** we have added acetic acid to each of the precursor solution and maintained a value of pH of 4. Having the same pH for all the solutions helps to analyze the films better. The other advantages of acetic acid are mentioned in the beginning of this section. The volume percentages of acetic acid in all the precursor solutions are mentioned in the ***Table 4.5***.

Table 4.5: Volume percentage of acetic acid in the precursor solutions**.**

Magnesium composition in the precursor solution (mol%)	**Magnesium acetate concentration in the precursor solution (mol/L)**	**Film stoichiometry**	**Acetic acid volume (%)**
0	0.0000	ZnO	0.80
3	0.0015	$Zn_{0.97}Mg_{0.03}O$	1.00
5	0.0026	$Zn_{0.95}Mg_{0.05}O$	1.30
7	0.0037	$Zn_{0.93}Mg_{0.07}O$	1.06
10	0.0056	$Zn_{0.90}Mg_{0.10}O$	0.80
13	0.0074	$Zn_{0.87}Mg_{0.13}O$	0.68
15	0.0088	$Zn_{0.85}Mg_{0.15}O$	1.20
20	0.0125	$Zn_{0.80}Mg_{0.20}O$	1.04
25	0.0167	$Zn_{0.75}Mg_{0.25}O$	0.80
30	0.0214	$Zn_{0.70}Mg_{0.30}O$	1.04
50	0.0500	$Zn_{0.50}Mg_{0.50}O$	0.80
70	0.1167	$Zn_{0.30}Mg_{0.70}O$	0.76

4.5.2 Design of Experiment

Many parameters are involved in the spray pyrolysis preparation process for depositing high-quality thin films. Variation in each parameter impacts the resulting film quality. This is the reason to set up the design of experiments, so that we can understand and analyze the nature and degree of impact of the parameters towards the prepared film quality. Using a precise design of experiment, a thorough investigation of the morphological, structural, and optical properties was carried out to identify the set of parameters that result in smooth, dense, wurtzite single phase, and highly transparent $Zn_{1-x}Mg_xO$ thin films. The nozzle speed and the spray flow rates were pre-fixed to 70 mm/sec and 0.5 mL/min based on the safety requirements of the spray system.

The list below shows the variation of other spray parameters along with range of their variation.

1. The zinc acetate [$Zn(Ac)_2$] molar concentration in the precursor solution varied in the range from 0.03 mol/L to 0.10 mol/L.

2. The number of spray cycles, which ranged from 10 to 100. The duration of each preparation is determined by this parameter.

3. The dwell times between each spray cycle varied between 0.5 s to 2 s.

4. The set temperature was varied between 400 °C to 480 °C.

5. The relative shaping air pressure was varied between 6.8 kPa to 20.6 kPa.

6. The height between nozzle to substrate was varied between 90 mm to 110 mm.

When one spray parameter was varied, all the other parameter remained fixed to a particular value. This helped in understanding the effect of the variation of the parameter on the film's quality. The repeatability of the ultrasonic spray pyrolysis method was constantly monitored by preparing each sample at least three times with the parameters listed above. For better understanding, the design of experiment to select the optimal ultrasonic spray pyrolysis parameters is shown below in the ***Table 4.6***.

Table 4.6: Design of experiment to select the optimal spray parameters for ZnO preparation**.**

Preparation Parameter	**Range**	**Optimal value selected after experiments**
$Zn(Ac)_2$ molar concentration	[0.03 mol/L ; 0.1 mol/L]	0.05 mol/L
Number of spray cycles	[10 ; 100]	20
Dwell times between each spray cycle	[0.5 s ; 2 s]	0.5 s
Set temperature	[400 °C ; 480 °C]	470 °C
Relative shaping air pressure	[6.8 kPa ; 20.6 kPa]	14.8 kPa
Height between nozzle to substrate	[90 mm ; 110 mm]	100 mm

4.6 Results and Discussions on the Preparation of ZnMgO

The optimal value of the spray parameters from the design of experiments scheme mentioned above has been used for the preparation of ZnMgO thin films. Various characterization techniques were used to understand the effect of the Mg incorporation (from 0 to 70 mol%) in the precursor solution on the quality of the prepared ZnMgO thin films.

4.6.1 Chemical and Structural Properties of the ZnMgO Thin Films

In the first step of the analysis of the thin films, we try to understand the miscibility limit of the magnesium incorporation. As mentioned before, the magnesium composition in the precursor solution is varied from 0 to 70 molar %. With X-ray fluorescence (XRF) analysis the solid composition in the prepared films can be analyzed. At a scale of 50 µm, these measurements revealed no substantial fluctuation on the sample surface, indicating a uniform composition in the film. Furthermore, the measured values of the films prepared under the identical conditions showed no significant variance.

There are two regimes in the variation of solid composition with solution molar composition. A linear variation is observed for molar compositions less than 30 mol%, with Mg incorporation efficiency in the solid film of roughly 80 %. The loss of magnesium can be explained by the fact that the magnesium precursor is less dense (1.454 g/cm^3 versus 1.735 g/cm^3) and more volatile than the zinc precursor, as seen in [15]. As a result, a fraction of the magnesium does not assist to the pyrolysis reaction that allows the ZnMgO solid film to develop. The variation of the magnesium molar composition in the solid films with reference to the molar composition in the solution is shown in the ***Figure 4.6*** and the values are shown in the ***Table 4.7***.

Figure 4.6: Relation between the magnesium composition in $Zn_{1-x}Mg_xO$ solid films and the magnesium composition in the precursor solution. The dotted line depicts the extrapolated linear fit from the first region (with single-phase $Zn_{1-x}Mg_xO$) to illustrate the phase separation impact for compositions below 30 mol%.

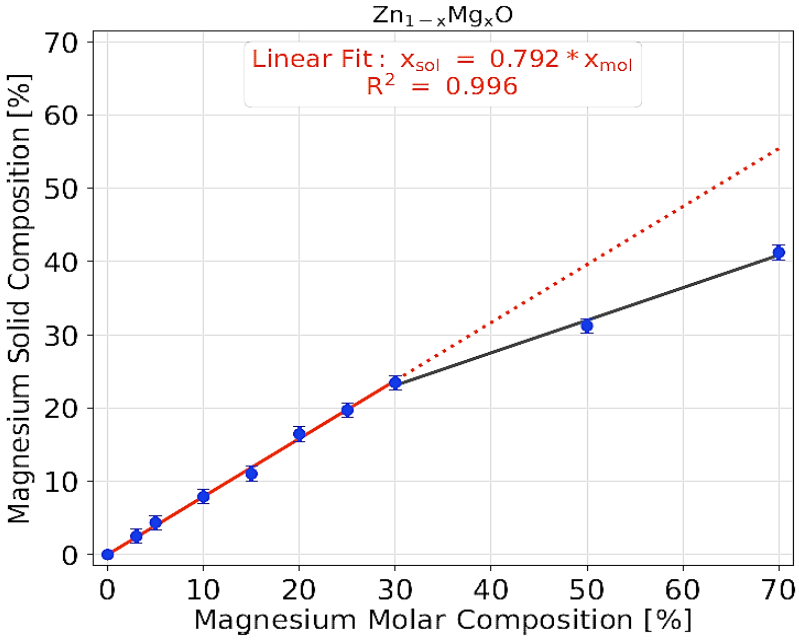

Table 4.7: Calibrated X-ray fluorescence system used to determine the magnesium molar composition in the precursor solution (mol%) and the corresponding composition in the $Zn_{1-x}Mg_xO$ solid films (sol%).

Magnesium composition in the precursor solution (mol%)	Magnesium acetate concentration in the precursor solution (mol/L)	Magnesium composition in the solid film (sol%)
0	0.0000	0.00
3	0.0015	2.52
5	0.0026	4.36
7	0.0037	5.56
10	0.0056	7.91
13	0.0074	10.32
15	0.0088	11.02
20	0.0125	16.46
25	0.0167	19.85
30	0.0214	23.82
50	0.0500	31.22
70	0.1167	41.23

To complete the findings from the XRF measurements, X-ray diffraction (XRD) measurements were done on the $Zn_{1-x}Mg_xO$ solid films. The diffractograms are shown in the ***Figure 4.7***.

Figure 4.7: XRD diffraction patterns for $Zn_{1-x}Mg_xO$ solid films with respect to the magnesium molar composition.

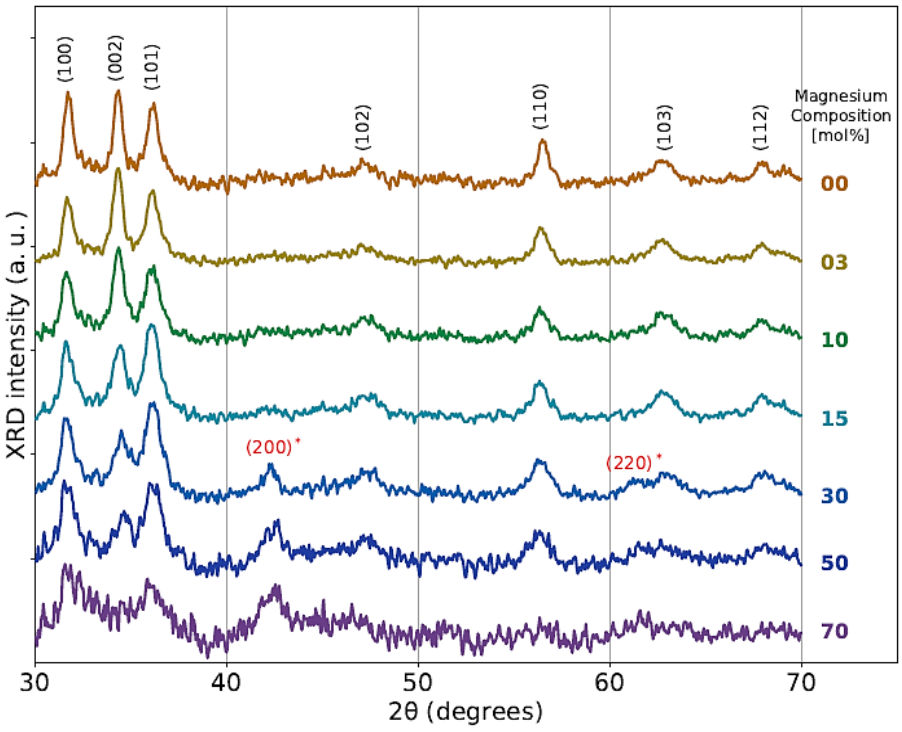

The $Zn_{1-x}Mg_xO$ thin films exhibit a single hexagonal wurtzite crystal structure with peaks for the (100), (002), (101), (102), (110), (103) and (112) planes of the space group $P6_3mc$, identified by using the ZnO powder diffractogram (RRUFF ID: R060027.1) [52] as a reference for magnesium compositions less than 30 mol%. The MgO cubic phase (periclase) emerges for magnesium compositions ranging from 30 to 70 mol%, with defined peaks for the (200) and (220) planes, allocated using the standard JCPDS card (No: 78-0430), showing the development of several phases (hexagonal and cubic). Due to the increased disorder and phase segregation in the $Zn_{1-x}Mg_xO$ thin films, the crystallite size for the wurtzite phase decreases approximately linearly from 28 nm down to 12 nm when the magnesium composition increases from 0 mol % up to 70 mol %, as determined using the procedure presented in the ***Sections 2.7.3.1 & 3.5.5*** of ***Chapters 2 & 3*** respectively.

From the XRF and the XRD measurements it can be confirmed that, the phase segregation in the films happens from Mg composition of 30 mol%. This value of 30 mol% of Mg from which phase segregation occurs is one of the highest ones, when compared to other literatures, where $Zn_{1-x}Mg_xO$ thin films are prepared using ultrasonic spray pyrolysis [15,16,53] or by sol-gel techniques [54]. This value achieved in our work is much higher when it is compared to other solution-based preparation technique such as chemical bath deposition (CBD) as the segregation happens in this process below 5 mol% of Mg [15].

The incorporation of Mg into ZnO to form compact and homogeneous films is presumably facilitated in our process by a combination of the constant pH of 4, which reduces the surface tension of the precursor solution [15,16,55], the higher preparation temperature, which aids the formation of thin compact films, and the lower number of spray cycles with the fast deposition rate. These findings show that the solid solubility limit of Mg in ZnO, and therefore the increase in Mg incorporation efficiency, is substantially influenced by a combination of solution qualities and preparation factors that favour a complete pyrolysis reaction.

To confirm the wurtzite phase of the $Zn_{1-x}Mg_xO$ thin films, all the films from Mg molar composition 0 % to 30 %, were analyzed using Raman line-scan measurements. The scans were performed using a step of 1 µm. The scans revealed no substantial spatial variation, indicating the prepared thin films' homogeneity at this scale of 1 µm, as demonstrated by the XRF measurements at a larger scale of 50 µm. The Raman modes of ZnO and $Zn_{1-x}Mg_xO$ anticipated for the wurtzite structure (C_{6v} symmetry) are classified using the irreducible representation $A_1+2B_1+E_1+2E_2$, with four Raman active modes: one A1, one doubly degenerate E_1, and two doubly degenerate E_2. Both the B_1 branches are IR and Raman inactive. The E_2^{High} and E_2^{Low} mode peaks were systematically observed for all samples with

magnesium content less than 30 mol%, and no other mode related to a different phase was detected. This demonstrates the single-phase wurtzite structure of the prepared $Zn_{1-x}Mg_xO$ films as already evidenced from the XRD and XRF measurements. The Raman spectrum corresponding to all the $Zn_{1-x}Mg_xO$ thin films prepared on soda lime glass (SLG) substrates are shown in the ***Figure 4.8***.

Figure 4.8: Raman spectra for $Zn_{1-x}Mg_xO$ thin films with different Mg composition. The Raman spectra of the soda-lime glass substrate is also presented as a reference for appropriately assigning the deposited $Zn_{1-x}Mg_xO$ Raman peaks.

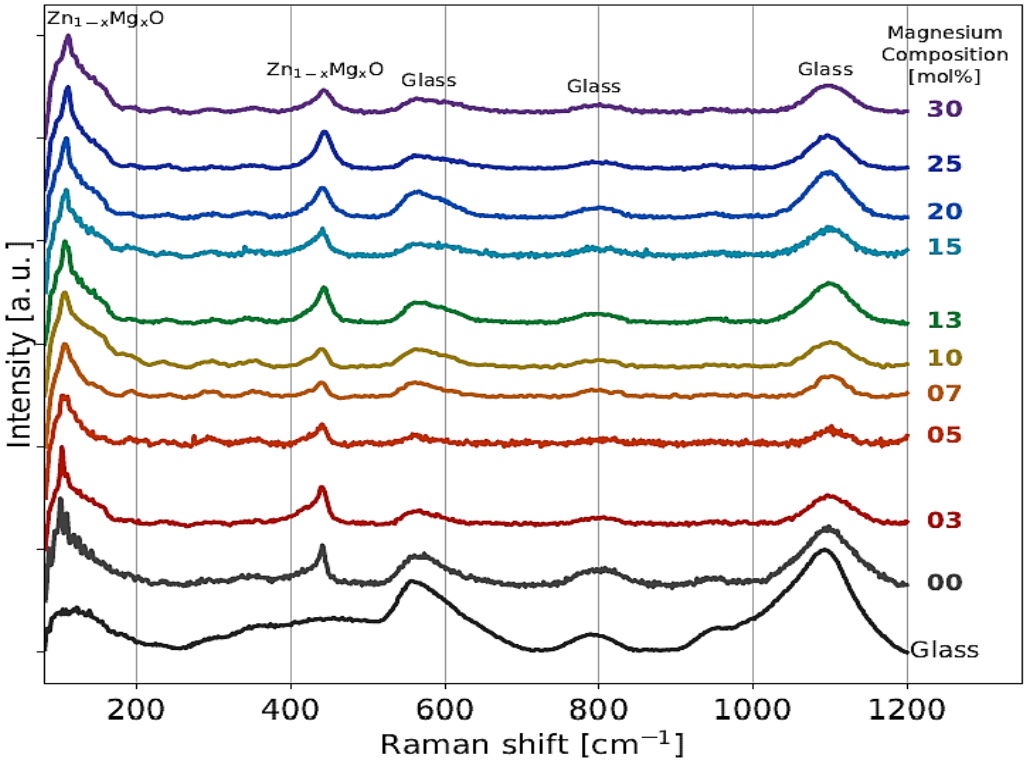

With a Raman shift of 110 cm^{-1} and 439 cm^{-1}, the E_2^{Low} and E_2^{High} peaks of the $Zn_{1-x}Mg_xO$ wurtzite structure are found. The Raman spectrum for the SLG substrate shows two large peaks at 550 cm^{-1} and 1100 cm^{-1} which could be erroneously assigned as the A_1^{LO} and $2A_1^{LO}$ modes for ZnO based compounds prepared on SLG substrates. The width and relative intensity of E_2^{Low} and E_2^{High} peaks are almost constant with respect to the Mg composition, considering the resolution of about 1 cm^{-1}. Due to phase separation, from Mg 30 mol% and at even higher compositions, as evidenced from the XRD diffractograms, the films consist of a mixture of $Zn_{1-x}Mg_xO$ wurtzite and MgO cubic crystal phases. The Raman spectra for these higher Mg composition films (not shown in the ***Figure 4.8***) shows that the E_2^{Low} and E_2^{High} peaks exhibit a substantial decline in intensity and in broadening and become nearly invisible and are almost like the SLG substrate spectra.

4.6.2 Morphological Properties of the ZnMgO Thin Films

The evolution of the surface morphology of $Zn_{1-x}Mg_xO$ thin films as a function of magnesium composition was investigated with the help of atomic force microscopy (AFM). The measurements were done in the non-contact mode with an oscillation frequency of 336 kHz with a scan rate of 0.74 Hz. ***Figure 4.9*** displays AFM images with a 5×5 µm scan area and magnesium compositions ranging from 0 to 70 mol%.

Figure 4.9: AFM images of $Zn_{1-x}Mg_xO$ thin films with Mg molar compositions. 5 µm × 5 µm is the scan area. To better display the morphology and avoid saturating the images, the vertical scale has been changed differently for the images.

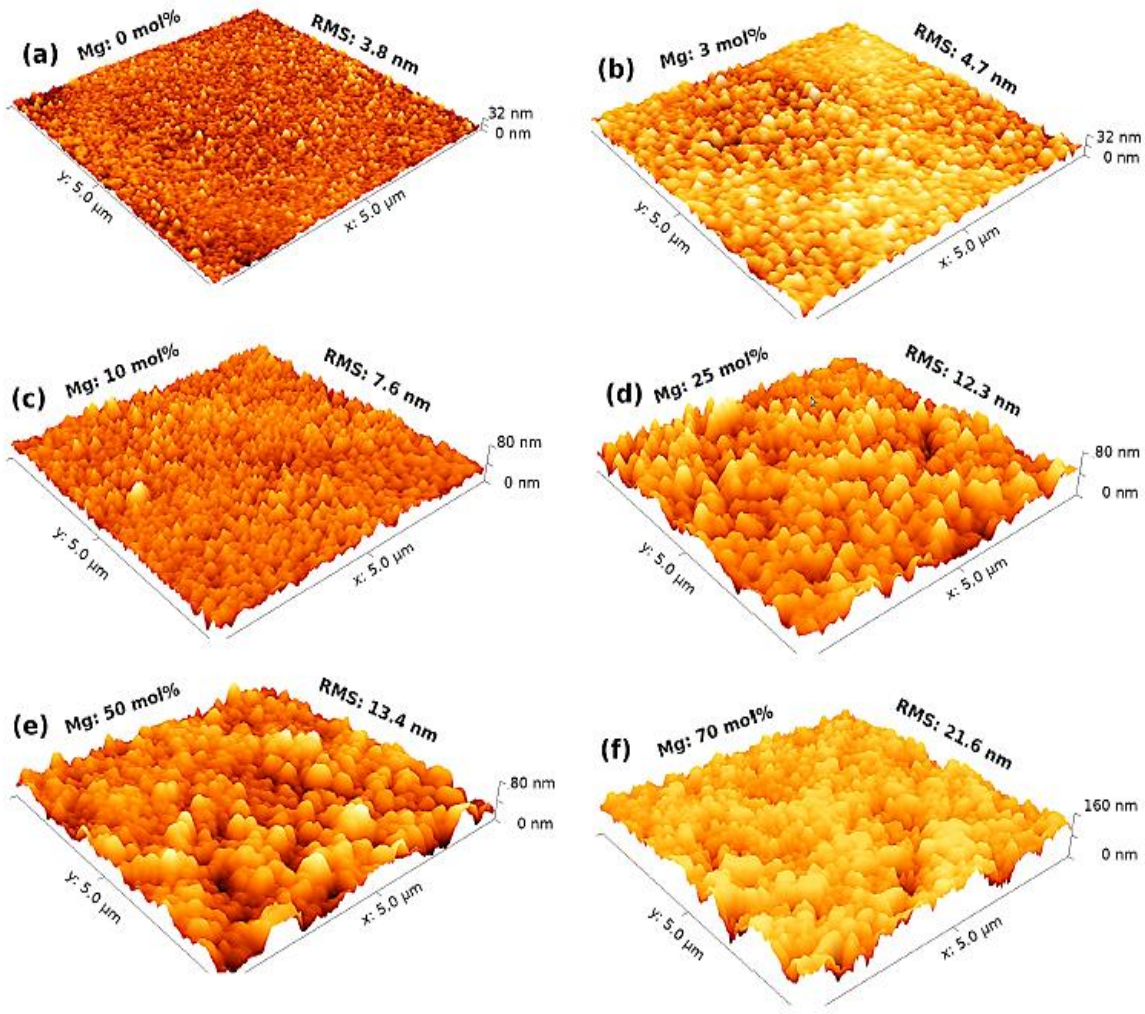

For magnesium compositions ranging from 0 to 70 mol%, the surface root mean square (RMS) roughness varies from around 3.8 nm to 21.6 nm. As indicated by XRD and XRF measurements, this variance is mostly due to two factors: first, alloy disorder in the $Zn_{1-x}Mg_xO$ material, and secondly, the phase separation that occurs for high magnesium composition (from 30 mol%). The maximum

RMS value of nearly 22 nm is consistent with values reported in the literature for $Zn_{1-x}Mg_xO$ films prepared on SLG substrates by sputtering [56] or by spray pyrolysis processes [24].

To support the results from AFM analysis, SEM micrographs were also captured for the $Zn_{1-x}Mg_xO$ films. The SEM micrographs are shown in the ***Figure 4.10*** and reveal polycrystalline nature of the films with no porosity. The surfaces are smooth when the magnesium content is low. With the incorporation of magnesium, the roughness of the surfaces increases with some grain facets becoming more prominent. This is also seen in the AFM images. At the higher magnesium content, the uniform morphology and grain distribution is completely lost. This change in the surface morphologies with the very high magnesium contact (above 30 mol%) can be attributed to the change of phase as also seen in the X-ray diffractograms.

Figure 4.10: SEM micrographs of $Zn_{1-x}Mg_xO$ thin films with Mg molar compositions of **(a)** 0 mol%; **(b)** 3 mol%; **(c)** 5 mol%; **(d)** 10 mol%; **(e)** 15 mol%; **(f)** 25 mol%; **(g)** 30 mol%; **(h)** 50 mol% and **(i)** 70 mol%.

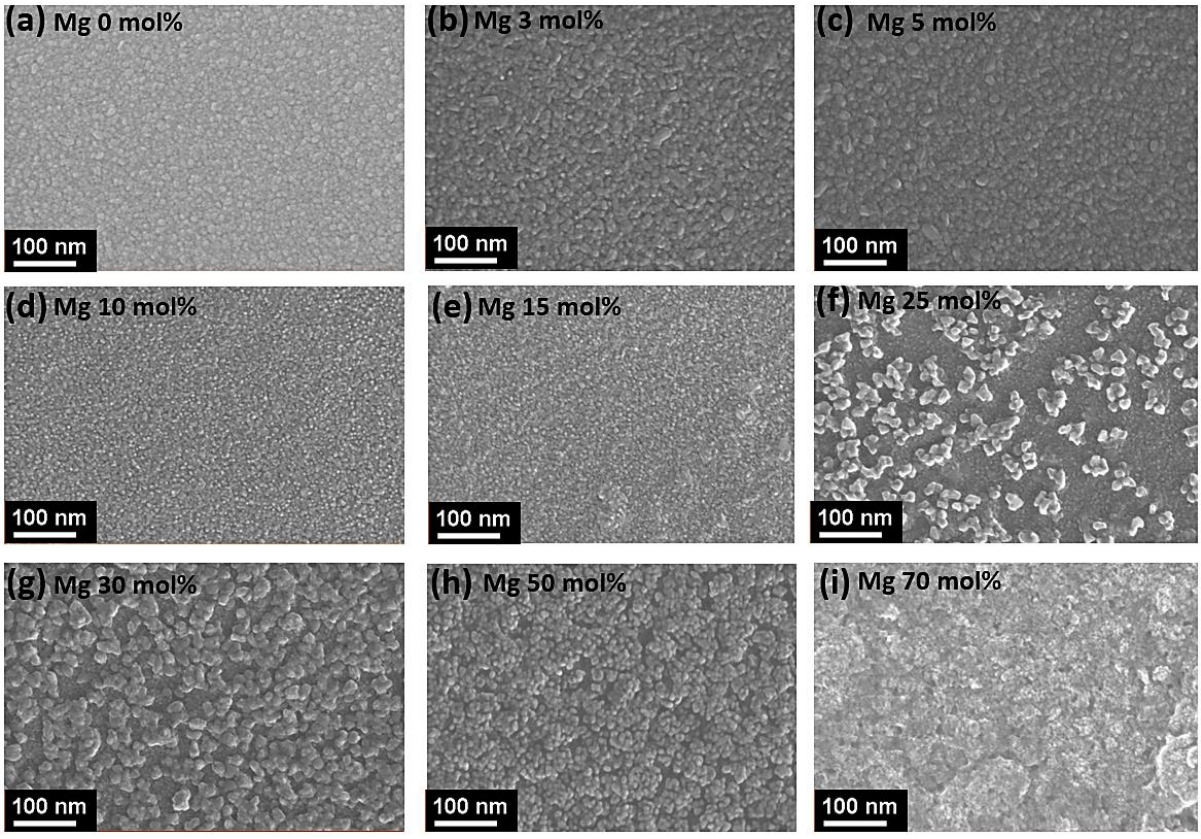

4.6.3 Optical Properties of the ZnMgO Thin Films

To investigate the optical characteristics of the $Zn_{1-x}Mg_xO$ thin films, the transmission of the films was assessed in relation to the magnesium incorporation effect. Also, the bandgap and Urbach energies of the films were studied in response to the increase of the Mg content. The thickness of the prepared films was systematically measured at three sites of the spray zone by a mechanical DekTak profilometer and then averaged. To verify the consistency of the films, the measurements were repeated three times by an optical profilometer at the spray zone of the films. Both the profilometers have a vertical resolution of 0.1 nm and the thickness measurements of the films were found to be very consistent with narrow range of differences ($\pm$ 10 nm). The transparency of all the $Zn_{1-x}Mg_xO$ thin films prepared with 20 spray cycles along with the average thickness measured in the spray zone are shown in the ***Table 4.8***.

As seen from the ***Table 4.8***, there was no discernible loss in transparency as the Mg content increased. This is also confirmed by the Raman studies, which show that increasing magnesium composition has no significant effect on film crystalline quality. The transmission spectra of the films are shown in the ***Figure 4.13***. All the films exhibit high transparencies, but exceptionally high transparencies noted for the films prepared with Mg 30 % and higher. This can be explained by the phase change and the dominance of the MgO phase which typically exhibits much higher bandgap energies than wurtzite ZnO.

Table 4.8: Transmission and thickness estimations of the $Zn_{1-x}Mg_xO$ solid films with respect to the increase of Mg molar composition (mol%).

Magnesium composition in the precursor solution (mol%)	**Average Transmission (%) in the wavelength range 450 nm to 850 nm**	**$Zn_{1-x}Mg_xO$ film thickness [nm; $\pm$10 nm]**
0	93.0	180
3	94.0	175
5	90.0	200
7	92.5	185
10	90.5	185
13	93.7	180
15	91.3	160
20	92.7	210
25	92.5	250
30	95.2	220
50	97.1	185
70	97.6	160

Figure 4.11: Transmission spectra of $Zn_{1-x}Mg_xO$ thin films as a function of magnesium molar composition. The spectrum of the SLG substrate is also shown, with nearly constant transmission at 100 %. A zoom in the absorption edge spectral region is shown in the inset plot.

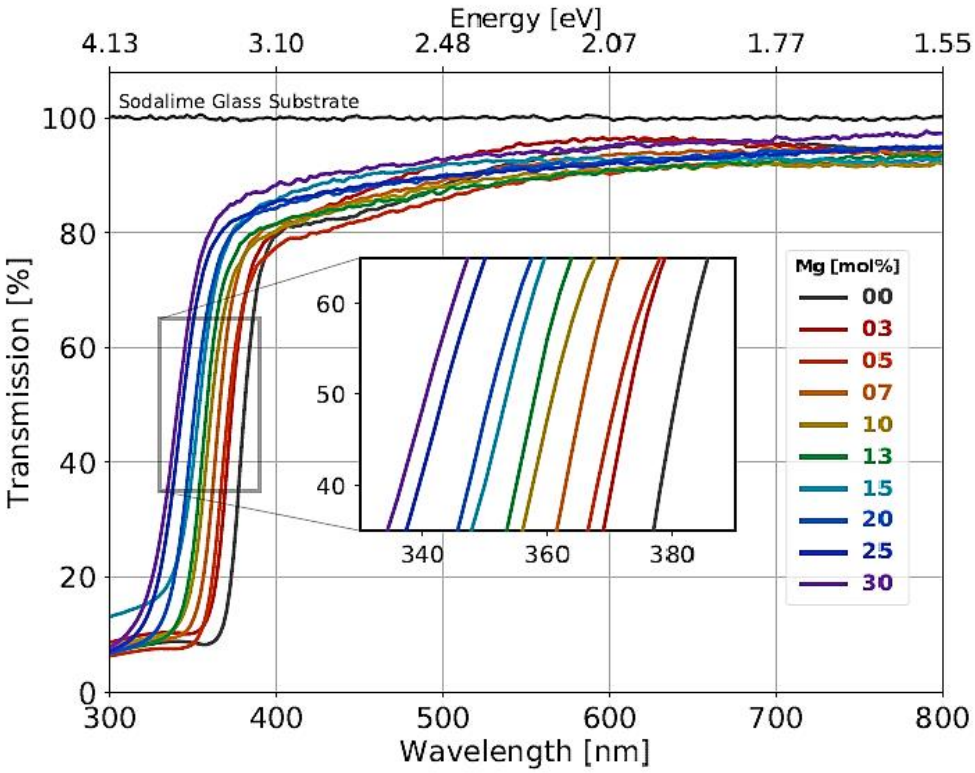

From the ***Figure 4.11***, it is evident that with the increase of the magnesium molar composition, the absorption edge of $Zn_{1-x}Mg_xO$ thin films monotonically shifts toward higher energies. The bandgap energies are estimated by applying the Tauc model as shown in the ***Figure 4.12***. The variation of the bandgap energies with respect to the magnesium molar composition is shown in the ***Figure 4.13***.

It is observed from the ***Figure 4.13***, that the variation of the bandgap energies as a function of increasing magnesium molar composition is almost linear. For a pure ZnO, the bandgap value is 3.265 eV while for the $Zn_{0.70}Mg_{0.30}O$ film (with Mg mol 30 %) the value increases to 3.656 eV. With no considerable bowing, this linear variation is identical to that obtained for $Zn_{1-x}Mg_xO$ thin films developed via sputtering [47,57]. This linear trend is compatible with XRF, XRD and the Raman studies, all of which confirms that a single-phase wurtzite structure is formed when the films are prepared with Mg molar compositions below 30 %.

Figure 4.12: Estimation of the bandgap energies of $Zn_{1-x}Mg_xO$ thin films as a function of magnesium molar composition using the Tauc plot.

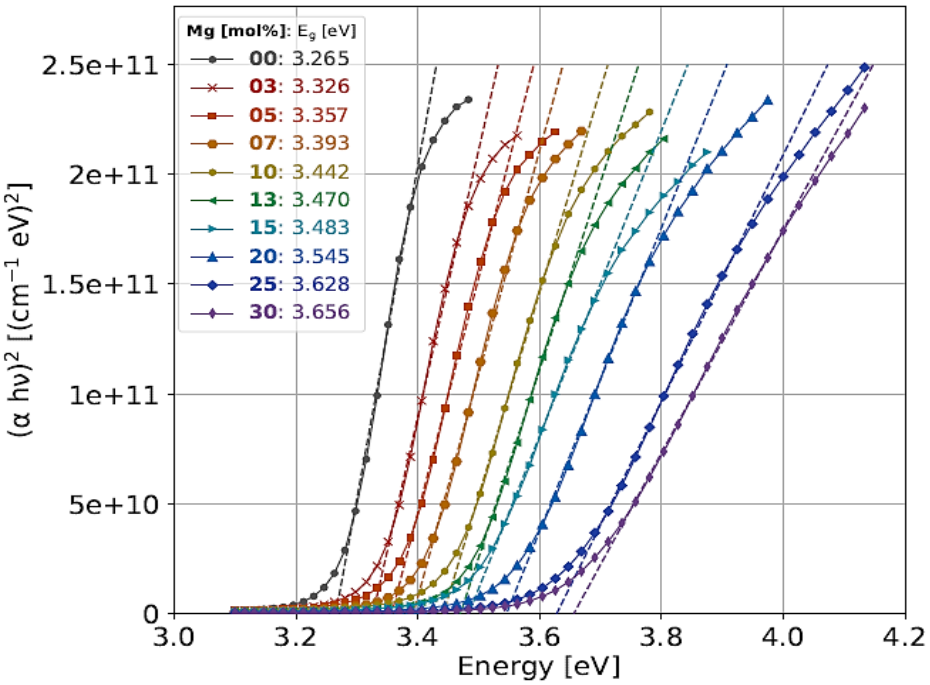

Figure 4.13: Variation of the bandgap energies of $Zn_{1-x}Mg_xO$ thin films as a function of magnesium molar composition. The bandgap energies were extracted using the Tauc model.

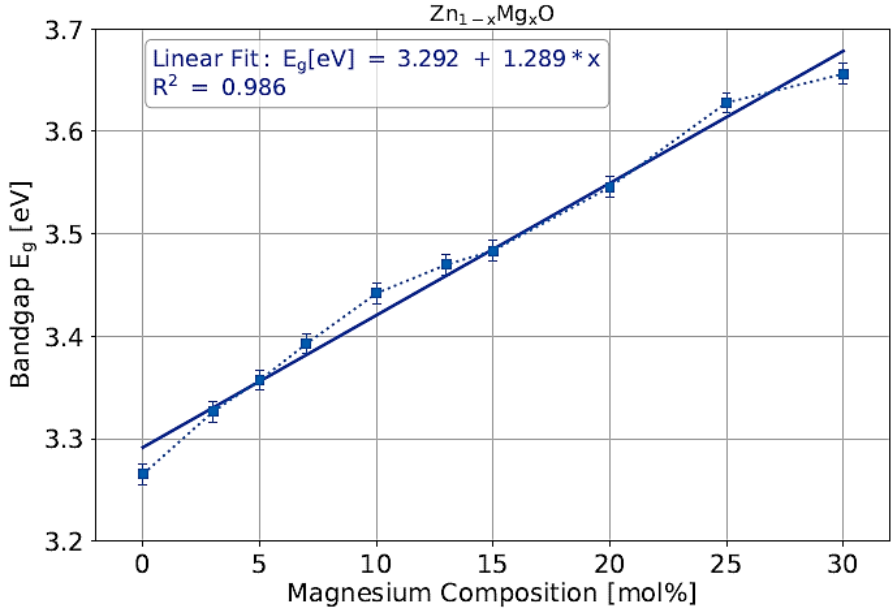

In general, when the Zn^{2+} gets substituted by Mg^{2+} ions in some of the sites of Zn^{2+}, there are no free carriers produced. The Zn 4s and O 2p electron states are present in the bottom of the conduction band, so for ZnO thin films the 4s state of the Zn atoms is dominant [58,59]. But with increasing Mg in the $Zn_{1-x}Mg_xO$ alloy, a dominant state of Mg 3s is present in the conduction band where the minima occur. This state has higher energy than the 4s state. So, a broadening of the bandgap happens with Mg incorporation [58–61]. So, there is a change in the electron state due to the directional migration of Mg. This effect has repercussions on the Fermi Level, which in effect modifies the bandgap [56,60].

We also calculated the Urbach energy or the "band-tail" to estimate the alloy disorders for the $Zn_{1-x}Mg_xO$ thin films. It is to be noted that for $Zn_{1-x}Mg_xO$ films prepared by ultrasonic spray pyrolysis process, the Urbach energy calculations are done for the very first time. The Urbach energies are also calculated to understand the increase of density of defects in the films with the increase in the magnesium content, which was evidenced from AFM images and the reduction in the dimensions of the crystallites from the XRD measurements. The Urbach energies are calculated from the absorption of the thin films in the wavelength regime 300 nm to 400 nm as shown in the transmission spectra of ***Figure 4.11***. The Urbach energy calculations are shown in the ***Figure 4.14*** and the variations of the Urbach energies with respect to the magnesium molar compositions are shown in the ***Figure 4.15***.

Figure 4.14: The Urbach energies of $Zn_{1-x}Mg_xO$ thin films as a function of magnesium molar composition.

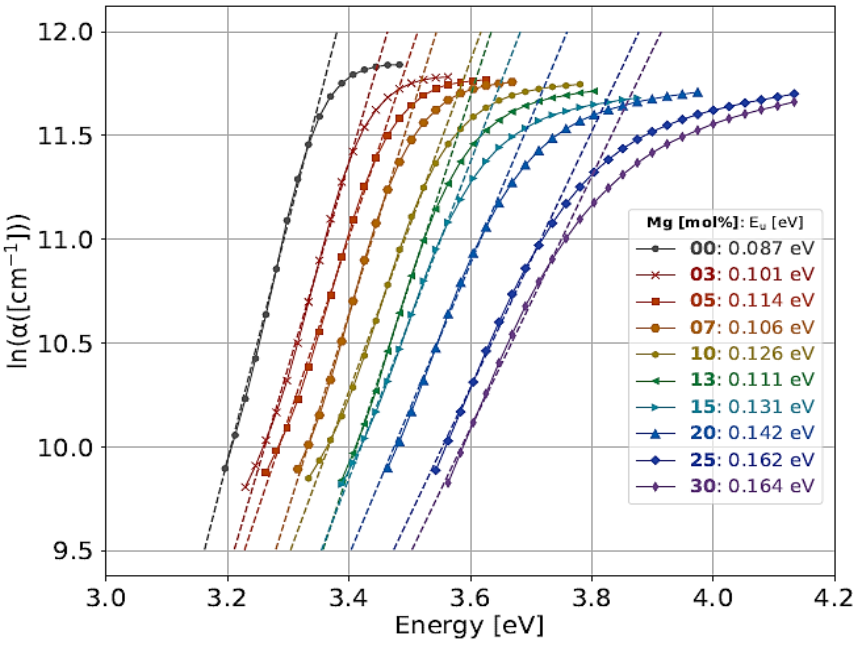

Figure 4.15: Variation of Urbach energies of $Zn_{1-x}Mg_xO$ thin films as a function of magnesium molar composition.

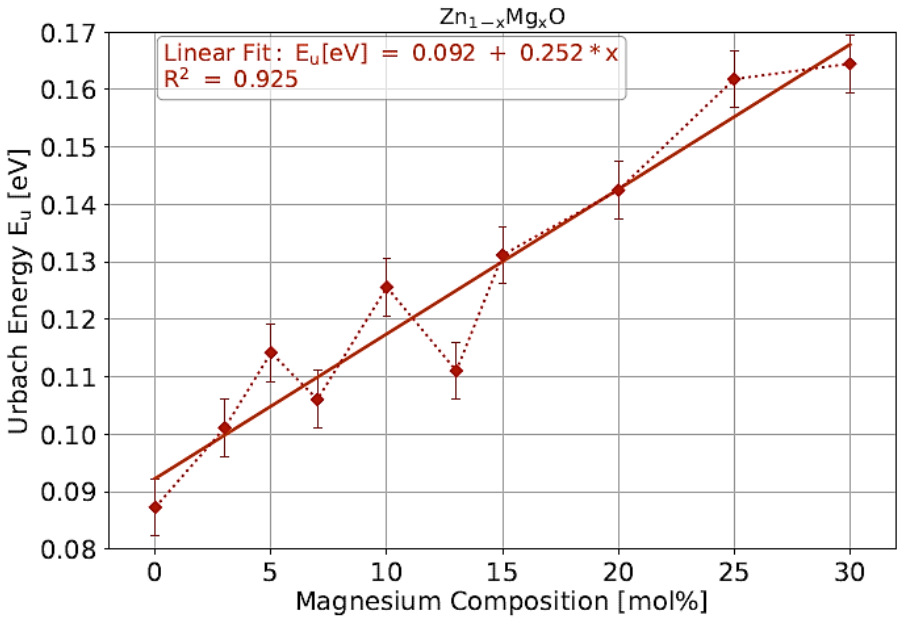

From the analysis, we can estimate that the obtained Urbach energy value for the films with low magnesium compositions, is equivalent to the usual reported values for ZnO grown by pulsed lased deposition (PLD) [62]. The Urbach energy increases considerably as the crystalline lattice alloy disorder grows due to magnesium incorporation, as expected.

4.6.4 Electrical Properties of the ZnMgO Thin Films

The electrical properties of the $Zn_{1-x}Mg_xO$ thin films were analyzed in terms of the changes to the resistivity, carrier concentration and mobility with the increase of the magnesium molar composition. After preparation, but prior to the electrical measurements, all the films were annealed using a rapid thermal annealing (RTA) system at a temperature of 300 °C for 30 minutes using the procedure detailed in the ***Section 3.5.5*** of ***Chapter 3***. The annealing was performed to increase the grain size, activate the shallow donors and to improve the overall crystal quality [63]. From the resistivity measurements, it is seen that when the magnesium molar composition increases from 0 % to 7 %, the resistivity of the films increases dramatically from 0.121 Ω×cm to 166 Ω×cm. The huge increase in the resistivity is collaterally supported by a decrease of the carrier concentration from about 2×10^{19} cm^{-3} to 5×10^{15} cm^{-3}. The carrier mobility increases from approximately 2 cm^2/Vs to 6 cm^2/Vs from Mg 0 mol% to Mg 7 mol%. Compared to the changes in the resistivity and the carrier concentrations, the change in the carrier mobility was nominal with the increase of magnesium. If

carefully observed, the gain in Urbach energy with Mg concentration in the films previously showed appears to have no effect on the diffusion and mobility of free carriers. The variations in the electrical properties of the $Zn_{1-x}Mg_xO$ thin films with the increase of the magnesium molar composition are shown in the ***Figures 4.16, 4.17 & 4.18*** respectively.

The prepared $Zn_{1-x}Mg_xO$ thin films become semi-insulating at magnesium concentrations greater than 7 mol%. Considering the equipment experimental limit and the semi-insulating nature of the thin film with this magnesium content, the resistivity can only be approximated at a value greater than 10^5 Ω×cm for magnesium content of 10 mol%.

Figure 4.16: Variation of resistivity of $Zn_{1-x}Mg_xO$ thin films as a function of magnesium molar composition.

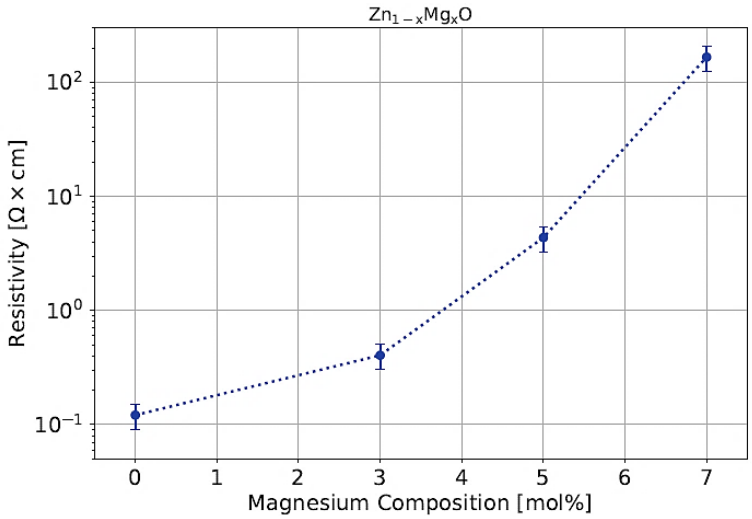

Figure 4.17: Variation of carrier concentration of $Zn_{1-x}Mg_xO$ thin films as a function of magnesium molar composition.

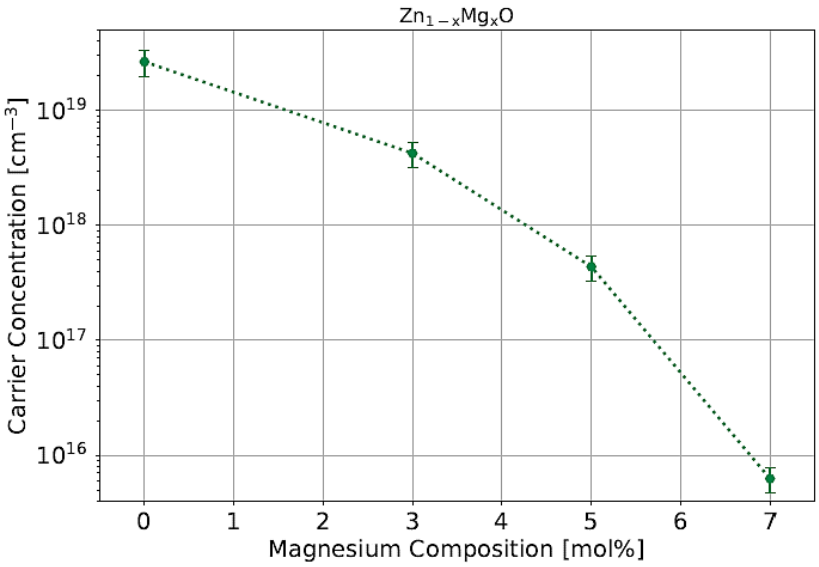

Figure 4.18: Variation of carrier mobility of $Zn_{1-x}Mg_xO$ thin films as a function of magnesium molar composition.

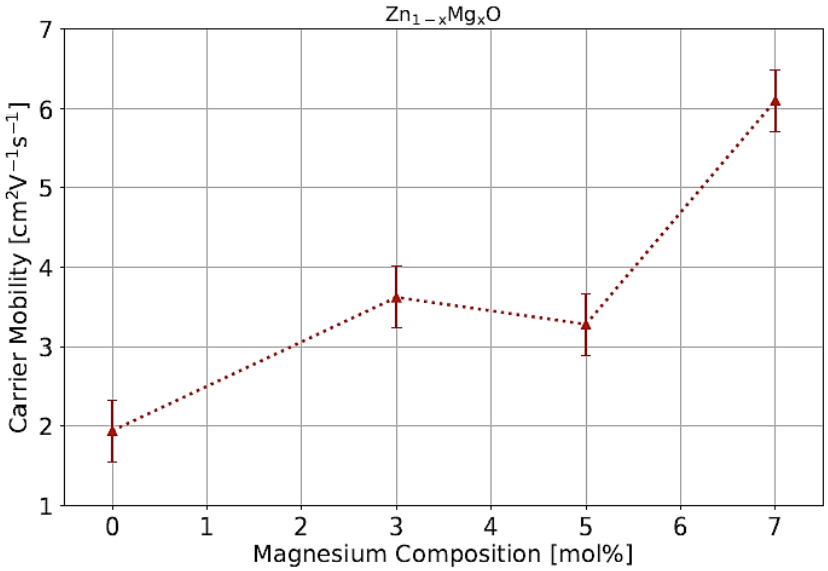

For $Zn_{1-x}Mg_xO$ thin films prepared by ultrasonic spray pyrolysis, it is for the first time, that this significant modifications in the electrical transport characteristics are being examined for. The changes can be attributed to two mechanisms: first, the bandgap increase as determined by transmission spectroscopy in conjunction with an increase in the activation energy of the background dopants, and second, a compensating mechanism as detailed below.

Interstitial Zn, which works as a shallow donor in ZnO with a low formation energy in both Zn-rich and O-rich environments, is commonly attributed to background n-type doping in ZnO [64]. Furthermore, magnesium incorporation may result in a reduction in the development of these interstitial Zn sites, lowering the free carrier concentration as seen before (***Figure 4.17***). Similar type of compensation mechanism has been observed by Li *et al.* [65] for $Zn_{1-x}Mg_xO$ films prepared by RF magnetron sputtering. With the increase in the Mg content in the films, a similar high decrease in the carrier concentration has been observed. According to Li *et al.*, this type of decrease happens because of the inhibition of interstitial Zn (Zn_i) by magnesium. This mechanism, which is based on the notion that the n-doping source in ZnO comes from Zn_i, is significantly more likely than compensation of oxygen vacancy (V_O), which is another commonly mentioned source of ZnO intrinsic doping. Zn_i behaves as a shallow donor in ZnO, which is projected to be significantly more prevalent than other defects, including V_O, according to theoretical calculations using the local density approximation [64] and experimental findings [66].

Thus, the $Zn_{1-x}Mg_xO$ material conductivity, which can be regulated by adding magnesium, allows the

material to be tuned for certain optoelectronic applications, such as ultraviolet detectors and solar cells. In the case of the former, a Mg-controlled reduction in inadvertent doping reduces the dark current, potentially increasing the final device's responsivity. For the latter, it allows for p-doping in ZnMgO, which could be important in the development of heterojunction solar cells, which is incredibly difficult with these materials.

4.7 Challenges Faced Towards the Preparation of ZnMgO

The entire process to successfully prepare ZnMgO thin films using only water-based precursor solution was quite challenging. Most literatures on ultrasonic spray pyrolysis prepared ZnMgO thin films report using toxic and inflammable solvents such as methanol and ethanol to dissolve the precursor salts. The disadvantages of using only water-based solution comes from the fact that water possess a high boiling point, strong hydrogen bonds and high surface tension. These properties are unfavourable for the spray process. Adding acetic acid in a controlled way aids in the reductions of the boiling point and the surface tension, which thereby aids in dissolving the precursor salts and in the atomization of the solution during the spray process. Also, Mg incorporation limit in the water-based precursor solutions at preparation temperatures below 400 °C is only 10 %. But in our process, it was possible to incorporate Mg to nearly 30 % molar compositions using precise control on the spray preparation parameters. The ceramic plate was used to provide a uniform heat distribution to the SLG substrate and the dwell time between each spray cycle was very carefully set with a duration such that the temperature quickly rises to the desired value and helps in completion of the pyrolysis reaction. This process must be in unison with the nozzle power, the shaping air pressure, the nozzle speed, and the nozzle to substrate height. Controlling and understanding the effects of these parameters operation in unison requires utmost precision and care. Adjusting the concentration of the $Zn(Ac)_2$ and the growth rate of the films is also very important as variations in these parameters can easily change the nature of the prepared thin films (from compact films to nanorods). From our previous experience with the ZnO thin films preparation in ***Chapter 3***, we have maintained a constant $Zn(Ac)_2$ molarity of 0.05 mol/L with a growth rate of approximately [120 $\pm$ 20] nm/min for the preparation of all the ZnMgO thin films with different magnesium compositions. These parameters values help us to have a uniform and compact films as evidenced from the AFM images and SEM images. The understanding of the effects of the preparation parameters were important as a whole as we wanted to prepare the ZnMgO thin films with high precision so that they could be utilized as a buffer layer for “all-oxide” solar cells.

4.8 Chapter Conclusions

We would like to conclude this chapter by stating the reasons for choosing to prepare the ZnMgO material with different magnesium contents. In the ***Section 1.3.2.5*** of ***Chapter 1*** we showed through numerical simulations that zinc germanium oxide ($Zn_{1-x}Ge_xO$) is a suitable non-toxic candidate for being employed as a buffer layer for "all-oxide" solar cells for enhancing the efficiency of the solar cells. But, in reality we were unable to find a suitable precursor salt that can be added to $Zn(Ac)_2$ for the pyrolysis process which does not require a heavy modification of our machine and/or the use of toxic solvents. We tried to prepare $Zn_{1-x}Ge_xO$ by using 99.99 % pure germanium oxide (GeO_2) mesh powder from Alfa Aesar, but the powder showed very poor solubility in water-based solution. Heating and stirring the solution for more than ten minutes improved the solubility but when the solution cooled down for the spray process, the solubility was again lost. Spray process was carried out using this mixture of GeO_2 mesh powder and $Zn(Ac)_2$ but it did not produce the film with the desired characteristics as no possible pyrolysis reaction took place. So, keeping in mind the factor earth-abundancy of magnesium over germanium and the easy availability of the suitable magnesium precursor salt which does not require the use of toxic solvents, we shifted our focus towards the preparation of $Zn_{1-x}Mg_xO$ thin films. The earth-abundancy of different materials are shown in the ***Figure 4.19***.

Figure 4.19: Chemical element abundance in the Earth's upper crust as a function of atomic number is shown. The elements that are circled with red are relevant materials for thin film technologies. Modified from [67].

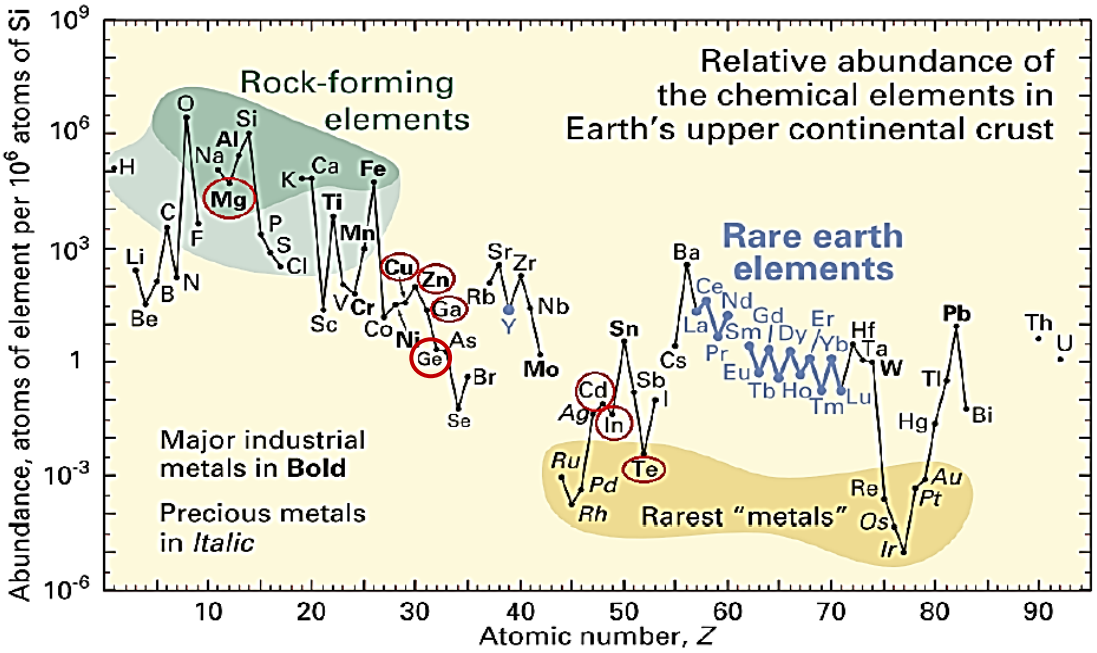

In this work, we designed a ZnMgO preparation method based on ultrasonic spray pyrolysis using water-based solutions in the Mg content range of up to 70 mol%. For magnesium compositions starting at 30 mol%, phase segregation was observed. All the films had a high transmittance of about 90 % in the visible range, with very little fluctuation in thickness, demonstrating the quality of the control on the spray preparation parameters. The variations in bandgap and Urbach energy with increase in magnesium composition was examined and connected to structural characteristics of the prepared films. The structural characteristics allowed the wurtzite structure to be identified as the single phase in all films with a Mg composition less than 30 mol%, while phase separation was observed at this value. When the Mg content was increased from 0 to 7 mol%, the electrical characteristics showed a significant drop in the n-type carrier concentration. When the Mg content exceeds 7 mol%, the thin films become semi-insulating. The electrical results imply that, in addition to the rise in bandgap, a compensation process involving defects generated in the alloy plays a key role in the drop in carrier concentration. The mobility increases slightly as the magnesium content rises, indicating that the crystal quality of the films does not deteriorate much when the magnesium content rises in the range studied. The high transparency of the films in the visible region of the spectrum along with the modulations of the bandgap energies and the conductivities can have interesting applications for the fabrication of solar cells, ultraviolet photodetectors, and other optoelectronic applications.

To summarize: the preparation by ultrasonic spray pyrolysis of ZnMgO with high magnesium content was developed and a combined structural, optical, and electrical investigations were conducted with a combination of optoelectronic properties that can be exploited for the optoelectronic devices. The main achievements are: (**i**) a miscibility limit of magnesium in zinc oxide of 30 %; (**ii**) transparency in the visible region above 90 %; (**iii**) modulated bandgap from 3.26 eV to 3.65 eV; (**iv**) dramatic decrease in the carrier concentration with Mg due to the bandgap modulation and the inhibition of Zn interstitials related shallow donors.

4.9 References

[1] C.F. Klingshirn, B.K. Meyer, A. Waag, A. Hoffmann, J. Geurts, Zinc Oxide: From Fundamental Properties Towards Novel Applications, Springer Berlin Heidelberg, Berlin, Heidelberg, 2010. https://doi.org/10.1007/978-3-642-10577-7.

[2] T. Negami, T. Minemoto, Y. Hashimoto, CIGS solar cells using a novel window $Zn_{1-x}Mg_xO$ film, in: Conf. Rec. Twenty-Eighth IEEE Photovolt. Spec. Conf. - 2000 (Cat. No.00CH37036), IEEE, n.d.: pp. 634–637. https://doi.org/10.1109/PVSC.2000.915923.

[3] Z.L. Wang, Zinc oxide nanostructures: growth, properties and applications, J. Phys. Condens. Matter. 16 (2004) R829–R858. https://doi.org/10.1088/0953-8984/16/25/R01.

[4] J. Amodeo, S. Merkel, C. Tromas, P. Carrez, S. Korte-Kerzel, P. Cordier, J. Chevalier, Dislocations and Plastic Deformation in MgO Crystals: A Review, Crystals. 8 (2018) 240. https://doi.org/10.3390/cryst8060240.

[5] E.R. Segnit, A.E. Holland, The System MgO-ZnO-SiO_2, J. Am. Ceram. Soc. 48 (1965) 409–413. https://doi.org/10.1111/j.1151-2916.1965.tb14778.x.

[6] C. Bergstein, Clarification of Phase Diagram in a (Zn,Mg)O Pseudo Binary System by Using Ultra-Fine MgO Source Powder, 2008 NNIN REU Res. Accompl. (2008) 150–151. https://www.nnin.org/sites/default/files/files/2008NNINreuRA.pdf.

[7] A. Sahay, Magnesium Oxide Formula: Structure, Properties, Reactions, EMBIBE. (2021). https://www.embibe.com/exams/magnesium-oxide-formula/ (accessed May 13, 2022).

[8] A. Ohtomo, M. Kawasaki, T. Koida, K. Masubuchi, H. Koinuma, Y. Sakurai, Y. Yoshida, T. Yasuda, Y. Segawa, $Mg_xZn_{1-x}O$ as a II–VI widegap semiconductor alloy, Appl. Phys. Lett. 72 (1998) 2466–2468. https://doi.org/10.1063/1.121384.

[9] A.K. Sharma, J. Narayan, J.F. Muth, C.W. Teng, C. Jin, A. Kvit, R.M. Kolbas, O.W. Holland, Optical and structural properties of epitaxial $Mg_xZn_{1-x}O$ alloys, Appl. Phys. Lett. 75 (1999) 3327–3329. https://doi.org/10.1063/1.125340.

[10] W.I. Park, G.-C. Yi, H.M. Jang, Metalorganic vapor-phase epitaxial growth and photoluminescent properties of $Zn_{1-x}Mg_xO(0\leqslant x\leqslant 0.49)$ thin films, Appl. Phys. Lett. 79 (2001) 2022–2024. https://doi.org/10.1063/1.1405811.

[11] A. Ohtomo, R. Shiroki, I. Ohkubo, H. Koinuma, M. Kawasaki, Thermal stability of supersaturated $Mg_xZn_{1-x}O$ alloy films and $Mg_xZn_{1-x}O$/ZnO heterointerfaces, Appl. Phys. Lett. 75 (1999) 4088–4090. https://doi.org/10.1063/1.125545.

[12] P. Bhattacharya, R.R. Das, R.S. Katiyar, Comparative study of Mg doped ZnO and multilayer ZnO/MgO thin films, Thin Solid Films. 447–448 (2004) 564–567. https://doi.org/10.1016/j.tsf.2003.07.017.

[13] A. Kaushal, D. Kaur, Effect of Mg content on structural, electrical and optical properties of $Zn_{1-x}Mg_xO$ nanocomposite thin films, Sol. Energy Mater. Sol. Cells. 93 (2009) 193–198. https://doi.org/10.1016/j.solmat.2008.09.039.

[14] A. Suryanarayana Reddy, P. Prathap, Y.P.V. Subbaiah, K.T. Ramakrishna Reddy, J. Yi, Growth and physical behaviour of $Zn_{1-x}Mg_xO$ films, Thin Solid Films. 516 (2008) 7084–7087. https://doi.org/10.1016/j.tsf.2007.12.098.

[15] N. Winkler, S. Edinger, J. Kaur, R.A. Wibowo, W. Kautek, T. Dimopoulos, Solution-processed all-oxide solar cell based on electrodeposited Cu_2O and ZnMgO by spray pyrolysis, J. Mater. Sci. 53 (2018) 12231–12243. https://doi.org/10.1007/s10853-018-2482-2.

[16] N. Winkler, R.A. Wibowo, W. Kautek, T. Dimopoulos, Influence of the aqueous solution composition on the morphology of $Zn_{1-x}Mg_xO$ films deposited by spray pyrolysis, J. Mater. Chem. C. 7 (2019) 3889–3900. https://doi.org/10.1039/c8tc06097e.

[17] D. Zhao, Y. Liu, D. Shen, Y. Lu, J. Zhang, X. Fan, Photoluminescence properties of $Mg_xZn_{1-x}O$ alloy thin films fabricated by the sol-gel deposition method, J. Appl. Phys. 90 (2001) 5561–5563.

https://doi.org/10.1063/1.1413948.

[18] H. Miyazaki, R. Mikami, A. Yamada, M. Konagai, Chemical-Bath-Deposited ZnO and $Mg(OH)_2$ Buffer Layer for Cu(InGa)Se 2 Solar Cells, Jpn. J. Appl. Phys. 45 (2006) 2618–2620. https://doi.org/10.1143/JJAP.45.2618.

[19] R.N. Gayen, S.N. Das, S. Dalui, R. Bhar, A.K. Pal, Zinc magnesium oxide nanofibers on glass substrate by solution growth technique, J. Cryst. Growth. 310 (2008) 4073–4080. https://doi.org/10.1016/j.jcrysgro.2008.06.049.

[20] S. Choopun, R.D. Vispute, W. Yang, R.P. Sharma, T. Venkatesan, H. Shen, Realization of band gap above 5.0 eV in metastable cubic-phase $Mg_xZn_{1-x}O$ alloy films, Appl. Phys. Lett. 80 (2002) 1529–1531. https://doi.org/10.1063/1.1456266.

[21] N.B. Chen, C.H. Sui, Recent progress in research on $Mg_xZn_{1-x}O$ alloys, Mater. Sci. Eng. B. 126 (2006) 16–21. https://doi.org/10.1016/j.mseb.2005.08.112.

[22] H. von Wenckstern, R. Schmidt-Grund, C. Bundesmann, A. Müller, C.P. Dietrich, M. Stölzel, M. Lange, M. Grundmann, Handbook of Zinc Oxide and Related Materials, CRC Press, 2012. https://doi.org/10.1201/b13071.

[23] A.R. Denton, N.W. Ashcroft, Vegards law, Phys. Rev. A. 43 (1991) 3161–3164. https://doi.org/10.1103/PhysRevA.43.3161.

[24] K. Yoshino, S. Oyama, M. Yoneta, Structural, optical and electrical characterization of undoped ZnMgO film grown by spray pyrolysis method, J. Mater. Sci. Mater. Electron. 19 (2008) 203–209. https://doi.org/10.1007/s10854-007-9333-2.

[25] X.D. Zhang, M.L. Guo, C.L. Liu, L.A. Zhang, W.Y. Zhang, Y.Q. Ding, Q. Wu, X. Feng, First-principles investigation of electronic and optical properties in wurtzite $Zn_{1-x}Mg_xO$, Eur. Phys. J. B. 62 (2008) 417–421. https://doi.org/10.1140/epjb/e2008-00186-9.

[26] G.V. Rao, F. Säuberlich, A. Klein, Influence of Mg content on the band alignment at CdS/(Zn,Mg)O interfaces, Appl. Phys. Lett. 87 (2005) 032101. https://doi.org/10.1063/1.1995951.

[27] D.C. Olson, S.E. Shaheen, M.S. White, W.J. Mitchell, M.F.A.M. van Hest, R.T. Collins, D.S. Ginley, Band-Offset Engineering for Enhanced Open-Circuit Voltage in Polymer–Oxide Hybrid Solar Cells, Adv. Funct. Mater. 17 (2007) 264–269. https://doi.org/10.1002/adfm.200600215.

[28] D.S. Ginley, J.D. Perkins, Handbook of Transparent Conductors, Springer US, Boston, MA, 2011. https://doi.org/10.1007/978-1-4419-1638-9.

[29] Q.-B. Ma, H.-P. He, Z.-Z. Ye, L.-P. Zhu, J.-Y. Huang, Y.-Z. Zhang, B.-H. Zhao, Effects of Mg doping on the properties of highly transparent conductive and near infrared reflective $Zn_{1-x}Mg_xO$:Ga films, J. Solid State Chem. 181 (2008) 525–529. https://doi.org/10.1016/j.jssc.2007.12.032.

[30] K. Matsubara, H. Tampo, H. Shibata, A. Yamada, P. Fons, K. Iwata, S. Niki, Bandgap modified Al-doped $Zn_{1-x}Mg_xO$ transparent conducting films deposited by pulsed laser deposition, Appl. Phys. Lett. 85 (2004) 1374–1376. https://doi.org/10.1063/1.1784544.

[31] J.G. Lu, S. Fujita, T. Kawaharamura, H. Nishinaka, Y. Kamada, T. Ohshima, Carrier concentration induced bandgap shift in Al-doped $Zn_{1-x}Mg_xO$ thin films, Appl. Phys. Lett. 89 (2006) 262107. https://doi.org/10.1063/1.2424308.

[32] A. Ohtomo, M. Kawasaki, T. Koida, K. Masubuchi, H. Koinuma, Y. Sakurai, Y. Yoshida, T. Yasuda, Y. Segawa, $Mg_xZn_{1-x}O$ as a II–VI widegap semiconductor alloy, Appl. Phys. Lett. 72 (1998) 2466–2468. https://doi.org/10.1063/1.121384.

[33] K. Maejima, H. Shibata, H. Tampo, K. Matsubara, S. Niki, Characterization of $Zn_{1-x}Mg_xO$ transparent conducting thin films fabricated by multi-cathode RF-magnetron sputtering, Thin Solid Films. 518 (2010) 2949–2952. https://doi.org/10.1016/j.tsf.2009.09.196.

[34] D.J. Cohen, K.C. Ruthe, S.A. Barnett, Transparent conducting $Zn_{1-x}Mg_xO$:(Al,In) thin films, J. Appl. Phys. 96 (2004) 459–467. https://doi.org/10.1063/1.1760239.

[35] K. Koike, K. Hama, I. Nakashima, S. Sasa, M. Inoue, M. Yano, Molecular Beam Epitaxial Growth of Al-doped ZnMgO Alloy Films for Modulation-doped ZnO/ZnMgO Heterostructures, Jpn. J. Appl. Phys. 44 (2005)

3822–3827. https://doi.org/10.1143/JJAP.44.3822.

[36] W. Wei, C. Jin, J. Narayan, R.J. Narayan, Optical and electrical properties of gallium-doped $Mg_xZn_{1-x}O$, J. Appl. Phys. 107 (2010) 013510. https://doi.org/10.1063/1.3271415.

[37] K. Fleischer, E. Arca, C. Smith, I. V. Shvets, Aluminium doped $Zn_{1-x}Mg_xO$ — A transparent conducting oxide with tunable optical and electrical properties, Appl. Phys. Lett. 101 (2012) 121918. https://doi.org/10.1063/1.4753937.

[38] S. Lany, A. Zunger, Dopability, Intrinsic Conductivity, and Nonstoichiometry of Transparent Conducting Oxides, Phys. Rev. Lett. 98 (2007) 045501. https://doi.org/10.1103/PhysRevLett.98.045501.

[39] D.C. Look, K.D. Leedy, L. Vines, B.G. Svensson, A. Zubiaga, F. Tuomisto, D.R. Doutt, L.J. Brillson, Self-compensation in semiconductors: The Zn vacancy in Ga-doped ZnO, Phys. Rev. B. 84 (2011) 115202. https://doi.org/10.1103/PhysRevB.84.115202.

[40] D.C. Look, T.C. Droubay, S.A. Chambers, Stable highly conductive ZnO via reduction of Zn vacancies, Appl. Phys. Lett. 101 (2012) 102101. https://doi.org/10.1063/1.4748869.

[41] J. T-Thienprasert, S. Rujirawat, W. Klysubun, J.N. Duenow, T.J. Coutts, S.B. Zhang, D.C. Look, S. Limpijumnong, Compensation in Al-Doped ZnO by Al-Related Acceptor Complexes: Synchrotron X-Ray Absorption Spectroscopy and Theory, Phys. Rev. Lett. 110 (2013) 055502. https://doi.org/10.1103/PhysRevLett.110.055502.

[42] D. Abou-Ras, T. Kirchartz, U. Rau, eds., Advanced Characterization Techniques for Thin Film Solar Cells, Wiley, 2011. https://doi.org/10.1002/9783527636280.

[43] S. Kim, C.-S. Lee, S. Kim, R.B. V. Chalapathy, E.A. Al-Ammar, B.T. Ahn, Understanding the light soaking effect of ZnMgO buffer in CIGS solar cells, Phys. Chem. Chem. Phys. 17 (2015) 19222–19229. https://doi.org/10.1039/C5CP01758K.

[44] D. Hariskos, B. Fuchs, R. Menner, N. Naghavi, C. Hubert, D. Lincot, M. Powalla, The Zn(S,O,OH)/ZnMgO buffer in thin-film $Cu(In,Ga)(Se,S)_2$ -based solar cells part II: Magnetron sputtering of the ZnMgO buffer layer for in-line co-evaporated $Cu(In,Ga)Se_2$ solar cells, Prog. Photovoltaics Res. Appl. 17 (2009) 479–488. https://doi.org/10.1002/pip.897.

[45] C. Platzer-Björkman, T. Törndahl, A. Hultqvist, J. Kessler, M. Edoff, Optimization of ALD-(Zn,Mg)O buffer layers and (Zn,Mg)O/$Cu(In,Ga)Se_2$ interfaces for thin film solar cells, Thin Solid Films. 515 (2007) 6024–6027. https://doi.org/10.1016/j.tsf.2006.12.047.

[46] Y. Hou, Z. Mei, X. Du, Semiconductor ultraviolet photodetectors based on ZnO and $Mg_xZn_{1-x}O$, J. Phys. D. Appl. Phys. 47 (2014) 283001. https://doi.org/10.1088/0022-3727/47/28/283001.

[47] K.W. Liu, D.Z. Shen, C.X. Shan, J.Y. Zhang, D.Y. Jiang, Y.M. Zhao, B. Yao, D.X. Zhao, The growth of ZnMgO alloy films for deep ultraviolet detection, J. Phys. D. Appl. Phys. 41 (2008) 125104. https://doi.org/10.1088/0022-3727/41/12/125104.

[48] H. Wu, J. Liang, G. Jin, Y. Lao, T. Xu, Transparent Thin-Film Transistors Using ZnMgO as Dielectrics and Channel, IEEE Trans. Electron Devices. 54 (2007) 2856–2859. https://doi.org/10.1109/TED.2007.907126.

[49] K. Koike, D. Takagi, M. Kawasaki, T. Hashimoto, T. Inoue, K. Ogata, S. Sasa, M. Inoue, M. Yano, Ion-Sensitive Characteristics of an Electrolyte-Solution-Gate ZnO/ZnMgO Heterojunction Field-Effect Transistor as a Biosensing Transducer, Jpn. J. Appl. Phys. 46 (2007) L865–L867. https://doi.org/10.1143/JJAP.46.L865.

[50] H.-C. Hsu, C.-Y. Wu, H.-M. Cheng, W.-F. Hsieh, Band gap engineering and stimulated emission of ZnMgO nanowires, Appl. Phys. Lett. 89 (2006) 013101. https://doi.org/10.1063/1.2218813.

[51] S. Bose, C. Chevallier, S. Ould Saad Hamady, N. Fressengeas, Optical and Electrical Properties of ZnMgO with High Mg Content Elaborated by Ultrasonic Spray Pyrolysis using Water-Based Solutions, Phys. Status Solidi. (2022). https://doi.org/10.1002/pssa.202200091.

[52] R. T. Downs, The RRUFF Project: An Integrated Study of the Chemistry, Crystallography, Raman and Infrared Spectroscopy of Minerals, Proceedings of the 19th General Meeting of the International Mineralogical Association, Kobe, 23-28 July 2006, pp. 3-13, (2006).

[53] M. Rouchdi, E. Salmani, B. Fares, N. Hassanain, A. Mzerd, Synthesis and characteristics of Mg doped ZnO thin films: Experimental and ab-initio study, Results Phys. 7 (2017) 620–627. https://doi.org/10.1016/j.rinp.2017.01.023.

[54] A. Singh, A. Vij, D. Kumar, P.K. Khanna, M. Kumar, S. Gautam, K.H. Chae, Investigation of phase segregation in sol–gel derived ZnMgO thin films, Semicond. Sci. Technol. 28 (2013) 025004. https://doi.org/10.1088/0268-1242/28/2/025004.

[55] S. Edinger, J. Bekacz, M. Richter, R. Hamid, R.A. Wibowo, A. Peić, T. Dimopoulos, Influence of the acetic acid concentration on the growth of zinc oxide thin films prepared by spray pyrolysis of aqueous solutions, Thin Solid Films. 594 (2015) 238–244. https://doi.org/10.1016/j.tsf.2015.04.027.

[56] P. Murkute, H. Ghadi, S. Sushama, S. Chakrabarti, Realization of high-quality RF sputtered ZnMgO (x=15%) thin films by post-growth annealing treatment, Superlattices Microstruct. 156 (2021) 106977. https://doi.org/10.1016/j.spmi.2021.106977.

[57] T. Minemoto, T. Negami, S. Nishiwaki, H. Takakura, Y. Hamakawa, Preparation of $Zn_{1-x}Mg_xO$ films by radio frequency magnetron sputtering, Thin Solid Films. 372 (2000) 173–176. https://doi.org/10.1016/S0040-6090(00)01009-9.

[58] Z. Li, W. Shen, S. Xue, X. Zu, Effect of annealing temperature on the structural and optical properties of $Zn_{1-x}Mg_xO$ particles prepared by oxalate precursor, Colloids Surfaces A Physicochem. Eng. Asp. 320 (2008) 156–160. https://doi.org/10.1016/j.colsurfa.2008.01.041.

[59] P. Liu, H. Wang, J. Chen, X. Li, H. Zeng, Rapid and High-Efficiency Laser-Alloying Formation of ZnMgO Nanocrystals, Sci. Rep. 6 (2016) 28131. https://doi.org/10.1038/srep28131.

[60] H. Ghadi, P. Murkute, A. Ghosh, S.M.M.D. Dwivedi, A. Mondal, S. Chakrabarti, Ultrasensitive zinc magnesium oxide nanorods based micro-sensor platform for UV detection and light trapping, Sensors Actuators A Phys. 278 (2018) 127–139. https://doi.org/10.1016/j.sna.2018.05.028.

[61] B.E. Sernelius, K.-F. Berggren, Z.-C. Jin, I. Hamberg, C.G. Granqvist, Bandgap tailoring of ZnO by means of heavy Al doping, Phys. Rev. B. 37 (1988) 10244–10248. https://doi.org/10.1103/PhysRevB.37.10244.

[62] G. Wisz, I. Virt, P. Sagan, P. Potera, R. Yavorskyi, Structural, Optical and Electrical Properties of Zinc Oxide Layers Produced by Pulsed Laser Deposition Method, Nanoscale Res. Lett. 12 (2017) 253. https://doi.org/10.1186/s11671-017-2033-9.

[63] S. Brochen, C. Granier, G. Feuillet, J. Pernot, Role of deep and shallow donor levels on n -type conductivity of hydrothermal ZnO, Appl. Phys. Lett. 100 (2012) 052115. https://doi.org/10.1063/1.3681168.

[64] S.B. Zhang, S.-H. Wei, A. Zunger, Intrinsic n -type versus p -type doping asymmetry and the defect physics of ZnO, Phys. Rev. B. 63 (2001) 075205. https://doi.org/10.1103/PhysRevB.63.075205.

[65] W. Li, L. Fang, G. Qin, H. Ruan, H. Zhang, C. Kong, L. Ye, P. Zhang, F. Wu, Tunable zinc interstitial related defects in ZnMgO and ZnCdO films, J. Appl. Phys. 117 (2015) 145301. https://doi.org/10.1063/1.4917207.

[66] A. Janotti, C.G. Van de Walle, Native point defects in ZnO, Phys. Rev. B. 76 (2007) 165202. https://doi.org/10.1103/PhysRevB.76.165202.

[67] J.B.H. Gordon, B. Haxel, G.J. Orris, Rare Earth Elements — Critical Resources for High Technology: U S Geological Survey, (2002) 1–11. https://pubs.usgs.gov/fs/2002/fs087-02/.

CHAPTER 5: Cuprous Oxide as an Absorber Layer: Effect of the Preparation Temperature and a New Reducing Agent

5.1 Introduction to Cuprous Oxide (Cu_2O)

Cuprous oxide (Cu_2O) is a stable binary copper compound with a lattice constant of 4.269 Å and crystallizes in a cubic structure (cuprite, space group Pn-3m). 4 copper atoms and 2 oxygen atoms make up the unit cell. As seen in ***Figure 5.1***, the copper atoms (blue balls) create a face-centered-cubic sublattice, while the two oxygen atoms (red balls) form a body-centered-cubic sublattice. ***Figure 5.1*** also shows that each oxygen atom is 4-fold coordinated with oxygen atoms, and each copper atom is linearly coordinated with the two oxygen atoms [1]. The typical bond lengths are: Cu-Cu: 3.019 Å ; Cu-O: 1.848 Å; O-O: 3.68 Å [2].

Figure 5.1: Cu_2O crystal structure (a) and a two-dimensional projection of 64 Cu_2O unit cells (b). The oxygen outward diffusion pathway is shown schematically with yellow arrows. Cu atoms are represented as blue balls, while oxygen atoms are represented by red balls [1].

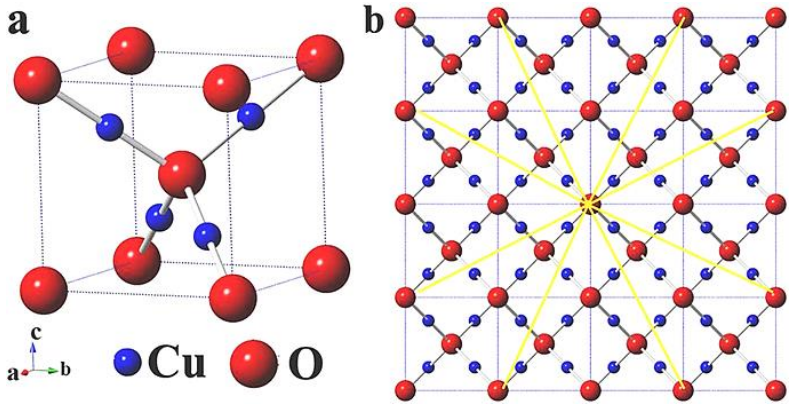

Cu_2O is a direct band gap semiconductor with a significant exciton binding energy of 150 meV [3]. At room temperature, the Cu_2O optical bandgap values ranging from 2.4 to 2.7 eV have been reported experimentally [4-9] as also shown in the present thesis.

Cu_2O films possess intrinsic p-type conductivity probably due to: (i) Cu vacancies (V_{Cu}) as theoretically predicted [11] and experimentally evidenced with measurements, using deep-level transient spectroscopy, of transition levels at 0.2 and 0.5 eV above the valence band maximum [12]; (ii) extrinsic shallow acceptors related to nitrogen or hydrogen complex with Cu [13,14]. These defects properties strongly depend on the preparation technique, resulting in a great disparity between the resistivity values measured with respect to the methods and the conditions of deposition. For instance, very high resistivity values ranging from 10^2 – 10^4 Ω×cm and 10^4 – 10^6 Ω×cm were reported for the films prepared by grown by thermal oxidation [15] and electrodeposition [16], corresponding to a very low hole carrier concentration at around 10^{14} cm^{-3} and a mobility of about 1 cm^2/Vs. Cu_2O prepared by sputtering or ALD have usually lower resistivity

[8,17-24] but comparable or even higher mobility than the electrodeposited films.

Cu_2O has a direct band gap with a very high absorption coefficient of about 3×10^5 cm^{-1} at a wavelength around 400 nm [25–28] and even more than 7×10^5 cm^{-1} in the ultraviolet spectral region. The refractive index of Cu_2O at room temperature is about 2.7 in the transparent spectral region [29-32].

One can note that the Cu_2O optoelectronic properties depend strongly on the crystallinity and phases present in the thin films. Indeed, Cu_2O is unstable in air at room temperature and can oxidize to CuO [33-39]. However, the kinetics of the transformation in CuO is so slow at room temperature that Cu_2O can be considered stable for practically all applications.

5.2 Cu_2O as Solar Cell Absorber Material

Cu_2O is a promising material for solar cells due to its non-toxic and abundant nature and its very high absorption coefficient. It also has a relatively decent mobility at ambient temperature and a relatively long minority carrier diffusion length if it is close to a single crystal [40]. Cu_2O has a direct band gap of about 2.1 eV (depends strongly on the preparation process) and is intrinsically p-type due to Cu vacancies in the lattice (as explained above in the ***Section 5.1***) [41]. All of this adds up to a theoretical conversion efficiency (Shockley-Queisser efficiency limit, cf. ***Section 1.1.2.3*** of ***Chapter 1***) of 20 %, which is quite high and indicates that Cu_2O should be investigated further for solar cell applications [17].

However, no Cu_2O solar cells have yet been manufactured that live up to the theoretical predictions. This is due to the fact that manufacturing can be difficult due to the presence of cupric oxide (CuO). This results in issues such as Schottky junctions and lattice defects, which reduce mobility and conductivity while also causing non-radiative recombination [42]. Furthermore, the Cu_2O films produced thus far have a low photoexcited carrier collection probability and considerable surface recombination [17]. Olson *et al.* [43] published a comprehensive study of Cu_2O solar cells, highlighting the difficulties that need to be solved to make commercial production of Cu_2O practical. Rakhshani *et al.* [44] examined the current methods for preparing Cu_2O which are to be used as absorbers in the solar cells. Most preparation techniques required high temperature oxidation of copper of more than 1000 °C [45], therefore this study investigated ways that required far less temperatures, even less than 300 °C. Cu_2O preparation at low temperatures has gotten a lot of attention since then. The readers are requested to please look into the ***Section 1.3.2*** of ***Chapter 1*** to find the details of the use of Cu_2O as absorber layers in “all-oxide” solar cells.

5.3 Preparation of Cu_2O by Ultrasonic Spray Pyrolysis

The preparation of Cu_2O films was done using our ExactaCoat system from Sono-Tek presented in detail in the ***Sections 2.4*** & ***2.5*** of ***Chapter 2***. The temperature on the heating plate was controlled by an in-built PID temperature controller and measured with thermocouple A. The temperatures of the substrate holder and the glass substrate were measured using a N-type thermocouple (thermocouple B). The schematic arrangement of the spray preparation system is shown in the ***Figure 5.2***.

Figure 5.2: Schematic view of the ultrasonic spray pyrolysis system used to prepare Cu_2O. The thermocouple A is used to measure the hot plate set temperature, whereas the thermocouple B is used to monitor the preparation temperature directly on the substrate.

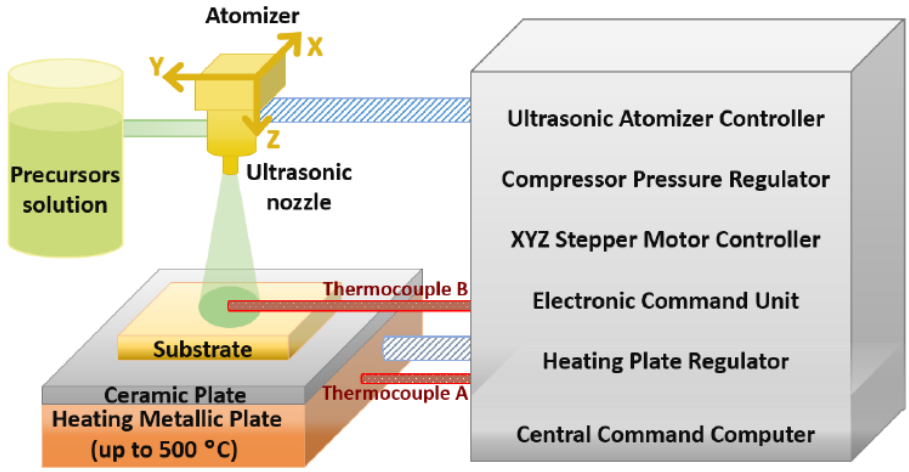

Copper acetate monohydrate, $Cu(CH_3COO)_2 \cdot H_2O$ was used the source precursor salt dissolved in deionized water. For simplicity henceforth, in this thesis we will always refer it as only $Cu(Ac)_2$. Always 50 mL of precursor solution was prepared before the start of the spray. D-sorbitol was used as a reducing agent and mixed in the $Cu(Ac)_2$ solution. D-sorbitol helps in the non-formation of the detrimental CuO phase. Acetic acid was also added to the precursor solution to reduce the formation of copper hydroxide, $Cu(OH)_2$. Usually, the dissolution of $Cu(Ac)_2$, in deionized water yields a pH value of about 5.5. At this value, $Cu(OH)_2$ starts to get precipitated [46–48]. Cu^{2+} ions and other copper-hydro-acetate complexes become highly soluble when acetic acid is added to bring down the pH value below 3 [49–51].

5.3.1 Chemicals Used, Chemical Reactions & Temperature Settings Involved for Cu_2O Preparation

All the chemicals used for the preparation of Cu_2O thin films are listed in the ***Table 5.1***.

Table 5.1: Chemicals with high purity used for spray pyrolysis deposition of Cu_2O.

Name	Formula	Supplier
Copper acetate monohydrate	$Cu(CH_3COO)_2 \cdot H_2O$	Merck 1.02710.0500
Acetic Acid	CH_3COOH	Alfa Aesar 10994-AE
D-Sorbitol	$C_6H_{14}O_6$	VWR 56755-1
Deionized water	H_2O	Avantor-VWR

Among the spray preparation parameters, the deposition temperature plays a key role to prevent the formation of unwanted copper phases such as CuO. As suggested by Kosugi *et al*. [52] the preparation of Cu_2O by spray pyrolysis follows a two-step process. Firstly, the Cu^{2+} ions in the solution are reduced by the reducing agent (glucose or D-sorbitol) to form elemental copper. The elemental copper gets adsorbed to the surface by forming clusters. These clusters in turn, depending on the temperature and the precursor solution composition gets oxidised to form Cu_2O film. The film formation process is shown below:

$$Cu^{2+} \rightarrow \ Cu^0 Cluster \ \rightarrow Cu^+ \quad \text{(i)}$$

$$O^2 Cluster \ \rightarrow Cu_2O \ film \quad \text{(ii)}$$

An alternate process for Cu_2O film formation could be over the reduction of an already formed CuO film by a suitable reducing agent as mentioned in the literatures [53–55]. All the pathways for Cu_2O formation are substantially influenced by the deposition temperature. The influence of the temperature is discussed in the ***Section 5.3.1.2***.

5.3.1.1 Choice of Reducing Agents

Depending on the pH value, the dissolution of copper acetate in a water-based precursor solution gives either Cu^{2+} ions or Cu^{2+} complexes with acetate and water ligands. So, in order to produce a Cu_2O film, the Cu^{2+} ions must be reduced to their +1 oxidation state [49,56,57]. D-glucose is commonly used a reducing agent because of the presence of the terminal aldehyde and hydroxyl groups which favours reduction. But sugar and sugar-based alcohols are very low-volatile substances [58], whose by-products after the pyrolysis remains in the deposited film and reduces the film quality [58,59]. D-glucose possess strong O-H bonds whose decomposition at high temperature pyrolytic reactions produces hydroxymethylfurfurol, which tends to be present in the Cu_2O film, thus declining its quality [60,61]. The other favourable reducing agents are glycerol and D-sorbitol. Both these sugar alcohols have a high number of OH-groups which helps in the reduction

of Cu^{2+} ions. Compared to D-glucose, glycerol is more volatile. D-sorbitol possess a much less complex thermal decomposition when compared to both glycerol and D-glucose. The thermal decomposition of D-sorbitol starts with the formation of sorbitan which gets entirely converted to volatile and harmless by-products such as H_2 and CO_2 [58,61–63].

Kosugi *et al.* [52] also suggested a two-step Cu_2O film formation process involving OH-group as shown below:

$$\text{Step 1: } Cu^{2+} + R{-}CH_2 - OH + \frac{1}{2}O_2 \rightarrow Cu^0 + R - CHO + H_2O$$

$$\text{Step 2: } 2Cu^0 + \frac{1}{2}O_2 \rightarrow Cu_2O\ film$$

If the deposition temperature is below 200 °C, then Cu will only be partially oxidised to produce a mixed Cu/Cu_2O film. Satta *et al.* [55] proposes a one-step process of Cu_2O film formation by reduction of already formed CuO film with utilization of a primary OH-group. The reaction can be described as written below:

$$2CuO + R - CH_2OH \rightarrow Cu_2O\ (film) + H_2O + R - CHO$$

For all the reaction schemes, the secondary OH-groups can undergo further reactions to form ketones, while the formed aldehydes can be oxidised to carboxylic acids [55]. The further oxidation of the Cu_2O film will be limited kinetically due to the presence of a very thin ($\approx 1\ nm$) surface oxide film of CuO. This film acts as a barrier for the oxygen diffusion which prevents the further oxidation of the Cu_2O film [64,65]. The ultra-thin CuO film will always be present above a Cu_2O film even under ambient conditions but as it is too thin, it will not be detected by characterization technique such as XRD [64–67]. In our published study [67], D-sorbitol is chosen as the reducing agent. The effect of the concentration of the D-sorbitol in the precursor solution on the quality of the Cu_2O film is studied and discussed in detail in the later sections of this chapter.

5.3.1.2 Setting the Deposition Temperature

When compared to other metal oxides such as zinc oxide or titanium dioxide, temperature control is very important for spray pyrolysis of copper oxide because the thermal degradation of copper acetate precursor can produce a combination of Cu, CuO, or Cu_2O phases [68]. The preparation temperature is usually not well defined in the spray pyrolysis related literatures. It's critical, especially for multi-phase materials, to identify the preparation temperature exactly, which could be the set temperature, the substrate temperature, or another observed or estimated temperature connected to the equipment and process. Using the approach below, we precisely define and examine the preparation temperature for the first time. During the preparation process, the temperature profile on the substrate surface is measured every second. ***Figure 5.3*** shows the

temperature profile for a given temperature of 390 °C, for example. The scanning of the nozzle across the surface begins at time t = 0 s as shown in the figure. The temperature at the surface is measured at an average of 321 °C, which is 69 °C lower than the set temperature, before the preparation begins. The comparatively low heat conductivity of the glass-ceramic holder and the soda lime glass substrate itself (≈ 1 W/m/K) causes the offset between the substrate temperature and the set temperature before the start of the spray.

Figure 5.3: Change in substrate temperature during the preparation of Cu_2O at 390 °C set temperature. The zero time corresponds to the beginning of spray, which takes 720 seconds to complete. The inset plot depicts two spray cycles, with one half of each cycle having a higher temperature than the other due to the thermocouple's off-center position in the nozzle path.

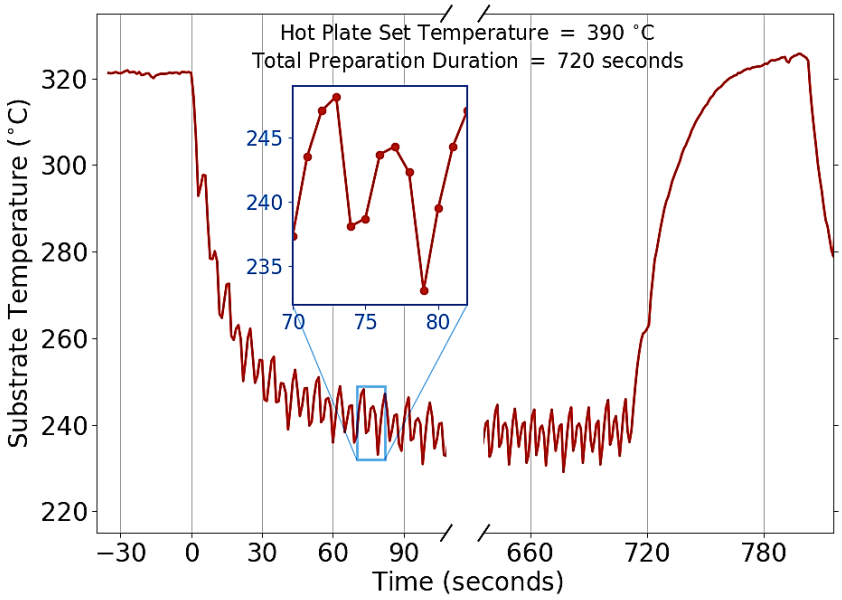

Due to the low temperature of the aerosol stream, the substrate temperature drops as the spray begins, eventually reaching a stable state with an average temperature of 240 °C. This corresponds to the preparation temperature. The periodic temperature changes at the substrate surface of about 240 °C average with an amplitude of 10 °C and a period of 6.5 second for one cycle, as shown in the inset plot in ***Figure 5.3***, reveals the scanning of the spray nozzle over the substrate. It's also worth noting that, due to the thermocouple's off-centre position in the nozzle path, each cycle comprises one half with a higher temperature than the second. Finally, the sample was removed less than 10 seconds after the last spray cycle ended to prevent uncontrolled in-situ annealing of the copper oxide thin layer. In ***Figure 5.3***, for example, the sample was taken away from the heating plate at t = 720 s. The correlation between the set temperature and the actual preparation temperature measured directly on the substrate is shown in ***Table 5.2***.

Table 5.2: Correlation between the set temperature obtained with thermocouple A and the actual temperature measured directly on the substrate with thermocouple B (as depicted schematically in the ***Figure 5.2***).

Hot Plate Set Temperature (°C)	Substrate Temperature (°C)
375	230
390	240
420	260
435	273

The effect of the increase of the set and preparation temperatures on the quality of the Cu_2O film is studied and discussed in detail in the later sections of this chapter.

5.3.2 Design of Experiment Along with the Chemical Protocol

Many parameters are involved in the spray pyrolysis preparation process for depositing high-quality thin films as detailed in the ***Section 2.5*** of ***Chapter 2***. Variation in each parameter impacts the resulting film quality. This is the reason to set up the design of experiments, so that we can understand and analyze the nature and degree of impact of the parameters towards the prepared film quality. The preparation temperature, the number of spray scans, the nozzle speed, the nozzle-to-substrate distance, the air flow pressure, the flow rate, and the precursor solution and reducing agent concentrations all play a role in the Cu_2O preparation process. The impact of the preparation temperature and the reducing agent concentration is the focus of this research. The effect of the other parameters was researched and, following a thorough investigation, they were set to their optimal values as follows:

1) The number of spray cycles has been set at 75 scans.

2) The spray flow rate was set to 0.5 mL/min.

3) The nozzle speed was set to 70 mm/s.

4) The height between the spray nozzle and the substrate is set to 10 cm.

5) The concentration of copper acetate in the precursor solution is set to 0.025 mol/L.

6) The acetic acid volume percent of about 7 % corresponding to a pH of 2.80.

7) The shaping air pressure fixed at 13.8 kPa.

8) The dwell time set to 1 sec between each spray cycle.

The following are the preparation parameters examined in this research:

1. The set temperature of the hot plate, which can range from 375 °C to 435 °C.

2. The reducing agent concentration, ranging from 0 mol/L to 0.075 mol/L.

The reproducibility of the preparation process was confirmed by repeating it at least two times with the same combination of the aforesaid parameters. The thickness of all the films in this study is

around 300 nm, as measured by mechanical and optical profilometry with same vertical resolutions of 0.1 nm. The thin film is formed by spray scanning the nozzle back and forth across the substrate surface 75 times for a total of 720 seconds. After each scan, the nozzle comes to a halt for 0.5 seconds before going back in the opposite direction, resulting in a total cycle time of 1 second. This period is called the dwell time. The time interval between two sprays over the same zone, and thus the preparation temperature, is affected by the dwell time in the spray pyrolysis process. Even though the hot plate is kept at a constant temperature, the preparation temperature changes substantially due to the aerosol stream that reaches the substrate and cools it down. The distinction between the set temperature and the preparation temperature is critical for understanding the spray pyrolysis process, and it has been monitored precisely in real-time in this study using two thermocouples A and B (as shown in the ***Figure 5.2***).

For all the preparations, the concentration of $Cu(Ac)_2$ powder in the precursor solution was 0.025 mol/L. So, the quantity of the $Cu(Ac)_2$ powder required in the solution to reach this concentration is calculated using the relation:

Equation (5.1):

$$m_{Cu} = C \times V \times M$$

Where, m is the mass (in g) of $Cu(Ac)_2$ powder; C is the concentration in mol/L; V is the solution volume in litres (L) and M is the molar mass of $Cu(Ac)_2$ (in g/mol).

So, mass of $Cu(Ac)_2$ needed for preparing a 100 mL solution is: $m_{Cu} = 0.025 \times 0.1 \times 199.65 = 0.499$ g ≈ 0.5 g.

Now, the quantity of the D-sorbitol powder required in the solution to reach a particular solution concentration is calculated using the relation:

Equation (5.2):

$$m_{D-sorbitol} = C \times V \times M$$

Where, $m_{D\text{-sorbitol}}$ is the mass (in g) of D-sorbitol powder; C is the concentration in mol/L; V is the solution volume in litres (L) and M is the molar mass of D-sorbitol (in g/mol).

So, for example, mass of D-sorbitol needed for preparing a 100 mL solution with concentration of 0.05 mol/L is: $m = 0.05 \times 0.1 \times 182.17 = 0.91$ g.

At first, the required quantity of $Cu(Ac)_2$ powder is dissolved in 50 mL deionized water. Then 30 mL more deionized water is added. After this the required quantity of D-sorbitol powder is added and

dissolved in 80 mL of the solution. The solution is shaken gently to dissolve the added powders. The pH of the solution was measured which was approximately always 5.5. The target is to bring down the pH to below 3. For all our preparations we have maintained a constant pH of 2.8 to make the Cu^{2+} ions and other copper-hydro-acetate complexes completely soluble. Approximately 7 mL of acetic acid was then added to the 80 mL of the solution to bring the pH value to 2.8 and then again 13 ml deionized water was added to make the final solution of volume 100 mL. For the first preparation study, when only the set temperature was changed, the D-sorbitol concentration in the solution was maintained always to 0.05 mol/L. For the second preparation study, the concentration of D-sorbitol was varied from 0.0000 mol/L to 0.0750 mol/L. Different solutions with increasing D-sorbitol concentrations in steps of 0.0125 mol/L were prepared, with the powder quantities calculated using the ***Equation 5.2***.

5.4 Results and Discussions on the Preparation of Cu_2O

The regulation of the phase, as mentioned earlier, is the main issue for copper oxide optimization. The ultrasonic spray pyrolysis technique allows for fine-tuning of the preparation parameters involved in phase formation, particularly the preparation temperature and precursor solution concentration. The influence of these factors is investigated here utilizing the new sorbitol reducing agent, first by adjusting the preparation temperature, and then by varying the sorbitol concentration. Using the conditions described in ***Chapter 2***, X-ray diffraction, micro-Raman spectroscopy, and UV-Vis transmission are used to analyze the structural and optical properties of the developed thin films respectively. The van der Pauw and Hall Effect techniques were used to determine the electrical characteristics.

5.4.1 Effect of the Preparation Temperatures on the Structural and Optical Properties of Cu_2O

When compared to other metal oxides, such as zinc oxide or titanium dioxide, the control on the preparation temperature is very important for spray pyrolysis of copper oxide because the thermal degradation of the copper acetate precursor can generate a combination of Cu, CuO, or Cu_2O phases [68].

X-ray diffractograms of four copper oxide samples are shown in the ***Figure 5.4***. The preparation temperatures were the ones mentioned in the ***Table 5.2***. The concentration of reducing agent D-sorbitol in the precursor solution is kept constant at 0.05 mol/L. At 36.69°, 42.53° and 61.85°,

respectively, the major cubic Cu_2O peaks ((111), (200), and (220) are identified. The measured $(\bar{1}11)$, (111), and $(\bar{1}12)$ peaks at 35.66°, 38.79° and 44.19°, respectively, are the signatures of the monoclinic CuO phase at the highest temperatures.

Figure 5.4: XRD diffractograms of copper oxide thin films with different preparation temperatures. The red lines represent the diffractogram fitting using a pseudo-Voigt peak function.

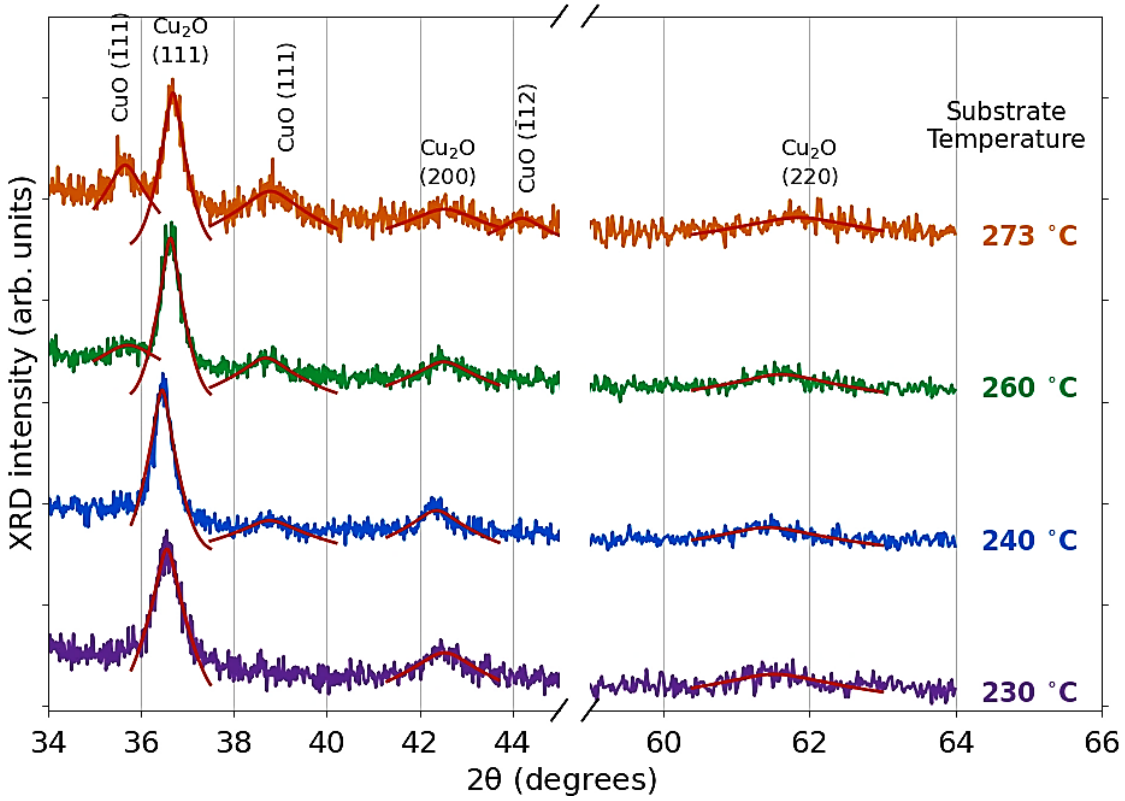

The monoclinic CuO phase was not identified at the lowest preparation temperature of 230 °C. At a preparation temperature of 240 °C, this CuO phase appears, and the relative peaks intensity grows as the temperature rises. With the increase of the preparation temperature, a rise in the ratio of CuO/Cu_2O of the integrated peak intensity of the two phases, is noticed. This effect is illustrated in the ***Figure 5.5***. In fact, the substantial increase in the monoclinic CuO phase predominance was found at higher temperatures, starting at 260 °C. The CuO/Cu_2O integrated peak intensity ratio shows a rapid increase with temperature, indicating that the CuO phase becomes dominant at high preparation temperatures. The ratio of the total of CuO integrated peak intensity over the sum of Cu_2O integrated peak intensity is used to define and calculate the CuO/Cu_2O peak ratio F, which is shown in the relation below:

Equation (5.3):

$$F = \frac{\sum_{CuO} I_{(hkl)}}{\sum_{Cu_2O} I_{(hkl)}}$$

Where $I_{(hkl)}$ is the integrated peak intensity corresponding to the (hkl) diffraction plane. This relation gives only a qualitative estimation of the CuO/Cu_2O phase ratio in the prepared thin films. The X-ray diffraction profiles were fitted using a pseudo-Voigt analysis procedure to extract the above parameters [69]. ***Figure 5.5*** also depicts the crystallite size determined using the procedure from Monshi *et al.* [70] as detailed in the ***Chapter 2***. The Cu_2O crystallite size seen at lower temperature (230 °C) is around 20 nm, which is close to the values often achieved for sprayed Cu_2O thin films using glucose, such as in [71], and greater than the value acquired for the first and only work employing D-sorbitol [59]. For comparable preparation temperatures, grain sizes in sputtered polycrystalline Cu_2O thin films can reach up to roughly 200 nm [17]. The crystallite size changes somewhat (up to 30 nm) as the temperature rises. Due to grain coalescence, such an increase in preparation temperature is commonly observed [17]. Since the CuO phase arises and becomes to dominate in our case, the transition cannot be described just by temperature-related grain coalescence. A limiting factor for the Cu_2O crystallite size increase could be the formation of CuO at the grain boundaries [72].

The observed phase transition between Cu_2O and CuO employing D-sorbitol as a novel reducing agent follows a similar pattern to that seen using glucose as a reducing agent [52]. The copper acetate precursor solution decomposes into CuO in ambient air without the use of a reducing agent such as glucose or, in our instance, D-sorbitol.

The formation of Cu_2O using spray pyrolysis preparation method can happen mostly by two chemical paths which are already detailed in the ***Section 5.3.1.1*** of this chapter.

Figure 5.5: The crystallite size and CuO/Cu_2O phase integrated peak intensity ratio with respect to the preparation temperature.

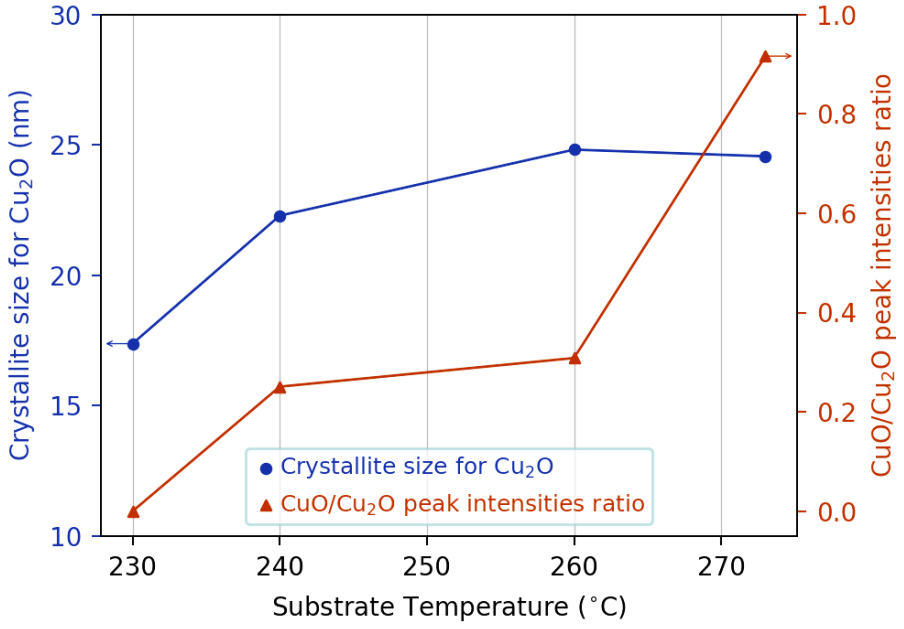

The oxidation rate of Cu_2O into CuO increases as the temperature rises, limiting the influence of the D-sorbitol reducing agent and explaining the evolution of the X-ray diffraction peaks. This agrees with the temperature range reported in [52] and the temperature profile recorded directly on the substrate as shown in the ***Figure 5.3***, indicating the temperature at which the pyrolytic reaction takes place. Furthermore, in ambient air, the formed thin films can be oxidized to generate CuO [73].

Micro-Raman measurements were taken on the produced copper oxide thin films to complete the structural study. ***Figure 5.6 (a, b, c & d)*** show Raman line-scans of samples prepared at temperatures of 230 °C, 240 °C, 260 °C, and 273 °C, respectively, with a lateral resolution of 1 µm. ***Table 5.3*** lists the primary Cu_2O and CuO Raman peaks that have been identified in the literature, along with their values and symmetry.

Cu_2O is a distinctive semiconductor from the standpoint of Raman spectroscopy because the theoretically predicted active Raman mode (T_{2g}) is rarely observed, whereas two peaks related to defects and breaking the selection rules, T_{1u} and $2E_u$, are consistently observed and dominate the Raman spectra [74–77]. These peaks are due to point defects related to the p-type doping of Cu_2O.

Table 5.3: Cu_2O, CuO, and Cu_4O_3 Raman peaks**.** Peak position is shown as a single value or a range of values, according to experimental or calculated data that has been published in the literature [74–77]. The corresponding Raman modes assigned to the peak are also shown. The peaks marked with an asterisk and bold are the most intense ones that were observed. Only the T_{2g} peak in Cu_2O is anticipated to be Raman active theoretically [75], however the two peaks T_{1u} and $2E_u$ are systematically seen and dominate the Raman spectra. These peaks are linked to point defects related to the p-type doping of Cu_2O [76]. In our thin films, the Cu_4O_3 phase Raman peaks were not detected.

Film	**Raman Shift (cm^{-1})**	**Mode**
Cu_2O	[140,160] ; 220 ; [500,550]	T_{1u}*; $2E_u$*; T_{2g}
CuO	[282,303] ; [330,350] ; [616,636]	A_g*; B_g*; B_g
Cu_4O_3	318 ; 510 ; 541	E_g; E_g; A_{1g}*

The Raman peaks associated with the Cu_4O_3 copper oxide paramelaconite phase were absent from our thin films. The CuO phase is not detectable in the sample prepared at 230 °C, as seen from the line-scans. This result agrees very well with X-ray diffraction measurements that reveal no CuO signature al the lowest preparation temperature. Even while the signal from Cu_2O is still prominent, the CuO Raman peaks are seen when the preparation temperature is raised to 240 °C. The CuO phase becomes totally dominant as the preparation temperature rises. In fact, because the response from the sample surface dominates the Raman signal, this result simply reveals that the thin films are covered by CuO, leaving no assumptions regarding the composition of the bulk and grains.

Transmittance spectroscopy was used to investigate the effect of preparation temperature on optical properties and to establish the relationship between these properties and the thin film structural properties. The transmission spectra are plotted with respect to the preparation temperatures in ***Figure 5.7***.

The absorption edge of Cu_2O is apparent at temperatures of 230 °C and 240 °C, while another absorption edge (due to formation of CuO) appeared at temperatures of 260 °C and 273 °C, keeping consistency with the previously reported XRD and Raman analysis. The use of the Tauc model yields the bandgap values illustrated in ***Figure 5.8***, which range between 2.38 eV and 2.34 eV with increase in the preparation temperature.

Figure 5.6: Raman line-scan spectra of copper oxide thin films with respect to different preparation temperatures: **(a)**: 230 °C ; **(b)**: 240 °C ; **(c)**: 260 °C ; **(d)**: 273 °C. All measurements were systematically replicated in different spots on the sample surface, with a lateral resolution of 1 µm (for a total scan width of 7 µm).

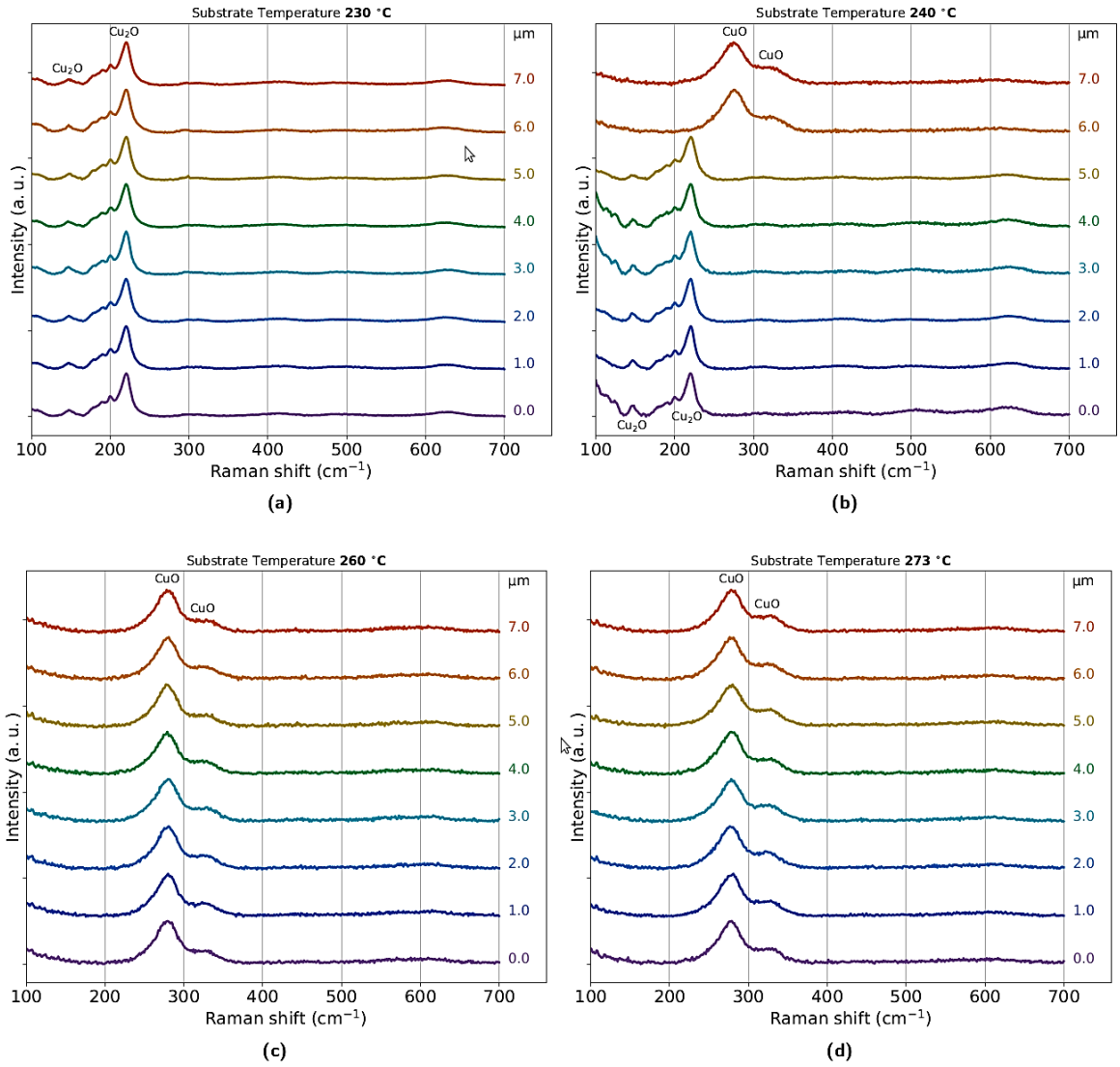

Figure 5.7: Transmission spectra for copper oxide thin films with respect to the preparation temperature.

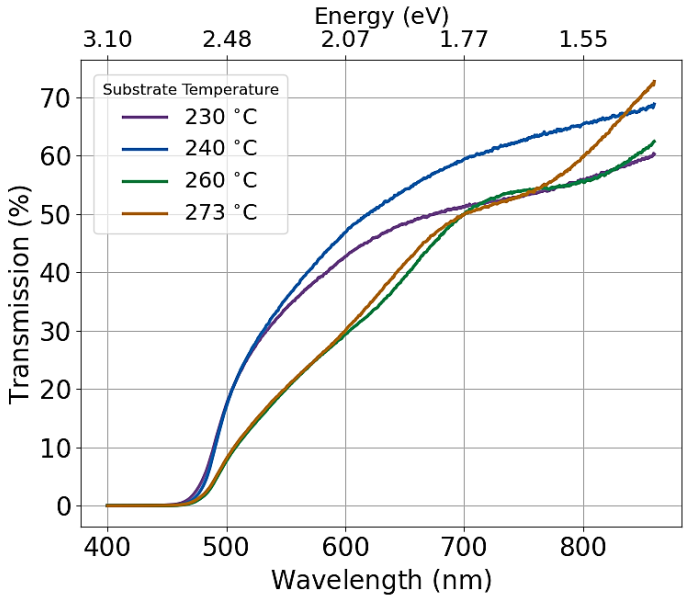

Figure 5.8: Tauc plots of the transmission spectra with respect to temperatures.

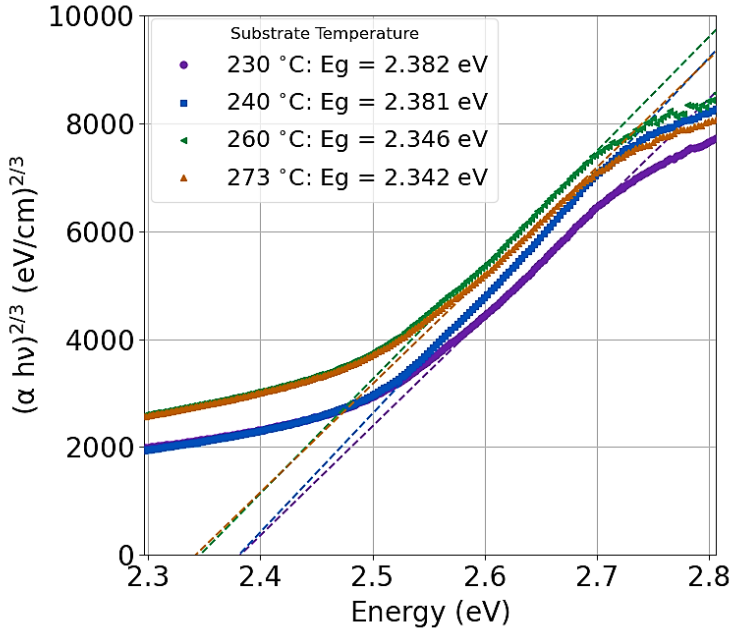

The Tauc model (including the indirect bandgap of CuO, ***Figure 5.9***) predicts a bandgap of 1.16 eV for the CuO phase at higher temperatures and a bandgap of 2.38 eV for Cu_2O at lower temperatures (***Figure 5.8***). These bandgap values are slightly different than those achieved using other preparation techniques such sputtering [78], and the value obtained using D-sorbitol as a reducing agent in ultrasonic spray pyrolysis [59]. The first difference in bandgap values when compared to

sputtering is typical and here too low to be meaningful, while the second difference could be attributable to the impact of the CuO phase, still present in the films, and the bandgap extraction procedure (***Section 2.7.2*** of ***Chapter 2*** gives details about the Tauc model). ***Figure 5.9*** shows an indirect bandgap value for CuO that is consistent with values commonly published [79]. ***Figure 5.10*** shows the extracted Urbach energy, which increases noticeably as the preparation temperature rises, which is compatible with Raman and X-ray diffraction studies demonstrating an increase in the proportion of CuO phase.

Figure 5.9: Tauc plot for the CuO phase for preparation temperatures of 260 °C and 273 °C, are plotted. The indirect bandgap model was utilized to compute the bandgap energy for the CuO phase, while the direct model was employed for the Cu_2O phase.

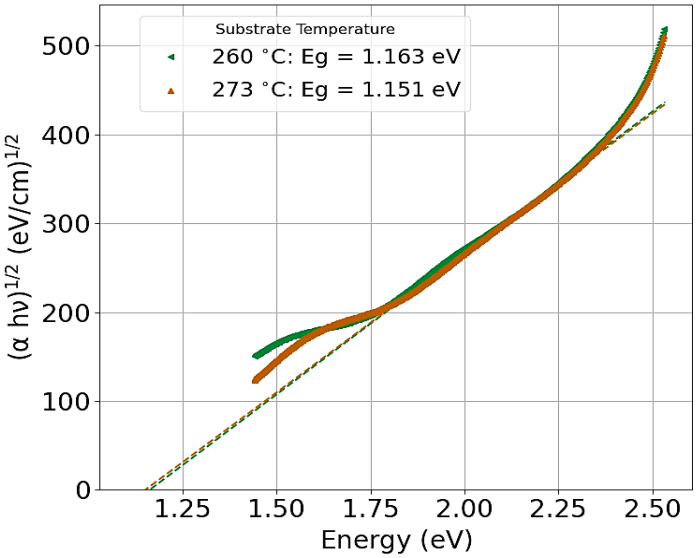

Figure 5.10: Absorption coefficient and the Urbach energies for Cu_2O and CuO thin films.

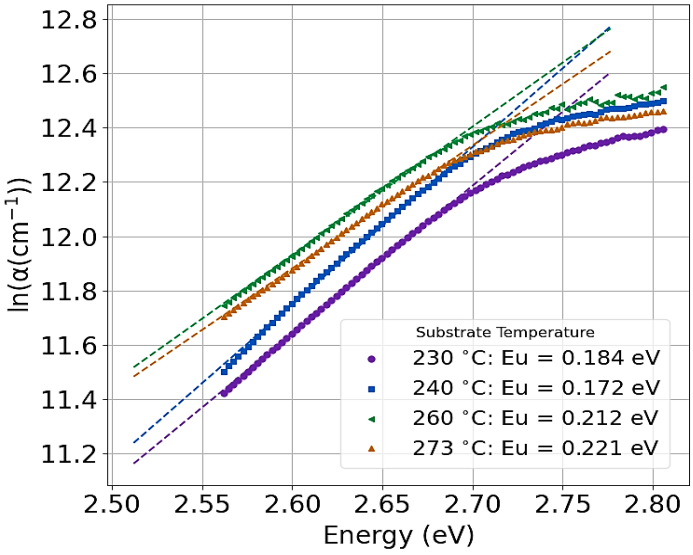

5.4.2 Effect of the D-Sorbitol Reducing Agent on the Structural and Optical Properties of Cu_2O

To understand in-depth the effect of D-sorbitol, which is a novel reducing agent, we set the preparation temperature to 240 °C and the copper acetate concentration to 0.025 mol/L, then adjusted the D-sorbitol concentration from 0 to 0.0750 mol/L in steps of 0.0125 mol/L. By consistently preparing a set of solutions with the same concentration and frequently preparing samples in the same conditions, the repeatability of the preparation process was tested. The Raman spectra for D-sorbitol concentration are shown in ***Figure 5.11***. The Raman spectra of all samples prepared without D-sorbitol (concentration 0 mol/L) reveal just the CuO phase peaks, as expected when employing a precursor solution without a reducing agent. In addition, another broad peak was found at roughly 1100 cm^{-1} for these samples without the reducing agent, which was tentatively assigned to multiphonon scattering or defects generated by the incomplete pyrolytic reaction.

The Raman results correlate well with XRD measurements shown in ***Figure 5.11*** for the same copper oxide films prepared with different D-sorbitol concentrations. For the sample prepared without D-sorbitol, the peaks of the monoclinic CuO phase are identified. With the addition of D-sorbitol, only the Cu_2O cubic phase is detected, as already evidenced in the Raman spectra.

Figure 5.11: Raman spectra of copper oxide thin films with respect to the concentration of D-sorbitol reducing agent. The preparation temperature is set at 240 °C (corresponding to a set temperature of 390 °C). M is the net concentration which can also be represented as mol/L. The peak fitting using the Lorentzian function is represented by black lines.

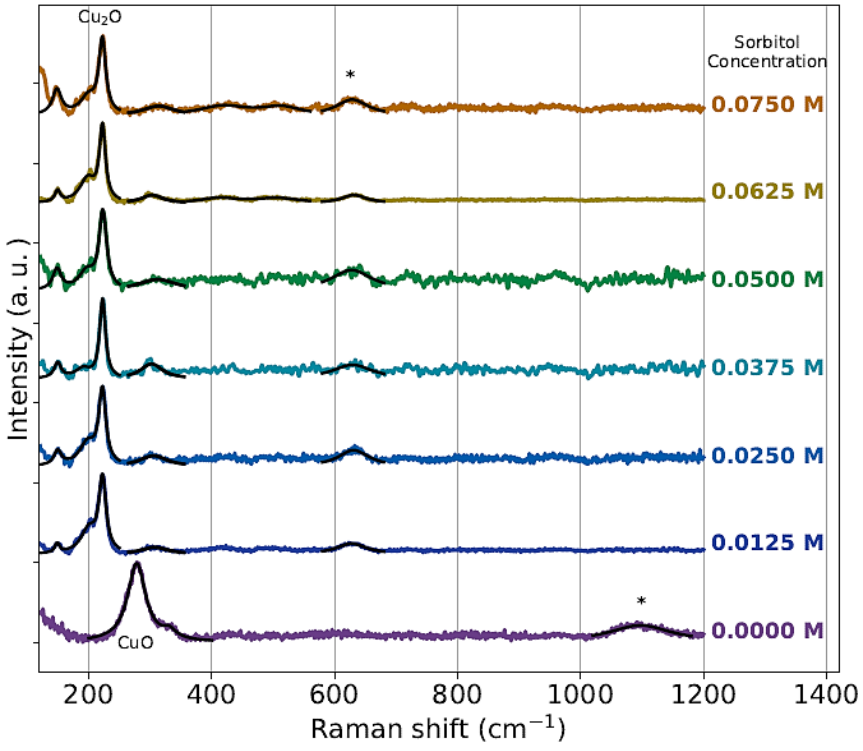

When D-sorbitol is added to the precursor solution, the Cu_2O phase appears, with no apparent CuO peaks. As previously described in the ***Section 5.3.1.1***, D-sorbitol's role in the formation of the Cu_2O phase is illustrated here. ***Figure 5.13*** shows how this action is observable in the optical transmission. Indeed, in the absence of D-sorbitol, only the CuO absorption edge is visible due to the low transparency. When the reducing agent is added to the solution at a concentration of 0.0125 mol/L, the transparency increases, and the absorption edge solely shows the presence of the Cu_2O phase (***Figure 5.14***), as the Raman and XRD measurements have shown. With values near to what we measured with respect to the preparation temperature, the derived bandgap values support the impact of D-sorbitol in preventing the formation of CuO. When the ratio of D-sorbitol to copper acetate achieves 1:1 stoichiometry, the bandgap and Urbach energy stay steady with the reducing agent concentration as shown in the ***Figure 5.15***. This finding shows that the conditions for preparing single phase Cu_2O can be achieved by using a relatively low reducing agent concentration and subsequently minimizing the carbon-related secondary products in thin films.

Figure 5.12: XRD diffractograms of copper oxide thin films with respect to the D-sorbitol concentration. Black lines represent the diffractogram fitting using a pseudo-Voigt peak function.

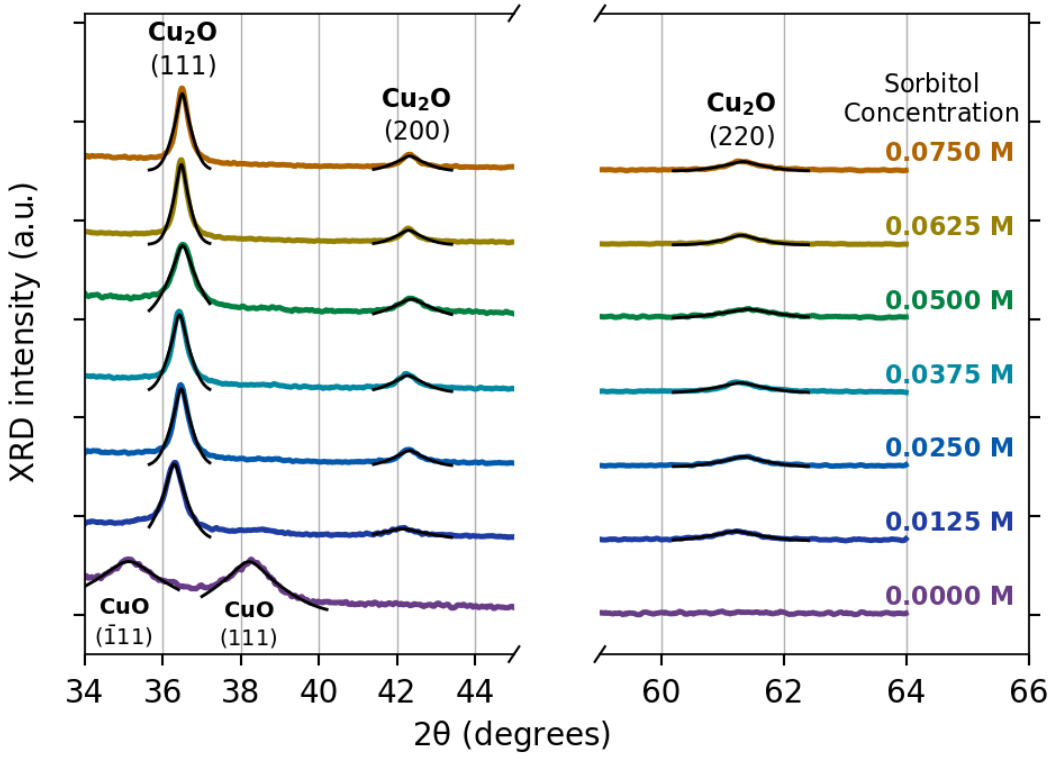

Figure 5.13: Transmission spectra for copper oxide thin films with respect to the D-sorbitol concentration.

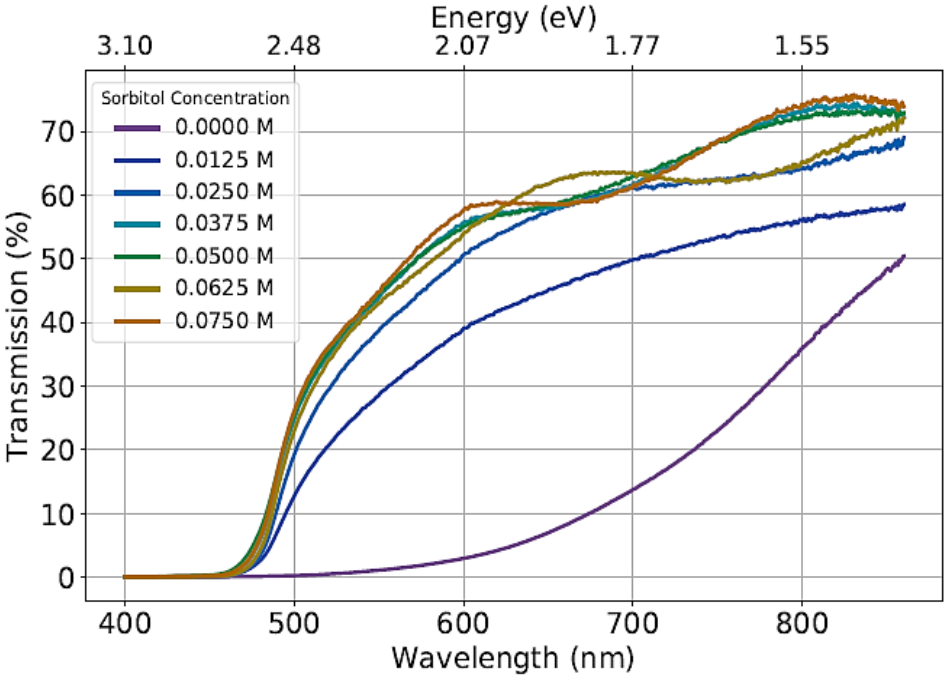

Figure 5.14: Tauc plots with respect to the sorbitol concentration for the Cu_2O thin films with respect to the D-sorbitol concentration.

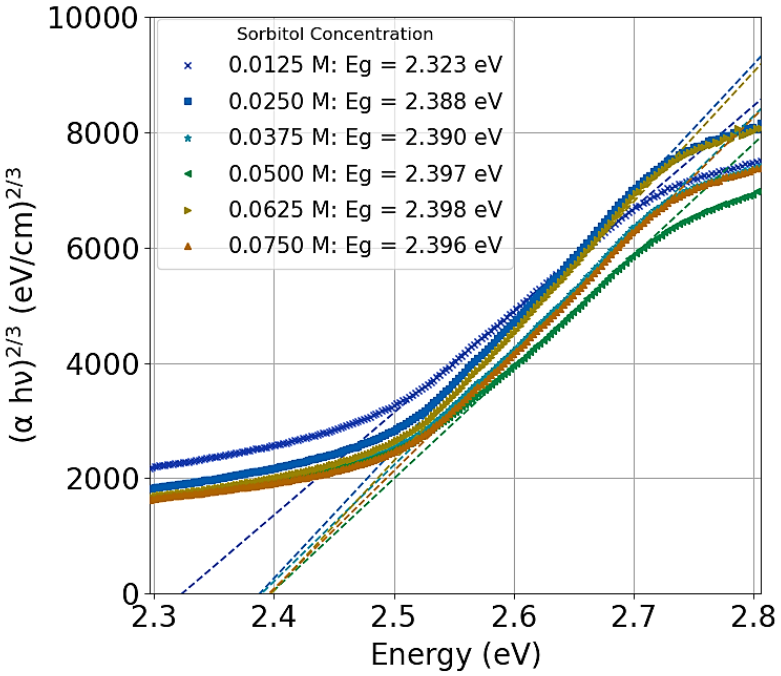

Figure 5.15: Bandgap and Urbach energy variation for Cu_2O thin films with respect to the D-sorbitol concentration.

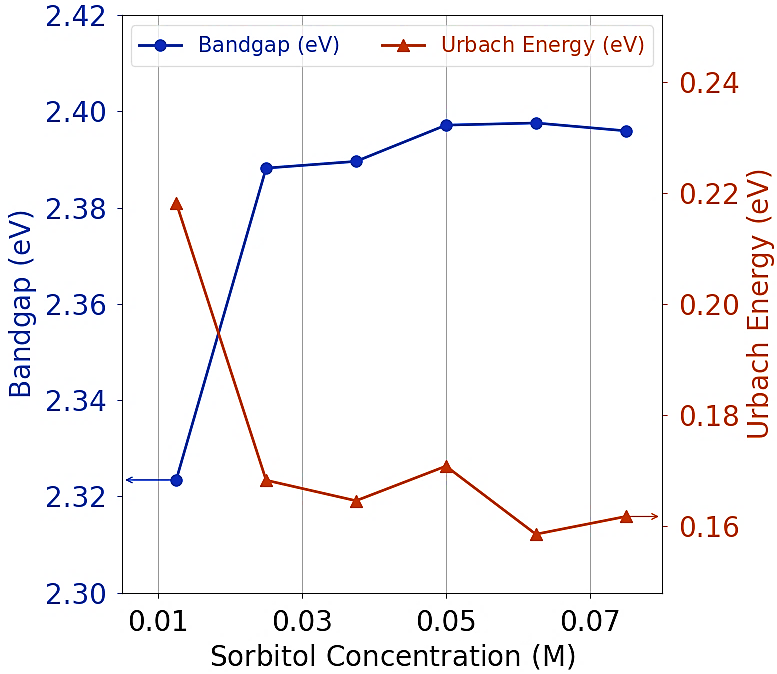

5.4.3 Electrical and Morphological Properties of the Prepared Cu_2O Films

The objective of the electrical study was to check for the ohmicity of the gold contacts on the Cu_2O prepared samples. 200 nm of gold was deposited on the prepared samples. The samples with the low preparation temperatures (230 °C and 240 °C) were chosen as in these samples the Cu_2O phase is dominant. The Cu_2O was films considered for the studies in this section is prepared with a pH of 2.8 and a D-sorbitol concentration of 0.05 mol/L in the precursor solution. The chosen samples with the gold contacts are shown in the ***Figure 5.16***. The samples (a) and (b) are prepared at 230 °C, while (c) prepared at 240 °C. The corresponding I-V curves are shown in the ***Figures 5.17, 5.18 & 5.19*** respectively.

Figure 5.16: Gold contact on different copper oxide samples. Samples **(a)** and **(b)** are prepared at 230 °C, while **(c)** prepared at 240 °C.

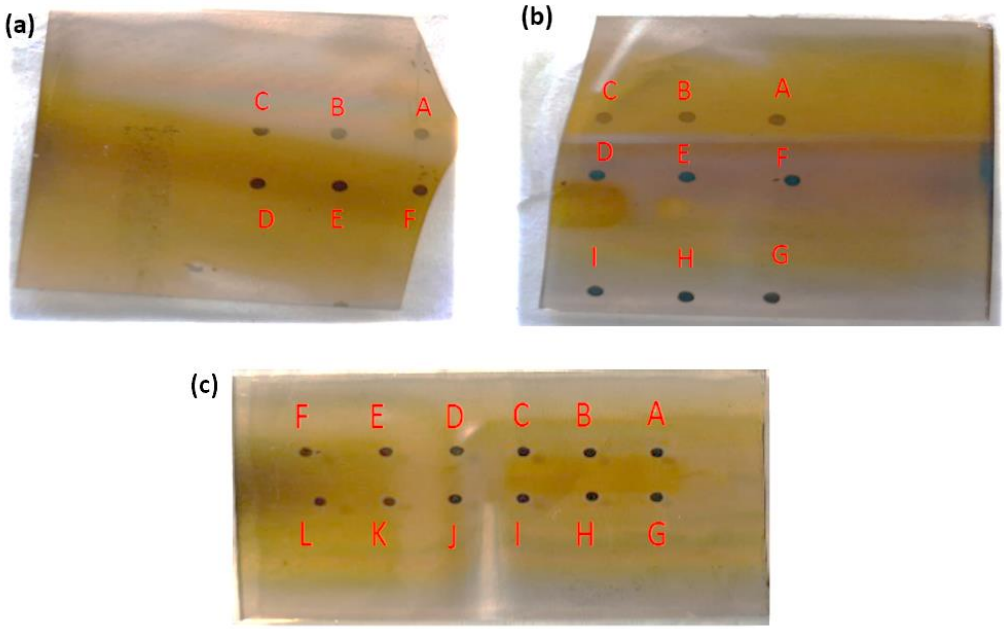

All the realized contacts showed a good ohmicity with a linear I-V characteristic as shown in the ***Figures 5.17, 5.18 & 5.19***. This shows that gold is well suited to make ohmic contacts on Cu_2O and that the interface does not impact negatively on the electrical properties of the Au/Cu_2O contact.

Figure 5.17: The current-voltage characteristic between different contacts of gold on copper oxide: Sample (a) prepared at 230 °C. The current maximum scale is at 1.00 × 10^{-5} A.

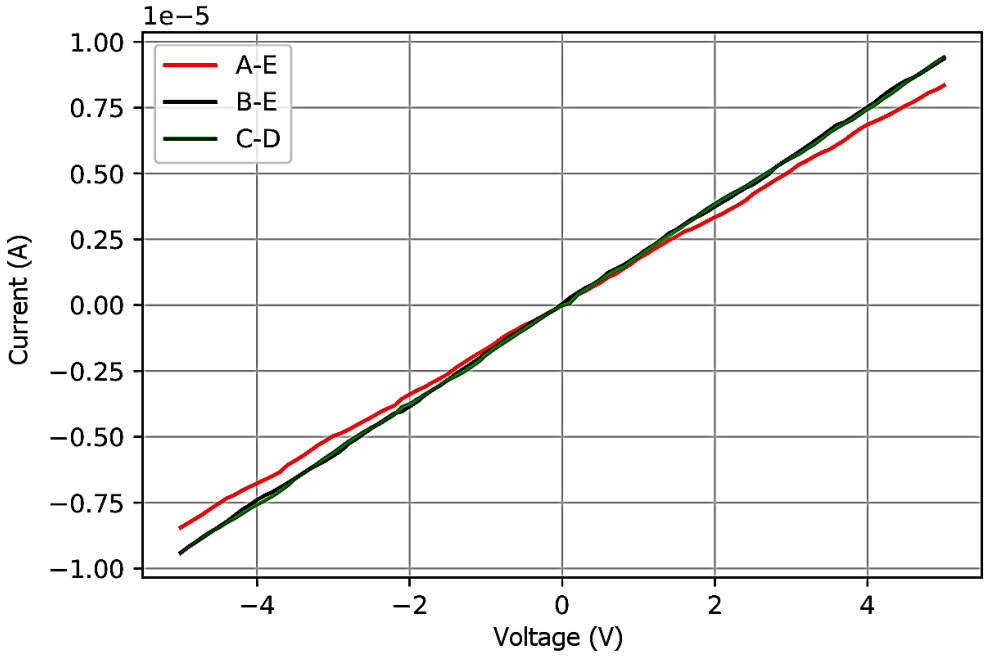

Figure 5.18: The current-voltage characteristic between different contacts of gold on copper oxide: Sample (b) prepared at 230 °C. The current maximum scale is at 8 × 10^{-6} A.

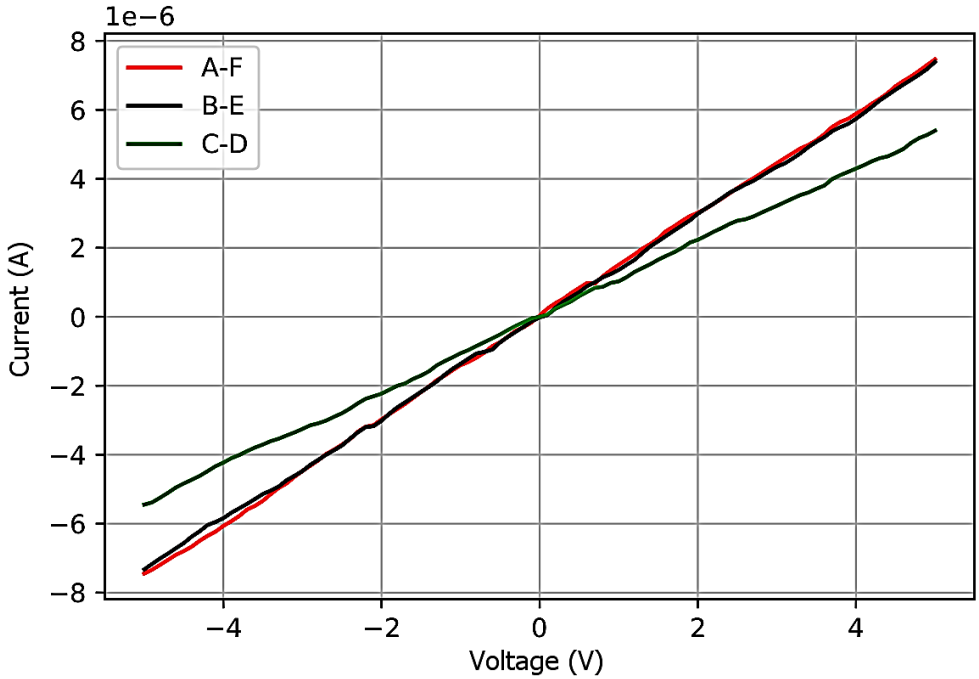

Figure 5.19: The current-voltage characteristic between different contacts of gold on copper oxide: Sample (c) prepared at 240 °C. The current maximum scale is at 5 × 10^{-6} A.

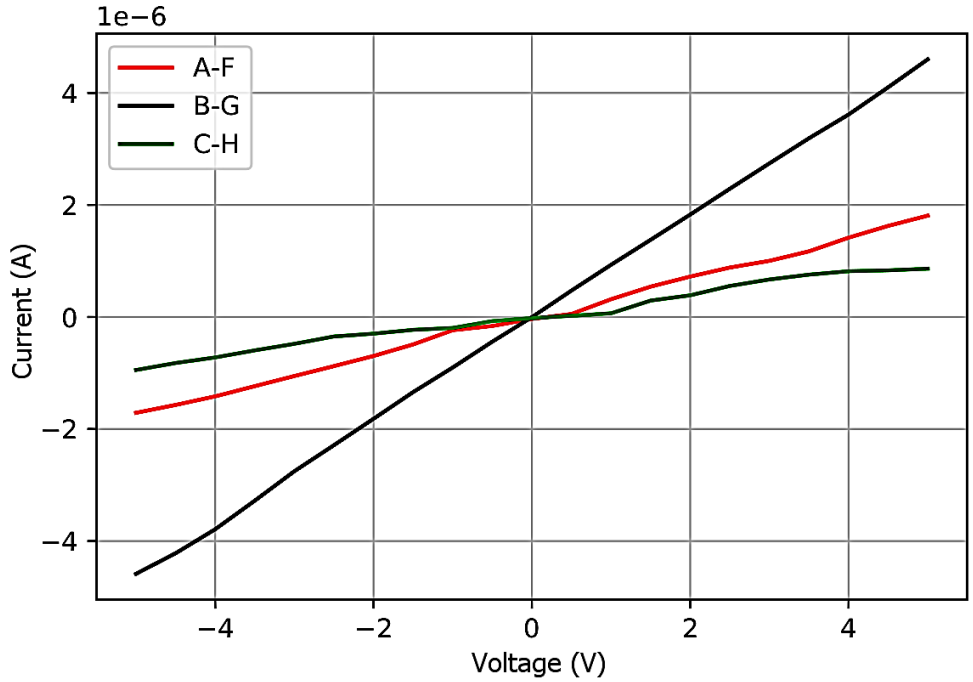

The same samples (a & c) were annealed and then measured again to check if there is any difference in ohmicity after the annealing. The annealing was done only after the gold contact deposition. The annealing for all the samples was performed in an oven for 15 minutes in a controlled atmosphere at 250 °C. As an example, the I-V characteristics before and after annealing are shown in the ***Figures 5.20 & 5.21*** respectively.

Figure 5.20: The current-voltage characteristic before annealing between different contacts of gold on copper oxide for sample (a) prepared at 230 °C. The current maximum scale is at 4×10^{-6} A.

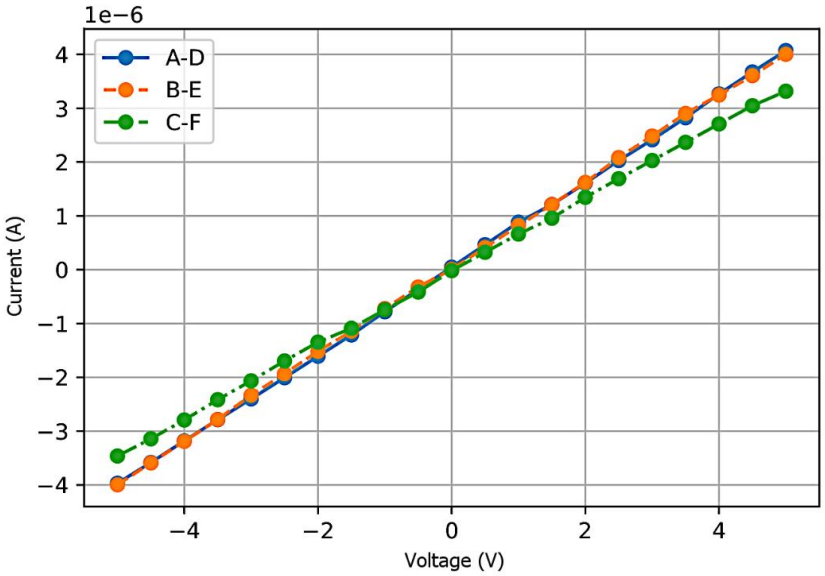

Figure 5.21: The current-voltage characteristic after annealing between different contacts of gold on copper oxide for sample (c) prepared at 240 °C. The current maximum scale is at 4×10^{-6} A.

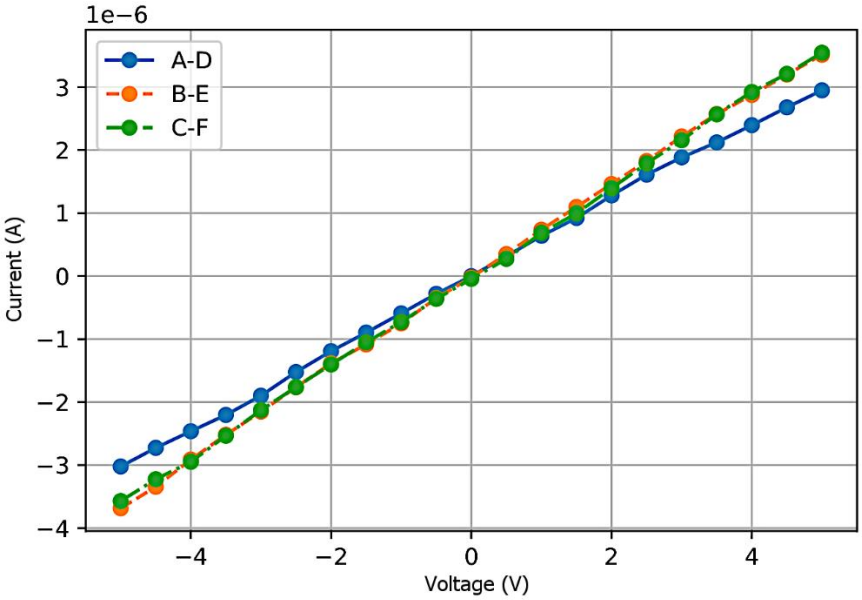

It is seen that there is not a big difference between the I-V characteristic before and after annealing (***Figures 5.20 & 5.21***) because the ohmic contact and the interface were already in good quality. The annealing therefore does not modify the electrical properties of the Au/Cu_2O contact.

As we have seen that good quality ohmic contacts were obtained using gold contacts on the Cu_2O thin films, we measured the other important electrical parameters (resistivity, p-type carrier concentration & mobility) using the van der Pauw / Hall Effect method. The results for the sample (c) prepared at 240 °C are shown in the ***Figure 5.22***.

Figure 5.22: The electrical parameters of copper oxide using gold contacts measured using the van der Pauw / Hall Effect method: Sample (c) prepared at 240 °C.

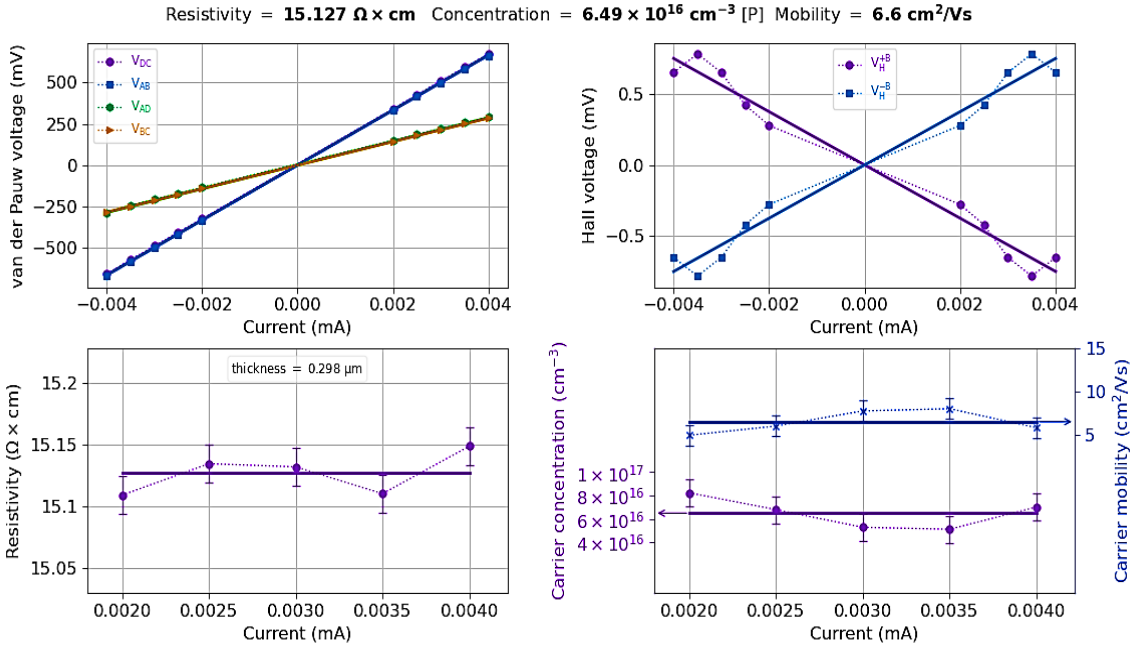

The electrical properties of the prepared Cu_2O thin films using this ultrasonic spray pyrolysis were tested, and a p-type conductivity was observed for the first time with the D-sorbitol reducing agent, with a carrier concentration of around 6×10^{16} cm^{-3}, a mobility of about 7 cm^2/Vs, and resistivity of 15 Ω×cm. The electrical properties were improved for the Cu_2O thin film of sample (a) which was prepared at 230 °C. This is because there is no formation of CuO phase, and the thin film is composed entirely of the Cu_2O phase. Carrier concentration of around 5×10^{16} cm^{-3}, a mobility of about 12 cm^2/Vs, and a lower resistivity of 10 Ω×cm is measured for this sample. The mobility is higher than that of spray pyrolysis [71] previously and comparable to that of thin films formed by sputtering [17]. This first electrical evaluation paves the way for a further in-depth examination of the transport properties and their improvement for optoelectronic applications using ultrasonic spray pyrolysis prepared Cu_2O thin films.

The copper oxide thin films prepared at 230 °C and 240 °C are checked for their surface morphologies by means of SEM. High magnification was used to visualize closely the distribution of the grains, their shapes, and sizes. The images were taken with a beam voltage at 2.0 kV and using an InLens detector.

For the sample prepared at 230 °C, we observe several things. First, the surface presents some moderate roughness in agreement with the previous observations of a non-uniform surface for e.g., in sputtering. Second, the sample is substantially uniform: we do not observe any difference in the morphology with respect to the position. The top surface image is shown in the ***Figure 5.23***. A cross-section of the film is also analyzed in the ***Figure 5.24*** with a much larger view of the film surface.

Figure 5.23: SEM surface image of Cu_2O thin film prepared at 230 °C.

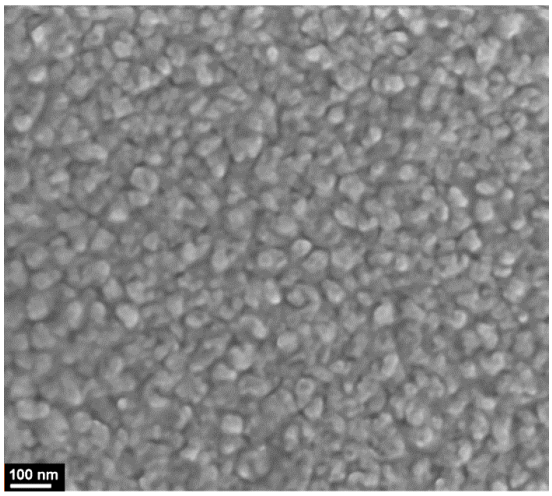

Figure 5.24: A lateral cum cross-sectional view taken using SEM for the same Cu_2O thin film prepared at 230 °C. The Cu_2O film thickness (marked by the white arrow) is about 300 nm.

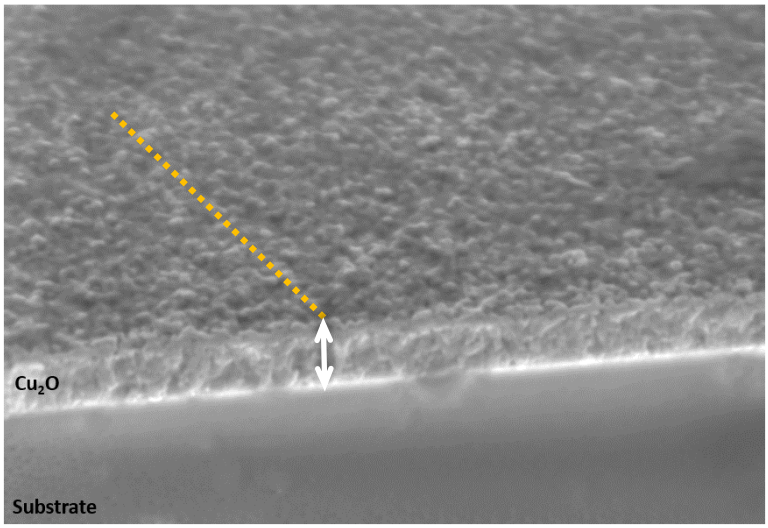

The top surface image of the Cu_2O film, prepared at 240 °C is presented in the ***Figure 5.25***. Uniform distribution of grains is visible with variable shapes, mostly rounded, with a diameter of about 50 nm for Cu_2O film prepared at 230 °C. Some bigger clusters are seen in the case of Cu_2O film prepared at 240 °C. It might be possible that the copper on the surface has started to be oxidized but is does not show any drastic change. Except the clusters, we could not isolate any major difference in the surface of the samples.

Figure 5.25: SEM surface image of Cu_2O thin film prepared at 240 °C.

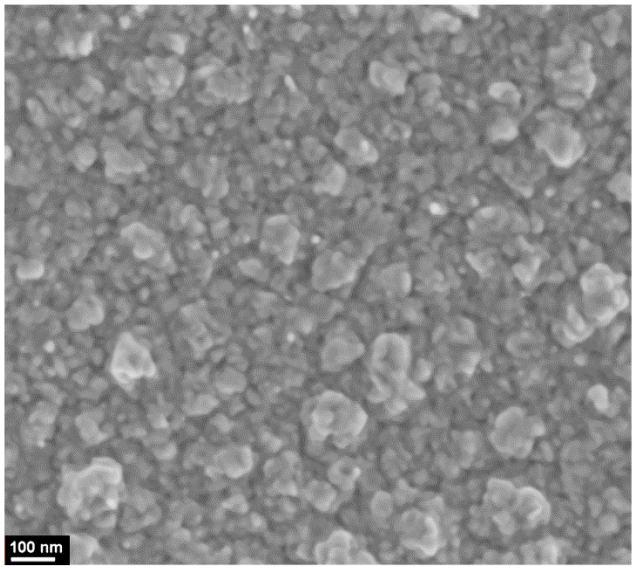

5.5 Challenges Faced Towards the Preparation of Cu_2O

The most important factor in the preparation of Cu_2O is the preparation temperature. We did an in-depth analysis to find the relation between the set and the actual spray preparation temperatures. The temperature plays an important role in controlling the rate of oxidation and the efficiency of the reducing agent. At higher temperatures, the efficiency of the reducing agent is diminished which paves the way for the formation of unwanted copper phases such as cupric oxide (CuO). By chance if CuO especially in nanoparticle condition is formed it can be toxic too [80]. The major disadvantage that CuO can cause is that introduce deep level trap states at the interface of the heterojunctions which will act as recombination centres for the charge carrier. This can impact greatly in the performance of solar cells and so CuO formation is highly undesirable. We tried to prepare the films at the lowest possible temperature so that the phase of CuO can be avoided in the films. It must also be taken care that the temperature should be such that the pyrolysis reaction is complete. Incomplete pyrolysis can deposit unwanted by-products such as sugar and sugar-based alcohols. D-sorbitol is chosen for this reason as it can decompose at low temperatures and can only give rise to non-

harmful by-products such as CO_2 and H_2. But control on the concentration of D-sorbitol in conjunction with the concentration of copper acetate and the pH in the precursor solution is very important. Once these are controlled, the other spray parameters need to be varied and then fixed to certain values so that a complete pyrolysis takes place to form thin films with only Cu_2O phase. The analysis through the design of experiments helped us to successfully prepare the films with the desired phase.

5.6 Chapter Conclusions

A detailed structural and optical investigation was carried out to evaluate the phase transition in copper oxide thin films prepared by ultrasonic spray pyrolysis with D-sorbitol, a new precursor solution reducing agent. Regarding the carefully determined preparation temperature, the study reveals the best range in which the single Cu_2O phase can be formed in the same way as with glucose, but with fewer carbon-related defects caused by pyrolytic reaction by-products. Indeed, the research of D-sorbitol concentration demonstrates that the optimal features were attained without the use of excessive D-sorbitol in comparison to copper acetate, as is common when utilizing glucose as the reducing agent. Using a lower concentration of reducing agent results in fewer pyrolysis secondary products, decreasing the defects, and improving electrical characteristics for optoelectronic applications.

To summarize: the ultrasonic spray pyrolysis preparation of copper oxide thin films was developed and optimized using a new reducing agent, D-sorbitol. A comprehensive optical and structural study was performed. The optimization of the preparation temperature using low concentration reducing agent was conducted to obtain single-phase cuprous oxide Cu_2O with good optical and structural properties.

5.7 References

[1] L. Gao, C. Pang, D. He, L. Shen, A. Gupta, N. Bao, Synthesis of Hierarchical Nanoporous Microstructures via the Kirkendall Effect in Chemical Reduction Process, Sci. Rep. 5 (2015) 16061. https://doi.org/10.1038/srep16061.

[2] B.K. Meyer, A. Polity, D. Reppin, M. Becker, P. Hering, P.J. Klar, T. Sander, C. Reindl, J. Benz, M. Eickhoff, C. Heiliger, M. Heinemann, J. Bläsing, A. Krost, S. Shokovets, C. Müller, C. Ronning, Binary copper oxide semiconductors: From materials towards devices, Phys. Status Solidi. 249 (2012) 1487–1509. https://doi.org/10.1002/pssb.201248128.

[3] S.T. Omelchenko, Y. Tolstova, H.A. Atwater, N.S. Lewis, Excitonic Effects in Emerging Photovoltaic Materials: A Case Study in Cu_2O, ACS Energy Lett. 2 (2017) 431–437. https://doi.org/10.1021/acsenergylett.6b00704.

[4] T. Kazimierczuk, D. Fröhlich, S. Scheel, H. Stolz, M. Bayer, Giant Rydberg excitons in the copper oxide Cu2O, Nature. 514 (2014) 343–347. https://doi.org/10.1038/nature13832.

[5] M. Saffman, T.G. Walker, K. Mølmer, Quantum information with Rydberg atoms, Rev. Mod. Phys. 82 (2010) 2313–2363. https://doi.org/10.1103/RevModPhys.82.2313.

[6] C. Malerba, F. Biccari, C. Leonor Azanza Ricardo, M. D'Incau, P. Scardi, A. Mittiga, Absorption coefficient of bulk and thin film Cu2O, Sol. Energy Mater. Sol. Cells. 95 (2011) 2848–2854. https://doi.org/10.1016/j.solmat.2011.05.047.

[7] F. Schöne, H. Stolz, N. Naka, Phonon-assisted absorption of excitons in Cu_2O, Phys. Rev. B. 96 (2017) 115207. https://doi.org/10.1103/PhysRevB.96.115207.

[8] Y. Wang, P. Miska, D. Pilloud, D. Horwat, F. Mücklich, J.F. Pierson, Transmittance enhancement and optical band gap widening of Cu_2O thin films after air annealing, J. Appl. Phys. 115 (2014) 073505. https://doi.org/10.1063/1.4865957.

[9] F. Schweiner, Theory of excitons in cuprous oxide, University of Stuttgart, 2017. https://doi.org/10.18419/opus-9483.

[10] A. Soon, X.-Y. Cui, B. Delley, S.-H. Wei, C. Stampfl, Native defect-induced multifarious magnetism in nonstoichiometric cuprous oxide: First-principles study of bulk and surface properties of $Cu_{2-\delta}O$, Phys. Rev. B. 79 (2009) 035205. https://doi.org/10.1103/PhysRevB.79.035205.

[11] D.O. Scanlon, B.J. Morgan, G.W. Watson, A. Walsh, Acceptor Levels in p-Type Cu_2O : Rationalizing Theory and Experiment, Phys. Rev. Lett. 103 (2009) 096405. https://doi.org/10.1103/PhysRevLett.103.096405.

[12] G.K. Paul, R. Ghosh, S.K. Bera, S. Bandyopadhyay, T. Sakurai, K. Akimoto, Deep level transient spectroscopy of cyanide treated polycrystalline p-Cu_2O/n-ZnO solar cell, Chem. Phys. Lett. 463 (2008) 117–120. https://doi.org/10.1016/j.cplett.2008.08.065.

[13] Y. Wang, J. Ghanbaja, D. Horwat, L. Yu, J.F. Pierson, Nitrogen chemical state in N-doped Cu2O thin films, Appl. Phys. Lett. 110 (2017) 131902. https://doi.org/10.1063/1.4979140.

[14] D.O. Scanlon, G.W. Watson, Uncovering the Complex Behavior of Hydrogen in Cu_2O, Phys. Rev. Lett. 106 (2011) 186403. https://doi.org/10.1103/PhysRevLett.106.186403.

[15] B.P. Rai, Cu_2O solar cells: A review, Sol. Cells. 25 (1988) 265–272. https://doi.org/10.1016/0379-6787(88)90065-8.

[16] K. Mizuno, M. Izaki, K. Murase, T. Shinagawa, M. Chigane, M. Inaba, A. Tasaka, Y. Awakura, Structural and Electrical Characterizations of Electrodeposited p-Type Semiconductor Cu_2O Films, J. Electrochem. Soc. 152 (2005) C179. https://doi.org/10.1149/1.1862478.

[17] Y.S. Lee, M.T. Winkler, S.C. Siah, R. Brandt, T. Buonassisi, Hall mobility of cuprous oxide thin films deposited by reactive direct-current magnetron sputtering, Appl. Phys. Lett. 98 (2011) 192115. https://doi.org/10.1063/1.3589810.

[18] D. Muñoz-Rojas, M. Jordan, C. Yeoh, A.T. Marin, A. Kursumovic, L.A. Dunlop, D.C. Iza, A. Chen, H. Wang,

J.L. MacManus Driscoll, Growth of ~5 cm^2/Vs mobility, p-type Copper(I) oxide (Cu_2O) films by fast atmospheric atomic layer deposition (AALD) at 225°C and below, AIP Adv. 2 (2012) 042179. https://doi.org/10.1063/1.4771681.

[19] H. Shimada, T. Masumi, Hall Mobility of Positive Holes in Cu2O, J. Phys. Soc. Japan. 58 (1989) 1717–1724. https://doi.org/10.1143/JPSJ.58.1717.

[20] B.A. Tazenkov, F.A. Gruzdev, Positive and negative photomemory in cuprous oxide, Sov. Phys. - Solid State. 16 (1974) 460.

[21] M. Zouaghi, M. Tapiero, J.P. Zielinger, R. Burgraf, Hall mobility and hole density in photoactivated Cu2O single crystals, Solid State Commun. 8 (1970) 1823–1825. https://doi.org/10.1016/0038-1098(70)90325-X.

[22] R. Kužel, F.L. Weichman, Surface and Bulk Conductivities of Cu_2O Single Crystals, J. Appl. Phys. 41 (1970) 271–279. https://doi.org/10.1063/1.1658333.

[23] F. Biccari, Defects and Doping in Cu_2O, Sapienza – University of Rome, 2009.

[24] V.N. Dobrovol'skii, Y.I. Gritsenko, Use of the Hall current for investigation of carrier scattering in semiconductors, Sov. Phys. - Solid State. 4 (1963).

[25] P.W. Baumeister, Optical Absorption of Cuprous Oxide, Phys. Rev. 121 (1961) 359–362. https://doi.org/10.1103/PhysRev.121.359.

[26] J.B. Grun, M. Sieskind, S. Nikitine, Etude spectrophotometrique des spectres continus de Cu_2O a diverses temperatures, J. Phys. Chem. Solids. 19 (1961) 189–197. https://doi.org/10.1016/0022-3697(61)90028-2.

[27] T. Ito, H. Yamaguchi, K. Okabe, T. Masumi, Single-crystal growth and characterization of Cu_2O and CuO, J. Mater. Sci. 33 (1998) 3555–3566. https://doi.org/10.1023/A:1004690809547.

[28] S. Nikitine, Excitons BT - Optical Properties of Solids: Papers from the NATO Advanced Study Institute on Optical Properties of Solids Held August 7–20, 1966, at Freiburg, Germany, in: S. Nudelman, S.S. Mitra (Eds.), Springer US, Boston, MA, 1969: pp. 197–237. https://doi.org/10.1007/978-1-4757-1123-3_9.

[29] J.-L. Calais, Introduction to solid state theory (Springer series in solid state sciences . Vol. 2) by O. Madelung, Acta Crystallogr. Sect. A. 35 (1979) 1087–1088. https://doi.org/10.1107/S0567739479002357.

[30] P.Y. Yu, M. Cardona, Fundamentals of Semiconductors, Springer Berlin Heidelberg, Berlin, Heidelberg, 2010. https://doi.org/10.1007/978-3-642-00710-1.

[31] R.J. Elliott, Intensity of Optical Absorption by Excitons, Phys. Rev. 108 (1957) 1384–1389. https://doi.org/10.1103/PhysRev.108.1384.

[32] P. Dawson, M.M. Hargreave, G.R. Wilkinson, The dielectric and lattice vibrational spectrum of cuprous oxide, J. Phys. Chem. Solids. 34 (1973) 2201–2208. https://doi.org/10.1016/S0022-3697(73)80067-8.

[33] L. Tertian, D. Hokim, J.P. Rivière, Transformations in thin foils of cuprous oxide as observed in an electron microscope, J. Phys. 39 (1978) 1135–1139. https://doi.org/10.1051/jphys:019780039010011350O.

[34] R.A. Yund, G. Kullerud, Stable mineral assemblages of anhydrous copper and iron oxides, Am. Mineral. 49 (1964) 689–696.

[35] L. Schramm, G. Behr, W. Löser, K. Wetzig, Thermodynamic reassessment of the Cu-O phase diagram, J. Phase Equilibria Diffus. 26 (2005) 605–612. https://doi.org/10.1007/s11669-005-0005-8.

[36] W.M. Haynes, CRC Handbook of Chemistry and Physics, 95th ed., CRC Press/Taylor and Francis, Boca Raton, Florida, 2014.

[37] M.T. Clavaguera-Mora, J.L. Touron, J. Rodríguez-Viejo, N. Clavaguera, Thermodynamic description of the Cu-O system, J. Alloys Compd. 377 (2004) 8–16. https://doi.org/10.1016/j.jallcom.2004.01.031.

[38] J. Christian, Constitution of binary alloys (Second edition), by M. Hansen, with the cooperation of K. Anderko. Pp. xix + 1305. McGraw-Hill Book Co. Inc., New York; McGraw-Hill Publishing Co. Ltd, London. 1958. E12 12s. net, Endeavour. 18 (1959) 165. https://doi.org/10.1016/0160-9327(59)90213-3.

[39] J. Xue, R. Dieckmann, The high-temperature phase diagram of the Cu-O system in the stability region of

cuprous oxide ($Cu_{2-\delta}O$), High Temp. High Press. 24 (1992) 271–284. http://pascal-francis.inist.fr/vibad/index.php?action=getRecordDetail&idt=4723351.

[40] B.K. Meyer, A. Polity, D. Reppin, M. Becker, P. Hering, B. Kramm, P.J. Klar, T. Sander, C. Reindl, C. Heiliger, M. Heinemann, C. Müller, C. Ronning, The Physics of Copper Oxide (Cu_2O), in: 2013: pp. 201–226. https://doi.org/10.1016/B978-0-12-396489-2.00006-0.

[41] M. Nolan, S.D. Elliott, The p-type conduction mechanism in Cu_2O: a first principles study, Phys. Chem. Chem. Phys. 8 (2006) 5350. https://doi.org/10.1039/b611969g.

[42] A. Mittiga, E. Salza, F. Sarto, M. Tucci, R. Vasanthi, Heterojunction solar cell with 2% efficiency based on a Cu_2O substrate, Appl. Phys. Lett. 88 (2006) 163502. https://doi.org/10.1063/1.2194315.

[43] L.C. Olsen, F.W. Addis, W. Miller, Experimental and theoretical studies of Cu_2O solar cells, Sol. Cells. 7 (1982) 247–279. https://doi.org/10.1016/0379-6787(82)90050-3.

[44] A.E. Rakhshani, Preparation, characteristics and photovoltaic properties of cuprous oxide—a review, Solid. State. Electron. 29 (1986) 7–17. https://doi.org/10.1016/0038-1101(86)90191-7.

[45] L.C. Olsen, R.C. Bohara, M.W. Urie, Explanation for low-efficiency Cu_2O Schottky-barrier solar cells, Appl. Phys. Lett. 34 (1979) 47–49. https://doi.org/10.1063/1.90593.

[46] L. Hidmi, M. Edwards, Role of Temperature and pH in Cu(OH)2 Solubility, Environ. Sci. Technol. 33 (1999) 2607–2610. https://doi.org/10.1021/es981121q.

[47] J.D. Cuppett, Evaluation of Copper Speciation and Water Quality Factors That Affect Aqueous Copper Tasting Response, Chem. Senses. 31 (2006) 689–697. https://doi.org/10.1093/chemse/bjl010.

[48] T.W.J. Albrecht, J. Addai-Mensah, D. Fornasiero, Effect of pH, concentration and temperature on copper and zinc hydroxide formation/precipitation in solution, In: Chemeca 2011: Engineering a Better World: Sydney Hilton Hotel, NSW, Australia, 18-21 September 2011. Barton, A.C.T.: Engineers Australia, 2011: [2100]-[2110]., 2022. https://doi.org/10.3316/informit.177133266985459.

[49] A. Tsybizova, B.L. Ryland, N. Tsierkezos, S.S. Stahl, J. Roithová, D. Schröder, Speciation Behavior of Copper(II) Acetate in Simple Organic Solvents – Revealing the Effect of Trace Water, Eur. J. Inorg. Chem. 2014 (2014) 1407–1412. https://doi.org/10.1002/ejic.201400036.

[50] S.J. Angyal, Complexing of carbohydrates with copper ions: A reappraisal, Carbohydr. Res. 200 (1990) 181–188. https://doi.org/10.1016/0008-6215(90)84189-2.

[51] A.E. Martell, R.M. Smith, Other Organic Ligands, Springer US, Boston, MA, 1977. https://doi.org/10.1007/978-1-4757-1568-2.

[52] T. Kosugi, S. Kaneko, Novel Spray-Pyrolysis Deposition of Cuprous Oxide Thin Films, J. Am. Ceram. Soc. 81 (1998) 3117–3124. https://doi.org/10.1111/j.1151-2916.1998.tb02746.x.

[53] J. Li, G. Vizkelethy, P. Revesz, J.W. Mayer, L.J. Matienzo, F. Emmi, C. Ortega, J. Siejka, Influence of carbon on the enhanced oxygen loss in copper oxide films, Appl. Phys. Lett. 58 (1991) 1344–1346. https://doi.org/10.1063/1.104305.

[54] R. Schubert, Degradation and regeneration of copper electrical junctions, Phys. Rev. B. 43 (1991) 1433–1440. https://doi.org/10.1103/PhysRevB.43.1433.

[55] A. Satta, D. Shamiryan, M.R. Baklanov, C.M. Whelan, Q. Toan Le, G.P. Beyer, A. Vantomme, K. Maex, The Removal of Copper Oxides by Ethyl Alcohol Monitored In Situ by Spectroscopic Ellipsometry, J. Electrochem. Soc. 150 (2003) G300. https://doi.org/10.1149/1.1564108.

[56] P. Sharrock, M. Melník, Copper(II) acetates: from dimer to monomer, Can. J. Chem. 63 (1985) 52–56. https://doi.org/10.1139/v85-009.

[57] L. Ciavatta, D. Ferri, R. Palombari, On the equilibrium Cu^{2+} + Cu(s) ⇄ 2Cu+, J. Inorg. Nucl. Chem. 42 (1980) 593–598. https://doi.org/10.1016/0022-1902(80)80091-1.

[58] B.W. Williams, A.P. Irsa, H. Zmora, R.J. Beuhler, Kinetics of volatilization in rapid heating mass spectroscopy: activation energies for some hydrogen-bonding species, J. Phys. Chem. 87 (1983) 2185–2190.

https://doi.org/10.1021/j100235a029.

[59] N. Plankensteiner, W. Kautek, T. Dimopoulos, Aqueous Spray Pyrolysis of Cu_2O Films: Influence of Reducing Agent and Acetic Acid Addition, ChemNanoMat. 6 (2020) 663–671. https://doi.org/10.1002/cnma.202000006.

[60] K. Heyns, R. Stute, H. Paulsen, Bräunungsreaktionen und fragmentierungen von kohlenhydraten, Carbohydr. Res. 2 (1966) 132–149. https://doi.org/10.1016/S0008-6215(00)81477-9.

[61] B. Lorant, M. Boros, Derivatographische Untersuchungen der Kohlenhydrate über Veränderung unter Hitzeeinwirkung, Z. Lebensm. Unters. Forsch. 128 (1965) 22–28. https://doi.org/10.1007/BF01788870.

[62] M.L. Castelló, J. Dweck, D.A.G. Aranda, Thermal stability and water content determination of glycerol by thermogravimetry, J. Therm. Anal. Calorim. 97 (2009) 627-630. https://doi.org/10.1007/s10973-009-0070-z.

[63] E.M. Schwarz, V. V. Grundstein, A.F. Ievins, Thermal investigation of polyols, J. Therm. Anal. 4 (1972) 331–337. https://doi.org/10.1007/BF01911695.

[64] S. Choudhary, J.V.N. Sarma, S. Pande, S. Ababou-Girard, P. Turban, B. Lepine, S. Gangopadhyay, Oxidation mechanism of thin Cu films: A gateway towards the formation of single oxide phase, AIP Adv. 8 (2018) 055114. https://doi.org/10.1063/1.5028407.

[65] S.W. Lee, Y.S. Lee, J. Heo, S.C. Siah, D. Chua, R.E. Brandt, S.B. Kim, J.P. Mailoa, T. Buonassisi, R.G. Gordon, Improved Cu_2O-Based Solar Cells Using Atomic Layer Deposition to Control the Cu Oxidation State at the p-n Junction, Adv. Energy Mater. 4 (2014) 1301916. https://doi.org/10.1002/aenm.201301916.

[66] C. Xiang, G.M. Kimball, R.L. Grimm, B.S. Brunschwig, H.A. Atwater, N.S. Lewis, 820 mV open-circuit voltages from Cu2O/CH3CN junctions, Energy Environ. Sci. 4 (2011) 1311. https://doi.org/10.1039/coee00554a.

[67] C. Chevallier, S. Bose, S. Ould Saad Hamady, D. Horwat, J.-F. Pierson, P. Boulet, N. Fressengeas, Effect of temperature and D-sorbitol reducing agent content on the structural and optical properties of copper oxide thin films deposited by ultrasonic spray pyrolysis, Thin Solid Films 758 (2022) 139435. https://doi.org/10.1016/j.tsf.2022.139435.

[68] Z. Lin, D. Han, S. Li, Study on thermal decomposition of copper(II) acetate monohydrate in air, J. Therm. Anal. Calorim. 107 (2012) 471–475. https://doi.org/10.1007/s10973-011-1454-4.

[69] F. Sánchez-Bajo, F.L. Cumbrera, The Use of the Pseudo-Voigt Function in the Variance Method of X-ray Line-Broadening Analysis, J. Appl. Crystallogr. 30 (1997) 427–430. https://doi.org/10.1107/S0021889896015464.

[70] A. Monshi, M.R. Foroughi, M.R. Monshi, Modified Scherrer Equation to Estimate More Accurately Nano-Crystallite Size Using XRD, World J. Nano Sci. Eng. 02 (2012) 154–160. https://doi.org/10.4236/wjnse.2012.23020.

[71] R. David Prabu, S. Valanarasu, V. Ganesh, M. Shkir, A. Kathalingam, S. AlFaify, Effect of spray pressure on optical, electrical and solar cell efficiency of novel Cu_2O thin films, Surf. Coatings Technol. 347 (2018) 164–172. https://doi.org/10.1016/j.surfcoat.2018.04.084.

[72] J. Deuermeier, H. Liu, L. Rapenne, T. Calmeiro, G. Renou, R. Martins, D. Muñoz-Rojas, E. Fortunato, Visualization of nanocrystalline CuO in the grain boundaries of Cu_2O thin films and effect on band bending and film resistivity, APL Mater. 6 (2018) 096103. https://doi.org/10.1063/1.5042046.

[73] J.F. Pierson, A. Thobor-Keck, A. Billard, Cuprite, paramelaconite and tenorite films deposited by reactive magnetron sputtering, Appl. Surf. Sci. 210 (2003) 359–367. https://doi.org/10.1016/S0169-4332(03)00108-9.

[74] A.S. Zoolfakar, R.A. Rani, A.J. Morfa, A.P. O'Mullane, K. Kalantar-zadeh, Nanostructured copper oxide semiconductors: a perspective on materials, synthesis methods and applications, J. Mater. Chem. C. 2 (2014) 5247–5270. https://doi.org/10.1039/C4TC00345D.

[75] L. Debbichi, M.C. Marco de Lucas, J.F. Pierson, P. Krüger, Vibrational Properties of CuO and Cu_4O_3 from

First-Principles Calculations, and Raman and Infrared Spectroscopy, J. Phys. Chem. C. 116 (2012) 10232–10237. https://doi.org/10.1021/jp303096m.

[76] T. Sander, C.T. Reindl, P.J. Klar, Breaking of Raman selection rules in Cu_2O by intrinsic point defects, MRS Proc. 1633 (2014) 81–86. https://doi.org/10.1557/opl.2014.47.

[77] M. Rashad, M. Rüsing, G. Berth, K. Lischka, A. Pawlis, CuO and Co_3O_4 Nanoparticles: Synthesis, Characterizations, and Raman Spectroscopy, J. Nanomater. 2013 (2013) 1–6. https://doi.org/10.1155/2013/714853.

[78] C. de Melo, M. Jullien, Y. Battie, A. En Naciri, J. Ghanbaja, F. Montaigne, J.-F. Pierson, F. Rigoni, N. Almqvist, A. Vomiero, S. Migot, F. Mücklich, D. Horwat, Semi-Transparent p-Cu_2O/n-ZnO Nanoscale-Film Heterojunctions for Photodetection and Photovoltaic Applications, ACS Appl. Nano Mater. 2 (2019) 4358–4366. https://doi.org/10.1021/acsanm.9b00808.

[79] N.R. Dhineshbabu, V. Rajendran, N. Nithyavathy, R. Vetumperumal, Study of structural and optical properties of cupric oxide nanoparticles, Appl. Nanosci. 6 (2016) 933–939. https://doi.org/10.1007/s13204-015-0499-2.

[80] M. Grigore, E. Biscu, A. Holban, M. Gestal, A. Grumezescu, Methods of Synthesis, Properties and Biomedical Applications of CuO Nanoparticles, Pharmaceuticals. 9 (2016) 75. https://doi.org/10.3390/ph9040075.

CHAPTER 6: Ternary and Quaternary Metal-Oxide Semiconductors: Toward the "All-Oxide" Photovoltaic Application

The development of ternary and quaternary semiconductor alloys is crucial for optoelectronic applications. For the photovoltaic application, these alloys can have versatile functions. They can be used as TCO as well as window layer, buffer layer or even, in some cases, as absorber. The alloys we develop are all oxides based on abundant and non-toxic elements. Beyond the "all-oxide" solar cell application, these materials can have other uses in optoelectronics and as an active layer in ultraviolet photodetectors with a modulated spectral range. The results of ternary and quaternary preparation and the study of their morphological, structural, optical, and electrical properties are the subject of this chapter. A brief numerical simulation study and a presentation of the perspectives of this work conclude the chapter.

6.1 Introduction to Zinc-Aluminum Oxide (ZnAlO)

Pure ZnO thin films are not resistant to corrosive environments, for example, the adsorption of O_2 reduces the electrical conductivity of the film and affects the surface morphology. Incorporating various elements in ZnO with in the hopes of making the ZnO system resistant to such changes has been researched [1,2], resulting in an interesting family of materials based on ZnO. Aluminum is a group 13 element, which can easily substitute Zn in the crystal lattice and such incorporation can lead to high carrier concentrations, $>10^{20}$ cm^{-3} [3-6].

The structural, electrical, and optoelectronic characteristics of ZnO due to Al incorporation have been studied using a quantum chemical approach, which explains the increase in n-type electrical conductivity [7]. The material should have a uniform and homogenous distribution of dopant ions in the correct regions, up to a limiting concentration, to achieve optimal performance.

In terms of donor behaviour from Al, [5] explains the rise in conductivity of ZnO when Al is incorporated. Because Al has one more valence electron than Zn, substituting Al for Zn or occupying the interstitial spaces with Al increases the concentration of charge carriers in the material. In the tetrahedral and octahedral configurations, the modest difference in electronegativity values of Zn (1.65) and Al (1.61), as well as the smaller ionic radii of Al (0.530, 0.675 Å) when compared to Zn (0.60, 0.710 Å), favour Al incorporation in ZnO. Half of the tetrahedral holes and all the octahedral holes in the hexagonal close packed lattice of the ZnO wurtzite structure are unfilled, allowing for more potential dopant sites. Although the Al^{3+} ion is smaller than the Zn^{2+} ion and might fit in either hole, geometry preference criteria suggest that Al would choose the octahedral hole [8]. The question of whether the conditions for maximum Al incorporation are the same as those required to make highly orientated thin films [9] and/or whether any of these results in optimal TCO properties raises an interesting subject.

6.2 Preparation of Ternary ZnAlO by Ultrasonic Spray Pyrolysis

The preparation of ZnAlO films was done on soda lime glass using an ExactaCoat system from Sono-Tek with an Impact nozzle operating at 120 kHz. The experimental details are given in the ***Section 2.4*** and ***2.5*** of ***Chapter 2*** and in the ***Section 3.4*** of ***Chapter 4***. Zinc acetate dihydrate [$Zn(Ac)_2 \cdot 2H_2O$] and Aluminum acetylacetonate ($C_{15}H_{21}AlO_6$) were used as the source precursor raw materials dissolved in deionized water and ethanol respectively. For simplicity henceforth, in this chapter we will always refer the precursor materials as $Zn(Ac)_2$ and $Al(acac)_3$ only. Always 50 mL of precursor solution was prepared before the start of the spray. Acetic acid was added to the precursor solution to reduce the formation and precipitation of hydroxides.

6.2.1 Chemicals Used for ZnAlO Preparation

All the chemicals used for the preparation of ZnAlO thin films are listed in the ***Table 6.1***.

Table 6.1: Chemicals with high purity used for spray pyrolysis deposition of ZnAlO.

Name	Formula	Supplier
Zinc acetate dihydrate	$Zn(CH_3COO)_2 \cdot 2H_2O$	Merck 108802
Aluminum acetylacetonate	$C_{15}H_{21}AlO_6$	Alfa Aesar 44538
Acetic Acid	CH_3COOH	Alfa Aesar 10994-AE
Ethanol anhydrous	CH_3CH_2OH	Merck-Sigma Aldrich 186414
Deionized water	H_2O	Avantor-VWR

The pH of the precursor solution is monitored using the acetic acid. The pH of the solution can also play a role in the film morphology: nanorods to compact films. We monitored the pH value in collaboration with other spray parameters to have dense, uniform, and compact films. Generally, the acetic acid can reduce the formation of the volatile Zn and Al species in the solution, thereby reducing the chances of them further reacting to form respective hydroxides. Further, the acetic acid addition helps to have a lower surface tension of the water-based precursor solution so that during the atomization uniform sized droplets are generated from the spray nozzle. But, when compared to the effect of the Al concentration in the solution, the effect of acetic acid concentration on the morphology of the spray prepared films is less pronounced.

The effects of the increase of the $Al(acac)_3$ concentration while keeping the $Zn(Ac)_2$ concentration fixed in the precursor solution on the ZnAlO film quality have been discussed later in this chapter. The calculation procedure to select the concentrations of $Zn(Ac)_2$ and $Al(acac)_3$ along with the

quantities of $Zn(Ac)_2$ and $Al(acac)_3$ powder needed is discussed below.

Based on the preparation experience of ZnO, as detailed in the ***Section 3.4.1*** of ***Chapter 3***, we select for $Zn(Ac)_2$ always a concentration of 0.05 mol/L. The chemical protocol for preparation of ZnAlO is based on 3 types of solutions: Solution 1 (S_1), Solution 2 (S_2) and solution 3 (S_3). The final alloy of ZnAlO film will be of the stoichiometry $Zn_{1-y}Al_yO$. y is the Al content in mol%.

The solution S1 of 100 mL is only a solution of $Zn(Ac)_2$ which is dissolved only in deionized water. The quantity of $Zn(Ac)_2$ powder needed is given by the equation below:

Equation (6.1):

$$m_{Zn(Ac)_2} = C \times V \times M$$

where, m is the mass (in g) of $Zn(Ac)_2$ powder; C is the $Zn(Ac)_2$ solution concentration in mol/L; V is the solution volume in litres (L) and M is the molar mass of $Zn(Ac)_2$ (in g/mol).

So, $m_{Zn(Ac)_2} = 0.05\ (mol/L) \times 0.1\ (L) \times 219.49\ (g/mol) = 1.09\ g \approx 1.1\ g$.

The solution S_2 of 100 mL is a solution of both $Zn(Ac)_2$ and $Al(acac)_3$. At first $Zn(Ac)_2$ is dissolved only in 50 mL deionized water with same concentration as in S1. But $Al(acac)_3$ is dissolved in 50 mL ethanol, as $Al(acac)_3$ is insoluble is water.

Initially, we choose y = 0.3, corresponding to Al content of 30 mol%. This value is taken as a base or reference for preparing solutions with other Al content mol%. The concentration for 30 % Al content with a corresponding constant concentration of $Zn(Ac)_2$ is given by:

Equation (6.2):

$$C_{Al(acac)_3} = \left(\frac{y}{1-y}\right) \times C_{Zn(Ac)_2}$$

So, for y =0.3:

$$C_{Al(acac)_3} = \left(\frac{0.3}{1-0.3}\right) \times 0.05 = 0.0214\ mol/L$$

Therefore, the quantity of $Al(acac)_3$ powder needed corresponding to the concentration of 0.0214 mol/L is given by the equation below:

Equation (6.3):

$$m_{Al(acac)_3} = C \times V \times M$$

where, $m_{Al(acac)_3}$ is the mass (in g) of $Al(acac)_3$ powder; C is the desired concentration of $Al(acac)_3$ in mol/L; V is the solution volume in litres (L) and M is the molar mass of $Al(acac)_3$ (in g/mol).

So, $m_{Al(acac)_3} = 0.0214\ (mol/L) \times 0.1\ (L) \times 324.30\ (g/mol) = 0.694\ g$.

Finally, the 100 mL solution S_2 is prepared by: dissolving 1.1 g of $Zn(Ac)_2$ in 50 mL deionized water first and then dissolving 0.694 g of $Al(acac)_3$ in ethanol and then mixing these two solutions together. For complete homogenization, the solution S2 after the mixing is put to ultrasound bath for 15 minutes.

Now let us assume that $C_{Al(acac)_3}$ = 0.0214 mol/L is the initial concentration. Using the ***Equation 6.2***, we can calculate the different values of concentration corresponding to different Al content %. The values are shown in the ***Table 6.2***.

Table 6.2: Calculation for different concentrations of $Al(acac)_3$.

Al content values (mol%)	**$C_{Zn(Ac)2}$ (mol/L)**	**$C_{Al(acac)3}$ (mol/L)**
0	0.05	0.0000
1	0.05	0.0005
2	0.05	0.0010
3	0.05	0.0015
4	0.05	0.0020
5	0.05	0.0025

Now, we need to prepare the solution S_3. It should be noted that S_3 will be the final solution that will be used for the actual preparation. For preparing the solution S_3, we need to mix different proportions of S_1 and S_2. Basically we, will collect a certain volume of S_2 based on the desired Al content % value and we will dilute it by adding S1. The final volume "V_3" of S_3 will be 50 mL. Volume of S1 needed is "V_1". The volume "V_2" of S_2 to be collected is given by:

Equation (6.4):

$$V_2 = \frac{Desired\ Al(acac)_3\ concentration}{Initial\ Al(acac)_3\ concentration} \times V_3$$

The different volumes of V1 and V2 are given in the ***Table 6.3***.

Table 6.3: Calculation for volumes of S_1 and S_2 to prepare the final precursor solution S_3.

Al content values (mol%)	**$C_{Al(acac)3}$ (mol/L)**	**Final stoichiometry of $Zn_{1-y}Al_yO$**	**Volume V_2 of S_2 (mL)**	**Volume V_1 of S_1 (mL)**
0	0.0000	ZnO	0	50
1	0.0005	$Zn_{0.99}Al_{0.01}O$	1.168	48.832
2	0.0010	$Zn_{0.98}Al_{0.02}O$	2.336	47.664
3	0.0015	$Zn_{0.97}Al_{0.03}O$	3.504	46.496
4	0.0020	$Zn_{0.96}Al_{0.04}O$	4.672	45.328
5	0.0026	$Zn_{0.95}Al_{0.05}O$	6.074	43.926

Although, in all the previous preparations we have not used ethanol, in this case we had to use, to dissolve the $Al(acac)_3$ soluble. But, as soon as it is mixed with water-based solution the solubility is hindered. So, keeping the poor solubility factor of $Al(acac)_3$ in mind we have only used up to molar concentration of 5 % $Al(acac)_3$. Also, most importantly we see that in the final solutions S_3 the volume percentages of ethanol can be only in the range from 1 % to 3 %. This low volume percentage will not be toxic for the pyrolysis process. Based on the experimental details mentioned in the ***Chapter 2*** we have also added acetic acid to each of the precursor solution and maintained a value of pH of 4. Having the same pH for all the solutions helps to analyze the films better. The other advantages of acetic acid are mentioned in the previous chapters.

6.2.2 Design of Experiment

Many parameters are involved in the spray pyrolysis preparation process for depositing high-quality thin films as detailed in the ***Section 2.5*** of ***Chapter 2***. Variation in each parameter impacts the resulting film quality. Using a precise design of experiment, a thorough investigation of the structural and optical properties was carried out to identify the set of parameters that result in high quality and transparent $Zn_{1-y}Al_yO$ thin films. The nozzle speed and the spray flow rates were pre-fixed to 70 mm/sec and 0.5 mL/min based on the safety requirements of the spray system.

The list below shows the variation of other spray parameters along with range of their variation.

1. The zinc acetate [$Zn(Ac)_2$] molar concentration in the precursor solution varied in the range from 0.03 mol/L to 0.10 mol/L.

2. The Aluminum acetylacetonate [$Al(acac)_3$] molar concentration in the precursor solution varied in the range from 0.0005 mol/L to 0.0055 mol/L.

3. The number of spray cycles, which ranged from 10 to 100. The duration of each preparation is determined by this parameter.

4. The dwell times between each spray cycle varied between 0.5 s to 2 s.

5. The set preparation temperature was varied between 400 °C to 480 °C.

6. The relative shaping air pressure was varied between 6.8 kPa to 27.6 kPa.

7. The height between nozzle to substrate was varied between 90 mm to 110 mm.

When one spray parameter was varied, all the other parameter remained fixed to a particular value and the repeatability of the preparation process was constantly monitored by preparing each sample at least three times with the parameters listed above. The used design of experiment to select the optimal ultrasonic spray pyrolysis parameters is shown below in the ***Table 6.4***.

Table 6.4: Design of experiment to select the optimal spray parameters for ZnAlO preparation.

Preparation Parameter	**Range**	**Optimal value selected from experiments**
$Zn(Ac)_2$ molar concentration	[0.03 mol/L ; 0.1 mol/L]	0.05 mol/L
Aluminum acetylacetonate concentration	[0.0005 mol/L ; 0.0055 mol/L]	0.0005 mol/L to 0.0026 mol/L
Number of spray cycles	[10 ; 100]	20
Dwell times between each spray cycle	[0.5 s ; 2 s]	0.5 s
Set preparation temperature	[400 °C ; 480 °C]	470 °C
Relative shaping air pressure	[6.8 kPa ; 27.6 kPa]	20.6 kPa
Height between nozzle to substrate	[90 mm ; 110 mm]	100 mm

6.3 Results and Discussions on ZnAlO Preparation

The optimal value of the spray parameters from the design of experiments scheme mentioned above has been used for the preparation of ZnAlO thin films. Various characterization techniques were used to understand the effect of the Al incorporation in the precursor solution on the quality of the prepared ZnAlO thin films.

6.3.1 Optical Properties of the ZnAlO Thin Films

In this section we try to analyze the optical properties of the ZnAlO thin films with respect to the increase of the Al molar concentration. At first the transmission of the films was assessed in relation to the aluminum incorporation effect as shown in the ***Figure 6.1***. Also, the bandgap and Urbach energies of the films were studied in response to the increase of the Al molar content. The thickness of the prepared films was systematically measured at three sites of the spray zone by the mechanical DekTak profilometer and then averaged to give about 200 nm thickness. To verify consistency of the films, the measurements were repeated by an optical profilometer at the spray zone of the films. Both the profilometers have a vertical resolution of 0.1 nm and the thickness measurements of the films were found to be very consistent with narrow range of differences (± 10 nm).

The average transmission of the ZnAlO thin films in the wavelength range 500-800 nm is shown in the ***Figure 6.2***. It is seen from the ***Figures 6.1 & 6.2*** that as the molar composition of aluminum increases the transparency decreases. This is mostly related to the poor solubility of the $Al(acac)_3$ precursor.

The estimation of the bandgap energies of the films are done using the Tauc model and shown in the ***Figure 6.3***. ***Figure 6.4*** shows the variation of the bandgap with respect to the Al molar composition.

Figure 6.1: Transmission spectra of $Zn_{1-y}Al_yO$ thin films as a function of Al molar composition. The spectrum of the SLG substrate is also displayed, with nearly constant transmission at 100 %. A zoom in the absorption edge spectral region is shown in the inset plot.

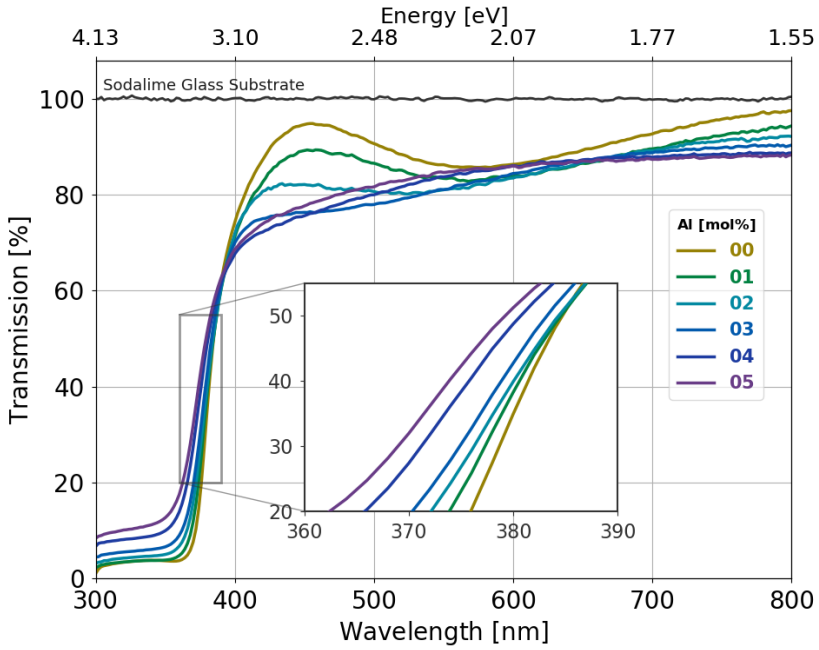

Figure 6.2: Average transmission of $Zn_{1-y}Al_yO$ thin films as a function of Al molar composition in the wavelength region 500 nm to 800 nm.

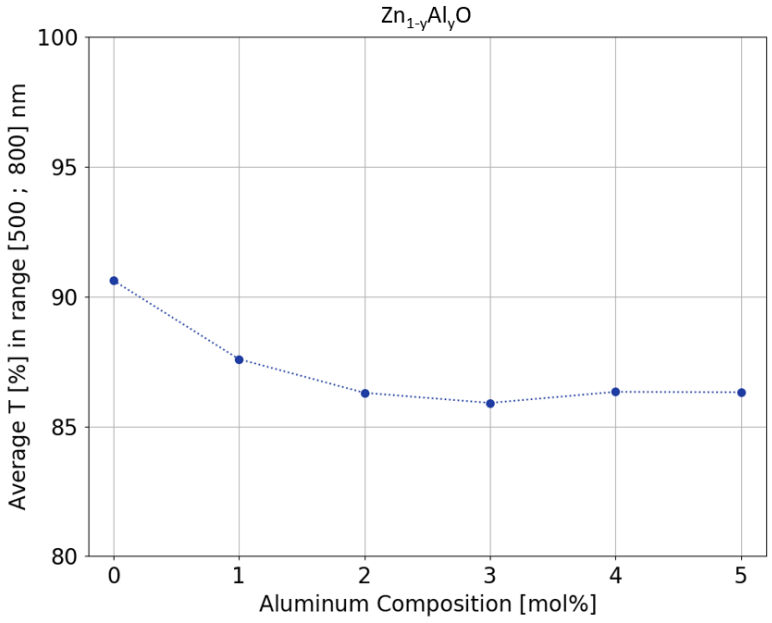

Figure 6.3: Estimation of the bandgap energies of $Zn_{1-y}Al_yO$ thin films as a function of Al molar composition using the Tauc model.

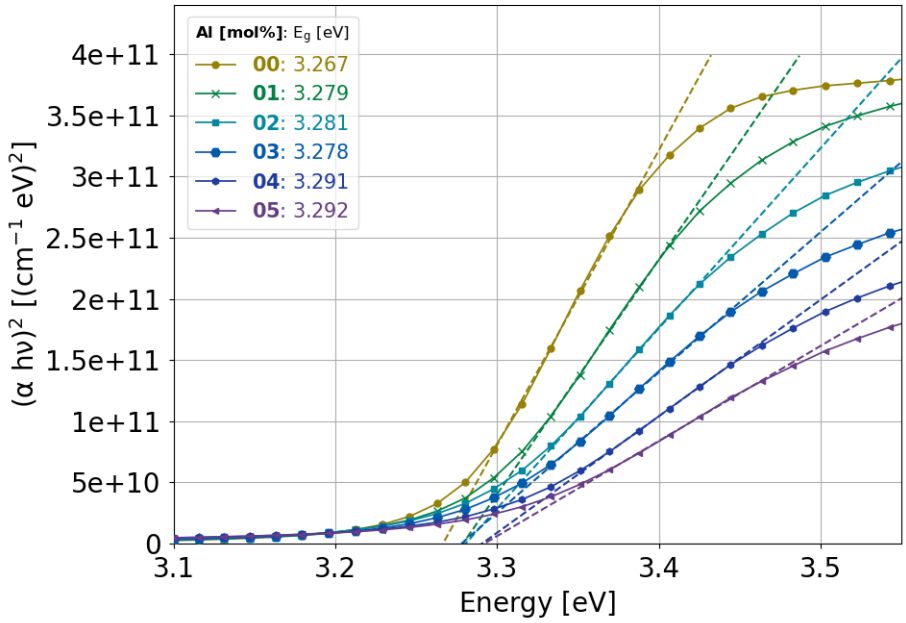

Figure 6.4: Variation of the bandgap energies of $Zn_{1-y}Al_yO$ thin films as a function of Al molar composition extracted using the Tauc model as shown in ***Figure 6.3***.

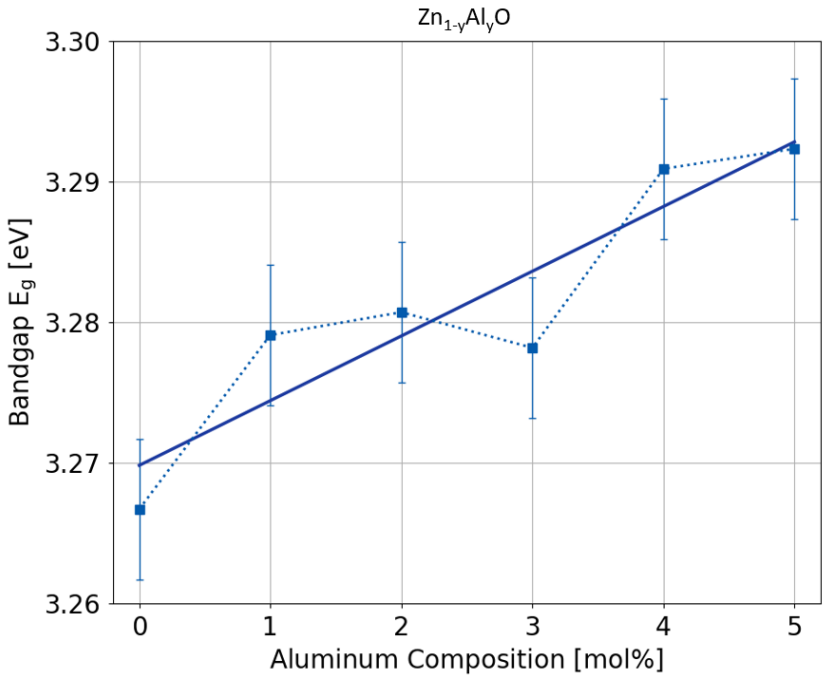

The variation of the bandgap energies as a function of increasing aluminum molar composition is not fully linear, although an increasing trend is noticed. For a pure ZnO, the bandgap value is 3.267 eV while for the $Zn_{0.95}Mg_{0.05}O$ film (with Al mol 5%) the value increases to 3.292 eV. At small concentrations of Al, the aluminum atoms most probably substitute the zinc atoms. Since the zinc atoms are divalent and the Al atoms are trivalent, there will be an increase in carrier concentration in corresponding to the blue shift of the bandgap absorption. The blue shift can be tentatively attributed to the Burstein-Moss effect [10]. This increase in the Al atom concentration shifts the Fermi level towards the conduction band. High possibility is that the conduction band minima will occur at the 3s and 3p state of Al which can be dominant over the Zn 4s state [11].

We also calculated the Urbach energy or the “band-tail” to estimate the alloy disorders and increase of density of defects in the films with the increase in the aluminum content for the $Zn_{1-y}Al_yO$ thin films. For $Zn_{1-y}Al_yO$ films prepared by ultrasonic spray pyrolysis process, the Urbach energy calculations are done for the very first time. The Urbach energies are calculated from the absorption of the thin films in the sub-bandgap spectral region as shown in the ***Figure 6.5***. The variations of the Urbach energies with respect to the magnesium molar compositions are shown in the ***Figure 6.6***.

Figure 6.5: Estimation of the Urbach energies of $Zn_{1-y}Al_yO$ thin films as a function of Al molar composition.

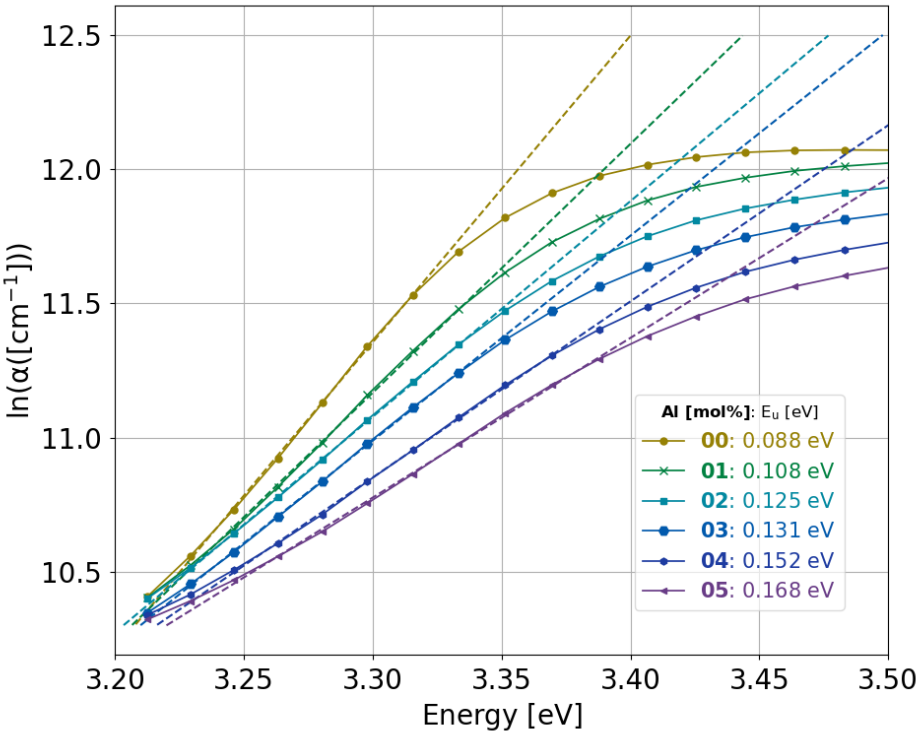

Figure 6.6: Variation of Urbach energies of $Zn_{1-y}Al_yO$ thin films as a function of Al molar composition.

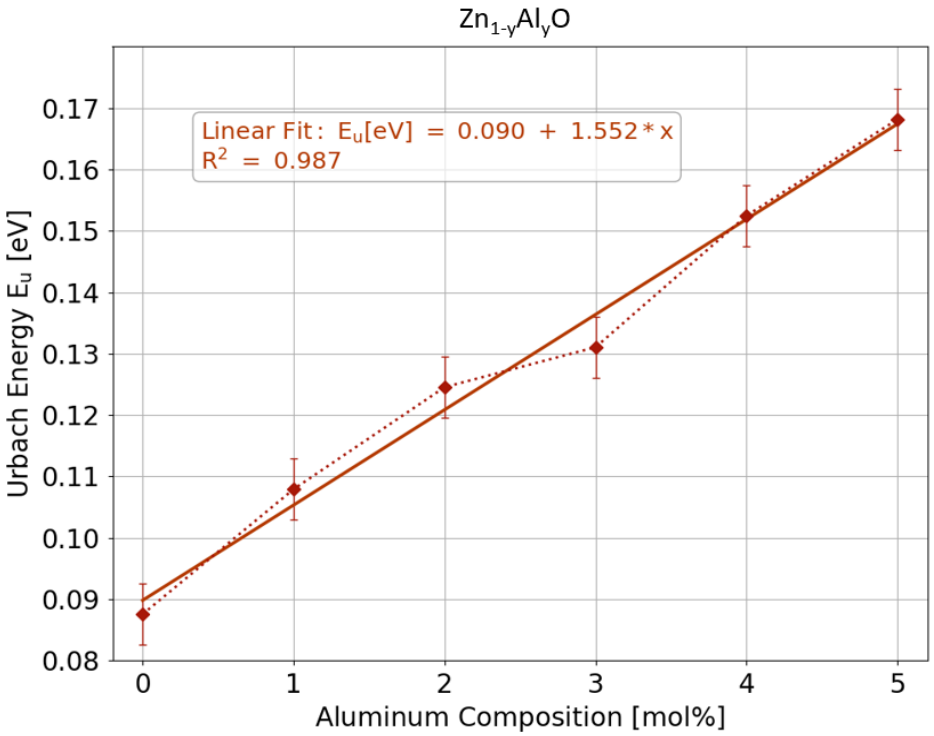

From the analysis, we can estimate that the obtained Urbach energy value for the films with low aluminum compositions, is equivalent to the usual reported values for ZnO grown by pulsed lased deposition (PLD) [12]. The Urbach energy increases considerably as the crystalline lattice alloy disorder grows due to aluminum incorporation, as expected.

6.3.2 Structural Properties of the ZnAlO Thin Films

To analyze the structural properties of the $Zn_{1-y}Al_yO$ thin films, X-ray diffraction (XRD) measurements were done on the films after preparation. The diffractograms are shown in the ***Figure 6.7***. The $Zn_{1-y}Al_yO$ thin films exhibit a single hexagonal wurtzite crystal structure with peaks for the (100), (002), (101), (102), (110), (103) and (112) planes of the space group $P6_3mc$, identified by using the ZnO powder diffractogram (RRUFF ID: R060027.1) [13] as a reference for aluminum compositions up to 5 mol%. From the diffractograms we could not identify any phase related to formation of Al_2O_3. At these low aluminum molar concentrations, no additional phase occurs and the original wurtzite phase of ZnO is retained.

Figure 6.7: XRD diffraction patterns for $Zn_{1-y}Al_yO$ solid thin films with respect to the Al molar composition.

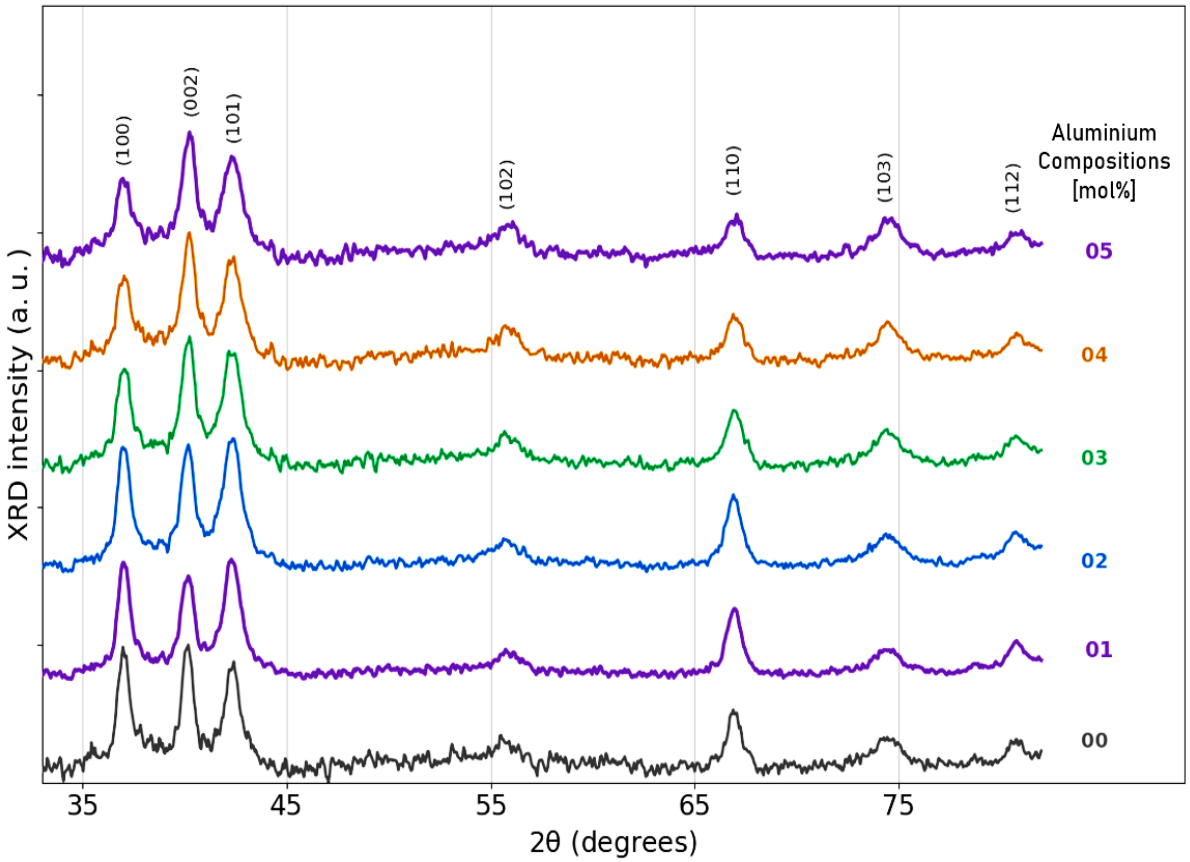

Due to the increased disorder in the $Zn_{1-y}Al_yO$ thin films, the crystallite size for the wurtzite phase (***Figure 6.8***) decreases approximately from 29 nm down to 25 nm when the aluminum composition increases from 0 mol% up to 5 mol%, as determined using the procedure presented in the ***Sections 2.7.3.1 & 3.5.5*** of ***Chapters 2 & 3*** respectively. Also, noticed is the decrease in the lattice parameters a (***Figure 6.9***) and c (***Figure 6.10***). Although the decrease in not so high and the values can be compared to the values obtained by USP for ZnO in our work (detailed in ***Table 3.5*** of ***Chapter 3***) [14].

Figure 6.8: Crystallite size estimation for $Zn_{1-y}Al_yO$ solid thin films with respect to the Al molar composition.

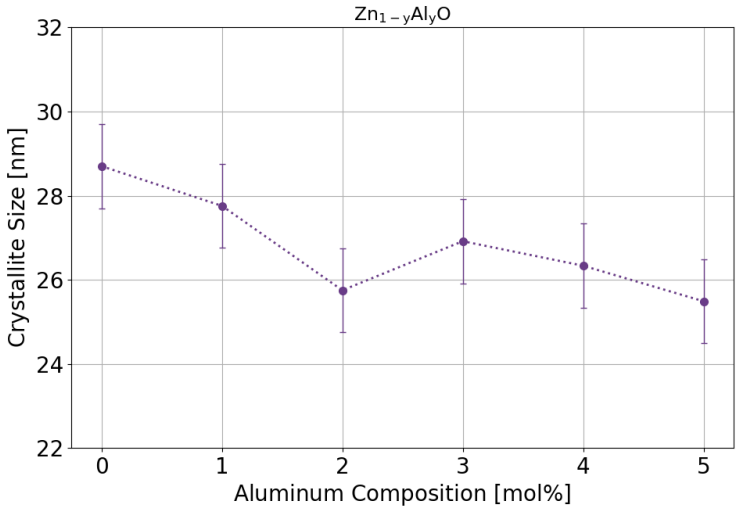

Figure 6.9: Variation of lattice parameter “a” for $Zn_{1-y}Al_yO$ solid thin films with respect to the Al molar composition.

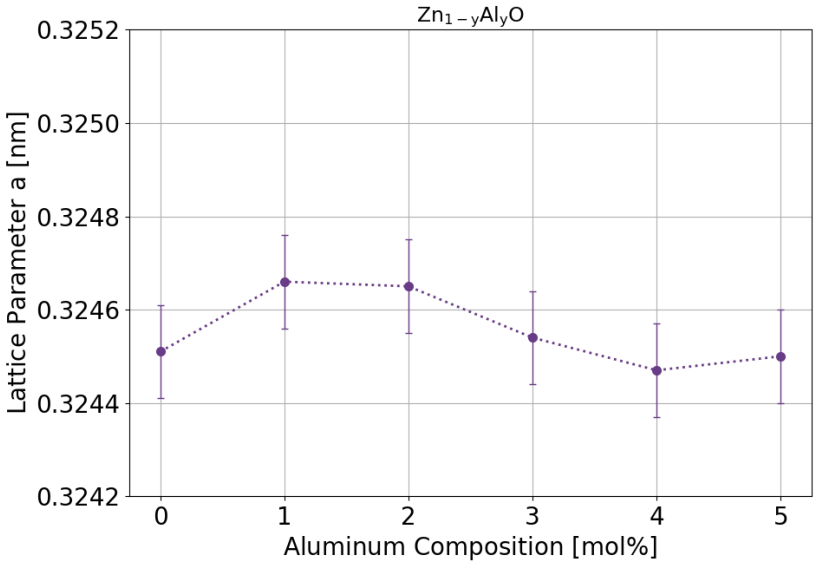

Figure 6.10: Variation of lattice parameter "c" for $Zn_{1-y}Al_yO$ solid thin films with respect to the Al molar composition.

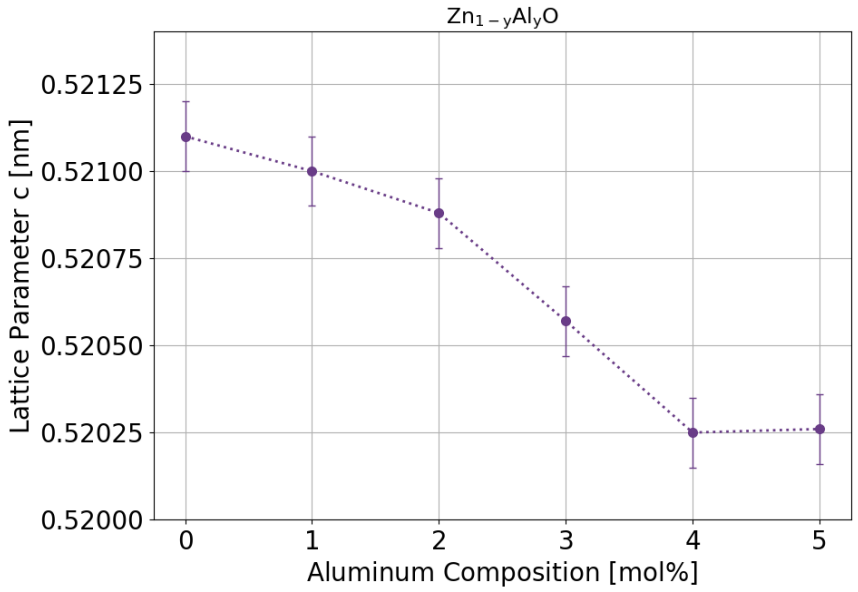

The texture quality of the films was also checked in terms of the Lotgering factor (LF). It is a simple method to determine the degree of orientation by comparing with the relative peak intensities of a powder XRD spectrum [15,16]. It is a quantitative metric representing the texture of the prepared film using the following expression (given for the (002) peak):

Equation (6.5):

$$LF_{002} = \frac{P_{002} - P_{002}^{0}}{1 - P_{002}^{0}}$$

Where LF_{002} is the Lotgering factor for this peak (002); $P_{002} = I_{002} / \sum I_{hkl}$ is the considered (002) peak integrated intensity divided by the integrated peak intensities of all the peaks for the thin film; $P_{002} = I_{002} / \sum I_{hkl}$; And, similarly, $P_{002}^{0} = I_{002}^{0} / \sum I_{hkl}^{0}$ (002) is peak integrated intensity divided by the integrated peak intensities of all the peaks for the powder used as the reference. For other peaks, the formula is similar by replacing (002) by any other peak indices.

For a randomly oriented film $LF_{002} = 0$. If a preferred orientation exists, the Lotgering factor of the corresponding peak will increase $LF_{002} > 0$ and the other Lotgering factors will decrease below zero. For a perfect monocrystalline thin film, the Lotgering factor will be equal to the unity for the peak corresponding to the unique orientation.

Values above 0.0 gives the indication of the most dominant peak which in our case is (002) as shown in the ***Figure 6.11***. As we have discussed in detail in the ***Section 3.5.5*** of the ***Chapter 3***, the (002) peak orientation gives an indication of high crystalline quality of the films.

Figure 6.11: Texture factor estimation of different peaks for $Zn_{1-y}Al_yO$ solid thin films with respect to the Al molar composition using the method of Lotgering.

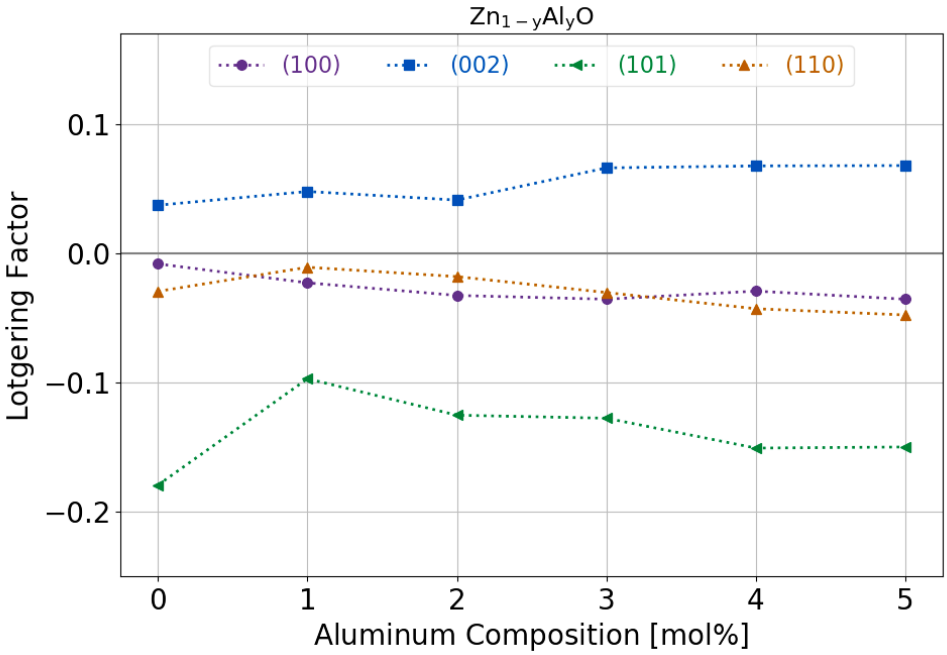

6.3.3 Resistivity Measurements of the ZnAlO Thin Films

Prior to the resistivity using the four-point probe technique, the films were annealed using the same conditions mentioned in the ***Section 4.6.4*** of ***Chapter 4*** for the ZnMgO films. The difference is that in this chapter the films are prepared with Impact nozzle instead of Accumist nozzle. The resistivity changes with respect to the increase in the Al molar concentration is shown in the ***Figure 6.12***. ZnO resistivity is found to be approx. 0.12 Ω×cm. The resistivity goes down to 0.08 Ω×cm and 0.09 Ω×cm as the Al molar concentration increases up to 1 mol% and 2 mol% respectively. For the ZnAlO film with Al molar composition 5 mol% the resistivity is increased to 0.6 Ω×cm. The initial decrease in the resistivity can be attributed to the increase of the free carrier concentration. The concentration of the free carriers is increased mostly due to the substitution of Zn^{2+} cation sites and in some interstitial positions by the donor Al^{3+} ions [17]. From molar content of 3 mol%, the resistivity values go above the one measured for ZnO. We have seen that with the increase in the molar Al content, the lattice disorder in increases and the crystallize size decreases. This can hinder the mobility of the carrier. Even with the Al increase, some intrinsic defects are produced in the films which acts as carrier traps rather than being electron donors [18,19]. Some non-conducting clusters of Al_2O_3 can form which causes resistivity increase but they were not evidenced from the XRD measurements.

Figure 6.12: Resistivity of $Zn_{1-y}Al_yO$ solid thin films with respect to the Al molar composition.

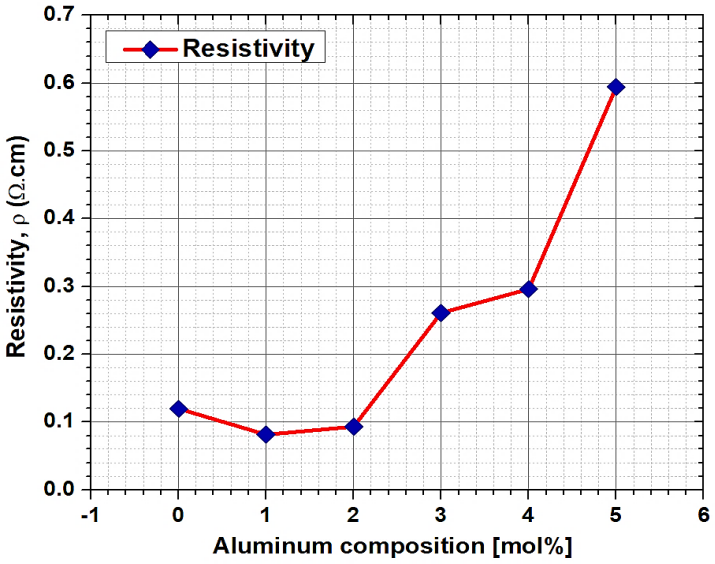

In the next section we will discuss about the preparation of a quaternary material Zinc-Aluminum-Magnesium-Oxide (ZnMgAlO). The aim to prepare the material is to modulate the bandgap as well as the conductivity. As we have seen, with increase of aluminum molar composition the increase of defects, loss of transparency and increase of resistivity happens, so for the preparation of the ZnMgAlO we limit ourselves to aluminum molar composition of 0 %, 1 % and 2 % with varying magnesium composition.

6.4 Introduction to Zinc Aluminum Magnesium Oxide (ZnMgAlO)

$Zn_{1-y-x}Mg_xAl_yO$ is a quaternary material with a relatively small content of Al and Mg which can be used as a transparent conducting oxide (TCO) in solar cells and display devices but also as an active layer in optoelectronic devices [20,21,22]. Our idea is to prepare a suitable material with sufficient transparency and conductivity so that it can be applied as a TCO for applications in "all-oxide" solar cells but, beyond that, as an active layer in optoelectronic devices such as ultraviolet detectors. Indeed, a material whose bandgap can be modulated so that it can either be used as a window or buffer layer with suitable band alignments for heterojunctions, or as an absorber in detectors with a modulable spectral response. Conduction band electrons in wider-bandgap layers transfer through heterojunction interfaces to intrinsic ZnO layers in these devices. Mg incorporation can broaden the bandgap of ZnO as shown in this work and detailed in ***Chapter 4***. Due to the similar valence states of Mg^{2+} and Zn^{2+}, Mg^{2+} substitution cannot generate any free carriers. To make a high-conducting ZnO with a wide bandgap and to improve device performance, Al and Mg need to be co-incorporated

to increase carrier concentration and widen the bandgap, respectively [23]. In [24] it was first shown that it was possible to make single crystalline ZnMgAlO films with deep UV bandgaps and lattice constants that match those of the ZnO and/or GaN substrates. This was achievable because the lattice constant of Al_2O_3 is higher than that of MgO, which is lower than that of ZnO. The ZnMgAlO films were suggested as a suitable candidate for high-quality deep-UV optoelectronic devices because they might reduce residual strain [25].

Another factor to keep in mind is the use of abundant and non-toxic materials for preparation of the quaternary ZnMgAlO. So far, this material has been developed using processes like RF magnetron sputtering [24–28], pulsed laser deposition (PLD) [29] and as nanoparticles by sol-gel technique [30]. But we used for the first-time ultrasonic spray pyrolysis to prepare quaternary ZnMgAlO keeping in mind the non-toxicity factor as much as possible.

6.5 Preparation of Quaternary ZnMgAlO by Ultrasonic Spray Pyrolysis

The preparation of ZnMgAlO films is being done for the first time using the process of ultrasonic spray pyrolysis based on the procedure explained above at the start of the ***Section 6.2***. Zinc acetate dihydrate ($Zn(Ac)_2 \cdot 2H_2O$), magnesium acetate tetrahydrate ($Mg(Ac)_2 \cdot 4H_2O$) and aluminum acetylacetonate ($C_{15}H_{21}AlO_6$) were used as the source precursor raw materials. ($Zn(Ac)_2 \cdot 2H_2O$) and ($Mg(Ac)_2 \cdot 4H_2O$) were dissolved in deionized water and ($C_{15}H_{21}AlO_6$) was dissolved in ethanol. For simplicity henceforth we will always refer the precursor materials as $Zn(Ac)_2$, $Mg(Ac)_2$ and $Al(acac)_3$ only. Always 50 mL of precursor solution was prepared before the start of the spray. Acetic acid was added to the precursor solution to reduce the formation and precipitation of hydroxides as mentioned earlier.

6.5.1 Chemicals Used for ZnMgAlO Preparation

All the chemicals used for the preparation of ZnMgAlO thin films are listed in the ***Table 6.5***.

Table 6.5: Chemicals with high purity used for spray pyrolysis deposition of ZnMgAlO.

Name	Formula	Supplier
Zinc acetate dihydrate	$Zn(CH_3COO)_2 \cdot 2H_2O$	Merck 108802
Aluminum acetylacetonate	$C_{15}H_{21}AlO_6$	Alfa Aesar 44538
Magnesium acetate tetrahydrate	$Mg(CH_3COO)_2 \cdot 4H_2O$	Sigma Aldrich M5661
Acetic Acid	CH_3COOH	Alfa Aesar 10994-AE
Ethanol anhydrous	CH_3CH_2OH	Merck-Sigma Aldrich 186414
Deionized water	H_2O	Avantor-VWR

The effects of the increase of the $Mg(Ac)_2$ and $Al(acac)_3$ concentration while keeping the $Zn(Ac)_2$ concentration fixed in the precursor solution on the ZnAlO film quality have been discussed in this chapter. The calculation procedure to select the concentrations of $Zn(Ac)_2$, $Mg(Ac)_2$ and $Al(acac)_3$ along with the quantities of $Zn(Ac)_2$, $Mg(Ac)_2$ and $Al(acac)_3$ powder needed is discussed below.

Based on the preparation experience of ZnO, as detailed in the ***Section 3.4.1*** of ***Chapter 3***, we select for $Zn(Ac)_2$ always a concentration of 0.05 mol/L. The chemical protocol for preparation of ZnMgAlO is based on 4 types of solutions: Solution 1 (S_1), Solution 2 (S_2), Solution 3 (S_3) and Solution 4 (S_4). The final alloy of ZnMgAlO film will be of the stoichiometry $Zn_{1-y-x}Mg_xAl_yO$. x and y are the Mg and Al contents in mol%.

The solution S_1 of 100 mL is only a solution of $Zn(Ac)_2$ which is dissolved only in deionized water. The details of S_1 can be found in the ***Section 6.2.1*** above.
The solution S_2 of 100 mL is a solution of $Zn(Ac)_2$ and $Mg(Ac)_2$. The preparation of S_2 is exactly same the preparation of S_2 in ***Chapter 4*** (described in detail in the ***Section 4.5.1***).
At first $Zn(Ac)_2$ is dissolved only in 100 mL deionized water with same concentration as in S_1. Then $Mg(Ac)_2$ powder corresponding to Mg content of 30 mol% (x = 0.3) is added to this solution and dissolved. This makes the concentration of $Mg(Ac)_2$ is S_2 as 0.0214 mol/L. Then, solution S_3 is prepared. The preparation of S_3 is exactly same as the preparation of S_2 as described above in details in the ***Section 6.2.1***. $Al(acac)_3$ is dissolved separately in 50 mL ethanol, as $Al(acac)_3$ is insoluble is water. The concentration for 30 % Al content is given by the ***Equation 6.2*** and ***Equation 6.3*** gives the required quantity of the $Al(acac)_3$ powder needed for the required concentration of 0.0214 mol/L. The 50 mL solution of $Al(acac)_3$ in ethanol is added to the 50 mL solution of $Zn(Ac)_2$. So, final volume of S_3 is 100 mL. The solution S_3 then is put to ultrasound bath for 15 mins for complete homogenization.

Now, we need to prepare the solution S_4. It should be noted that S_4 will be the final solution that will be used for the actual preparation. For preparing the solution S_4, we need to mix different proportions of S_1, S_2 and S_3. Basically we, will collect a certain volume of S_2 and S_3 based on the desired Mg and Al composition values and we will dilute it by adding S_1.

The final volume "V_4" of S_4 will be 50 mL. Volume of S_1 needed is "V_1".

The volume "V_2" of S_2 to be collected is given by:

Equation (6.6):

$$V_2 = \frac{Desired\ Mg(Ac)_2\ concentration}{Initial\ Mg(Ac)_2\ concentration} \times V_4$$

The volume "V_3" of S_3 to be collected is given by:

Equation (6.7):

$$V_3 = \frac{Desired\ Al(acac)_3\ concentration}{Initial\ Al(acac)_3\ concentration} \times V_4$$

The different volumes of V_1, V_2 and V_3 are given in the ***Table 6.6***.

Table 6.6: Calculation for volumes of S_1, S_2 and S_3 to prepare the final precursor solution S_4 for the preparation of ZnMgAlO.

Al content values (mol%)	**Mg content values (mol%)**	**$C_{Al(acac)3}$ (mol/L)**	**$C_{Mg(Ac)2}$ (mol/L)**	**Final stoichiometry of $Zn_{1-x-y}Mg_xAl_yO$**	**Volume V_1 of S_1 (mL)**	**Volume V_2 of S_2 (mL)**	**Volume V_3 of S_3 (mL)**
0	0	0.0000	0.0000	ZnO	50	0	0
1	1	0.0005	0.0005	$Zn_{0.98}Mg_{0.01}Al_{0.01}O$	47.652	1.18	1.168
1	3	0.0005	0.00154	$Zn_{0.96}Mg_{0.03}Al_{0.01}O$	45.232	3.6	1.168
1	5	0.0005	0.0026	$Zn_{0.94}Mg_{0.05}Al_{0.01}O$	42.758	6.074	1.168
1	7	0.0005	0.0037	$Zn_{0.92}Mg_{0.07}Al_{0.01}O$	40.182	8.65	1.168
2	1	0.0010	0.0005	$Zn_{0.97}Mg_{0.01}Al_{0.02}O$	46.484	1.18	2.336
2	3	0.0010	0.00154	$Zn_{0.95}Mg_{0.03}Al_{0.02}O$	44.064	3.6	2.336
2	5	0.0010	0.0026	$Zn_{0.93}Mg_{0.05}Al_{0.02}O$	41.59	6.074	2.336
2	7	0.0010	0.0037	$Zn_{0.91}Mg_{0.07}Al_{0.02}O$	39.014	8.65	2.336

Except ZnAlO, in all the previous preparations we have not used ethanol, in this case we had to use, to dissolve the $Al(acac)_3$. But the solubility is hindered when it is mixed with water-based solution. So, keeping the poor solubility factor of $Al(acac)_3$ in mind and the detrimental effects of increasing aluminum molar concentration on the film quality, we have only used up to molar concentration of 2 % $Al(acac)_3$. Most importantly we see that in the final solutions S4 the volume percentages of ethanol can be only in the range from 1 % to 2.3 %. This low volume percentage will not be toxic for the pyrolysis process. Based on the experimental details mentioned in the ***Chapter 2*** we have added acetic acid to each of the precursor solution and maintained a value of pH of 4. Having the same pH for all the solutions helps to analyze consistently the films. The other advantages of acetic acid are mentioned in the previous chapters.

6.5.2 Design of Experiment

The nozzle speed and the spray flow rates were pre-fixed to 70 mm/sec and 0.5 mL/min based on the safety requirements of the spray system. The list below shows the variation of other spray parameters along with range of their variation, and the ***Table 6.7*** summarized the used design of experiment.

1. The zinc acetate ($Zn(Ac)_2$) molar concentration in the precursor solution varied in the range from 0.03 mol/L to 0.10 mol/L.

2. The magnesium acetate tetrahydrate ($Mg(Ac)_2 \cdot 4H_2O$) molar concentration in the precursor solution varied in the range from 0.0015 mol/L to 0.0214 mol/L.

3. The aluminum acetylacetonate ($Al(acac)_3$) molar concentration in the precursor solution varied in the range from 0.0005 mol/L to 0.0026 mol/L.

4. The number of spray cycles, which ranged from 10 to 100. The duration of each preparation is determined by this parameter.

5. The dwell times between each spray cycle varied between 0.5 s to 2 s.

6. The hot plate set temperature was varied between 400 °C to 480 °C.

7. The relative shaping air pressure was varied between 6.8 kPa to 27.6 kPa.

8. The height between nozzle to substrate was varied between 90 mm to 110 mm.

Table 6.7: Design of experiment to select the optimal spray parameters for ZnMgAlO preparation.

Preparation Parameter	**Range**	**Optimal value selected from experiments**
$Zn(Ac)_2$ molar concentration	[0.03 mol/L ; 0.1 mol/L]	0.05 mol/L
Magnesium acetate tetrahydrate concentration	[0.0015 mol/L ; 0.0214 mol/L]	0.0015 mol/L to 0.0037 mol/L
Aluminum acetylacetonate concentration	[0.0005 mol/L ; 0.0026 mol/L]	0.0005 mol/L & 0.0010 mol/L
Number of spray cycles	[10 ; 100]	20
Dwell times between each spray cycle	[0.5 s ; 2 s]	0.5 s
Set preparation temperature	[400 °C ; 480 °C]	470 °C
Relative shaping air pressure	[6.8 kPa ; 27.6 kPa]	20.6 kPa
Height between nozzle to substrate	[90 mm ; 110 mm]	100 mm

6.6 Results and Discussions on the Preparation of ZnMgAlO

The optimal value of the spray parameters from the design of experiments scheme mentioned above has been used for the preparation of ZnMgAlO thin films. Various characterization techniques were used to understand the effect of the Al and Mg incorporation in the precursor solution on the quality of the prepared ZnMgAlO thin films. In all the films prepared using the precursor solutions, the Mg molar concentrations were varied from 0 % to 7 % by keeping Al molar concentrations fixed to 0 %, 1 % and 2 % respectively. The details are shown in the ***Table 6.6*** along with the stoichiometry of the prepared films.

6.6.1 Optical and Morphological Properties of the ZnMgAlO Thin Films

In this section we try to analyze the optical properties of the ZnMgAlO thin films with respect to the increase of the Al and Mg molar concentration. The thickness of the prepared films was measured within a variation of ± 10 nm as done for the other metal oxides films.

At first the transmission of the films was assessed in relation to the magnesium incorporation effect by keeping the aluminum concentrations fixed. Using the same process, the bandgap and Urbach energies of the prepared films were studied. The transmission spectra of the $Zn_{1-y-x}Mg_xAl_yO$ thin films with aluminum molar compositions 0 %, 1 % and 2 % and with varying magnesium molar compositions are shown in the ***Figure 6.13 (a, b & c)*** respectively.

The average transmission of the films in the wavelength range 500-800 nm is shown in the ***Figure 6.14 (a, b & c)***. It is seen from the ***Figures 6.13 & 6.15*** that without aluminum, when only magnesium composition is increased, the transparency is always more than 90 %. This is in accordance with the optical results of ZnMgO films prepared by Accumist nozzle in the ***Section 4.6.3*** of ***Chapter 4***. As aluminum is introduced the transparency falls due to the poor solubility of the aluminum precursor. With aluminum 1 mol%, the average transmission in the films is approx. 90 %, but with aluminum 2 mol%, the average transmission in the films is always below 90 %.

Figure 6.13: Transmission spectra of $Zn_{1-y-x}Mg_xAl_yO$ thin films as a function of Mg molar composition with fixed Al molar compositions of 0 % **(a)**, 1 % **(b)** and 2 % **(c)**. The spectrum of a SLG substrates is also shown, with nearly constant transmission at 100 %. A zoom in the absorption edge spectral region is shown in the inset plots of each figure.

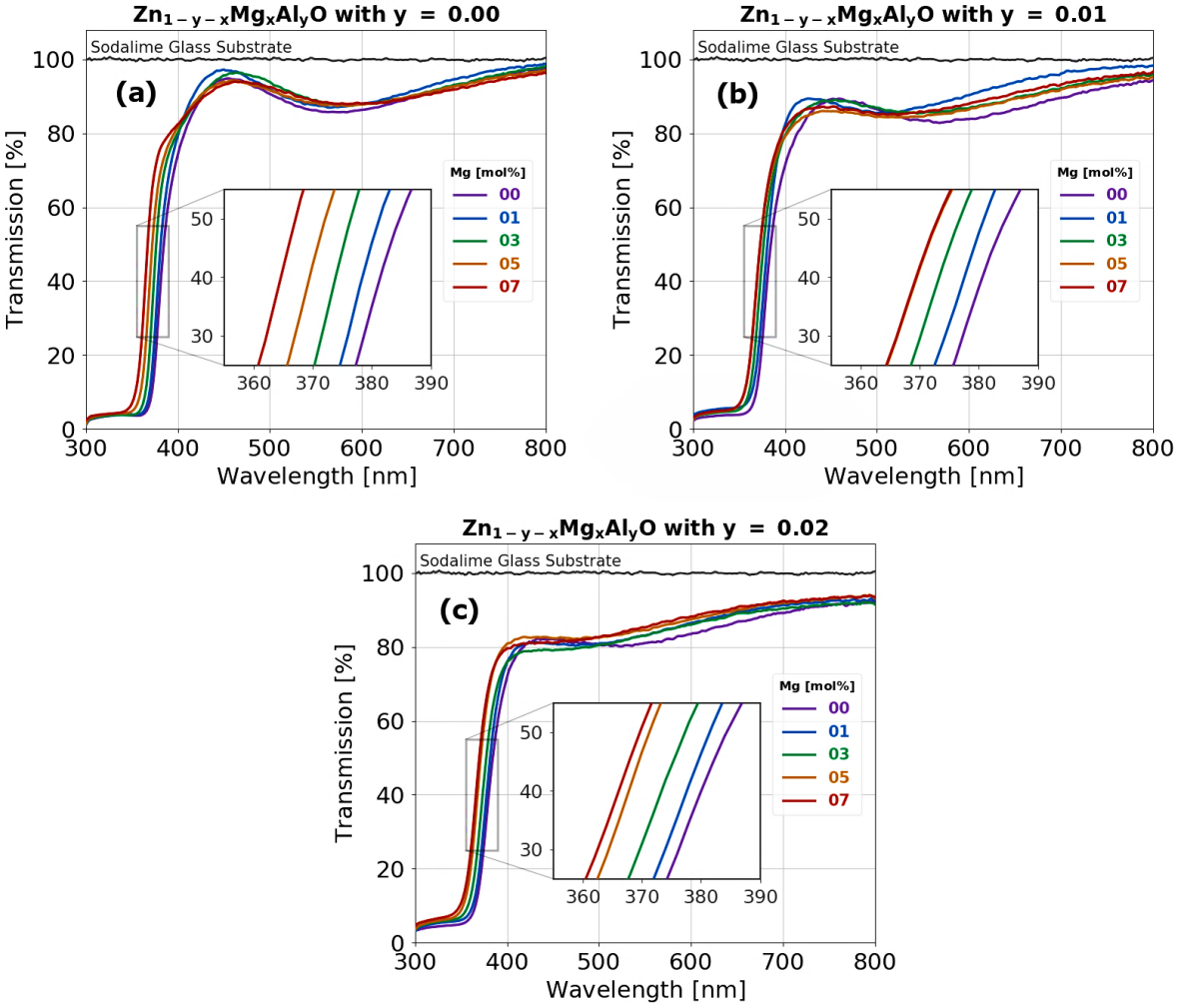

Figure 6.14: Average transmission of $Zn_{1-y-x}Mg_xAl_yO$ thin films as a function of Mg molar composition with fixed Al molar compositions of 0 % **(a)**, 1 % **(b)** and 2 % **(c)** in the wavelength region 500 nm to 800 nm.

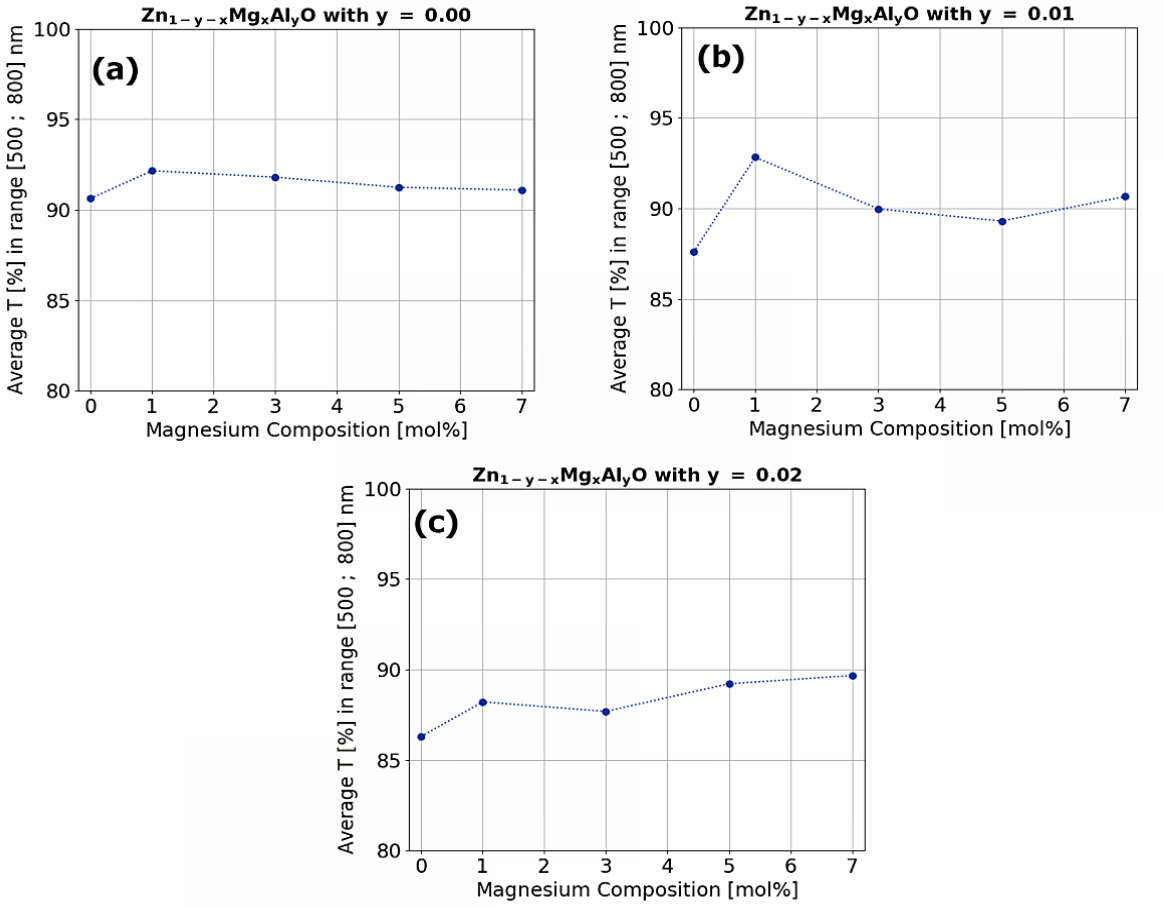

The estimation of the bandgap energies of the $Zn_{1-y-x}Mg_xAl_yO$ films are done using the Tauc plot model and shown in the ***Figure 6.16 (a, b & c)***. ***Figure 6.17 (a, b & c)*** shows the variation of the bandgap energies with fixed Al molar composition and increasing Mg molar compositions.

Figure 6.15: Estimation of the bandgap energies of $Zn_{1-y-x}Mg_xAl_yO$ thin films as a function of Mg molar composition with fixed Al molar compositions of 0 % **(a)**, 1 % **(b)** and 2 % **(c)**.

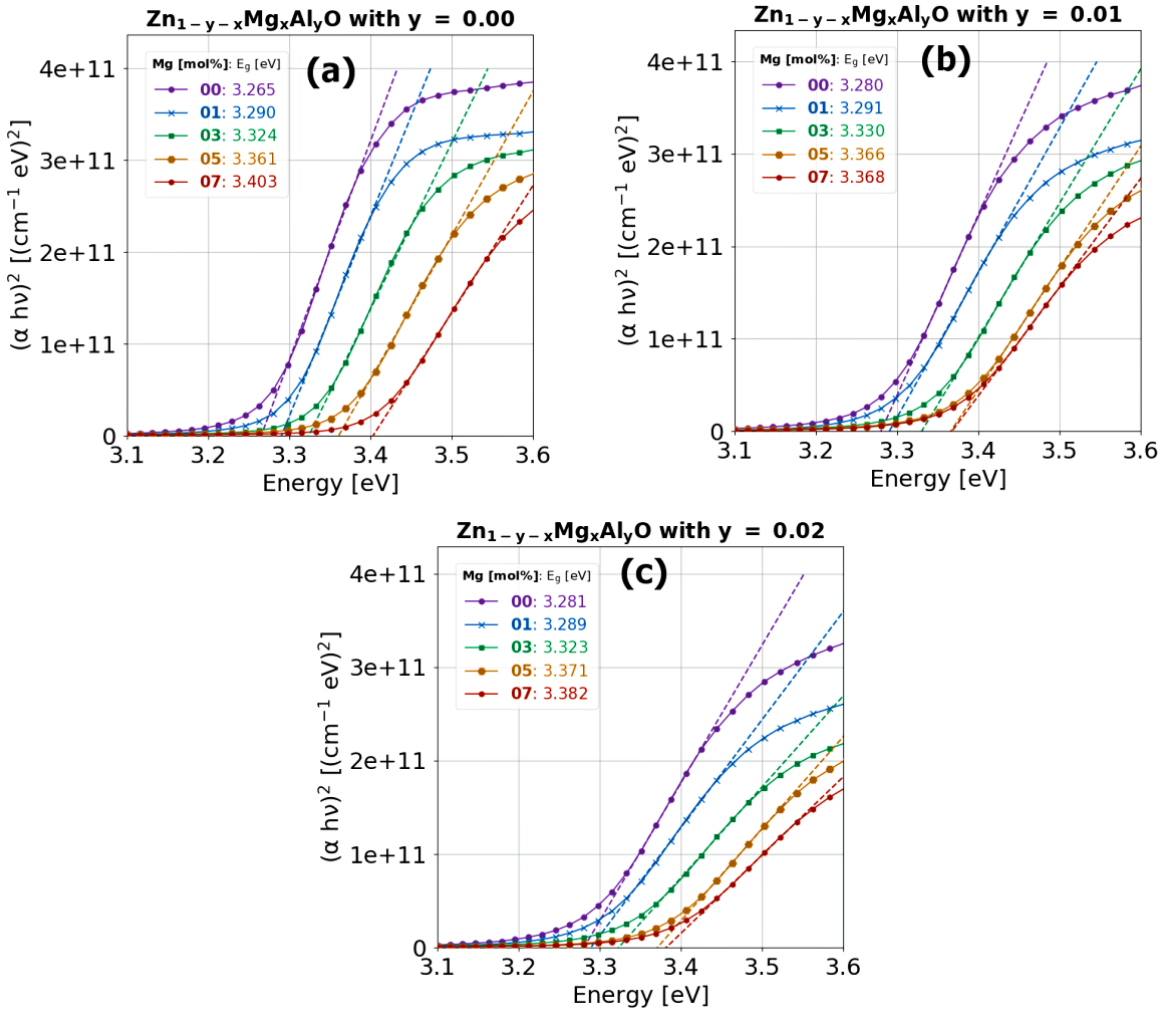

The bandgap increases almost linearly with increase in Mg molar composition. As explained in ***Chapter 4***, this can be attributed to substitution of Zn^{2+} ions by Mg^{2+} ions in some of the sites of Zn^{2+} and without any excess free carriers. A dominant state of Mg 3s is usually noticed where the conduction band minima occur. This state has higher energy than the 4s state [31]. So, a broadening of the bandgap happens with Mg incorporation. Because of the disorders introduced in the crystals, the bandgap variation slightly loses linearity with Al incorporation.

Figure 6.16: Variation of the bandgap energies of $Zn_{1-y-x}Mg_xAl_yO$ thin films as a function of Mg molar composition with fixed Al molar compositions of 0 % **(a)**, 1 % **(b)** and 2 % **(c)**.

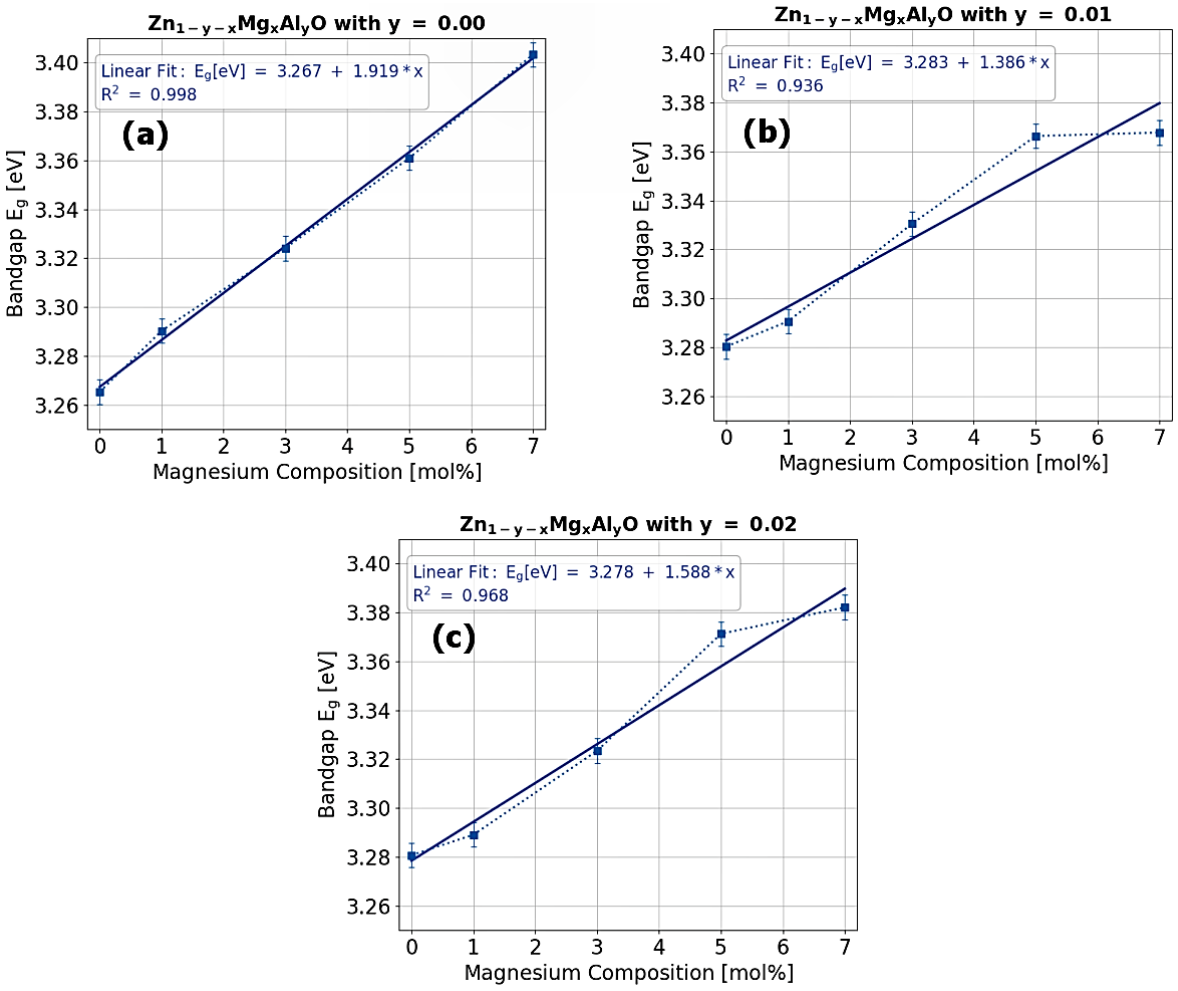

We also calculated the Urbach energy to estimate the alloy disorders and increase of density of defects in the $Zn_{1-y-x}Mg_xAl_yO$ films with the increase in the magnesium content with fixed aluminum contents. The Urbach energies are calculated from the absorption of the thin films in the wavelength regime 300 nm to 400 nm as shown in the transmission spectra of ***Figure 6.13***. The Urbach energy calculations are shown in the ***Figure 6.17*** and the variations of the Urbach energies are shown in the ***Figure 6.18***.

Figure 6.17: Estimation of the Urbach energies of $Zn_{1-y-x}Mg_xAl_yO$ thin films as a function of Mg molar composition with fixed Al molar compositions of 0 % **(a)**, 1 % **(b)** and 2 % **(c)**.

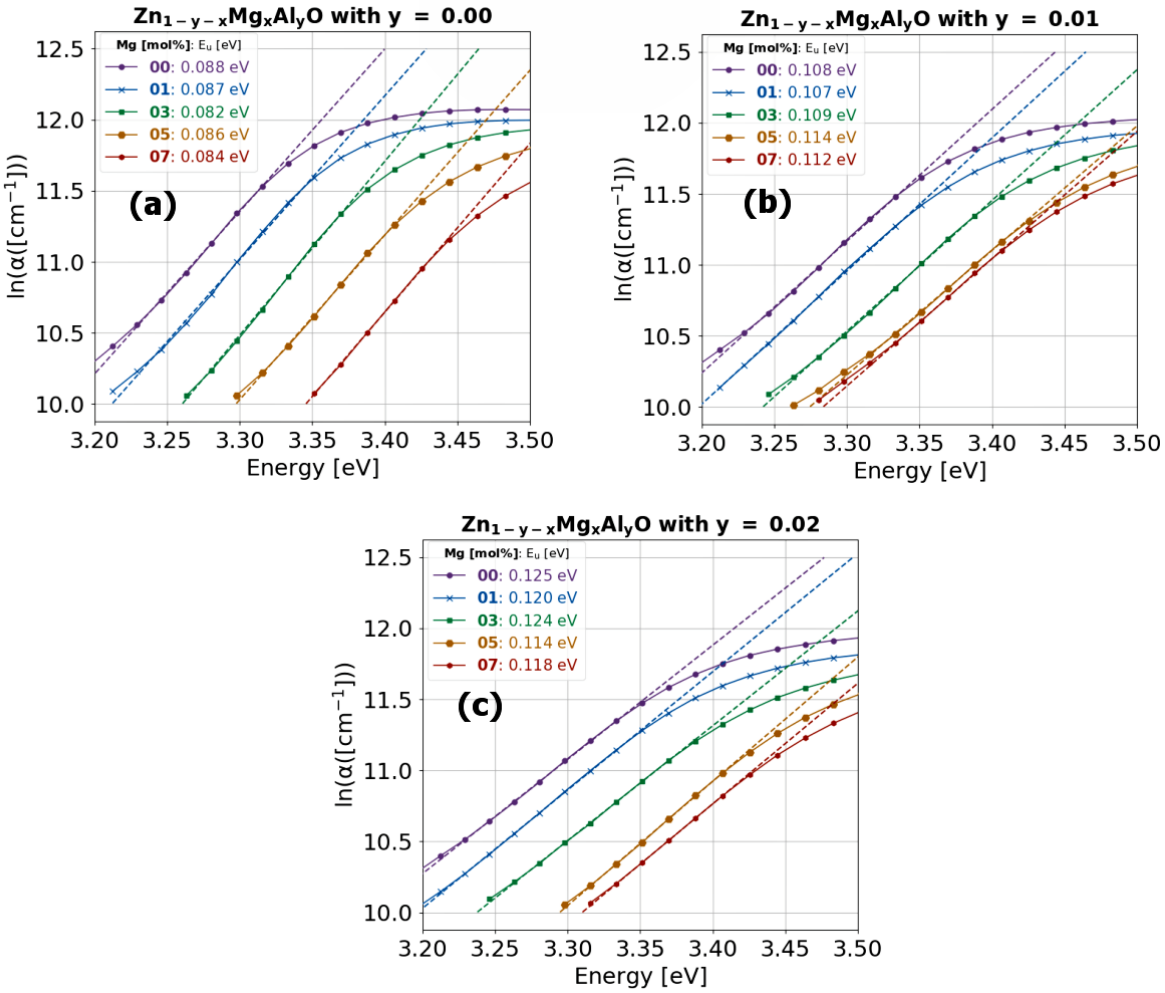

From the analysis, we can estimate that the obtained Urbach energy value for the films without aluminum compositions, the Urbach energy values remains almost constant. This is contrary to our results obtained for the ZnMgO films, where the Urbach energy increased with increase in the Mg content. So, we can say that with an efficient control on the spray parameters with the Impact nozzle does not sufficiently introduce lattice alloy disorders in the films. Even when the Al is introduced, there is not enough lattice alloy disorder in the films. Although the Al molar composition is too low, but still without much disorder the films show high optical quality with the increase in composition. As stated in the ***Section 2.7.2.1*** of ***Chapter 2***, Urbach energy is only a qualitative indicator and does not quantify the disorder in the material, nor is it sensitive to any kind of disorder. It is one indicator among others and should be correlated to other characterization results.

Figure 6.18: Variation of the Urbach energies of $Zn_{1-y-x}Mg_xAl_yO$ thin films as a function of Mg molar composition with fixed Al molar compositions of 0 % **(a)**, 1 % **(b)** and 2 % **(c)**.

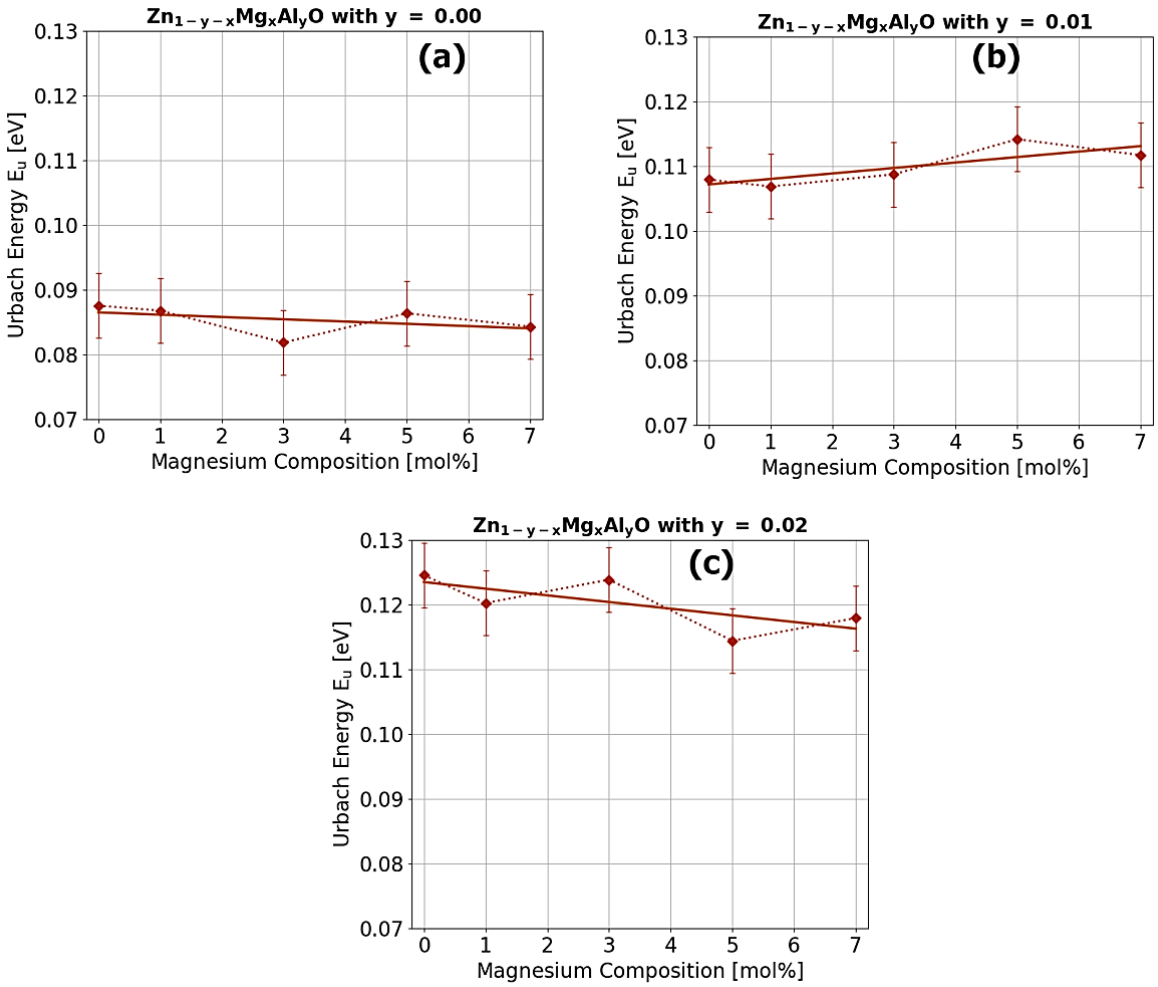

The morphological analysis of the thin films was done by SEM. For the films without any Mg, for Al molar compositions 1 % and 2 %, the surfaces reveal polycrystalline nature with some roughness. Some small clusters can even be seen on the sample with Al mol 2 %. The surfaces tend to get better and smoother with the incorporation of Magnesium. Big clusters are not visible in the micrographs. This can be related to the less lattice disorders with the increase in the Mg content in the films as seen from the Urbach analysis. Although, some small agglomerations could be noticed for the film with Al mol 2 % with 7 mol % of Mg. All the films showed high quality with uniform grain distribution and without any voids. These morphological results when compared to films developed by RF magnetron sputtering [24,27] are quite similar.

Figure 6.19: SEM micrographs of $Zn_{1-y-x}Mg_xAl_yO$ thin films with different Al and Mg molar compositions.

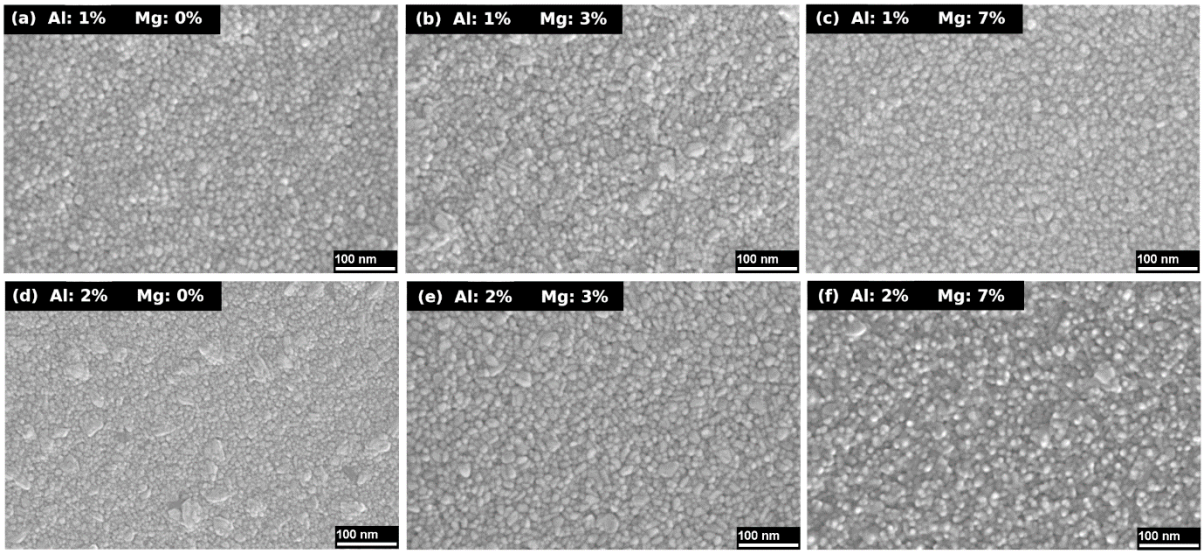

6.6.2 Structural Properties of the ZnMgAlO Thin Films

To analyze the structural properties of the $Zn_{1-y-x}Mg_xAl_yO$ thin films, X-ray diffraction (XRD) measurements were done on the films. The diffractograms are shown in the ***Figure 6.20***. The $Zn_{1-y-x}Mg_xAl_yO$ thin films exhibit a single hexagonal wurtzite crystal structure with peaks for the (100), (002), (101), (102), (110), (103) and (112) planes of the space group $P6_3mc$, identified by using the ZnO powder diffractogram (RRUFF ID: R060027.1) [13] as a reference for magnesium compositions up to 7 mol% with fixed aluminum compositions of 1 mol% and 2 mol%. From the diffractograms we could not identify any phase related to formation of MgO or Al_2O_3. At the low molar concentrations of Mg and Al no additional phase occurs and only the wurtzite phase of ZnO is detected. This is like the XRD analysis done for ZnMgO thin films in ***Chapter 4***.

Figure 6.20: XRD diffraction patterns for $Zn_{1-y-x}Mg_xAl_yO$ solid thin films with respect to the Mg and Al molar compositions.

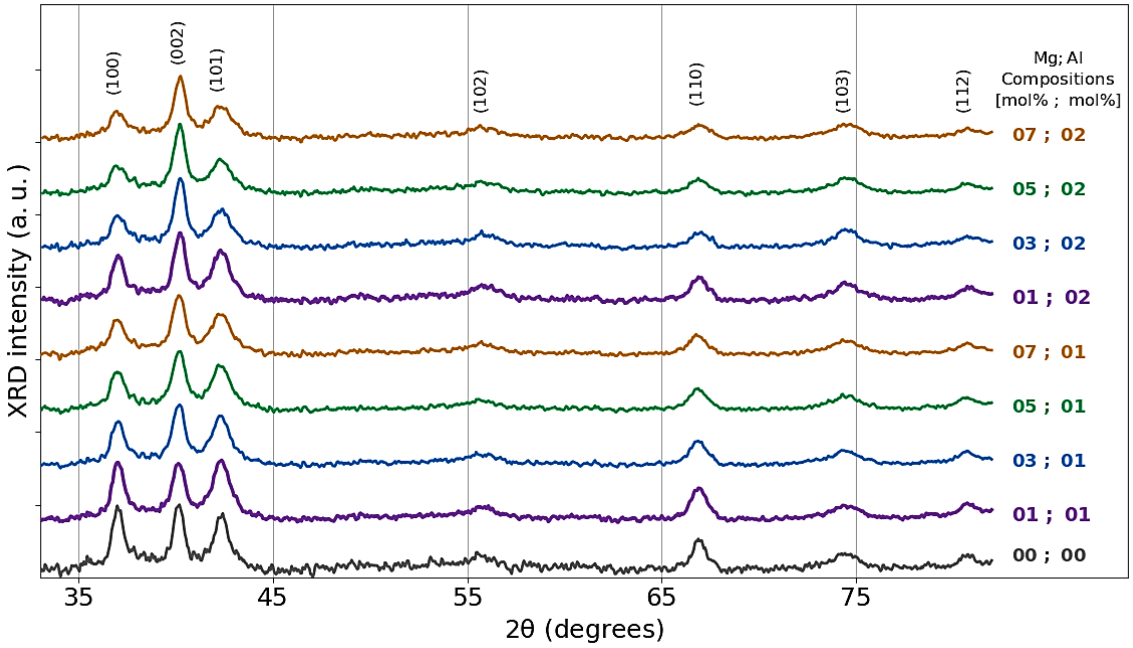

The texture quality of the films was also checked in terms of the Lotgering factor [15,16] as done for the ZnAlO ternary. Values above 0.0 gives the indication of the most dominant peak which in our case is (002) as shown in the ***Figure 6.21 (a, b)***. As we have discussed in detail in the ***Section 3.5.5*** of the ***Chapter 3***, the (002) peak orientation gives an indication of the crystalline quality of the wurtzite c-axis oriented films. The texture factor increased with the increase in the Mg composition with the fixed Al molar composition. This agrees with prior findings [32,33] that films with c-axis orientation have the lowest surface energy, uniformly aligned crystallites, and few defects and trapping sites. From the Urbach analysis we have seen lower disorders with increasing Mg. The c-axis orientation is mostly dominating because of a faster growth rate along this direction during the spray preparation. The Mg and Al gets more mean free path to substitute the Zn ions with the lower concentration of ZnO in the precursor solution. With lower Mg and Al, the films are more like powder diffraction because the substitution of Zn is low, so the growth is more random.

Figure 6.21: Texture factor estimation of different peaks for $Zn_{1-y-x}Mg_xAl_yO$ thin films with respect to the Mg molar compositions and fixed Al molar compositions using the method of Lotgering factor.

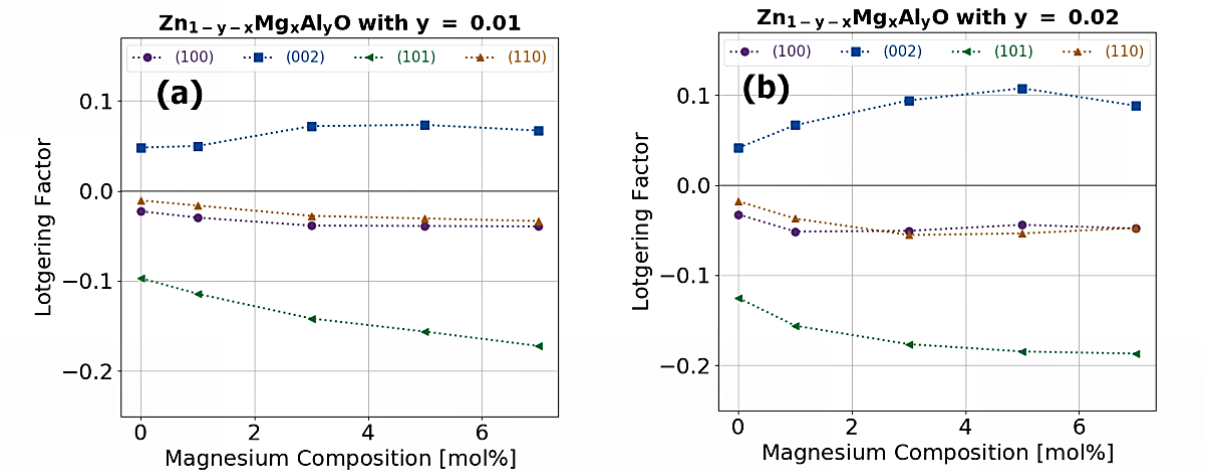

In correspondence to the texture analysis of the films, we also estimated the crystallite sizes with respect to the different peaks along with the increase in Mg molar composition. The ***Figure 6.22 (a, b)*** shows the estimated values of the crystallite sizes. The values estimated with the (002) peaks, corresponding the wurtzite phase always shows higher values which agree with our previously prepared ZnO and ZnMgO films. The procedure for the estimation of the crystallite sizes is explained in the ***Section 2.7.3.1*** of ***Chapter 2***.

Figure 6.22: Crystallite size estimations of different peaks for $Zn_{1-y-x}Mg_xAl_yO$ thin films with respect to the Mg molar compositions and fixed Al molar compositions of 1 % **(a)** and 2 % **(b)**.

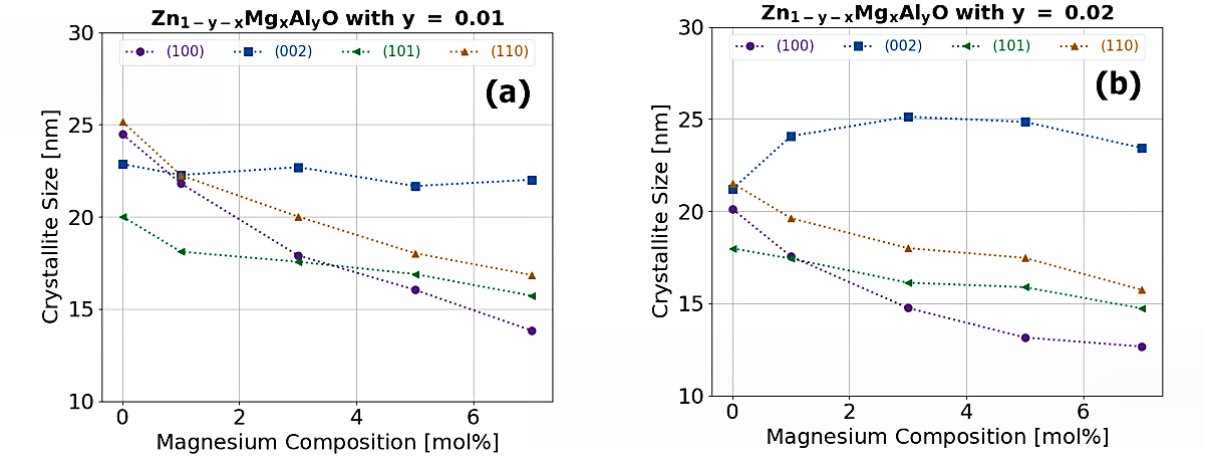

Also, noticed is that the lattice parameters **a** and **c** do not change much with the increase in Mg for both the molar compositions of Al.

The variation in the lattice parameters corresponding to (002) peak is shown in the ***Figure 6.23 (a to d***). The obtained values can be compared to the values obtained by USP for ZnO in our work [14] (detailed in ***Table 3.5*** of ***Chapter 3***). For the lattice parameters our results disagree with coatings developed by Tsai *et al.* [26] using RF magnetron sputtering. In our case, we do not have too much of shrinkage in the lattice parameters as obtained by Tsai *et al.* This could be due to less disorders in our films with effective control on the spray preparation parameters.

Figure 6.23: Lattice parameter estimations for $Zn_{1-y-x}Mg_xAl_yO$ thin films with respect to the Mg molar compositions and fixed Al molar compositions of 1 % **(a, c)** and 2 % **(b, d)**.

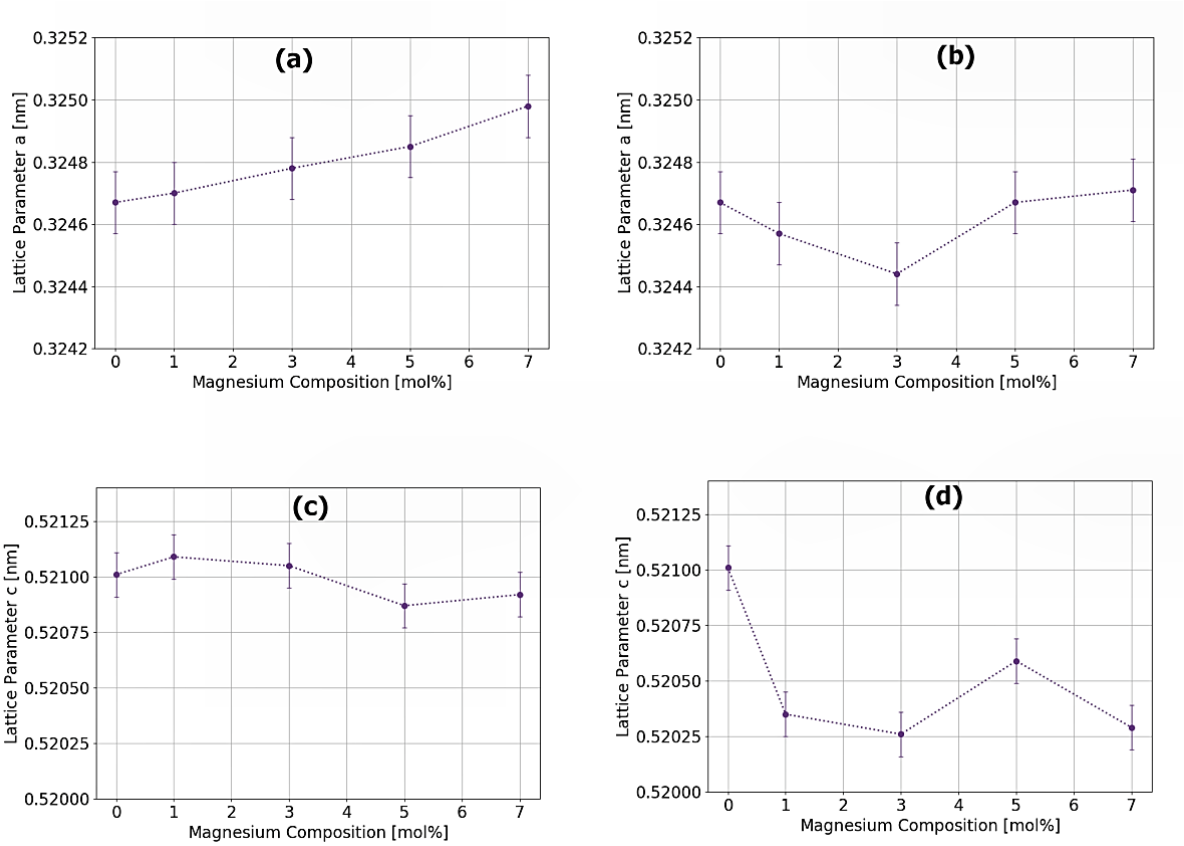

To complete the XRD results, all the films from Mg molar composition 0 % to 7 %, with the Al molar compositions 1 % and 2 % were analyzed using Raman line-scan. The scans were performed using a lateral resolution of 1 µm. The scans revealed no substantial spatial variation, indicating the prepared thin films' homogeneity at this scale of 1 µm. The E_2^{High} and E_2^{Low} mode peaks of the wurtzite structure (C6v symmetry) were systematically observed for all the films and no other mode related to a different phase was detected. This demonstrates the single-phase wurtzite structure of the prepared $Zn_{1-y-x}Mg_xAl_yO$ films as already evidenced from the XRD measurements and optical

analysis. The Raman spectrum corresponding to all the $Zn_{1-y-x}Mg_xAl_yO$ thin films prepared on soda lime glass (SLG) substrates are shown in the ***Figure 6.24***.

Figure 6.24: Raman spectra for $Zn_{1-y-x}Mg_xAl_yO$ thin films with respect to Mg molar composition and fixed Al molar compositions. The Raman spectra of the soda-lime glass substrate is also presented as a reference for appropriately assigning the deposited $Zn_{1-y-x}Mg_xAl_yO$ Raman peaks.

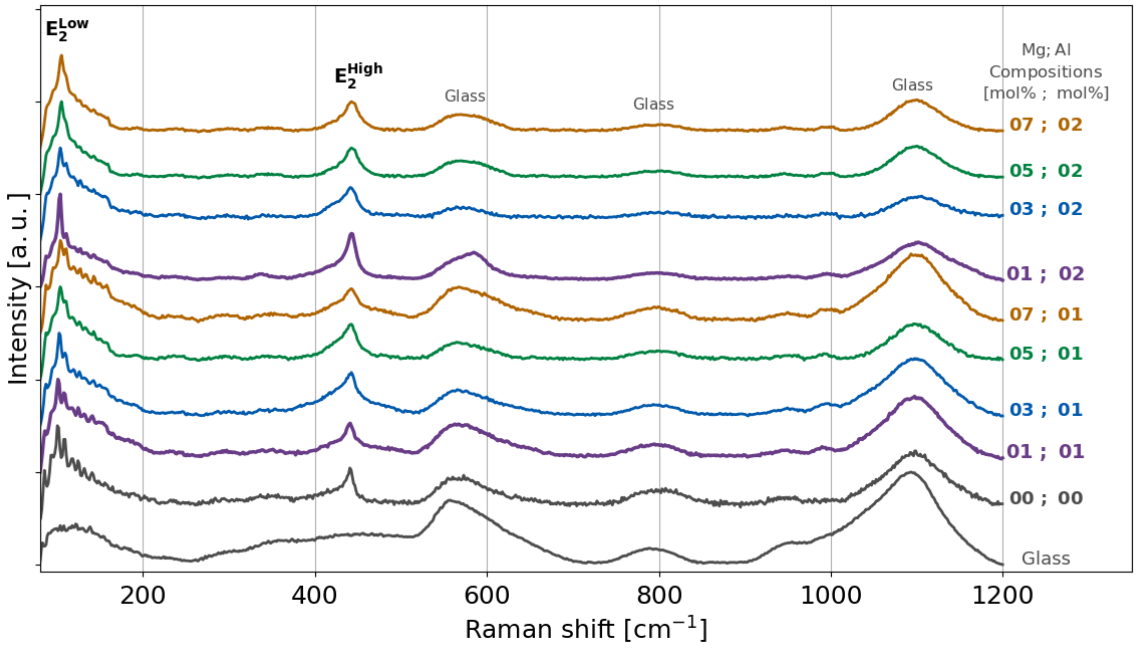

With a Raman shift of 110 cm^{-1} and 439 cm^{-1}, the E_2^{Low} and E_2^{High} peaks of the $Zn_{1-y-x}Mg_xAl_yO$ wurtzite structure are found. The Raman spectrum for the SLG substrate shows two large peaks at 550 cm^{-1} and 1100 cm^{-1} which could be erroneously assigned as the A_1^{LO} and 2 A_1^{LO} phonon vibration modes for ZnO based compounds prepared on SLG substrates. The E_2^{Low} and E_2^{High} peaks did not show a significant change in either peak width or in Raman shift within our experimental spectral resolution of 1 cm^{-1}. These results agree with the Raman studies for ZnMgO films presented in ***Chapter 4***. So, the low molar incorporation of Al does not change the wurtzite phase of the films as seen the XRD analysis.

6.6.3 Electrical Properties of the ZnMgAlO Thin Films

The electrical properties of the $Zn_{1-y-x}Mg_xAl_yO$ thin films were analyzed in terms of the changes to the resistivity, carrier concentration and mobility with the increase of the magnesium molar composition along with the fixed aluminum compositions. After preparation, and prior to the electrical measurements, all the films were annealed using the rapid thermal annealing (RTA) system at a temperature of 300 °C for 30 minutes. The annealing was performed to increase the

grain size, activate the shallow donors and to improve the overall crystal quality as shown in the ***Section 3.5.5*** of ***Chapter 3***.

Figure 6.25: Variation of resistivity for $Zn_{1-y-x}Mg_xAl_yO$ thin films with respect to Mg molar composition and fixed Al molar compositions of 0 %, 1 % and 2 %.

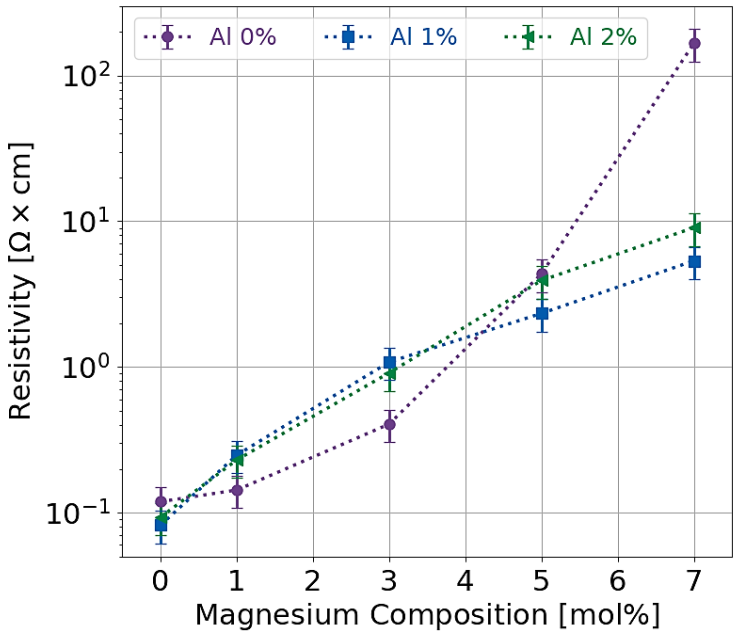

Figure 6.26: Variation of carrier concentration for $Zn_{1-y-x}Mg_xAl_yO$ thin films with respect to Mg molar composition and fixed Al molar compositions of 0 %, 1 % and 2 %.

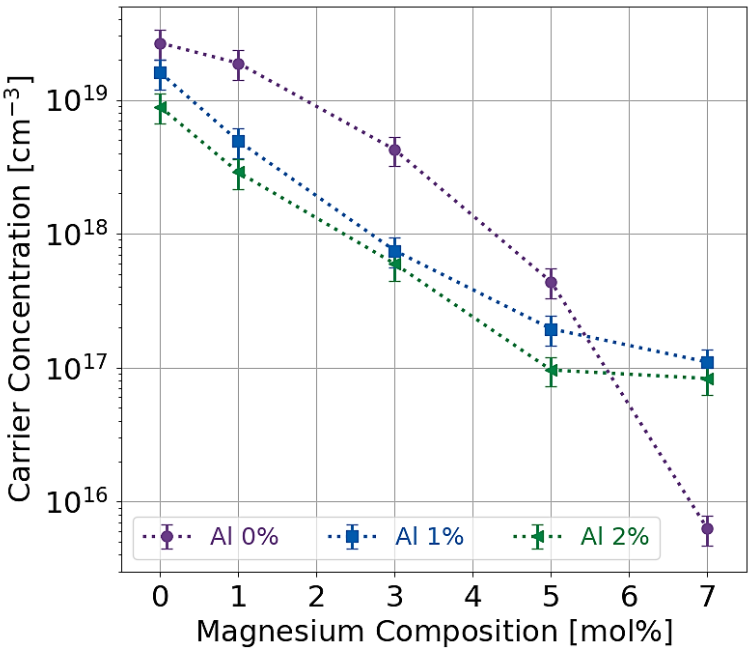

Figure 6.27: Variation of mobility for $Zn_{1-y-x}Mg_xAl_yO$ thin films with respect to Mg molar composition and fixed Al molar compositions of 0 %, 1 % and 2 %.

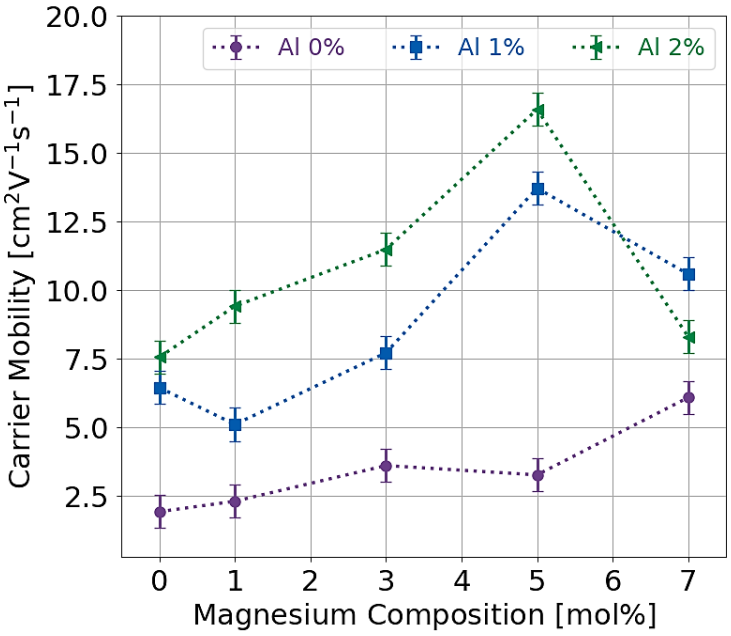

From the resistivity measurements (***Figure 6.25***), it is seen that when without Al incorporation, the magnesium molar composition increases from 0 % to 7 %, the resistivity of the films increases dramatically. The huge increase in the resistivity is collaterally supported by a decrease in the carrier concentrations (***Figure 6.26***). The carrier mobility slightly increases with Mg content (***Figure 6.27***). Interstitial Zn acts as n-type dopants, but Mg incorporation inhibits these sites causing the decrease of free carriers and increasing the resistivity [29]. But interestingly when Al is introduced in the films, the resistivity still increases but, when for the higher Mg contents (5 and 7 mol%), with Al, the resistivities are lower. Magnesium induces a bandgap increase and inhibits shallow donors. Aluminum introduces free carriers to some extent by replacing the Zn^{2+} sites with donor Al^{3+} ions which keeps the resistivity lower. But it can also induce a decrease in the formation of interstitial Zn sites with the change in the stoichiometry, and its activation energy can increase due to the Mg incorporation. There is therefore a complex compensation mechanism between the effect of Al and the effect of Mg. For this reason, correspondingly, the carrier concentration also remains low, for the films with Al. The rate of decrease of the carrier concentration become slower, at the higher Mg contents (***Figure 6.26***). Contrarily, the carrier mobilities for the films with Al, always remains high (***Figure 6.27***).

Thus, the $Zn_{1-y-x}Mg_xAl_yO$ material conductivity, which can be regulated by adding magnesium with fixed aluminum contents, allows the material to be tuned for certain optoelectronic applications, such as ultraviolet detectors and solar cells. For "all-oxide" solar cells, with modulated bandgap in conjunction with the conductivity it can even be used as top window or buffer layers.

6.7 Challenges Faced Towards the Preparation of the Materials

The entire process to successfully prepare the ternary ZnAlO and the quaternary ZnMgAlO thin films by using ultrasonic spray pyrolysis (USP) was quite challenging. For ZnAlO the most challenging task was to optimize the precursor solution. The precursor raw material $Al(acac)_3$ was insoluble in water, so we had to use ethanol to dissolve it first. Then it was mixed with water-based solution for having the ultimate solution for the spray. For this reason, high Al molar compositions were not used. The design of experiments was done carefully to set up the preparations. The set spray temperature was varied to check for the completeness of the pyrolysis reaction to have uniform films with high transparency. The preparation was repeated few times with the same parameters to check for the consistency of the process.

The task to prepare the quaternary ZnMgAlO was far more challenging as the preparation for this material was being done for the first time using USP. Also, as mentioned earlier, handling the Al precursor to first dissolve it and then mix it with water-based solution was complex. The entire process of the preparation of the precursor solutions was done with extreme care and precision. Controlling the stoichiometry in the precursor solution with specific molar compositions of both Al and Mg had to be done very precisely. As this material was completely new for the preparation process, we had a certain degree of freedom to have the design of experiments. Lots of parameters were varied by keeping the others fixed to have in-depth idea about the effect of the spray parameters on the quality of the prepared films. In this case too, keeping the same parameters the preparations were repeated a few times to check the consistency. Our idea was to have high transparency in the films along with enough conductivity and good crystalline quality, so both the Al and Mg molar compositions were varied in conjunction with the other spray parameters to have these qualities in the prepared quaternary films.

6.8 Numerical Simulation using Solis

To initiate a study related to the perspectives of the use of the materials developed in this work (ZnO, ZnMgO, ZnAlO, Cu_2O and lastly the quaternary ZnMgAlO), the Solis 1D semiconductor device simulator [35] was used. Solis solves the drift–diffusion transport equations considering a large variety of physical models, recombination processes (Shockley-Read-Hall nonradiative, radiative and Auger), position-dependent physical parameters (e.g., for graded devices), nonideal ohmic and Schottky contacts, spontaneous and piezoelectric polarizations (in wurtzite materials such as ZnO

and GaN), etc. Solis can calculate the band diagram, carrier concentration, ionized dopant, and trap concentrations, current–voltage and capacitance–voltage characteristics, quantum efficiency, etc. The device can be illuminated using the standard solar spectrum AM1.5, a monochromatic source, or any other user-defined source.

The simulated solar cell structure is show in the ***Figure 6.28***.

Figure 6.28: The simulated “all-oxide” solar cell structure.

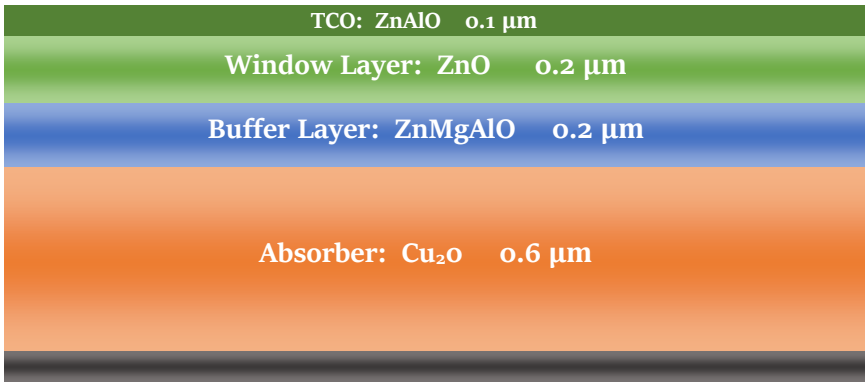

Most parameters given as input to Solis were taken from the measurements performed in this work, to conduct realistic simulations. The Urbach band-tail parameters was included as well one donor-like and one acceptor-like defects. The absorption coefficient was taken from the transmission measurements as well as the bandgap. The doping concentrations and mobilities are those measured by the van der Pauw / Hall Effect technique. The thicknesses are those measured but the profilometer. Other parameters such as dielectric permittivity and density of states in the conduction and valence band are extrapolated from those of ZnO (for the quaternary) or extracted from the literature as developed in [36].

The simulated current-voltage characteristic is shown in the ***Figure 6.30*** with an efficiency of 7.03 %, a short-circuit current of 4.9 mA/cm² and an open-circuit voltage of 1.87 V. The fill factor is about 76 %.

The considering of realistic simulation parameters makes it possible to find similar photovoltaic efficiency than the experimental record and theoretical one found by using ZnGeO as a buffer layer as detailed in [36] and in the ***Section 1.3.2.5*** of ***Chapter 1***, which opens very interesting perspectives. A comprehensive numerical study with respect to the parameters of the materials will provide useful guideline for the development for the first time of the complete “all-oxide” solar cell with the ultrasonic spray pyrolysis technique, using the materials prepared in this work.

Figure 6.29: Simulated current-voltage characteristic under AM1.5 illumination of the ZnO/ZnMgAlO/Cu_2O solar cell structure shown in the ***Figure 6.29***.

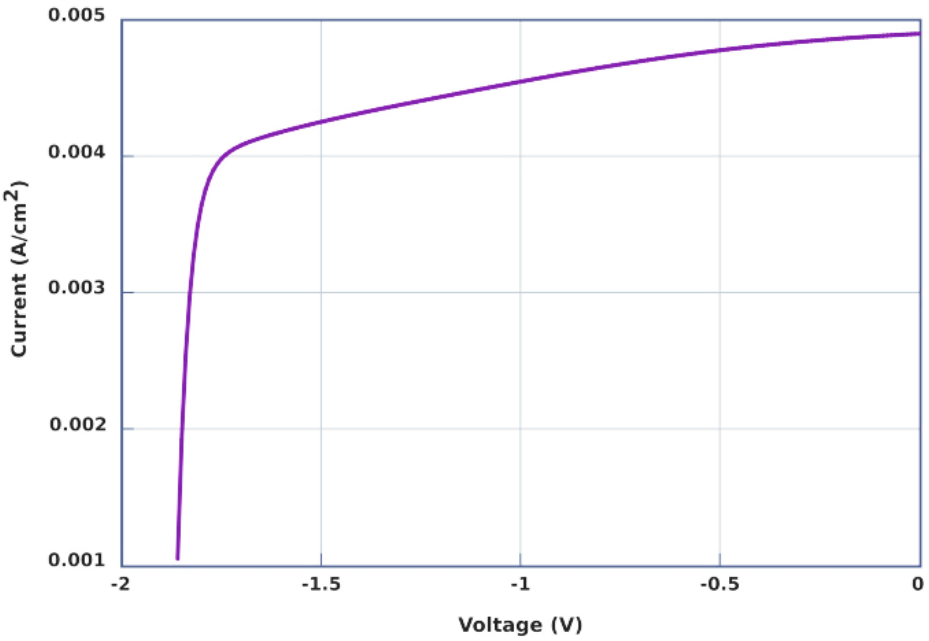

6.9 Chapter Conclusions

In this chapter we design the experiments for the preparation of both ternary (ZnAlO) and quaternary (ZnMgAlO) materials. ZnAlO was primarily prepared to be used as TCO by enhancing the conductivity with Al incorporation. With low Al molar compositions (1 and 2 mol%) the conductivities were found to be better than only ZnO, however the conductivities decreased beyond 2 mol%. Also, due to extremely poor solubility limit of the Al precursor, the transparency of the films decreases when prepared with high Al molar composition. Even there is a decline in the crystal qualities and conductivity for the films prepared using Al molar compositions beyond 2 %. These results were very useful when Al and Mg were co-incorporated to prepare the ZnMgAlO. When the Mg molar compositions were varied the Al molar compositions were kept only at 1 mol% and 2 mol%. By this we have seen that the transparencies were much better (above 90 %) with higher bandgap energies.

Even the crystallinity of the films was better with less disorder than with only Al. With the different Al and Mg compositions, the wurtzite structure of the crystals was retained. These results demonstrate the quality of the control on the spray preparation parameters. The electrical properties were better with Al and Mg co-incorporation especially for the cases when the Mg

compositions are high. The mobilities were higher for the films with Al and Mg co-incorporation. The high transparency of the films in the visible region of the spectrum along with the modulations of the bandgap energies and the conductivities can be interesting for application as TCO’s, window or buffer layers in “all-oxide” solar cells. The ZnMgAlO quaternary can even have useful applications in ultraviolet photodetectors and other optoelectronic devices.

6.10 References

[1] J.K. Srivastava, L. Agarwal, A.B. Bhattacharyya, Electrical Characteristics of Lithium-Doped ZnO Films, J. Electrochem. Soc. 136 (1989) 3414–3417. https://doi.org/10.1149/1.2096463.

[2] T. Minami, H. Nanto, S. Takata, Highly Conductive and Transparent Aluminum Doped Zinc Oxide Thin Films Prepared by RF Magnetron Sputtering, Jpn. J. Appl. Phys. 23 (1984) L280–L282. https://doi.org/10.1143/JJAP.23.L280.

[3] T. Makino, Y. Segawa, S. Yoshida, A. Tsukazaki, A. Ohtomo, M. Kawasaki, Gallium concentration dependence of room-temperature near-band-edge luminescence in n-type ZnO:Ga, Appl. Phys. Lett. 85 (2004) 759–761. https://doi.org/10.1063/1.1776630.

[4] K.-K. Kim, S. Niki, J.-Y. Oh, J.-O. Song, T.-Y. Seong, S.-J. Park, S. Fujita, S.-W. Kim, High electron concentration and mobility in Al-doped n-ZnO epilayer achieved via dopant activation using rapid-thermal annealing, J. Appl. Phys. 97 (2005) 066103. https://doi.org/10.1063/1.1863416.

[5] A.E. Jiménez-González, J.A. Soto Urueta, R. Suárez-Parra, Optical and electrical characteristics of aluminum-doped ZnO thin films prepared by solgel technique, J. Cryst. Growth. 192 (1998) 430–438. https://doi.org/10.1016/S0022-0248(98)00422-9.

[6] H. Serier, M. Gaudon, M. Ménétrier, Al-doped ZnO powdered materials: Al solubility limit and IR absorption properties, Solid State Sci. 11 (2009) 1192–1197. https://doi.org/10.1016/j.solidstatesciences.2009.03.007.

[7] F. Maldonado, A. Stashans, Al-doped ZnO: Electronic, electrical and structural properties, J. Phys. Chem. Solids. 71 (2010) 784–787. https://doi.org/10.1016/j.jpcs.2010.02.001.

[8] J.K. Burdett, G.D. Price, S.L. Price, Role of the crystal-field theory in determining the structures of spinels, J. Am. Chem. Soc. 104 (1982) 92–95. https://doi.org/10.1021/ja00365a019.

[9] M.C. Kao, H.Z. Chen, S.L. Young, Effects of preannealing temperature of ZnO thin films on the performance of dye-sensitized solar cells, Appl. Phys. A. 98 (2010) 595–599. https://doi.org/10.1007/s00339-009-5467-9.

[10] B.E. Sernelius, K.-F. Berggren, Z.-C. Jin, I. Hamberg, C.G. Granqvist, Bandgap tailoring of ZnO by means of heavy Al doping, Phys. Rev. B. 37 (1988) 10244–10248. https://doi.org/10.1103/PhysRevB.37.10244.

[11] M.J. Akhtar, H.A. Alhadlaq, A. Alshamsan, M.A. Majeed Khan, M. Ahamed, Aluminum doping tunes band gap energy level as well as oxidative stress-mediated cytotoxicity of ZnO nanoparticles in MCF-7 cells, Sci. Rep. 5 (2015) 13876. https://doi.org/10.1038/srep13876.

[12] G. Wisz, I. Virt, P. Sagan, P. Potera, R. Yavorskyi, Structural, Optical and Electrical Properties of Zinc Oxide Layers Produced by Pulsed Laser Deposition Method, Nanoscale Res. Lett. 12 (2017) 253. https://doi.org/10.1186/s11671-017-2033-9.

[13] R. T. Downs, The RRUFF Project: An Integrated Study of the Chemistry, Crystallography, Raman and Infrared Spectroscopy of Minerals, Proceedings of the 19th General Meeting of the International Mineralogical Association, Kobe, 23-28 July 2006, pp. 3-13, (2006).

[14] S. Bose, C. Chevallier, S. Ould Saad Hamady, D. Horwat, J.-F. Pierson, P. Boulet, T. Gries, T. Aubert, N. Fressengeas, Elaboration of high-transparency ZnO thin films by ultrasonic spray pyrolysis with fast growth rate, Superlattices Microstruct. 156 (2021) 106945. https://doi.org/10.1016/j.spmi.2021.106945.

[15] F.K. Lotgering, Topotactical reactions with ferrimagnetic oxides having hexagonal crystal structures—I, J. Inorg. Nucl. Chem. 9 (1959) 113–123. https://doi.org/10.1016/0022-1902(59)80070-1.

[16] R. Furushima, S. Tanaka, Z. Kato, K. Uematsu, Orientation distribution-Lotgering factor relationship in a polycrystalline material-as an example of bismuth titanate prepared by a magnetic field, J. Ceram. Soc. Japan. 118 (2010) 921–926. https://doi.org/10.2109/jcersj2.118.921.

[17] H. Kim, A. Piqué, J.. Horwitz, H. Murata, Z.. Kafafi, C.. Gilmore, D.. Chrisey, Effect of aluminum doping on zinc oxide thin films grown by pulsed laser deposition for organic light-emitting devices, Thin Solid Films. 377–378 (2000) 798–802. https://doi.org/10.1016/S0040-6090(00)01290-6.

[18] J. Hu, R.G. Gordon, Textured aluminum-doped zinc oxide thin films from atmospheric pressure chemical-vapor deposition, J. Appl. Phys. 71 (1992) 880–890. https://doi.org/10.1063/1.351309.

[19] A.F. Aktaruzzaman, G.L. Sharma, L.K. Malhotra, Electrical, optical and annealing characteristics of ZnO:Al films prepared by spray pyrolysis, Thin Solid Films. 198 (1991) 67–74. https://doi.org/10.1016/0040-6090(91)90325-R.

[20] S.R.F.S. Panahi, A. Abbasi, V. Ghods, M. Amirahmadi, Improvement of CIGS solar cell efficiency with graded bandgap absorber layer, J. Mater. Sci. Mater. Electron. 32 (2021) 2041–2050. https://doi.org/10.1007/s10854-020-04971-7.

[21] D. Thapa, J. Huso, K. Miklos, P.M. Wojcik, D.N. McIlroy, J.L. Morrison, C. Corolewski, M.D. McCluskey, T.J. Williams, M. Grant Norton, L. Bergman, UV-luminescent MgZnO semiconductor alloys: nanostructure and optical properties, J. Mater. Sci. Mater. Electron. 28 (2017) 2511–2520. https://doi.org/10.1007/s10854-016-5825-2.

[22] R.A. Afre, N. Sharma, M. Sharon, M. Sharon, Transparent Conducting Oxide Films for Various Applications: A Review, Rev. Adv. Mater. Sci. 53 (2018) 79–89. https://doi.org/10.1515/rams-2018-0006.

[23] J.D. Ye, S. Pannirselvam, S.T. Lim, J.F. Bi, X.W. Sun, G.Q. Lo, K.L. Teo, Two-dimensional electron gas in Zn-polar ZnMgO/ZnO heterostructure grown by metal-organic vapor phase epitaxy, Appl. Phys. Lett. 97 (2010) 111908. https://doi.org/10.1063/1.3489101.

[24] I.-S. Kim, B.-T. Lee, Design and Growth of Deep UV-Range Single Crystalline ZnMgAlO Thin Films Lattice-Matched to ZnO, Cryst. Growth Des. 10 (2010) 3273–3276. https://doi.org/10.1021/cg100454z.

[25] J.-H. Park, J.-B. Lim, B.-T. Lee, Optical and electrical properties of sputter-deposited ZnMgAlO UV-range transparent conducting films, Semicond. Sci. Technol. 28 (2013) 065004. https://doi.org/10.1088/0268-1242/28/6/065004.

[26] D.-C. Tsai, F.-K. Chen, Z.-C. Chang, B.-H. Kuo, E.-C. Chen, Y.-L. Huang, F.-S. Shieu, Influence of substrate temperature on the structural and optoelectronic properties of ZnMgO:Al coatings deposited by radio frequency magnetron sputtering, J. Ceram. Soc. Japan. 129 (2021) 21062. https://doi.org/10.2109/jcersj2.21062.

[27] J.-H. Park, N.-S. Yoon, J.-S. Lee, B.-T. Lee, Effects of growth variables on the properties of deep-UV ZnMgAlO thin films lattice matched to ZnO, J. Cryst. Growth. 381 (2013) 160–164. https://doi.org/10.1016/j.jcrysgro.2013.07.015.

[28] M.-S. Kim, B.-T. Lee, Growth and characterization of single crystalline $Zn_{0.8-x}Mg_{0.2}Al_xO$ films with UV band gap on GaN/Al_2O_3 template by RF magnetron sputtering, J. Cryst. Growth. 364 (2013) 155–157. https://doi.org/10.1016/j.jcrysgro.2012.11.026.

[29] C. Yang, X.M. Li, X.D. Gao, X. Cao, R. Yang, Y.Z. Li, ZnMgAlO based transparent conducting oxides with modulatable bandgap, Solid State Commun. 151 (2011) 264–267. https://doi.org/10.1016/j.ssc.2010.11.008.

[30] O. Cakiroglu, M. Acikgoz, L. Arda, D. Akcan, N. Dogan, Synthesis, structure and ESR studies of Mg doped ZnAlO nanoparticles, J. Magn. Magn. Mater. 373 (2015) 60–64. https://doi.org/10.1016/j.jmmm.2014.03.032.

[31] H. Ghadi, P. Murkute, A. Ghosh, S.M.M.D. Dwivedi, A. Mondal, S. Chakrabarti, Ultrasensitive zinc magnesium oxide nanorods based micro-sensor platform for UV detection and light trapping, Sensors Actuators A Phys. 278 (2018) 127–139. https://doi.org/10.1016/j.sna.2018.05.028.

[32] J.K. Saha, R.N. Bukke, N.N. Mude, J. Jang, Significant improvement of spray pyrolyzed ZnO thin film by precursor optimization for high mobility thin film transistors, Sci. Rep. 10 (2020) 8999. https://doi.org/10.1038/s41598-020-65938-6.

[33] M.P.F. de Godoy, L.K.S. de Herval, A.A.C. Cotta, Y.J. Onofre, W.A.A. Macedo, ZnO thin films design: the role of precursor molarity in the spray pyrolysis process, J. Mater. Sci. Mater. Electron. 31 (2020) 17269–17280. https://doi.org/10.1007/s10854-020-04281-y.

[34] S. Brochen, C. Granier, G. Feuillet, J. Pernot, Role of deep and shallow donor levels on n -type conductivity of hydrothermal ZnO, Appl. Phys. Lett. 100 (2012) 052115. https://doi.org/10.1063/1.3681168.

[35] S. Ould Saad Hamady. Solis: a modular, portable, and high-performance 1D semiconductor device simulator. Journal of Computational Electronics 19 (2020) 640-647. https://doi.org/10.1007/s10825-020-01477-7.

[36] C. Chevallier, S. Bose, S. Ould Saad Hamady, N. Fressengeas, Numerical investigations of the impact of buffer germanium composition and low cost fabrication of Cu_2O on AZO/ZnGeO/Cu_2O solar cell performances, EPJ Photovoltaics. 12 (2021) 3. https://doi.org/10.1051/epjpv/2021003.

CHAPTER 7: Conclusions and Future Work

Ultrasonic spray pyrolysis (USP) preparation technique has been used in this thesis work to prepare all the thin films based on earth-abundant and easy-procurable metal oxides. The purpose of the preparation of metal oxides thin films was to make them suitable for use in “all-oxide” solar cells. The goal of the thesis work was to prepare the metal oxides with optimum quality using only the technique of USP and incorporating non-toxic raw materials. The research followed a unique process where all the materials necessary for use in “all-oxide” solar cells are developed using a single equipment. The materials are prepared in such a process such that they can be easily upgraded to industrial scale for large area depositions. In general, the preparation process using USP is flexible, quick, and easily adaptable which makes it a very promising technique for preparation of metal oxide thin films as it can lower the fabrication costs to a great extent.

At the beginning of the thesis, we discussed about the basics of photovoltaics and oxide-based semiconductors. The advantages and disadvantages of the different categories of solar cells are discussed. In this context, the necessity for developing metal oxide based solar cells were discussed. The typical heterojunctions based on ZnO-Cu_2O along with their functionalities were discussed. The various methods to develop such heterojunctions along with the typical power conversion efficiencies achieved by these devices were enlisted. Numerical simulations were performed using Silvaco Atlas® software to understand in-depth about the type and quality of materials needed to fabricate an “all-oxide” solar cell device. By default, Cu_2O was chosen as the absorber layer. ZnAlO was used as the window/top contact layer. A ternary material, zinc germanium oxide (ZnGeO) was chosen as the buffer layer. The implications of the content of germanium in the ternary on the performance of solar cells are discussed and analyzed in detail. With a certain percentage of germanium doping the “all-oxide” solar cells can reach conversion efficiencies up to 9.57 %. This also must be in conjunction with certain thickness and quality of absorber and the window layers. The impact of the interface defect layers is also studied to reach high conversion efficiencies. This study helped us to understand the role of each layer along with fair amount of idea about the qualities of each layer necessary to develop “all-oxide” solar cells.

Prior to the preparations, the idea was to understand in detail the ultrasonic spray process with the involved spray parameters and their possible effect on the prepared films. The spray process and the parameters are discussed in detail in the chapter 2 of the thesis. The ultrasonic spray pyrolysis

for preparation process was classified by the generation and transport of the atomized droplets and ultimately getting deposited on a heated substrate with a pyrolysis chemical reaction. The spray parameters were optimized to work in tandem to produce high-quality films. The parameters that we optimized for our preparations are as follows: Substrate temperature; shaping air pressure; nozzle-substrate height; solution flow rate; nozzle speed; dwell time; nozzle power; spray cycles; spray position; substrate choice; precursor solution concentration. With in-depth knowledge about these parameters, we proceeded towards the preparation of the specific films. For the preparations of all the films, specific design of experiments was set up to understand the role of a specific parameter on the quality of the prepared films.

We started with preparation of zinc oxide (ZnO). As zinc oxide properties can be tuned with respect to the preparation conditions, it has the potential to be used as a window or top contact layer. We found a higher set preparation temperature of 450 °C is necessary to have a complete pyrolysis reaction which can give highly transparent ZnO films. Certain volumes of acetic acid were used in the precursor solutions to have a certain pH which helps in the spray atomization of the solution droplets by reducing the surface tension of water and aids in the non-formation of hydroxides in the final prepared films. With these settings highly transparent films were prepared with certain values of spray flow rate and nozzle speed. Even the transparency remained nearly unchanged with the increase in thickness of the films. Less concentration of zinc acetate precursor salt in the precursor solution (0.03 & 0.05 mol/L) was important to have improved texture quality in the films as found from the XRD analysis. Annealing post-preparation helped to increase the conductivity of ZnO thereby proving its effectiveness for a conductive window layer for applications in “all-oxide” solar cells.

Next, we moved on to prepare zinc magnesium oxide (ZnMgO). The molar composition of magnesium precursor was varied from 0 % to 70 %. This range is the most as of now compared to other literatures. Mostly, low magnesium incorporation in zinc oxide is favoured due to the low solubility limit. For, our case it was even more challenging as we used only water-based precursor solution for the preparations. So, precise control on the spray preparation parameters was of utmost importance. In this preparation also high set temperature of 470 °C was used with acetic acid in the precursor solution. From the chemical and structural analysis of the films we found the miscibility limit of magnesium in zinc oxide to be nearly 30 mol%. This range is quite high compared to other solution-based preparation processes. The XRD analysis showed that till nearly 30 mol% of magnesium incorporation the wurtzite crystalline structure of the films is retained. The bandgap

energies of the films increase monotonously with the increase in magnesium content in the films. All the films with the different compositions of magnesium (0 mol% to 70 mol%) showed high transparency. The measurement of the electrical properties was limited to films with magnesium 7 mol%, beyond which the films were semi-insulating. With the high transparency of the films, with good crystalline properties the films with specific magnesium compositions could be used as buffer layers for "all-oxide" solar cells.

Cuprous oxide (Cu_2O) was next prepared as the possibility to be used as absorber layers in "all-oxide" solar cells. The temperature plays a huge role in the preparations to maintain the Cu_2O phase in the films. We have seen from the structural analysis of the films that beyond 240 °C preparation temperature (390 °C set temperature) the films have only the CuO phase. So, control on the temperature in conjunction with the other spray preparation are important. Also, another important aspect is the use of the reducing agent with certain concentrations. Whatever the preparation temperature is, without using the reducing agent which is D-sorbitol in our case we will not be able to control the formation of the "cupric" phase. A typical concentration of D-sorbitol (0.05 mol/L) which is easily dissolved in the precursor solution can be used at the low preparation temperatures to prepare Cu_2O. The optical analysis revealed films with only the cuprous phase (Cu_2O) with high absorption in the visible spectrum region. The current-voltage measurements showed an ohmic nature of the Cu_2O films with gold contacts on top. These characteristics makes the Cu_2O films suitable candidate for absorber layers in "all-oxide" solar cells.

To broaden the horizon of the preparation process using USP, two more materials, one ternary and the other a quaternary were prepared. These two materials were prepared keeping in mind their applicability for implementation in "all-oxide" solar cells. The ternary zinc aluminum oxide (ZnAlO) was prepared to be used a window cum top contact layer with good conductivities. The quaternary zinc aluminum magnesium oxide (ZnAlMgO) was prepared to be used window or top contact or as buffer layers for "all-oxide" solar cells. For preparing ZnAlO, low molar compositions of Al (0 % to 5 %) were used in the precursor solution due to extremely low solubility limit of the Al precursor. XRD analysis showed the wurtzite nature for all the films with the different Al compositions. On the contrary, the optical properties especially the transparency of the films degraded with the increase of the Al content in the films. Even the films exhibited higher resistivity for the higher Al content films. From the perspective of ZnAlO being used as the top contact layers, it is essential to maintain very low molar concentrations of Al precursor (up to 2 mol%) in the precursor solution for successful high-quality film preparations. The quaternary ZnAlMgO was prepared with magnesium

molar composition varying from (0 % to 7 %) but the Al molar concentration were always fixed to 1 and 2 mol%. The texture quality of the films was better with the higher Mg contents with no impact on the lattice disorders as revealed from the structural (XRD measurements) and optical analysis (Urbach energy estimations). The films were highly transparent (more than 90 %) with higher bandgap energies compared to only ZnO. Compared to films with only Mg, the films prepared with co-doped Mg and Al, showed improved electrical properties with higher Mg compositions. So, with the high optical and structural properties the ZnAlMgO films can be used as either top contact, window, or buffer layers for "all-oxide' solar cells. Simulation performed using Solis device simulator showed a conversion efficiency of about 8 % using the "all-oxide" solar cell structure: ZnAlO/ZnO/ZnAlMgO/Cu_2O/ITO substrate. The results are comparable with the results obtained by using Silvaco Atlas® with ZnGeO as the buffer layer.

The preparation of all the above-mentioned films opens the pathway for the actual fabrication of an "all-oxide" solar cell device. But the fabrication won't be an easy task to achieve. We have prepared all the films on soda lime glass substrates. For the device fabrication, the films need to be prepared on different substrates and on top of other prepared films. So, the spray parameters that we have used for a particular film preparation may be not as effective in these cases. Suitable adjustment and modifications in the spray parameters and even in the spray process should be essential for preparing the layers. The spray preparation temperature would be particularly crucial in this aspect. We have seen that different set preparation temperatures are necessary for preparation of the different films with optimum quality. So, for e.g., if ZnO requiring a high set preparation temperature is prepared on top of Cu_2O that demands a low preparation temperature, very easily an interface defect layer (CuO in all possibilities) can be formed. So, the control on the spray parameters to have a control on the interfaces will be important. Using different sample holders with different levels of heat conductivities can be tried.

The spray process along the parameters needs to be adjusted keeping the desired structure of the "all-oxide' solar cells. The structure can be either a substrate based (light from the front/top) or superstrate based (light from the back/rear). So, the sequence of the preparation of the films would be different and hence the preparation process needs to be suitably adjusted.

Another idea is to try to prepare other materials as buffer layers. The buffer layers are essential to have a better heterojunction quality. Gallium oxide (Ga_2O_3) is one such material that can be prepared to be used as buffer layers in "all-oxide" solar cells. Even we tried to prepare Ga_2O_3, but we needed

more time to control the precursor solution properties and the suitable adjustment of the spray preparation parameters to be able to deposit Ga_2O_3 with optimum quality. The Ga_2O_3films that we prepared were mostly amorphous. With better control on the preparation process, Ga_2O_3 films can be prepared by USP.

Another aspect that can be looked upon is the uniformity of the deposited films. In our case, we have prepared the films using a linear to and from movement of the spray nozzle. The films were very uniform at the spray zone. But for large area depositions, uniformity of the films can be an issue. In this case, different schematic for the movement of the spray nozzle during the actual spray process can be tried. The thickness of the films would not be the same, but with control on the spray flow rate, the nozzle speed, the preparation temperature, and the control on the precursor solution concentration can make the large area films uniform. The resistivity of the films can also vary with the uniformity. Highly uniform films are desired to have large-area controlled resistivity in the films.

All our films were prepared keeping in mind their applicability for “all-oxide” solar cells. But the metal oxide thin films can be used for other opto-electronic applications. The preparations can be upgraded according to the quality of the films that needs to be achieved for a particular application. Doping and co-doping can play a big role in this matter. A thorough understanding is required about the chemistry behind the process. Then only the spray preparation parameters need to be adjusted for preparation of high-quality films.

At the end we can say that the USP process to prepare metal oxide thin films has high potential in laboratory-based research and in the industry. This process can prepare high-quality films for different optoelectronic applications with much less time and energy consumption compared to other vacuum-based techniques.

CV

Sourav BOSE

RESEARCH EXPERIENCE

[2019 – 2022 (September)] - Doctoral Researcher

Laboratoire Matériaux Optiques, Photonique et Systèmes (LMOPS), CentraleSupélec, Metz, France

- Development and Study of Earth-Abundant Oxides based Thin Films for Solar Cells by Ultrasonic Spray Pyrolysis

[2020 – 2022 (September)] - Visiting Doctoral Researcher

Institut Jean Lamour (IJL), Université de Lorraine, Nancy, France

- Development and Characterization of Oxides based Thin Films for Solar Cells

[2017 – 2019] - Research Fellow

International Iberian Nanotechnology Laboratory (INL), Braga, Portugal

- Development of Passivation Layers for Ultra-thin CIGS Solar Cells

[2014 – 2017] - Research Assistant (Wissenschaftlicher Mitarbeiter - HiWi) Positions

Fraunhofer Institute for Solar Energy Systems (ISE), Freiburg im Breisgau, Germany

- Development and Characterization of ITO Layers for Silicon Heterojunction Solar Cells
- Silicon Solar Cell Characterization
- Characterization of Catalyst Coated Membranes (CCMs) for PEM fuel Cells by Scanning Electron Microscopy (SEM), Preparation of CCMs using Transfer decal, hot-pressing & Laser cutting

EDUCATION

[2019 – 2022 (September)] - PhD in Materials Sciences

University of Lorraine, Ecole Doctorale: C2MP, Metz & Nancy, France

- **Thesis:** **Development and Study of Earth-Abundant Oxides based Thin Films for Solar Cells by Ultrasonic Spray Pyrolysis: "From Unbeknownst to Erudite Processes"** – LMOPS - CentraleSupélec, Metz, France

[2013 – 2016] - Master of Science (M.Sc.) in Microsystems Engineering

Albert Ludwig University of Freiburg, Freiburg im Breisgau, Germany

- **Thesis:** **Development of Industrial Feasible TCO Layers for Silicon Heterojunction Solar Cells by MF Sputtering** – Fraunhofer ISE (Dept. PTQ); Freiburg, Germany

[2009 – 2013] - Bachelor of Technology (B.Tech) in Electronics & Communication Engineering (ECE)

West Bengal University of Technology (WBUT), Kolkata, India

- **Thesis:** **Microcontroller Based Automatic Multi-Storied Car Parking System** – Dream Institute of Technology (Dept. ECE); Kolkata, India

RESEARCH LINKS

Details of Research activities can be found from the links mentioned below:

- **Google Scholar:** https://scholar.google.com/citations?user=UIzk_e4AAAAJ&hl=en
- **ResearchGate:** https://www.researchgate.net/profile/Sourav_Bose7
- **Publons:** https://publons.com/researcher/1857275/sourav-bose/

SKILLS

Technical: Semiconductor process technology, Photolithography, Reactive Ion Etching, Plasma and Sputter Depositions, Ultrasonic Spray Pyrolysis, Raman Spectroscopy, Thin Film Characterizations, Surface Analysis: SEM/EDX, AFM, Profilometry, Solar Cell Characterization Techniques: Current-voltage, EQE and Hall measurements, Sheet Resistance; QSSPC, Photoluminescence Imaging, Reflection Measurements, Ellipsometry

Software:

- LANGUAGES KNOWN: VHDL, C Programming, Python (Basic)
- TOOLS: Orcad, P Spice, Target 3001, Origin 9G; Statistica, CES Edupack, AutoCAD
- SIMULATION TOOLS: Matlab, SCAPS

Managerial: Problem solving, Team Player, Project Management, Adaptive, Creative, Self-motivation, Eagerness to grow, Enthusiastic, Effective Communication

List of Publications

Articles

[1] S. Bose, C. Chevallier, S. Ould Saad Hamady, N. Fressengeas. Optical and Electrical Properties of ZnMgO with High Mg Content Elaborated by Ultrasonic Spray Pyrolysis using Water-Based Solutions, Physica Status Solidi A: Applications and Materials Science. (**2022**). https://doi.org/10.1002/pssa.202200091.

[2] C. Chevallier, **S. Bose**, S. Ould Saad Hamady, D. Horwat, J.-F. Pierson, P. Boulet and N. Fressengeas. Effect of temperature and D-sorbitol reducing agent content on the structural and optical properties of copper oxide thin films deposited by ultrasonic spray pyrolysis, Thin Solid Films (**2022**). https://doi.org/10.1016/j.tsf.2022.139435.

[3] S. Bose, C. Chevallier, S. Ould Saad Hamady, D. Horwat, J.-F. Pierson, P. Boulet, T. Gries, T. Aubert, N. Fressengeas. Elaboration of high-transparency ZnO thin films by ultrasonic spray pyrolysis with fast growth rate, Superlattices and Microstructures 156 (**2021**) 106945. https://doi.org/10.1016/j.spmi.2021.106945.

[4] C. Chevallier, **S. Bose**, S. Ould Saad Hamady, N. Fressengeas. Numerical investigations of the impact of buffer germanium composition and low cost fabrication of Cu_2O on AZO/ZnGeO/Cu_2O solar cell performances, EPJ Photovoltaics. 12 (**2021**) 3. https://doi.org/10.1051/epjpv/2021003.

[5] J. Lontchi, M. Zhukova, M. Kovacic, J. Krc, W.-C. Chen, M. Edoff, **S. Bose**, P.M.P. Salomé, J. Goffard, A. Cattoni, L. Gouillart, S. Collin, V. Gusak, D. Flandre. Optimization of Back Contact Grid Size in Al_2O_3-Rear-Passivated Ultrathin CIGS PV Cells by 2-D Simulations, IEEE J. Photovoltaics (**2020**). https://doi.org/10.1109/JPHOTOV.2020.3012631.

[6] J. M. V. Cunha, T.S. Lopes, **S. Bose**, A. Hultqvist, W.C. Chen, O.D. Gargand, R. M. Ribeiro, A. J. N. Oliveira, M. Edoff, P. A. Fernandes, P. M. P. Salomé. Decoupling of Optical and Electrical Properties of Rear Contact CIGS Solar Cells, IEEE J. Photovoltaics. (**2019**). https://doi.org/10.1109/JPHOTOV.2019.2933357

[7] T. S. Lopes, J. M. V. Cunha, **S. Bose**, J. R. S. Barbosa, J. Borme, O. D. Gargand, C. Rocha, R. Silva, A. Hultqvist, W. C. Chen, A. G. Silva, M. Edoff , P. A. Fernandes, P. M. P. Salomé. Rear Optical Reflection and Passivation Using a Nanopatterned Metal/Dielectric Structure in Thin-Film Solar Cells, IEEE J. Photovoltaics (**2019**). https://doi.org/10.1109/JPHOTOV.2019.2922323

[8] P.A. Fernandes, A. Shongalova, A.F. da Cunha, J.P. Teixeira, J.P. Leitão, J.M.V. Cunha, **S. Bose**, P.M.P. Salome, M.R. Correia. Phase selective growth of $Cu_{12}Sb_4S_{13}$ and Cu_3SbS_4 thin films by chalcogenization of simultaneous sputtered metal precursors, Journal of Alloys and Compounds (**2019**). https://doi.org/10.1016/j.jallcom.2019.05.149.

[9] S. Bose, J. M. V. Cunha, J. Borme, W. C. Chen, N. S. Nilsson, J. P. Teixeira, J. Gaspar, J.P. Leitão, M. Edoff, P. A. Fernandes, P. M. P. Salomé. A morphological and electronic study of ultrathin rear passivated $Cu(In,Ga)Se_2$ solar cells, Thin Solid Films (**2019**). https://doi.org/10.1016/j.tsf.2018.12.028

[10] S. Bose, J. M. V. Cunha, S. Suresh, J. D. Wild, T. S. Lopes, J. R. S. Barbosa, R. Silva, J. Borme, P. A. Fernandes, B. Vermang, P. M. P. Salomé. Optical Lithography Patterning of SiO_2 Layers for Interface Passivation of Thin Film Solar Cells, Solar RRL (**2018**). https://doi.org/10.1002/solr.201800212

International Conferences

[1] S. Bose, C. Chevallier, S. Ould Saad Hamady, and N. Fressengeas. Elaboration of ZnMgO thin films by ultrasonic spray pyrolysis for optoelectronic applications using water-based solutions. European Materials Research Society (E-MRS) Spring Meeting, Strasbourg, France. Live. **2022**.

[2] S. Bose, C. Chevallier, S. Ould Saad Hamady, D. Horwat, J. F. Pierson, P. Boulet, T. Gries, A. T, and N. Fressengeas. Effect of the precursor concentration on structural properties of ZnO thin films by ultrasonic spray pyrolysis. European Materials Research Society (E-MRS) Spring Meeting, Strasbourg, France. Live. 2021.

[3] S. Bose, C. Chevallier, S. Ould Saad Hamady, N. Maloufi, J. Guyon, O. Perroud, and N. Fressengeas. Ultrasonic spray pyrolysis deposition of cuprous oxide thin films: Microstructure and optical investigations. European Materials Research Society (E-MRS) Spring Meeting, Strasbourg, France. Live. **2021**.

[4] S. Ould Saad Hamady, S. Yusof, **S. Bose**, C. Chevallier, N. Fressengeas, Q. Kieffer, Z. Hassan, M. A. Anas, W. F. Lim, and S. S. Ng. Development of InGaN based solar cells: present status and challenges. 5th Meeting of Malaysia Nitrides Research Group (MNRG 2020), Penang, Malaysia. Invited keynote speaker. Live. **2020**.

***[5] S. Bose**, C. Chevallier, S. Ould Saad Hamady, J. F. Pierson, D. Horwat, and N. Fressengeas. Development of New Materials for Thin Film Photovoltaics Using the Ultrasonic Spray Pyrolysis. European Materials Research Society (E-MRS) Spring Meeting, Strasbourg, France. Poster. Cancelled due to the COVID-19 (coronavirus) pandemic. **2020**.*

***[6]** C. Chevallier, **S. Bose**, S. Ould Saad Hamady, Q. Kieffer, Z. Hassan, S. Yusof, A. Mohd, W. F. Lim, and S. S. Ng. Ultraviolet micro-Raman spectroscopy study of high indium composition InGaN thin film grown on patterned sapphire substrate. International Workshop on Nitride Semiconductors, Berlin, Germany. Oral. Cancelled due to the COVID-19 (coronavirus) pandemic. **2020**.*

Abstract

The results on preparation of environmentally compatible, earth-abundant metal oxide thin films using the technique of ultrasonic spray pyrolysis are presented. Three essential materials are developed for the purpose of realization of an “all-oxide” solar cell device: Zinc oxide (ZnO) as window layer; zinc magnesium oxide (ZnMgO) as a buffer layer and cuprous oxide (Cu_2O) used as an absorber layer. Comprehensive design of experiments was set up for the preparation of each material. Highly transparent ZnO was prepared in wide range of thickness with high crystalline qualities with specific preparation temperature with a precise control on the concentration of the precursors. ZnMgO was prepared by varying the molar compositions of the magnesium precursor in the precursor solution. Up to nearly 30 % of Mg, the ZnMgO films exhibited single crystalline phase with high transparencies. High-absorbing Cu_2O preparation was optimized with effective control on the preparation temperature and the concentration of a new reducing agent (D-sorbitol). To expand the horizon of efficiency of our preparation process, two more materials, ZnAlO and ZnAlMgO, were prepared. It was found that the optical, electrical, and structural properties of the ZnAlO films could be modulated for use in “all-oxide” solar cells by varying magnesium (up to 7 mol%) and aluminum (up to 2 %). The bandgap energies and the electrical properties of the films were modulated with the co-doping so that they can be integrated as window/top-contact/buffer layers in “all-oxide” solar cells. Additionally, simulations performed using Silvaco Atlas® and Solis also demonstrates the applicability of these films for “all-oxide” solar cells.

Keywords: Ultrasonic Spray Pyrolysis, Semiconductors, Zinc Oxide, Zinc Magnesium Oxide, Copper Oxide, Preparation, Thin Film, Structural Properties, Optical properties, Electrical properties, All-Oxide Solar Cell, Photovoltaics.

Résumé

Dans ce travail de recherche, sont présentés les résultats de l'élaboration de couches minces d'oxydes à base d’éléments abondants par la technique de spray pyrolyse ultrasonique. Trois matériaux constituant les briques de base de la cellule solaire « tout oxyde » ont été développés : l'oxyde de zinc (ZnO) comme couche fenêtre ; l'oxyde de zinc et de magnésium (ZnMgO) comme couche tampon et l'oxyde de cuivre (Cu_2O) comme couche absorbante. Un plan d’expériences précis a été mis en place pour chaque type d’élaboration afin de comprendre l'effet des paramètres d'élaboration sur les propriétés des films. Des caractérisations optiques, structurelles, morphologiques et électriques ont été utilisées pour étudier les propriétés du film et les résultats discutés et analysés en détail. Des films minces de ZnO avec une transparence élevée dans une large gamme d'épaisseurs ont été obtenus. Le ZnMgO a été élaboré avec une phase monocristalline et une transparence élevée. La limite de miscibilité du magnésium (près de 30 % dans notre cas) est supérieure à celle habituellement obtenue avec les méthodes d’élaboration sans vide. L'élaboration de l’absorbeur Cu_2O a été optimisée avec un contrôle efficace de la température d'élaboration et de la concentration d'un nouvel agent réducteur (D-sorbitol). Pour élargir les perspectives de ce travail, deux autres matériaux, ZnAlO et ZnAlMgO, ont été élaborés. Nous avons ainsi mis en évidence le fait qu’avec de faibles concentrations d'aluminium (jusqu’à 2 %) et de magnésium (jusqu’à 7 %), les propriétés optiques, électriques et structurales des films de ZnAlO pouvaient être modulées pour une utilisation en tant que couche fenêtre ou TCO dans les cellules solaires « tout-oxyde ». De plus, les simulations réalisées à l'aide des logiciels Silvaco Atlas® et Solis démontrent également le potentiel de ces films pour les cellules solaires « tout-oxyde ».

Mots-clés : Spray pyrolyse ultrasonique, Semi-conducteurs, Oxyde de zinc, Oxyde de zinc et de magnésium, Oxyde de cuivre, Élaboration, Couche mince, Propriétés structurales, Propriétés optiques, Propriétés électriques, Cellule solaire « tout-oxyde », Photovoltaïque.